A new vision on (Extrasolar) Giant Planets Internal Structure and Evolution

Jeremy Leconte

N° d'ordre : TBD
N° attribué par la bibliothèque : TBD

ÉCOLE NORMALE SUPÉRIEURE DE LYON

THÈSE

présentée le 5 octobre 2011 pour obtenir le grade de

Docteur en Physique
de l'École normale supérieure de Lyon
Spécialité : Astrophysique

par Jérémy LECONTE

A new vision on (Extrasolar) Giant Planets Internal Structure and Evolution

-

Un nouveau regard sur

la Structure interne et l'Évolution des Planètes Géantes Solaires et Extrasolaires

Membres du jury :

M. Michel MAYOR	Président
M. Jean Paul ZAHN	Rapporteur
M. Yann ALIBERT	Rapporteur
M. Franck SELSIS	Examinateur
M. Gilles CHABRIER	Directeur de thèse
Mme. Isabelle BARAFFE	Directrice de thèse

Thèse préparée au sein du
Centre de Recherche Astrophysique de Lyon
École normale supérieure de Lyon

Contents

Remerciements

Alors que je me réjouissais à l'idée d'écrire ces quelques lignes, aussi bien grâce à la réminiscence des moments passés avec ceux à qui elles s'adressent que parce qu'elles mettent, au moins chronologiquement, un point final à l'écriture de ce manuscrit, je me rends compte à quel point il m'est difficile d'exprimer par des mots toute la gratitude que j'éprouve pour toutes les personnes qui m'ont permis d'arriver jusque là... Essayons quand même.

Je tiens d'abord à remercier mes deux directeurs, Gilles et Isa, pour leur présence qui m'a souvent aidé à trouver la bonne voie, pour leurs absences qui m'ont permis d'en explorer d'autres, et surtout pour leur complémentarité qui m'a apporté aussi bien de nombreuses idées que la méthode pour les développer.

Un grand merci à tous les membres de mon jury, Yann Alibert, Michel Mayor, Franck Selsis et Jean Paul Zahn qui m'ont fait le plaisir et l'honneur d'accepter de présider/rapporter/examiner cette thèse malgré leurs emplois du temps chargés et un meeting du DPS aux dates plus qu'incongrues.

Merci à tous mes collaborateurs qui m'ont accordé leur temps et leur confiance, en particulier Franck Selsis, avec qui on n'a jamais réussi à finir un projet malgré ses idées, ses conseils, son enthousiasme et ses invitations à Bordeaux. Je ne désespère pas pour le post-doc. Une pensée particulière aussi pour Rémi Soummer, qui m'a fait découvrir le monde passionnant de l'astro et des exoplanètes. Même s'il ne nous a pas été donné d'en découvrir une, un grand merci parce qu'une fois n'est pas coutume, il a toujours pris du temps pour moi, même quand le temps se faisait rare.

Un petit mot mais un grand merci à tous les professeurs, M Bavey, Mme Cordier, M Gillois et Mme Thor pour ne citer qu'eux, qui ont su me donner le goût des sciences et de l'enseignement, mais qui ont surtout su aiguiser ma curiosité.

Je souhaite aussi exprimer ma gratitude à tous les artistes de l'ombre qui ont toujours été là, rendant tout simplement ces trois ans possibles, et allant parfois jusqu'à faire le travail à ma place. Je veux bien sur parler de la SNCF (2h30 porte à porte même par tempête, je crois qu'on n'en parle pas assez), des Velo'v (non je ne me suis pas trompé), du Chandrasekhar, du poly de TP d'optique d'agreg, de MATHEMATICA, et de tant d'autres.

Malgré toutes les attaches qui me rapprochaient de la capitale, cela a toujours été un plaisir de revenir à Lyon pour y faire de la recherche, pour y enseigner et pour y rigoler. Ça, je le dois à tous les gens fabuleux que j'y ai côtoyés et qui n'ont pas fait l'économie de leur joie de vivre :

- Ceux qui ont du me supporter au labo d'abord, Albéric (discret mais toujours là), Béatrice, Christine et Stéphanie (sans qui j'essaierais toujours de comprendre comment prendre mes billets d'avion), Benjamin (c'est M Bibendum, il est...), Benoit (a star is born), Bernd, Cédric (dit le rouge), Christophe (who else), Elisabeth (le *petit* élément féminin du bureau), France, François (et toute la fédé de patinage artistique), GG (qui me pique régulièrement mon diminutif), Guillaume (avec sa **** et son couteau), Jacques (le seul thésard qui est encore plus virtuel que moi), Jean-François (le roi du DISCO), Laure (super maman), Marie Christine (super grand maman), Maxime

(et toute la section spéciale noise du Grounnnnnd Zero), Nathaniel (et ses blagues plus que douteuses), Ahne (qui les supporte), Neil (sportivement vôtre), Rolf, Doris et Cyril (la swiss touch), Samira (sans qui le papier se ferait rare), Serena (sans qui je serais peu être encore bloqué a Turin) et Vincent (attention, tortue du calembour).

- Ceux qui ont su égayer mes nombreuses, et parfois laborieuses, heures de TP, Aude, Bernard, Cendrine, Eric, Patrick, et tous les élèves qui n'en finiront jamais de me surprendre. Même ceux qui comme moi à leur place avaient une motivation plus que volatile.

- Ceux avec qui j'ai partagé plus qu'un appart enfin, Anne (et son rire), Laure (la plus Vernant de toutes), Manu (anthropo forever), Marion (et ses pyjamas sexys) et mes Marines adorées.

Parce que les parisiens ne sont pas en reste, et parce que même si ils nous insupportent dans le métro, la vie ne serait pas tout à fait aussi drôle sans eux (et les autres), je veux aussi remercier Anne (Sans France Psycho Girl, on s'était dit rendez vous...), les manches du toujours idoine Jean Michel l'Huillier (malgré le néant qui les encombre), Benoit (dit Johnny Utah, désolé mec je t'avais pas reconnu), Elsa ("sorry ranger, yes we are"), Etienne (le grand gourou), Isa (redfish eater shark), JD (ours blaaaaaaaanc), Julie (hard training future mom), Julien (dit Paulo le poulpito), Lorie (c'est ma meilleure amie), Lorraine (notre petit génie), Marianna (le docteur Maboul est appelé pour la contre-soirée cuisine), Marine rousse (globe trotteuse et toujours à l'écoute), Nicolas (et le Jurançon perdu), Nicole (une marraine comme on en voudrait tous), Raphou (born to be wild), Romain (le blond qui viendrait vous chercher même au milieu d'un goulet surplombant une barre rocheuse) et Sarah (entre les retours de Cocarde, de soirées rose, de soirées X... comment choisir).

La liste ne saurait être complète sans mon compagnon de galère, l'ange gardien mélomane des coups durs, l'avant centre des entreprises absurdes, le plus insupportable colloc-relais de tous les temps... Merci mon lapinou.

Parce qu'ils sont très nombreux, c'est brièvement mais de tout mon coeur que je fais de gros bisous à toute ma famille et à la Normandie. Il m'aurait été impossible d'imaginer en arriver là sans eux, et en particulier sans mes parents et mon frangin qui m'ont tout appris... et bien plus que de la physique.

Enfin, à mon amour,
et mon grain de folie.
À mon astre du jour,
et celui de mes nuits.

500 BC - 1995 AD: 8 /
1995 AD - 2011 AD: 500

-Pourquoi l'azur muet et l'espace insondable ?
Pourquoi les astres d'or fourmillant comme un sable ?

Arthur Rimbaud, Soleil et chair

Finding planets seems to be a sport we are getting good at. While it took more than two thousand years of astronomical observations for the ancients to find the eight planets[1] orbiting with the Earth around the Sun, more than 500 exoplanets have been found in the last fifteen years. If it is difficult to give an exact number, it is not only because determining what is a planet is complex, but also because this number is now growing by the day. Doubling every three years, it grows nearly as rapidly as the complexity of micro-processors predicted by the *Moore* law.

This offers a unique chance for the physicist. While the planets in our solar system offer exquisite information on the internal and atmospheric physics, exoplanets, and especially the transiting ones, provide the possibility to probe the physics of planetary sciences in a wider diversity of extreme conditions and with a statistically significant number of objects. However, if space and ground based detection missions are numerous, theoretical studies aimed at the analysis and comprehension of the present and future data are necessary.

Figure 1: Cumulative number of solar and extrasolar planets discovered (solid). Exponential fit (dashed).

Even with the few data that we can get for any single exoplanetary system, unexpected features appear. More than fifteen years ago, Doppler spectroscopy alone already changed our vision of planetary formation by finding giant planets[2] nearly ten times closer from their star than is mercury from our Sun (Mayor and Queloz 1995). But in the last decade, thanks to the additional photometric monitoring of the transit of some of these planets, yielding their true masses and radii, an even more disturbing pattern arose (Henry et al. 2000). For a given mass, Giant exoplanets look much bigger than expected by the same theory which (more or less) accords with our present understanding of Solar System giant planets.

To unravel the origin of these peculiar properties, we thus have to deconstruct part of the sophisticated theories that were developed to understand our Solar System, and reconstruct them with less restrictive hypotheses. To that purpose, the large size of the exoplanet sample is a significant asset as it

---

[1]Pluto will always be a planet in my heart.

[2]Also called Hot Jupiters or Pegasids.

allows us to directly test the generality of our theoretical predictions. However, one should not forget about the planets that are closest to us. Even if it is hard to reproduce exactly all the observed features of these well documented objects with the simple general models that we are trying to develop, the large amount of data coming from various origins can provide much more precise constraints. Moreover Solar System planets offer the advantage of reminding us that a planet is much more complex to understand than a data point in a mass-radius diagram.

This is in that spirit that this thesis makes an attempt to address some unresolved problems of the structure and evolution of giant planets, taking advantage of the information that can be found both inside and outside our Solar System.

As the so called *radius anomaly* I was depicting above had clearly been identified from the very beginning of this work as one of the main contemporary unanswered question in this particular field, it can often be found, among others, as one of the underlying motivations for the various studies described hereafter. However, if it has been a motivation, it has not been an end in itself, as the problem was not so much to explain an unexpected property than to identify and understand the main physical processes at work in exoplanetary systems.

Thus, in the following chapters, I tried not only to characterize and quantify the effect of the different ingredients considered (stellar irradiation, double-diffusive convection, tidal heating) on the radius of extrasolar giant planets, but also to develop the analytical and numerical tools necessary to model these processes in a wider context. For this reason, I tried as much as possible to compare the models used or developed here with others found in the literature to highlight their strengths and limitations. When possible, I also tried to provide numerical estimates of the main physical parameters needed to directly apply these models to different specific cases.

User guide

As the various subjects treated here are rather independent, I chose to dedicate the first part of each chapter to the introduction and definition of the most necessary physical concepts. Even if some of these concepts are well known, it will allow me to detail the context in which the work presented hereafter, has been done.

In addition, for pedagogic purposes, and so that the interested reader may have all the equations at hand, I will also develop in length the analytical theories that I used and often extended during this thesis. However, as much as possible, these developments have been put in the appendices that can be found at the end of the present manuscript.

Thus, to ease the progression of the reader through these various sections, at the beginning of each chapter, a framed paragraph summarizes the goals of each section of the chapter, and where the main results of the present work can be found.

Abstract

The detection and characterization of extrasolar planets clearly appears as one of the main goals of observational astronomy for the coming years. Space and ground based projects are numerous, but theoretical studies aimed at analyzing and understanding available and future data are needed.

During this thesis, I study various physical processes affecting the internal structure and evolution of both solar, and extrasolar giant planets. Here are some of the main goals of this work which is divided in four independent parts presented in the chapters 2 to 5.

- In a first study, I investigate the impact of the intense stellar irradiation received by a close in planet on its subsequent internal evolution. This allows me to quantify the *radius anomaly* of bloated Hot Jupiters and to constrain their internal composition. I also show that most features of the mechanical structure of gaseous substellar objects can be well captured by a single effective polytropic index, and that this index is linked to the behavior of the mass-radius relationship. Finally, I propose an observational criterion based on the mean density of the object to distinguish massive giant planets from mini brown dwarfs.

- Then, I use both analytical and numerical models to study the tidal and centrifugal distortion of a fluid planet, and infer its shape. This allows me to provide numerical estimates of various quantities characterizing the mechanical internal structure of giant planets and brown dwarfs (e.g. Love number, ...). I find that because close in planets are tidally elongated toward the star, they exhibit a smaller cross section, yielding major implications for transit measurements. In particular, an underestimation of the radius.

- In Chapter 4, I examine how the presence of double-diffusive convection caused by a heavy elements gradient in the gaseous envelope of a planet can decrease the efficiency of its internal heat transport, and affect its structure and evolution. To do so, I develop a completely analytical model of layered convection and apply it to the Solar System gas giants. These models yield a metal enrichment for our gaseous giants up to 30 to 60% larger than previously thought. As the heavy elements tend to be redistributed within the gaseous envelope, the models predict smaller than usual central cores inside Saturn and Jupiter, with possibly no core for this latter.

- Finally, I investigate the coupling between the orbital and the thermal evolution of a planet arising from the strong star-planet tidal interaction. Using an analytical model for the secular tidal evolution which is fit to describe highly eccentric orbits, I first show that using tidal models based on a quasi circular approximation can lead to quantitatively, and sometimes qualitatively different orbital evolutions, and can overestimate the evolution timescales by orders of magnitude. Subsequently, I find that tidal heating alone is not a viable explanation for the observed radius anomaly of transiting planets.

Through these different studies, I developed various analytical models and numerical codes (such as CHESS) that are both flexible and robust, and which now allow me to study the properties of new extrasolar planets and brown dwarfs as they are discovered.

Résumé

La détection et la caractérisation d'exoplanètes apparaissent clairement comme des thèmes centraux de l'observation astronomique pour les années à venir. Les projets spatiaux ou au sol sont nombreux (HARPS, CoRoT, Kepler, JWST, SPHERE...), mais les études théoriques visant à l'analyse et à la compréhension des données recueillies et à venir sont nécessaires. Durant cette thèse j'ai étudié divers processus physiques affectant la structure interne et l'évolution des planètes géantes, aussi bien au sein, qu'à l'extérieur de notre système solaire. J'ai notamment modélisé en détail :

- L'impact de l'irradiation intense émise par l'étoile sur l'atmosphère d'une planète à faible distance orbitale, et l'effet induit sur l'évolution interne de cette planète.

- Le couplage par dissipation de marée de l'évolution orbitale et thermique d'une planète interagissant avec sa proche étoile parente.

- L'effet de la déformation due aux marées sur les paramètres observables d'une planète en transit grâce au suivi photométrique de son passage devant l'étoile.

- L'incidence sur la structure et l'évolution d'une diminution de l'efficacité du transport de chaleur par convection due à un gradient d'éléments lourd dans l'enveloppe gazeuse d'une planète géante, conduisant au phénomène de convection double-diffusive.

A travers l'étude des ces divers processus, j'ai développé différents modèles analytiques et codes numériques qui sont à la fois flexibles et robustes, et qui permettent maintenant d'étudier certaines propriétés des nouveaux objets sub-stellaires détectés à mesure qu'ils sont découverts.

Chapter 1

The syntax of planetary structure

The heavenly motions... are nothing but a continuous song for several voices,
perceived not by the ear but by the intellect,
a figured music which sets landmarks
in the immeasurable flow of time.

John Banville

Contents

Before starting to introduce any new or exotic physics into the standard theory of giant planets structure, it seems mandatory to introduce its most basic concepts, and to define the notations that will be used throughout this work.

Hence, in this introductory chapter, we will only concern ourselves with the derivation of the basic equations and conservation laws applying to (sub)stellar objects (§ 1.1), and to the various physical ingredients needed to compute planetary models (§ 1.4 and § 1.5). Fortunately, to some extent, the physics of giant planets and brown dwarfs are very similar to stellar physics in their basic principles, and the reader can take advantage of the numerous outstanding textbooks in this area (Eddington 1926 ; Chandrasekhar 1939 ; Kippenhahn and Weigert 1990 ; Hansen and Kawaler 1994 ; to cite only a few).

In addition, in § 1.5.2, considering a toy model describing the radiative transfer in the atmosphere of a strongly irradiated giant planet, I show that numerical 1D calculations of the atmospheric boundary conditions of substellar objects that consider a redistribution of the stellar flux over the day side only may overestimate the impact of the irradiation on the structure of the object.

Even FOR THE MOST STUDIED CELESTIAL BODY IN THE UNIVERSE, namely, the Earth, when it comes to the problem of internal structure, direct observational data are very sparse. In order to fill the numerous gaps, and to get a global understanding of how the physics at play interact in planetary interiors, and make planets evolve the way they do, a global theory is needed. During the past two decades, this need has been strongly revived by the discovery of the first extrasolar planet (Mayor and Queloz 1995), of the first cool brown dwarf (Oppenheimer et al. 1995), and of the many that followed. But these discoveries also raised new constraints and challenges for the theory of planetary evolution: (i) observational data available for a given system are even more scarce, and often limited to a few global quantities (mass, radius, luminosity, etc... depending on the observational methods available), and (ii) the number and diversity of the systems discovered is huge, and still growing by the day.

A direct consequence of the first point is that modeling becomes mandatory to infer the values of even the most basic physical quantities describing the observed objects - such as their surface pressure and temperature, atmospheric composition and rotation speed, among others - from the limited set of available data (incoming stellar flux, spectrum, orbital configuration...), when it is possible at all. This is evidently a first call for simple but robust models with the ability to constrain the basic features of an object from a few global observables. Another, and maybe more stimulating consequence of this lack of data, is that it somewhat gives some license and freedom to the theorist, who can more freely explore known mechanisms in the most extreme regimes, or completely new exotic ones. Fortunately, the second point bears a subtle but powerful constraint. We are not looking at *single* objects anymore, but at *populations* ! Thus, any theory must be general and robust enough to account for the similarities and differences arising between members of what could seem, when looking at a limited set of parameters, an homogeneous family.

In any case, before starting to introduce any new or exotic physics into our model, or simply to get a basic picture of the problem at hand, it seems proper to review the basic concepts that underlie the theory of the structure and evolution of gaseous bodies, the assumptions that are commonly made, and the most robust features that can be drawn from these basic assumptions.

1.1   The basics of planetary and stellar structure

As in every problem of compressible fluid mechanics, the solution consists in finding expressions for the density (ρ), pressure (P), temperature (T), specific entropy ($\tilde{S}$), velocity ($\mathbf{v}$) as a function of both the radius vector, $\mathbf{r}$, and time t. To solve the problem, we thus need seven scalar equations[1] that will be provided by the conservation of mass, momentum (3 scalar relations), energy, and by the *fundamental relation* for the fluid constituting our object which encompasses two relations, one for the pressure (the famous *equation of state*) and one for the internal energy, or equivalently for the entropy.

---

[1]Reducing to five equations for the spherical case.

Deferring thermodynamical considerations for § 1.4.1, in this section, I have made an attempt to derive rigorously the basic equations of (sub)stellar structure and evolution directly from the equations of fluid dynamics (that can be found for example in Rieutord 1997) and not from macroscopic considerations. Thus spherical symmetry will only come as a simplification when needed, and will not be one of the fundamental assumptions. It will then be easier to break this assumption in Chapter 3.

1.1.1   Mass conservation and Lagrangian coordinate

In the general case, the continuity equation, which simply express the mass conservation reads

$$\left.\frac{\partial \rho}{\partial t}\right|_{\mathbf{r}} = -\nabla \cdot (\rho \mathbf{v}), \tag{1.1}$$

where the time derivative is taken at a constant location $\mathbf{r}$. In classical hydrodynamics, it is often convenient to introduce a Lagrangian derivative which is following a given mass element of fluid. This reads

$$\frac{D}{Dt} = \left.\frac{\partial}{\partial t}\right|_{\mathbf{r}} + (\mathbf{v} \cdot \nabla), \tag{1.2}$$

and yields

$$\frac{D\rho}{Dt} = -\rho \left(\nabla \cdot \mathbf{v}\right). \tag{1.3}$$

We see that expressing the problem in a Lagrangian form greatly reduces, at least formally, the complexity of the equations. In the following, we will thus try to find a suitable set of Lagrangian coordinates.

Fortunately, for fluid objects where centrifugal, tidal and magnetic forces can be neglected[2], all our variables are constant on concentric spherical shells. Then, they depend only on two scalar variables, $r = \parallel \mathbf{r} \parallel$ and t. In this case, our Lagrangian coordinate is provided by the mass contained inside the spherical shell of radius r at the time t,

$$m(r,t) = 4\pi \int_0^r \rho(r,t) r^2 \mathrm{d}r. \tag{1.4}$$

Indeed, as we will see, this variable *moves with the fluid*, and has the sought for properties. In order to correctly carry out the coordinate change $(r,t) \rightarrow (m,t)$, we must express the differential form $\mathrm{d}m$. Thanks to the continuity equation, which now writes

$$\left.\frac{\partial \rho}{\partial t}\right|_r = -\frac{1}{r^2} \left.\frac{\partial (r^2 \rho v)}{\partial r}\right|_t, \tag{1.5}$$

with $v = \mathbf{v} \cdot \hat{\mathbf{r}}$, this yields

$$\begin{aligned}
\mathrm{d}m &\equiv \left.\frac{\partial m}{\partial r}\right|_t \mathrm{d}r + \left.\frac{\partial m}{\partial t}\right|_r \mathrm{d}t \\
&= 4\pi r^2 \rho(r,t)\,\mathrm{d}r + 4\pi \int_0^r \left.\frac{\partial \rho}{\partial t}\right|_r r^2 \mathrm{d}r\,\mathrm{d}t \\
&= 4\pi r^2 \rho(r,t)\,\mathrm{d}r - 4\pi \int_0^r \left.\frac{\partial (r^2 \rho v)}{\partial r}\right|_t \mathrm{d}r\,\mathrm{d}t,
\end{aligned} \tag{1.6}$$

---

[2]A more precise and quantitative version of this statement will be given in Chapter 3, where we will discuss in detail the departure from sphericity of a fluid object in hydrostatic equilibrium under the action of a perturbing force.

and finally, after integration,

$$\mathrm{d}m = 4\pi r^2 \rho(r,t)\,\mathrm{d}r - 4\pi r^2 \rho(r,t) v\,\mathrm{d}t. \tag{1.7}$$

The first term is simply the mass enclosed between the shell of radius r and $r + \mathrm{d}r$, and the second, the mass loss rate trough a shell of constant radius r, due to the fluid motion at the speed v. One can see that the speed of a given mass element labeled by m (meaning $\mathrm{d}m = 0$), is given by $\frac{Dr}{Dt} = v$. This is why m is a Lagrangian coordinate. The change of variable can then be carried out using

$$\begin{aligned}
\left.\frac{\partial}{\partial r}\right|_t &= 4\pi r^2 \rho \left.\frac{\partial}{\partial m}\right|_t, \\
\left.\frac{\partial}{\partial t}\right|_r &= \left.\frac{\partial}{\partial t}\right|_m + \left.\frac{\partial m}{\partial t}\right|_r \left.\frac{\partial}{\partial m}\right|_t \\
&= \left.\frac{\partial}{\partial t}\right|_m - 4\pi r^2 \rho v \left.\frac{\partial}{\partial m}\right|_t.
\end{aligned} \tag{1.8}$$

From the second equation above, we can see that, as expected, $\left.\frac{\partial}{\partial t}\right|_m$ is simply the total derivative, $\frac{D}{Dt}$ expressed here for a spherical configuration.

With the Lagrangian coordinate system, we will see hereafter, that it is convenient to replace the equation for mass conservation by

$$\left.\frac{\partial r}{\partial m}\right|_t = \frac{1}{4\pi r^2 \rho}. \tag{1.9}$$

However, r then appears explicitly in this equation, and is no longer a dummy variable, as it has been replaced by m. We must therefore find an additional relation. Fortunately, we already encountered it, whatever simple it seems:

$$v = \left.\frac{\partial r}{\partial t}\right|_m. \tag{1.10}$$

Therefore, in the following, we will always replace v using Eq. (1.10). Our problem can now be stated as finding five equations, two being provided by the thermodynamics, involving r, ρ, P, T and $\tilde{S}$ as a function of m and t.

1.1.2 Momentum equation

It is now easy to rewrite the other equations in our new set of coordinates. Let us start with the Navier-Stockes equation (in the inviscid limit ; Rieutord 1997)

$$\rho \frac{D\mathbf{v}}{Dt} = -\nabla P - \rho \nabla (V_G + V_{\mathrm{ext}}), \tag{1.11}$$

where $-\nabla (V_G + V_{\mathrm{ext}})$ is the acceleration due to all the external forces acting in volume[3]. Considering only gravity and in the spherical case, we get

$$\left.\frac{\partial P}{\partial m}\right|_t = -\frac{g}{4\pi r^2} - \frac{1}{4\pi r^2} \left.\frac{\partial^2 r}{\partial t^2}\right|_m, \tag{1.12}$$

where $\hat{\mathbf{r}} \cdot \nabla V_G = g = \frac{Gm}{r^2}$ is the module of the local gravity acceleration ($\mathbf{g}$). The two first term are the usual pressure gradient and gravitational acceleration, which are equal when hydrostatic equilibrium is reached. The last term arises when a given shell undergo an accelerated contraction or expansion.

---

[3]This equation is general, but in this section, only central forces will be discussed. For a detailed discussion of the effect of non central forces, the reader is referred to Chapter 3.

1.1.3 Energy conservation

Local conservation

As discussed in Rieutord (1997), if $\tilde{U}$ is the specific internal energy of the fluid, its Lagrangian variation is given by

$$\frac{D\tilde{U}}{Dt} = -\frac{1}{\rho}\left(\nabla \cdot \mathbf{F}_{\text{int}} + P\nabla \cdot \mathbf{v}\right) + \dot{\varepsilon}_{\text{nuc}} + \dot{\varepsilon}_{\text{ext}}, \tag{1.13}$$

where $\mathbf{F}_{\text{int}}$ is the energy flux density vector, and $\dot{\varepsilon}_{\text{nuc}}$ and $\dot{\varepsilon}_{\text{ext}}$ are the specific energy production rate of nuclear reactions, and of a source that yet remains to be determined. The first two terms between brackets represent respectively the *thermal* and *mechanical* energy exchanged with the other mass elements, whereas, the last terms represents a production of energy within a given mass element itself. This energy can be produced by different processes, the first coming in mind being chemical, or in our context nuclear, reactions ($\dot{\varepsilon}_{\text{nuc}}$) and viscous dissipation. We will see in Chapter 2 that other sources can come into play, and in particular tidally generated friction ($\dot{\varepsilon}_{\text{tid}}$) that is extensively discussed in Chapter 5. To remain general, but make a difference between *internal* and *external* sources of energy, we will consider separately $\dot{\varepsilon}_{\text{nuc}}$ and an arbitrary source which produces $\dot{\varepsilon}_{\text{ext}}$ Joules per second and per gram of matter.

Thanks to the second principle of thermodynamics, we can define a thermodynamical function $\tilde{S}$ (the specific entropy of the fluid) whose differential form is related to the other thermodynamical quantities by

$$T\,\mathrm{d}\tilde{S} = \mathrm{d}\tilde{U} - \frac{P}{\rho^2}\mathrm{d}\rho. \tag{1.14}$$

Because the infinitesimal variations are taken along the transformation of a given fluid element, and thanks to the continuity equation, Eq. (1.13) directly rewrites

$$\begin{aligned}
T\frac{D\tilde{S}}{Dt} &= -\frac{1}{\rho}\left(\nabla \cdot \mathbf{F}_{\text{int}} + P\nabla \cdot \mathbf{v}\right) + \dot{\varepsilon}_{\text{nuc}} + \dot{\varepsilon}_{\text{ext}} - \frac{P}{\rho^2}\frac{D\rho}{Dt} \\
&= -\frac{1}{\rho}\left(\nabla \cdot \mathbf{F}_{\text{int}} + P\nabla \cdot \mathbf{v}\right) + \dot{\varepsilon}_{\text{nuc}} + \dot{\varepsilon}_{\text{ext}} + \frac{P}{\rho}\nabla \cdot \mathbf{v} \\
&= -\frac{1}{\rho}\nabla \cdot \mathbf{F}_{\text{int}} + \dot{\varepsilon}_{\text{nuc}} + \dot{\varepsilon}_{\text{ext}}.
\end{aligned} \tag{1.15}$$

This just shows that, as expected, the entropy created in a particle of fluid does not depend on the amount of work that it receives. For a spherical configuration, defining the luminosity as $l(m,t) \equiv 4\pi r^2 \mathbf{F}_{\text{int}} \cdot \hat{\mathbf{r}} \equiv 4\pi r^2 F_{\text{int}}$, and using the (m,t) coordinates we get

$$\boxed{\dot{\varepsilon}_{\text{nuc}} + \dot{\varepsilon}_{\text{ext}} - T\left.\frac{\partial \tilde{S}}{\partial t}\right|_m = \frac{1}{r^2\rho}\left.\frac{\partial r^2 F_{\text{int}}}{\partial r}\right|_t = 4\pi\left.\frac{\partial r^2 F_{\text{int}}}{\partial m}\right|_t = \left.\frac{\partial l}{\partial m}\right|_t.} \tag{1.16}$$

Global conservation

The above relation express the fact that locally, the energy that exits a given shell of mass $\mathrm{d}m$ ($\left.\frac{\partial l}{\partial m}\right|_t \mathrm{d}m$) comes either from a release of entropy ($-T\left.\frac{\partial \tilde{S}}{\partial t}\right|_m \mathrm{d}m$) or of a local energy production (($\dot{\varepsilon}_{\text{ext}} + \dot{\varepsilon}_{\text{nuc}}$)$\mathrm{d}m$). However, the gravitational energy

$$E_{\text{grav}} \equiv -\int \frac{Gm}{r}\mathrm{d}m, \tag{1.17}$$

never explicitly appears, nor the total macroscopic kinetic energy

$$E_{\text{kin}} \equiv \int \frac{1}{2} \left. \frac{\partial r}{\partial t} \right|_m^2 \, \mathrm{d}m, \tag{1.18}$$

and one may wonder if the total energy of our object is conserved as a direct consequence of this local energy conservation. To reassure the reader, and show that it is, we must integrate our local energy conservation (Eq. (1.16)) over the whole mass of our body.

Let us define the total internal luminosity $L_{\text{int}}(t) \equiv l(M_1, t)$, $E_{\text{int}} \equiv \int \tilde{U} \mathrm{d}m$ and E_{nuc} the total internal and nuclear energy, and E_{ext}, the energy contained in an external reservoir[4]. From these definitions, $\dot{E}_{\text{int}} = \int \left. \frac{\partial \tilde{U}}{\partial t} \right|_m \mathrm{d}m$, and the total energy produced per unit of time in the object by nuclear reactions and by external processes are respectively $-\dot{E}_{\text{nuc}} = \int \dot{\varepsilon}_{\text{nuc}} \mathrm{d}m$ and $-\dot{E}_{\text{ext}} = \int \dot{\varepsilon}_{\text{ext}} \mathrm{d}m$[5]. Then the integration yields

$$L_{\text{int}} = -\dot{E}_{\text{int}} - \dot{E}_{\text{ext}} - \dot{E}_{\text{nuc}} + \int \frac{P}{\rho^2} \left. \frac{\partial \rho}{\partial t} \right|_m. \tag{1.19}$$

The last term appears as the energy produced (consumed) by the contraction (expansion) of our body ($\left. \frac{\partial \rho}{\partial t} \right|_m$ being respectively positive or negative). In order to link this to the variation of the gravitational and kinetic energy, we must derive a *derivative* of the well known *Virial theorem* as follows. Let us multiply both sides of the momentum equation (Eq. (1.12)) by $4\pi r^2 \left. \frac{\partial r}{\partial t} \right|_m$ and integrate over the mass. We have

$$\int 4\pi r^2 \left. \frac{\partial r}{\partial t} \right|_m \left. \frac{\partial P}{\partial m} \right|_t \mathrm{d}m = -\int \frac{Gm}{r} \frac{1}{r} \left. \frac{\partial r}{\partial t} \right|_m \mathrm{d}m - \int \left. \frac{\partial r}{\partial t} \right|_m \left. \frac{\partial^2 r}{\partial t^2} \right|_m \mathrm{d}m. \tag{1.20}$$

On the left hand side, because m can move inside the time derivatives, and that $\left. \frac{\partial r}{\partial t} \right|_m \left. \frac{\partial^2 r}{\partial t^2} \right|_m = \frac{1}{2} \frac{\partial}{\partial t} \left(\left. \frac{\partial r}{\partial t} \right|_m^2 \right) \Big|_m$, we immediately recognize $-\dot{E}_{\text{grav}}$ and $-\dot{E}_{\text{kin}}$. Integrating by part the right hand side, we get

$$\int 4\pi r^2 \left. \frac{\partial r}{\partial t} \right|_m \left. \frac{\partial P}{\partial m} \right|_t \mathrm{d}m = \left[4\pi r^2 \left. \frac{\partial r}{\partial t} \right|_m P \right]_0^{M_1} - \int P \frac{\partial}{\partial m} \left(4\pi r^2 \left. \frac{\partial r}{\partial t} \right|_m \right) \Big|_t. \tag{1.21}$$

Because

$$\frac{\partial}{\partial m} \left(r^2 \left. \frac{\partial r}{\partial t} \right|_m \right) \Big|_t = \frac{1}{3} \frac{\partial^2 r^3}{\partial m \partial t} = \frac{1}{3} \frac{\partial^2 r^3}{\partial t \partial m} = \frac{\partial}{\partial t} \left(r^2 \left. \frac{\partial r}{\partial m} \right|_t \right) \Big|_m = \frac{\partial}{\partial t} \left(\frac{1}{4\pi \rho} \right) \Big|_m, \tag{1.22}$$

this rewrites

$$\int 4\pi r^2 \left. \frac{\partial r}{\partial t} \right|_m \left. \frac{\partial P}{\partial m} \right|_t \mathrm{d}m = P_{\text{atm}} \frac{\mathrm{d}}{\mathrm{d}t} \left(\frac{4}{3} \pi R_1^3 \right) + \int \frac{P}{\rho^2} \left. \frac{\partial \rho}{\partial t} \right|_m, \tag{1.23}$$

where P_{atm} is the external pressure, and R_1 is the external mean radius of the object. Recasting Eq. (1.20), we get

$$\int \frac{P}{\rho^2} \left. \frac{\partial \rho}{\partial t} \right|_m + \dot{E}_{\text{kin}} = -\dot{E}_{\text{grav}} - P_{\text{atm}} \frac{\mathrm{d}}{\mathrm{d}t} \left(\frac{4}{3} \pi R_1^3 \right). \tag{1.24}$$

---

[4]For tidal friction, for example, this reservoir is the macroscopic kinetic (orbital) energy of the whole system, which can be dissipated in the interior by the tides.

[5]The minus signs are merely conventional, and just come from the fact we defined the various $\dot{\varepsilon}$ as energy *production* rates per unit mass and not as energy *variation* rates, so that they are positive.

As we could have guessed, the mechanical work exerted by the gravitational force and the the pressure of the external medium (even if small in all the cases of interest), is transferred into both macroscopic and microscopic kinetic energy. Substituting this into Eq. (1.19) finally gives the expected global energy conservation

$$\dot{E}_{\text{int}} + \dot{E}_{\text{kin}} + \dot{E}_{\text{grav}} + \dot{E}_{\text{nuc}} + \dot{E}_{\text{ext}} = -L_{\text{int}} + P_{\text{atm}} \frac{\mathrm{d}}{\mathrm{d}t}\left(\frac{4}{3}\pi R_1^3\right), \tag{1.25}$$

where the left hand side is the variation in volume of the total energy, and the right hand side represents the energy exchanged through the surface, either by thermal (radiative) losses, or by mechanical work[6,7].

1.1.4 Energy transport

We now have the three dynamical equations that we were looking for (Eq. (1.9), (1.12) and (1.16)). However, we can see that the energy equation involve a new variable, namely the luminosity of any given layer, $l(m,t)$, and thus, a new relation must be found which describe the way energy is transported throughout our medium as a function of its thermodynamical properties. For this, however, one cannot rely on a fundamental physical principle, and there enters some modeling and parametrization.

Diffusive transport

Let us first consider the energy that is transported by radiation. Indeed, we expect temperature (and thus radiative energy[8], $\tilde{U}_{\text{rad}} = aT^4$) of the matter to increase with depth, which should lead to a flux of radiative energy. As the mean free path of a photon inside a medium of mean opacity κ_r is equal to $(\kappa_r\rho)^{-1} \approx 10^{-2}$m which is much smaller than the size of the object we are considering, a huge simplification occurs, and the radiative flux can be treated as a pure diffusion[9].

Then, in each spectral interval $[\nu, \nu + \mathrm{d}\nu]$, the diffusing component is the radiative energy density, $\tilde{U}_\nu$, and it is transported by photons whose diffusion coefficient is $c/(3\kappa_\nu\rho)$. Here, κ_ν is the *radiative opacity* and is expressed in m^2.kg^{-1}. This yields for the flux

$$\mathbf{F}_\nu = -\frac{c}{3\kappa_\nu\rho}\nabla\tilde{U}_\nu. \tag{1.26}$$

Deep in the interior, local thermodynamic equilibrium is achieved, so that the energy density is given by the planck function for the intensity, $B(\nu,T)$, by

$$\tilde{U}_\nu = \frac{4\pi}{c}B(\nu,T) = \frac{8\pi h}{c^3}\frac{\nu^3}{\mathrm{e}^{h\nu/k_{\text{B}}T} - 1}. \tag{1.27}$$

Thus in a given spectral bin, the flux depends only on the temperature and its gradient, and is given by

$$\mathbf{F}_\nu = -\frac{c}{3\kappa_\nu\rho}\frac{4\pi}{c}\left.\frac{\partial B}{\partial T}\right|_\nu \nabla T. \tag{1.28}$$

---

[6]Because the pressure of the interplanetary or interstellar medium are vanishingly small compared to the pressures reached in the interior once the body is massive enough, excepted for the very early phases of the formation, the external mechanical work is negligible

[7]Eqs. (1.20) and (1.25) extend the relation found in Kippenhahn and Weigert (1990) to objects that are not in hydrostatic equilibrium and in contact with an external pressure reservoir.

[8]The constant related to the total energy radiated by a blackbody is $a \equiv \frac{8\pi^5 k_{\text{B}}^4}{15c^3h^3} \equiv \frac{4\sigma_{\text{SB}}}{c}$, where σ_{SB} is the Stefan-Boltzmann constant.

[9]This approximation is valid for optical depth larger than unity, i.e. not in the atmosphere where we will need a proper treatment of the radiative transfer, as we will see in § 1.5.2.

We can then integrate this over the frequencies which yields the total radiative flux

$$\mathbf{F}_{\text{rad}} = -\left[\frac{4\pi}{3\rho} \int \frac{1}{\kappa_v} \left.\frac{\partial B}{\partial T}\right|_v \mathrm{d}v\right] \nabla T. \tag{1.29}$$

Then, it is rather useful to define the Rosseland mean opacity

$$\frac{1}{\kappa_{\text{r}}} = \frac{\int \frac{1}{\kappa_v} \left.\frac{\partial B}{\partial T}\right|_v \mathrm{d}v}{\int \left.\frac{\partial B}{\partial T}\right|_v \mathrm{d}v} = \frac{\pi}{4\sigma_{\text{SB}}T^3} \int \frac{1}{\kappa_v} \left.\frac{\partial B}{\partial T}\right|_v \mathrm{d}v, \tag{1.30}$$

which as we see, is an harmonic average weighted by the derivative of the Planck function. In other words, this mean opacity indeed measures the *transparency* of the gas at the frequencies were most of the flux can be transported (where $\left.\frac{\partial B}{\partial T}\right|_v$ is maximum). Sometimes, however, another equivalent quantity describing the radiative transport is used, namely the *thermal diffusivity* ($\kappa_{T,\text{r}}$, in m^2.s^{-1}), which is defined by

$$\mathbf{F}_{\text{rad}} = -\rho c_P \kappa_{T,\text{r}} \nabla T \quad \Rightarrow \quad \kappa_{T,\text{r}} \equiv \frac{16\sigma_{\text{SB}}T^3}{3\rho^2 c_P} \frac{1}{\kappa_{\text{r}}}. \tag{1.31}$$

But energy is not transported only by radiation. Indeed, in the interior, because the matter is partially ionized, the free electron can efficiently transport heat by *conduction* (The flux being $\mathbf{F}_{\text{cond}}$). This is also a diffusive process, and by analogy, a conductive thermal diffusivity ($\kappa_{T,\text{c}}$) and a conductive opacity (κ_{c}) can also be defined following

$$\mathbf{F}_{\text{cond}} = -\rho c_P \kappa_{T,\text{c}} \nabla T \quad \Rightarrow \quad \kappa_{T,\text{c}} \equiv \frac{16\sigma_{\text{SB}}T^3}{3\rho^2 c_P} \frac{1}{\kappa_{\text{c}}}. \tag{1.32}$$

Then, because diffusive fluxes are additive, the total flux transported by diffusion is simply $\mathbf{F}_{\text{d}} = \mathbf{F}_{\text{rad}} + \mathbf{F}_{\text{cond}}$, and by analogy, we can define a global thermal diffusivity

$$\kappa_T = \kappa_{T,\text{r}} + \kappa_{T,\text{c}}, \tag{1.33}$$

and mean diffusive opacity

$$\frac{1}{\bar{\kappa}} = \frac{1}{\kappa_{\text{r}}} + \frac{1}{\kappa_{\text{c}}}. \tag{1.34}$$

As for the Rosseland mean, the fact that this opacity is defined by an harmonic average simply translates the fact that the energy preferentially goes through the most *transparent* window.

In the spherical case, considering the total diffusive flux[10], we have

$$L_{\text{d}} = 4\pi r^2 F_{\text{d}} = -\frac{64\pi r^2 \sigma_{\text{SB}} T^3}{3\rho \bar{\kappa}} \frac{\mathrm{d}T}{\mathrm{d}r}, \tag{1.35}$$

and using Eqs. (1.8) and (1.12) (without the inertia term) yields

$$L_{\text{d}} = \frac{64\pi\sigma_{\text{SB}}T^4 mG}{3\bar{\kappa}P} \frac{\mathrm{d}\ln T}{\mathrm{d}\ln P} = 4\pi\rho^2 c_P \kappa_T \sigma_{\text{SB}} mG \frac{T}{P} \frac{\mathrm{d}\ln T}{\mathrm{d}\ln P}, \tag{1.36}$$

---

[10]To avoid confusion, we will use the generic denomination ∇_{d} and use the index d for quantities describing diffusive processes in general while keeping in mind that, except for the fact that κ_T now includes the contribution of conductive processes, ∇_{d} plays exactly the same role than the usual ∇_{rad}.

were the flux transported by radiation is expressed as a function of the thermal gradient

$$\nabla_T \equiv \frac{\mathrm{d}\ln T}{\mathrm{d}\ln P}. \tag{1.37}$$

Here, the derivative is taken along the actual profile in the planet.

It is customary to define the *diffusive* gradient as the temperature gradient (as a function of pressure) needed to transport all the energy through both radiation and conduction. Thus setting $L_{\mathrm{d}} = l(m) \equiv 4\pi r^2 \sigma_{\mathrm{SB}} T_{\mathrm{int}}^4(m)$[11] in Eq. (1.36) yields

$$\nabla_{\mathrm{d}} \equiv \left(\frac{\mathrm{d}\ln T}{\mathrm{d}\ln P}\right)_{\mathrm{d}} = \frac{3\,\bar{\kappa}P}{64\,\pi\,\sigma_{\mathrm{SB}}T^4}\frac{l}{mG} = \frac{3}{16}\frac{\bar{\kappa}P}{T^4}\frac{T_{\mathrm{int}}^4}{g}, \tag{1.38}$$

or equivalently

$$\nabla_{\mathrm{d}} = \frac{1}{4\pi\,\rho^2 c_P \kappa_T}\frac{P}{T}\frac{l}{mG} = \frac{1}{\rho^2 c_P \kappa_T}\frac{P}{T}\frac{\sigma_{\mathrm{SB}}T_{\mathrm{int}}^4}{g}. \tag{1.39}$$

With this definition, if there is no other available means to transport energy in the zone considered, which is therefore called either a *radiative zone* or a *conductive zone* depending on the dominant process, the local thermal gradient must adjust itself to the diffusive gradient so that our missing equation is simply

$$\nabla_T = \nabla_{\mathrm{d}}. \tag{1.40}$$

Advective transport: convection

Note that the flux ($\mathbf{F}_{\mathrm{int}}$) present in Eq. (1.15) should in principle only include such diffusive processes for which energy can be transferred from one mass element to the other without any mass transfer (or advection). Indeed, in 3D, a significant inhomogeneity of temperature within the fluid can lead to large scale fluid motion and to turbulence that will homogenize the energy distribution at the macroscopic level, diffusion then being able to homogenize the remaining small scale inhomogeneities. However, in 1D, such processes cannot be accounted for properly, as we would have hot plumes moving upward smashing into the descending cold plumes, without any possibility for them to simply go around. We thus have to include advection (or convection) in a parametrized way.

As convection is extensively discussed in Chapter 4, we will not reproduce the argument here. Let us just agree for the moment that if the medium is convectively unstable, which arises when the diffusive gradient is larger than the adiabatic one

$$\nabla_{\mathrm{d}} > \nabla_{\mathrm{ad}} \equiv \left.\frac{\partial\ln T}{\partial\ln P}\right|_{\tilde{S}}, \tag{1.41}$$

then convection transports energy to restore the equilibrium. Because convection is very efficient in planetary interiors, the thermal gradient is then very close to the adiabatic one, and our missing relation in such *convective zones* is given by

$$\nabla_T = \nabla_{\mathrm{ad}}, \tag{1.42}$$

and is nearly independent of the luminosity.

---

[11]Note that this relation is indeed a definition of $T_{\mathrm{int}}(m)$, which is the effective temperature at depth m.

Furthermore, as will also be discussed in Chapter 2, under the physical conditions encountered in substellar object and gaseous planets, the fluid is convectively unstable in all the interior but a thin outer layer. Hence the interior is mostly adiabatic and the $T - P$ profile can be integrated from the values of the temperature and pressure just below the radiative zone using Eq. (1.42) independently of the luminosity equation. This means that, in the fully convective case, only the *total* luminosity, L_{int}, and not the luminosity profile, $l(m)$, affects the structure, and only through its impact on the boundary conditions (see § 1.5.2).

1.2 Evolution timescales

We now have our system of equations to solve. However, all the terms in this system do not have the same importance, some even being completely negligible by orders of magnitude. In order to quantify this statement, let us introduce some representative timescales

1.2.1 Dynamical timescale and free fall time

In Eq. (1.12), we see that the acceleration results of the possible unbalance between the gravitational pull and the pressure support. However, excepted during the very early contraction or the red giant phase of more massive stars, this term can be neglected, because its associated timescale is much shorter than the evolution timescale.

Indeed, if we freeze all the microscopic degree of freedom of our gas, in a classical sense, then pressure vanishes and nothing can counteract gravitational contraction. Then, following Kippenhahn and Weigert (1990), we can define the hydrodynamical timescale τ_{dyn}, as the time needed for the fluid to undergo gravitational collapse without any thermal support. Then,

$$\frac{R_1}{\tau_{\text{dyn}}^2} \approx g \approx \frac{GM_1}{R_1^2} \quad \Rightarrow \quad \tau_{\text{dyn}} \approx \sqrt{\frac{R_1^3}{GM_1}}. \tag{1.43}$$

A rigorous calculation provides

$$\tau_{\text{dyn}} = \frac{\pi}{2}\sqrt{\frac{R_1^3}{2\,GM_1}} = \frac{1}{4}\sqrt{\frac{3\pi}{2\,G\bar{\rho}_1}}, \tag{1.44}$$

where $\bar{\rho}_1$ is the mean density of the body. For Jupiter or our Sun (which most surprisingly have the same mean density !), this hydrodynamical timescale is on the order of half an hour, and for a brown dwarf near the hydrogen burning minimum mass ($M_{\text{HBMM}} \approx 0.075 M_{\odot} \approx 75 M_{\text{Jup}}$, and $R_1 \approx 0.7 - 1 R_{\text{Jup}}$; see § 2.2), it can be as low as 2 minutes. As we obviously see that the radius of the Sun or of Jupiter does not increase or decrease significantly over an hour, the low value of τ_{dyn} tells us that inertia can be neglected in Eq. (1.12) and that *hydrostatic equilibrium* is reached with a high degree of accuracy. In this case, the central pressure is roughly given by

$$P_{\text{c}} \approx \frac{GM_1^2}{R_1^4}, \tag{1.45}$$

and the dynamical timescale is also equal to the time needed for a sound wave (with the speed $c_{\text{s}} \approx \sqrt{P_{\text{c}}/\bar{\rho}_1}$ to propagate throughout our object

$$\tau_{\text{dyn}} \approx R_1\sqrt{\frac{\bar{\rho}_1}{P_{\text{c}}}}. \tag{1.46}$$

1.2.2 Kelvin-Helmholtz timescale

Now that we have exhibited a dynamical time, we can concern ourselves with the problem of finding the characteristic time taken by an object in quasi-static equilibrium to irradiate its energy. First neglecting nuclear reactions and any external source, this should read

$$\tau_{\text{KH}} \approx \frac{E_{\text{int}}}{L_{\text{int}}}. \tag{1.47}$$

However, this relation is of mild interest if we cannot somehow quantify the content of our energy reservoir. Fortunately, this is possible through the so-called *Virial theorem*, which in our context can be derived as follows.

Because $\partial P/\partial m|_t$ has the dimension of an energy per unit of volume and mass, multiplying both sides of Eq. (1.12) by $4\pi r^3$ and integrating over the whole mass of the body (Kippenhahn and Weigert 1990), we get

$$\int 4\pi r^3 \left.\frac{\partial P}{\partial m}\right|_t \mathrm{d}m = -\int \frac{Gm}{r}\mathrm{d}m - \int r \left.\frac{\partial^2 r}{\partial t^2}\right|_m \mathrm{d}m, \tag{1.48}$$

which obviously looks like an energy. Let us treat each term in turn. Integrating the first term by part, and using the fact that, $r = 0$ at the center, and $\partial r/\partial m|_t = 1/(4\pi r^2 \rho)$, we get

$$\int 4\pi r^3 \left.\frac{\partial P}{\partial m}\right|_t \mathrm{d}m = \left[4\pi r^3 P\right]_0^{M_1} - \int 12\pi r^2 \left.\frac{\partial r}{\partial m}\right|_t P\,\mathrm{d}m = 4\pi \bar{R}_1^3 P_{\text{atm}} - 3\int \frac{P}{\rho}\mathrm{d}m. \tag{1.49}$$

To recast this expression in term of the internal energy $E_{\text{int}} = \int \tilde{U}\mathrm{d}m$, we define a dimensionless constant ζ as

$$E_{\text{int}} \equiv \frac{3}{\zeta}\int \frac{P}{\rho}\mathrm{d}m. \tag{1.50}$$

Thus

$$\int 4\pi r^3 \left.\frac{\partial P}{\partial m}\right|_t \mathrm{d}m = 4\pi \bar{R}_1^3 P_{\text{atm}} - \zeta E_{\text{int}}. \tag{1.51}$$

The second term in Eq. (1.48) is of course the total gravitational energy of our configuration. Finally, because

$$r \left.\frac{\partial^2 r}{\partial t^2}\right|_m = \frac{1}{2}\left.\frac{\partial^2 r^2}{\partial t^2}\right|_m - \left.\frac{\partial r}{\partial t}\right|_m^2,$$

the third term can be rewritten

$$\int \left.\frac{\partial r}{\partial t}\right|_m^2 - \frac{1}{2}\left.\frac{\partial^2 r^2}{\partial t^2}\right|_m \mathrm{d}m \equiv 2E_{\text{kin}} - \frac{1}{2}\frac{\mathrm{d}^2 I}{\mathrm{d}t^2}, \tag{1.52}$$

where E_{kin} is the macroscopic kinetic energy, and $I_1 \equiv \int r^2 \mathrm{d}m$ the central moment of inertia of the body. We are then left with the *Virial theorem*

$$\boxed{\frac{1}{2}\frac{\mathrm{d}^2 I_1}{\mathrm{d}t^2} + 4\pi \bar{R}_1^3 P_{\text{atm}} = 2E_{\text{kin}} + E_{\text{grav}} + \zeta E_{\text{int}}.} \tag{1.53}$$

As shown above, the terms on left hand side, as well as E_{kin} are negligible, and this reduces to

$$E_{grav} + \zeta\, E_{int} = 0. \tag{1.54}$$

We will come back in more detail on the fundamental consequences of this relation in Chapter 2, where the evolution is studied more thoroughly, but for the moment, this already tells us that the internal and gravitational energies are commensurable. As the latter scales as GM_1^2/R_1, we can define the *Kelvin-Helmholtz timescale*

$$\tau_{KH} \equiv \frac{GM_1^2}{R_1 L_{int}}, \tag{1.55}$$

which is the typical rate at which an object in hydrostatic equilibrium radiates its internal energy. For Jupiter, τ_{KH} is now on the order of 10^{11} years because the planet is old, but was probably no shorter than 10^{5-6} years during its young age. Thus, as expected, $\tau_{KH} \gg \tau_{dyn}$ and the hydrostatic assumption is validated.

1.2.3 Nuclear time

However, for the Sun, $\tau_{KH} \approx 10^7$ yr ! As we have observational evidences that the Sun has been radiating for a few billion years, unfortunately for Lord Kelvin, another energy source must be present in our star, and in others. This energy, this is the mass energy contained in atoms nuclei that can be released by thermonuclear reactions. In the low mass star and substellar domain, the main atoms concerned are deuterium (^{2}H ; which ignites around $T \sim 4.5 \times 10^5$ K), lithium (Li ; $T \sim 2.5 \times 10^6$ K) and hydrogen (H ; $T \sim 3 \times 10^6$ K). As the central temperature of a substellar object of a given age generally increases with its mass, the ignition temperature of a compound X can be recast into the minimal mass (M_{XBMM}) needed for a body to be able to burn the given compound. We thus define (Chabrier and Baraffe 1997, 2000),

- $M_{HBMM} \approx 75\, M_{Jup}$

- $M_{LiBMM} \approx 60\, M_{Jup}$

- $M_{^2HBMM} \approx 13.5\, M_{Jup}$.

For $M_1 < M_{^2HBMM}$, no nuclear reactions occur, and $\dot{\varepsilon}_{nuc}$ can be set to 0 in our set of equations. For $M_1 > M_{HBMM}$, on the contrary, the nuclear reactions dominate the energy budget of the star during its stay on the main sequence, meaning $\tau_{KH} \ll \tau_{nuc}$, and the energy equation is well approximated by

$$\left.\frac{\partial l}{\partial m}\right|_t = \dot{\varepsilon}_{nuc}. \tag{1.56}$$

In this case, the star is both in *mechanical* and *thermal equilibrium*, and evolves only because of its varying chemical composition. Finally, in the intermediate case, because both Lithium and Deuterium are not very abundant, and that the reaction rates of ^{2}H+H and Li+H reactions are very short, these species are burnt in about 10 to 100 Myr. This entails that, at early ages, $\tau_{KH} \sim \tau_{nuc}$ and no simplification can be made.

1.3 Canonical set of equations

In view of these simplifications, and for further reference, we can now rewrite the canonical set of equations describing the internal structure of gaseous objects and their evolution in Lagrangian coordi-

nates[12]

$$\frac{\partial P}{\partial m} = -\frac{Gm}{4\pi r^4},\tag{1.57}$$

$$\frac{\partial r}{\partial m} = \frac{1}{4\pi r^2 \rho},\tag{1.58}$$

$$\frac{\partial l}{\partial m} = \dot{\varepsilon}_{\text{nuc}} + \dot{\varepsilon}_{\text{ext}} - T\frac{\partial \tilde{S}}{\partial t},\tag{1.59}$$

$$\frac{\partial T}{\partial m} = \frac{T}{P}\frac{\partial P}{\partial m}\nabla_T,\tag{1.60}$$

with

$$\nabla_T = \nabla_{\text{d}} \ \ (\text{radiative/conductive zone}) \quad \text{or} \quad \nabla_T = \nabla_{\text{ad}} \ \ (\text{convective zone}).\tag{1.61}$$

Note that only Eq. (1.59) explicitly involves a time derivative. This means that our object, while not in *thermal* equilibrium, is always near *mechanical* equilibrium, and that it evolves only because it radiates its entropy and increases its internal order. This also means that in certain cases, with a simple pre-scription for the luminosity, the structure of the object can be computed without any knowledge about its evolution, as has been successfully done for Solar System giant planets (Hubbard and Marley 1989 ; Chabrier et al. 1992 ; Guillot 2005 ; to cite only a few. See also Chapter 4).

1.4 Key physical ingredients

However useful these equations are, they are not sufficient to yet solve our problem. Indeed, we need at least three additional relations, namely $\rho(P,T)$, $\tilde{S}(P,T)$ and $\nabla_{\text{ad}}(P,T)$ (or $\nabla_{\text{d}}(P,T,l)$, meaning that κ_{r} and κ_{c} must be provided) to complete them. In fact, the calculations of the various thermodynamic quantities are the very core of any numerical model, and are often the main factors limiting its accuracy. In this section, we will review some simple analytical models that can be used to grasp general properties, as well as the various numerical models used in our numerical code.

1.4.1 Equation of state

Definitions

Before describing the macroscopic state of our fluid $(P,\rho,T,\tilde{S})$, we have to introduce some quantities that describe the microscopic state of our mixture. Our fluid is composed of many different particles, e.g. molecules, atoms, ions - hereafters referred to as ions labeled by i of particle density (in m^{-3}), atomic mass (in units of the proton mass m_{H}) and charge given by n_{i}, A_{i} and Z_{i} respectively, and free electrons whose particle density is n_{e}. The chemical composition of the mixture is usually described by the mass fraction[13] of Hydrogen (X), Helium (Y) and heavy elements (Z), for which by definition

$$X + Y + Z = 1.\tag{1.62}$$

---

[12]We have dropped the $|_x$ stating the variable kept constant because, unless otherwise stated, we now differentiate only with respect to m or t.

[13]The mass ratio of a chemical species is the ratio of the mass of all the constituents of this species contained in a small volume over the total mass enclosed in the same volume

For the mechanical properties of the gas, an important quantity is the mean molecular weight (μ) defined by

$$\frac{1}{\mu} \equiv \frac{n_{\rm tot} m_{\rm H}}{\rho} = \frac{(\sum_i n_i + n_{\rm e}) m_{\rm H}}{\rho} \equiv \sum_i \frac{1}{\mu_i} + \frac{1}{\mu_{\rm e}}, \tag{1.63}$$

which implicitly defines the mean molecular weight of each ion (μ_i) and of free electrons ($\mu_{\rm e}$). Defining the mean atomic mass of ions $\langle A \rangle_{\rm ion} \equiv \frac{\sum_i n_i A_i}{\sum_i n_i}$ and the mean degree of ionization $\langle Z \rangle_{\rm ion} \equiv \frac{\sum_i n_i Z_i}{\sum_i n_i} = \frac{n_{\rm e}}{\sum_i n_i}$, and thanks to electro-neutrality we get

$$\sum_i \frac{1}{\mu_i} = \frac{1}{\langle A \rangle_{\rm ion}} \qquad \text{and} \qquad \frac{1}{\mu_{\rm e}} = \frac{\langle Z \rangle_{\rm ion}}{\langle A \rangle_{\rm ion}}. \tag{1.64}$$

This mean molecular weight is the translation in mechanical terms of the enrichment of our mixture in volatiles, metals, or generally, heavy elements[14].

To know wether our gas must be described by classical or quantum mechanics, we must also compare the mean thermal energy of a given particle to its zero energy level, i.e. the Fermi energy[15]

$$\varepsilon_{\rm F} \equiv \frac{\hbar^2}{2 m_{\rm e}} \left(3\pi^2 n_{\rm e} \right)^{2/3}. \tag{1.65}$$

This defines the electron degeneracy parameter

$$\Xi_{\rm e} \equiv \frac{k_{\rm B} T}{\varepsilon_{\rm F}} \equiv \frac{k_{\rm B} T}{k_{\rm B} T_{\rm F}} = \frac{2}{(3\pi^2)^{2/3}} \frac{m_{\rm e} m_{\rm H}^{2/3} k_{\rm B}}{\hbar^2} \frac{T \mu_{\rm e}^{2/3}}{\rho^{2/3}}, \tag{1.66}$$

which allows us to separate the classical domain ($\Xi_{\rm e} \gg 1$) from the quantum one ($\Xi_{\rm e} \ll 1$).

Classical ideal gas

For the outermost layers of planets and brown dwarfs, the density is small enough for the gas to be in the classical domain. The pressure is thus given by the ideal gas law

$$P = \left(\sum_i n_i + n_{\rm e} \right) k_{\rm B} T = \rho \frac{k_{\rm B}}{\mu m_{\rm H}} T. \tag{1.67}$$

For energetic considerations, one also needs to specify the nature of the gas, which can be encompassed in the specific heat capacity at constant *volume* (c_V), or constant *pressure* ($c_P = c_V + k_{\rm B}/m_i$ for a perfect gas of particles of mass m_i). For a monoatomic gas, $c_V = \frac{3}{2} \frac{k_{\rm B}}{m_i}$. For a diatomic gas, for example, internal degrees of freedom can be excited and brought into equipartition. In general we will consider temperatures where rotational states are excited but not the vibrational states ($\Theta_{\rm rot} < T < \Theta_{\rm vib}$)[16], which yields $c_V = \frac{5}{2} \frac{k_{\rm B}}{m_i}$. The energy is then given by

$$\tilde{U} = c_V T \tag{1.68}$$

---

[14] For further numerical application, if we have a fully ionized mixture of Hydrogen (with the mass fraction X) and Helium (Y), $\mu = 4/(8 - 5Y)$, and $\mu_{\rm e} = 2/(2 - Y)$, and are approximately equal to 0.6 and 1.16, respectively, for a cosmic mixture ($Y = 0.275$).

[15] The Fermi energy is defined here for the free electrons. For another specie, one just has to use the mass and number density of the chosen particle.

[16] For H_2, $\Theta_{\rm rot} \approx 85.4\,{\rm K}$, and $\Theta_{\rm vib} \approx 6210\,{\rm K}$. H_2 thus acts mostly like a diatomic gas in the atmosphere of Jupiter and Saturn, but like a monoatomic one in Uranus and Neptune which are much colder.

and the entropy (Reif 1985)

$$\tilde{S} = \frac{k_\mathrm{B}}{m_\mathrm{i}} \left\{ \ln \left[\left(\frac{m_\mathrm{i}^{5/3} k_\mathrm{B}}{2\pi\hbar^2} \right)^{3/2} \frac{T^{3/2}}{\rho} \right] + \frac{5}{2} \right\} \quad \text{(monoatomic)}, \tag{1.69}$$

$$\tilde{S} = \frac{k_\mathrm{B}}{m_\mathrm{i}} \left\{ \ln \left[\left(\frac{m_\mathrm{i}^{5/3} k_\mathrm{B}}{2\pi\hbar^2} \right)^{3/2} \frac{T^{5/2}}{\rho \, \Theta_\mathrm{rot}} \right] + \frac{7}{2} \right\} \quad \text{(diatomic)}. \tag{1.70}$$

Differentiating this at constant entropy, we can derive the adiabatic gradient

$$\nabla_\mathrm{ad} \equiv \left. \frac{\partial \ln T}{\partial \ln P} \right|_{\tilde{S}} = \frac{2}{5} \ \text{(monoatomic)},$$

$$= \frac{2}{7} \quad \text{(diatomic)}. \tag{1.71}$$

Degenerate matter

On the contrary, in the deep interior, the density is much higher. If we put the mean temperature and density of Jupiter in Eq. (1.66), we obtain a degeneracy parameter on the order of 0.05. It thus follows that the electrons cannot be considered classical anymore. However, because ions are around a thousand time more massive than electrons, their degeneracy parameter is on the order of 50 and they remain classical. Thus, adding up the electrons and ions contributions[17], we get

$$P = P_\mathrm{e} + P_\mathrm{i}$$
$$= \frac{2}{5} n_\mathrm{e} \varepsilon_\mathrm{F} + \sum_\mathrm{i} n_\mathrm{i} k_\mathrm{B} T$$
$$= \frac{2}{5} \varepsilon_\mathrm{F} \left(n_\mathrm{e} + \Xi_\mathrm{e} \frac{5}{2} \sum_\mathrm{i} n_\mathrm{i} \right)$$
$$= K_\mathrm{F} \left(1 + \frac{5}{2} \frac{\Xi_\mathrm{e}}{\langle Z \rangle_\mathrm{ion}} \right) \left(\frac{\rho}{\mu_\mathrm{e}} \right)^{5/3}, \tag{1.72}$$

where $K_\mathrm{F} \equiv \frac{\hbar^2 \left(3\pi^2 \right)^{2/3}}{5 m_\mathrm{e} m_\mathrm{H}^{5/3}}$ is a constant. The main interest of this ideal equation of state is that, if ionization (and composition) can be considered constant in the interior, Eq. (1.72) takes the form of a polytrope

$$P = K \rho^{1 + 1/\tilde{n}}, \tag{1.73}$$

with a polytropic *temperature* $K = K_\mathrm{F} \mu_\mathrm{e}^{-5/3} \left(1 + 5 \Xi_\mathrm{e} / 2 \langle Z \rangle_\mathrm{ion} \right)$, and index $\tilde{n} = 3/2$, which provides rather useful analytic relations, as described in § 2.2.1. The mean internal energy of the electrons can then be found by integrating the Fermi energy over the number of particles, which writes

$$\tilde{U}_\mathrm{e} = \int \varepsilon_\mathrm{F} \, \mathrm{d}\rho = \frac{3}{5} \varepsilon_\mathrm{F} \rho = \frac{2}{3} P_\mathrm{e}. \tag{1.74}$$

---

[17]This expression is correct to first order in Ξ_e, as we have neglected the thermal contribution of the electrons which is proportional to Ξ_e^2 (Chabrier 1990).

Fortunately, because the ions we consider have only one nuclei (H, H$^-$, He$^-$, He^{2-}), their specific heat capacity is equal to 3/2, so that the total internal energy can be written

$$\tilde{U} = \tilde{U}_e + \tilde{U}_i = \frac{2}{3} P_e + \frac{2}{3} P_i = \frac{3}{2} P. \tag{1.75}$$

Even if useful, at the level of accuracy that we are looking for, these simplified equations of state are not completely satisfying. In our numerical model, we thus use tabulated equation of state.

Hydrogen-Helium mixture

The most widely used EOS to describe the thermodynamics properties of the gaseous H/He envelope of giant planets is the Saumon-Chabrier-VanHorn EOS (SCVH; Saumon et al. 1995). This semi-analytical equation of state recovers numerical simulations and experimental results in the high-density and low-density regimes, respectively, while, in its simplest form, interpolating over the pressure ionization regime.

Interestingly enough, high-pressure experiments on fluid deuterium or helium are now able to reach pressures and temperatures typical of the giant planet interiors ($P \gtrsim 1$ Mbar, $T \gtrsim 10^4$ K), probing the equation of state in its most uncertain pressure-range. Various experimental techniques, however, give different results, with a $\sim$30-50% difference in $P(\rho)$ in the maximum compression region for deuterium, $\sim 0.5 - 1.5$ Mbar, although the most recent experiments seem to converge towards substantially less compressible equation of state for hydrogen, i.e. predict a lower density for a given pressure, than SCVH in the pressure-ionization domain, $P \sim 0.5 - 4$ Mbar. This seems to agree with recent first-principle (ab-initio; Militzer et al. 2008; Nettelmann et al. 2008; Caillabet et al. 2011) or nearly first-principle quantum mechanical calculations, and bears significant impact on the internal structure of giant planets, in particular the size of the central core. A less compressible planet will tolerate less heavy material for a given radius or, conversely, will have a larger radius for the same internal composition (Saumon and Guillot 2004). As these other equations of state are not yet publicly available in a usable form, we decided to keep the SCVH equation.

In addition, we must keep in mind that the combined interactions of H and He in the mixture increase drastically the degree of complexity in the characterization of the plasma. Not only the interactions between the two fluids will affect the regime of pressure ionization compared with the pure components, but partial immiscibility between the two species has been suggested to explain Saturn's excess luminosity for the age of the Solar System, and may occur inside some exoplanets. Unfortunately, given the aforementioned difficulty in modeling the properties of H or He alone, and the necessity to simulate a large enough number of particles for the minor species (He in the present case) to obtain statistically converged results, no reliable calculation of the H/He phase diagram can be claimed so far. As mentioned above, pressure-ionization of pure hydrogen and helium must first be fully mastered before the reliability of the calculations exploring the behavior of the mixture can be unambiguously assessed.

Resolving these important issues concerning the H and He EOS must await (i) unambiguous experimental confirmation of the H and He EOS at high pressure, (ii) unambiguous confirmation of the reliability of the theoretical calculations, in particular in the pressure ionization regime, (iii) guidance from experiments to predict the behavior of the H/He mixture under planetary interior conditions. Progress both on the experimental and theoretical side will hopefully enable us to fulfill these criteria within the coming years.
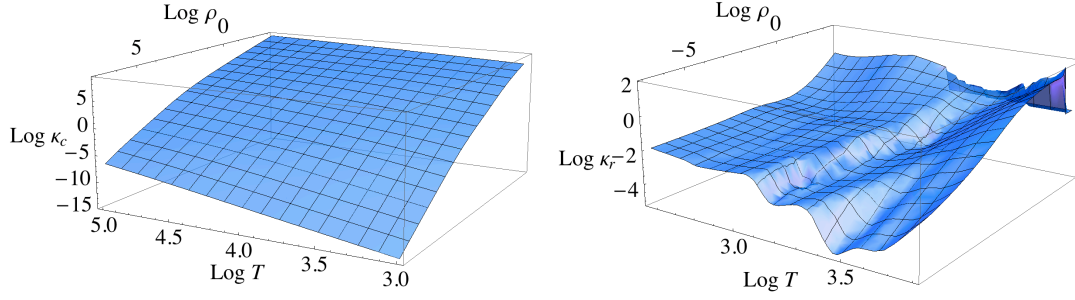
Figure 1.1: Left: Conductive opacities (κ_c in $m^2.kg^{-1}$) from Potekhin et al. (1999) as a function of density (in $kg.m^{-3}$) and temperature (in K). Right: Decimal logarithm of the COND Rosseland radiative opacities (κ_r in $m^2.kg^{-1}$) from Ferguson et al. (2005) as a function of density (in $kg.m^{-3}$) and temperature (in K).

Heavy elements

According to the composition of the protosolar nebula, the next most abundant constituents after hydrogen and helium in gaseous giant planets, but the most abundant ones in ice giants and Earth-like planets, consist of C, N and O, often referred to as "ices", or volatiles (H_2O, CH_4, NH_3, CO, N_2 and possibly CO_2). The remaining constituents consist of silicates (Mg, Si and O-rich material) and iron (as mixtures of more refractory elements under the form of metal, oxide, sulfide or substituting for Mg in the silicates). The behavior of these different elements as a function of pressure, under the conditions typical of giant planet interiors is not or poorly known. At very high pressure, the categorizations of gas, ice and rock become meaningless and these elements should become a mixture of closed-shell ions.

The most widely used EOS models for such elements are ANEOS (Thompson and Lauson 1972) and SESAME (Lyon and Johnson 1992), which describe the thermodynamic properties of water, "rocks" (olivine (fosterite Mg2SiO4) or dunite in ANEOS) and iron. These EOS consist of interpolations between existing Hugoniot data at low to moderately high (≈ 0.5 Mbar) pressure and Thomas-Fermi or more sophisticated first-principle calculations at very high density ($P > 100$ Mbar), where ionized species dominate. Interpolation, however, provides no insight about the correct structural and electronic properties of the element as a function of pressure, and thus no information about its compressibility, ionization stage (thus conductibility), or even its phase change, solid or liquid. All these properties can have a large impact on the internal structure and the evolution of the planets. A detailed comparison between these EOS, and the impact of the uncertainties on the radius determination for Neptune-like and Jupiter-like planets has been conducted by Baraffe et al. (2008), who showed that the discrepancies between these two equations of state can lead to difference of about 10% on the radius of a Neptune like planet at 1Gyr. Without conducting either ab-initio calculations or higher pressure experiments, we decided to use ANEOS. For practical purposes, some thermodynamic relations needed to implement the ANEOS package are provided in Appendix B.

1.4.2 Opacities

Deep in the interior, the large radiative opacity of planetary material yields completely inefficient heat transport by photons. Transport by conduction, resulting from collisions during random motion of particles, may in some cases be relevant. To account for these process, the numerical model uses the conductive opacity tables from Potekhin et al. (1999) and Cassisi et al. (2007), which are shown in

Fig. 1.1. In the central part of H/He dominated planets, thermal conductivity is dominated by electronic transport, and Eq. (1.32) yields a thermal diffusivity $\kappa_T \sim 10^{-5}\,\mathrm{m^2.s^{-1}}$. If no electrons are available, as in the outer envelope, conductive transport is dominated by the less efficient molecular motions with thermal conductivity $\kappa_T \sim 10^{-6}\,\mathrm{m^2.s^{-1}}$. Conduction by electrons (or eventually phonons) may also dominate in central cores composed of heavy material.

In the most outer layers, close to the planet photosphere, matter in less opaque, and radiative opacities must be used. There, one must take into account both continuous opacities (such as H^-, He^-, H_2^-, H_2^+, bound-free and free-free absorptions), molecular bonds and atomic lines. Their relative contribution depending greatly on the range of temperatures considered. Here we use the opacity tables from Ferguson et al. (2005) (see right panel of Fig. 1.1).

1.5   Boundary conditions

As for any set of differential equations, boundary conditions are needed to solve the system of structure equations. At the center, these are rather trivial

$$r(m = 0) = 0$$
$$l(m = 0) = 0. \tag{1.76}$$

However, it is not the case for the upper boundary. Indeed, one can start to see the problem in the fact that we still have not defined properly what we meant by the mass and radius of the object studied (M_1 and R_1). If this seems intuitive for terrestrial planets, for which there is a clear separation between a solid and gaseous phase that can be called *surface*, it is not so clear for giant planets. In this case, the mass and radius of the planet are not uniquely defined, but depend on the isobar (of pressure P_{atm}) taken as the reference surface, yielding $M_1 = m(P = P_{\mathrm{atm}})$. Hence, the boundary conditions we are looking for are

$$P(m = M_1) = P_{\mathrm{atm}}$$
$$T(m = M_1) = T_{\mathrm{atm}}, \tag{1.77}$$

where the first one is purely conventional. As thermodynamic quantities are constant on concentric shells, the radius of the object is defined as

$$R_1 = r(m = M_1). \tag{1.78}$$

Even if one could be tempted to use $P_{\mathrm{atm}} = 0$ to define the surface, one needs to remember that the equations that we have derived above are based on many assumptions, in particular the diffusion approximation, that is not valid at such low pressures where both radiative escape and incoming radiation cannot be neglected. Therefore, one must choose a reference isobar which is deep enough for the aforementioned approximations to be valid. Our problem can then be stated as finding the corresponding atmospheric temperature ($T_{\mathrm{atm}} = \mathrm{func}(P_{\mathrm{atm}})$). If *in situ* measurements are available, as, thanks to the *Cassini* and *Galileo* missions among others, it is the case for solar system giant planets, the atmospheric $T - P$ profile is directly measured down to the convective region (e.g. Guillot (2005) and reference therein). Thus any couple ($T_{\mathrm{atm}}, P_{\mathrm{atm}}$) taken in this region can be readily used as boundary conditions to infer the internal structure.

For far remote objects, modeling must be used. However, we can separate our planet in two zones

- the interior, below the $P = P_{\mathrm{atm}}$ isobar, that contains the mass M_1, have a radius R_1, and which is described by Eq. (1.57) through Eq. (1.60).
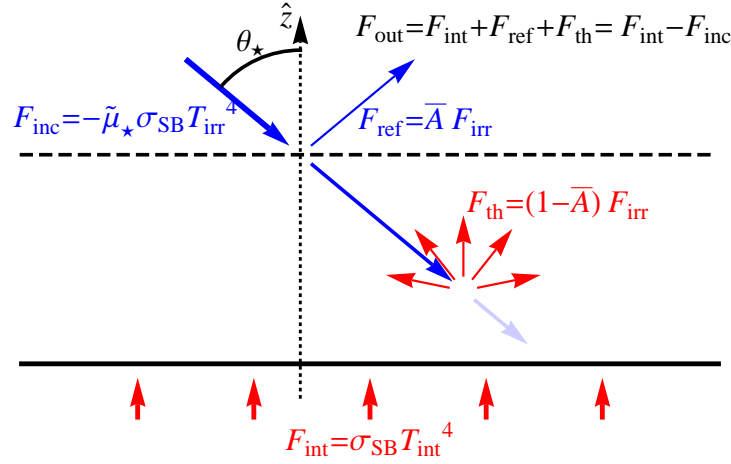
Figure 1.2: Schematic representation of the energy balance of the atmosphere. The planet receives a flux $\sigma_{SB}T_{irr}^4$ with an incidence $\theta_\star$ ($\mu_\star = \cos\theta_\star$). A fraction $\bar{A}$ is reflected directly and $1-\bar{A}$ is absorbed. Fluxes that are mostly characterized by visible wavelengths are drawn in blue. Fluxes in the infrared are drawn in red.

- the atmosphere, above the $P = P_{atm}$ surface, which contains a negligible mass, and where all the incoming external radiation is reflected or absorbed.

To find our missing relation, we will thus have to model this atmosphere. Even if our model uses complex numerical calculations provided by Allard and Hauschildt (1995) for non-irradiated objects, and Barman et al. (2001) for irradiated planets (see Baraffe et al. 2010 for a review), in this section, I will turn to simple analytical model to get a sense of the various physical parameters that determine the energetic and mechanical equilibrium state of an atmosphere.

1.5.1 Atmospheric energy budget and redistribution factor

From an energetic point of view, the atmosphere is the window by which the planet can release internal energy and receive incoming radiation. Its state must hence depend on the value of the incoming stellar flux, F_{inc}, and of the intrinsic gravo-thermal outgoing flux F_{int}. However, to extract the important parameters, let us consider the energy balance of this layer. As shown on Fig. 1.2, if we consider an area of the atmosphere positioned at an angle $\theta_\star$ from the substellar point[18] (with $\mu_\star \equiv \max[\cos\theta_\star, 0]$), the flux received perpendicularly to the surface[19] reads

$$F_{inc} = -\left(\frac{R_\star}{r_\star}\right)^2 \mu_\star \sigma_{SB} T_{eff,\star}^4 \equiv -\mu_\star \sigma_{SB} T_{irr}^4, \tag{1.79}$$

where $R_\star$, $r_\star$ and $T_{eff,\star}$ are respectively the stellar radius, distance, and effective temperature. T_{irr} is thus the temperature which characterizes the incoming radiation. From this total impinging flux, a fraction $F_{ref} \equiv \bar{A} \cdot F_{inc}$, where $\bar{A}$ is the Bond Albedo, can be considered as directly reflected by the top of the atmosphere, while the remaining energy, $(1-\bar{A}) \cdot F_{inc}$ penetrates deeper down. In addition, the atmosphere is heated from below by the intrinsic internal flux of the planet F_{int}.

---

[18]The point at the surface for which the star is at its zenith.

[19]The convention taken here is that fluxes are positive if energy is actually transported upward, i.e. toward the positive $\hat{z}$ direction as shown on Fig. 1.2.

Because we have chosen the base of our atmosphere to be deep enough, there, the total net flux is equal to the internal flux

$$F_{\text{net}} = F_{\text{int}}. \tag{1.80}$$

If thermal equilibrium is achieved, this net flux must be conserved throughout the atmosphere, and particularly at the top where, F_{out} being the flux escaping the atmosphere,

$$F_{\text{net}} = F_{\text{out}} + F_{\text{inc}}. \tag{1.81}$$

Thus,

$$F_{\text{out}} = F_{\text{int}} - F_{\text{inc}} = F_{\text{int}} + F_{\text{th}} + F_{\text{ref}}. \tag{1.82}$$

Thus we see that the outgoing flux - the one that is seen by an observer - is the sum of the reflected light, which contributes mainly at optical wavelengths, of the internal flux, and of $F_{\text{th}} \equiv (1 - \bar{A}) \cdot F_{\text{inc}}$ which is the part of the oncoming radiation that has been absorbed and thermalized in the atmosphere, and which is re-emitted mainly at thermal wavelengths.

It is customary to define an *internal effective temperature*[20] as the temperature of the blackbody that would radiate like the interior

$$\boxed{F_{\text{int}} \equiv \sigma_{\text{SB}} T_{\text{int}}^4,} \tag{1.83}$$

and an *outgoing effective temperature* that similarly characterize the local escaping thermal radiation

$$\boxed{F_{\text{int}} + F_{\text{th}} \equiv \sigma_{\text{SB}} T_{\text{eff}}^4.} \tag{1.84}$$

It thus follows that

$$\begin{aligned} T_{\text{eff}}^4(\mu_\star) &= T_{\text{int}}^4 + \frac{1 - \bar{A}}{\sigma_{\text{SB}}} F_{\text{inc}}(\mu_\star) \\ &= T_{\text{int}}^4 + \mu_\star (1 - \bar{A}) T_{\text{irr}}^4, \end{aligned} \tag{1.85}$$
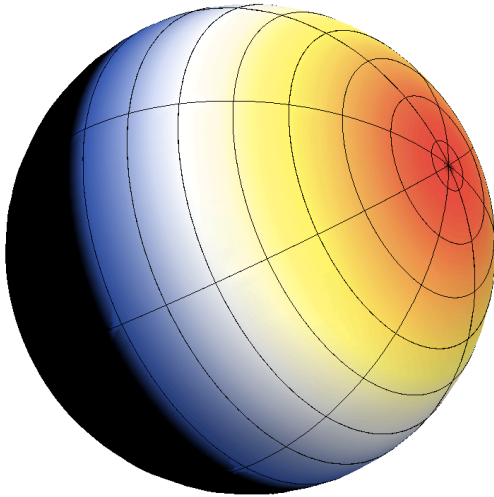
Figure 1.3: Equilibrium temperature map. The substellar point is the convergence point of the mesh lines.

which shows that this outgoing effective temperature varies with the position on the planet. This is just due to the fact that we are considering local equilibrium, and thus, the re-radiated energy is proportional to the incoming energy which varies from one point of the surface to another. This can be used, for example, to calculate the temperature of a well defined surface in thermal equilibrium with an incoming radiation at the temperature T_{irr} and with an incidence characterized by $\mu_\star$, which is given by

$$T_{\text{eq}}^4(\mu_\star) = \mu_\star (1 - \bar{A}) T_{\text{irr}}^4, \tag{1.86}$$

and shown on Fig. 1.3.

---

[20]In the literature concerning internal structure and evolution, the energy absorbed and re-emitted by the atmosphere is often *not* considered as it does not affect the interior. Thus, there is no call for creating a distinction between T_{int} and T_{eff}, which are lumped together and called *effective temperature*. Here, as we are also concerned with the atmospheric boundary problem, I have decided to make the distinction between the *internal effective temperature*, T_{int}, and the *outgoing effective temperature*, T_{eff}. However, as T_{int} is the quantity that is most used in the following, it will be called *effective temperature* for brevity.

Spatial averaging

However, in our case, the modeling is essentially one dimensional. Thus, we are looking for a quantity that would characterize the equilibrium of the total object. In addition, the thermal gradients created at the surface by the temperature distribution of Eq. (1.86) will cause some horizontal energy transport, both by conduction and advection. Thus considering that energy is only globally conserved, we can define a mean outgoing effective temperature

$$\bar{T}_{\text{eff}}^4 \equiv \frac{1}{2} \int_{-1}^{1} T_{\text{eff}}^4(\tilde{\mu}) \mathrm{d}\tilde{\mu} = \frac{1}{2} \int_{-1}^{1} \left(T_{\text{int}}^4 + \tilde{\mu}(1-\bar{A}) T_{\text{irr}}^4 \right) \mathrm{d}\tilde{\mu} = T_{\text{int}}^4 + \frac{1-\bar{A}}{4} T_{\text{irr}}^4, \tag{1.87}$$

and the mean equilibrium temperature, that is the temperature that would have the planet once in complete thermal equilibrium

$$\boxed{\bar{T}_{\text{eq}}^4 = \frac{1-\bar{A}}{4} T_{\text{irr}}^4.} \tag{1.88}$$

This is also the equilibrium temperature reached by a planet that would be irradiated uniformly by an average flux

$$\bar{F}_{\text{inc}} = -\bar{f} \left(\frac{R_\star}{r_\star} \right)^2 \sigma_{\text{SB}} T_{\text{eff},\star}^4 = -\bar{f} \sigma_{\text{SB}} T_{\text{irr}}^4, \tag{1.89}$$

where $\bar{f}$, the redistribution factor, is here equal to 1/4th, which corresponds to a redistribution over the whole surface of the planet. If redistribution over the dayside only is considered, $\bar{f} = 1/2$. Intermediate values between these two are often used in complex numerical calculations (Allard et al. 1997 ; Barman et al. 2001). However, as is discussed in § 1.5.2, thanks to a simple analytical model, it is possible to make a more educated guess about $\bar{f}$.

If T_{irr} is a good parametrization of the incoming stellar irradiation[21], $\bar{T}_{\text{eq}}$ quantifies more specifically the way this irradiation will affect the planet. For low albedo planets, as seems to be the case of Giant planets (Sudarsky et al. 2003 ; Hood et al. 2008), these two temperature are however redundant. In the following, we will thus use T_{irr}.

Temporal averaging

As planets are possibly on eccentric orbits, their distance to their host star, and thus the incoming flux, is not constant in time. As this variation is periodic, and with a period which is typically shorter than the evolutionary timescale of our planet[22] (see § 1.2), we can average it on an orbit to get the mean flux and irradiation temperature

$$\langle \bar{F}_{\text{inc}} \rangle = -\bar{f} \langle \frac{R_\star^2}{r_\star^2} \rangle \sigma_{\text{SB}} T_{\text{eff},\star}^4 = -\frac{\bar{f}}{\sqrt{1-e^2}} \left(\frac{R_\star}{a} \right)^2 \sigma_{\text{SB}} T_{\text{eff},\star}^4, \tag{1.90}$$

where a and e are the semi-major axis and eccentricity of the orbit. Details of the calculations can be found in §I.1.1. Interestingly enough, when a planet is on an eccentric orbit, the mean flux that it receives and the mean star-planet distance increase at the same time. In the following, this rescaling of the incident flux is always assumed to be done and included in T_{irr} when needed.

---

[21]Note that here, we have not considered the spectral dependance of the incoming stellar flux at all. Therefore, T_{irr} informs us on the amount of incoming energy, but not at all on its spectral distribution.

[22]Rigorously, we should compare the orbital period to the radiative timescale of the atmosphere, which can be on the same order of magnitude. However, the error introduced here should be comparable to the one already caused by our spatial averaging.

1.5.2 Atmospheric boundary conditions

We can now state our basic problem as

1. choosing a parameter x_{atm} which defines a level in the atmosphere at which incoming stellar energy has been absorbed, but that lies above where most of the mass of the object is enclosed,

2. solving the hydrostatic equilibrium and the radiative transfer in our atmosphere to find the two missing relations, $P_{atm}(T_{irr}, T_{int}, x_{atm})$, and $T_{atm}(T_{irr}, T_{int}, x_{atm})$.

In general, to solve this problem properly, one should take into account the whole spectral dependance of the incident and internal radiations, and of the opacity of the mixture, and can be treated only numerically, as done for example by Allard and Hauschildt (1995) ; Barman et al. (2001), among others. In this section, in order to have an integrable system that allows us to grasp the main physics at work, we will use the semi-grey approach developed by Hansen (2008) and Guillot (2010).

Using this toy model, in the end of this section, I will also show that numerical 1D calculations of the atmospheric boundary conditions of substellar objects that consider a redistribution of the stellar flux over the day side only (i.e. which use $\bar{f} = 1/2$) overestimate the impact of the irradiation on the structure of the object. Indeed, I will show that, taking into account the horizontal advection that must take place at depth is equivalent to using a redistribution factor that is bracketed between $1/4$ and $1/(2\sqrt{3})$.

Two-band approximation

In this approach, scattering, and thus reflection, is neglected ($\bar{A} = 0$), and we consider that the spectrum can be split in two bands

- a visible band where the radiation field is mostly set by the stellar irradiation, which is characterized by $\bar{f}$, T_{irr}, and the opacity is considered constant and equal to κ_{vis},

- a thermal band where the internal energy, described by T_{int}, and the absorbed stellar flux is emitted. The opacity in this band is called κ_{th}.

Note that, the weight to be used in the spectral averaging leading to κ_{vis} and κ_{th} can depend on the physical conditions, and is in itself a complex matter which is not discussed here. It is further assumed that there is *no vertical heat flux due to convection*, and that the atmosphere is in complete radiative equilibrium. Because the complete derivation of all the formula used hereafter would lead us into a lengthy development that is not needed here, we will just define the main variable used. For details the reader is referred to Mihalas (1978) ; Hansen (2008) ; Guillot (2010). To define our parameter, we can use the *column mass*[23],

$$m^* \equiv \int_r^\infty \rho \, dr'. \tag{1.91}$$

This can be linked to the *optical depth* in one of the two bands, which can be integrated from the surface to the local position r using

$$d\tau_{th} \equiv -\kappa_{th}\rho \, dr \quad \Rightarrow \quad \tau_{th} = \kappa_{th}m^*, \tag{1.92}$$

---

[23] With this definition, it is obvious that m^* is the mass per unit area contained between the top of the atmosphere and a given radius r. To convert this in actual mass, one can use the fact that the vertical size of the atmosphere is far smaller than the planet radius R_1. Then the mass of the atmosphere above the radius r is roughly $m_{atm}(r) \equiv 4\pi \int_r^\infty \rho \, r'^2 dr' \approx 4\pi R_1^2 m^*$.

or

$$d\tau_{\text{vis}} \equiv -\kappa_{\text{vis}} \rho \, dr \quad \Rightarrow \quad \tau_{\text{vis}} = \kappa_{\text{vis}} m^*. \tag{1.93}$$

where each definition can be used to characterize respectively the thermal and visible radiations. Finally, if hydrostatic equilibrium holds, Eq. (1.11) tells us that

$$\left. \frac{\partial P}{\partial r} \right|_t = -g\rho, \tag{1.94}$$

where g is the gravitational acceleration that can be considered constant in the outer layers. Then the pressure at any given level reads

$$P = g m^* = \frac{g}{\kappa_{\text{th}}} \tau_{\text{th}} = \frac{g}{\kappa_{\text{vis}}} \tau_{\text{vis}}. \tag{1.95}$$

Guillot (2010) showed that, for an isotropic incoming radiation, the energy density of the visible radiation decreases as $e^{-\sqrt{3}\tau_{\text{vis}}}$. Then our first constraint on the choice of the boundary yields $\kappa_{\text{vis}} m^* \gg 1$. As typical opacities in the visible under the relevant conditions are on the order of $10^{-3} - 10^{-4} \, \text{m}^2.\text{kg}^{-1}$, this implies $m^* \gg 10^{3-4} \, \text{kg.m}^{-2}$, and pressures $P_{\text{atm}} \gg g/\kappa_{\text{vis}} \approx 0.1 - 0.01$ bar. Because the mass of the atmosphere contained above the m^* level is given by $m_{\text{atm}} \approx 4\pi R_1^2 m^* \approx 10^{-7} M_1$ for Jupiter, the second condition ($m_{\text{atm}} \ll M_1$) is not very restrictive.

Temperature profile

We now turn to the temperature at the boundary. Guillot (2010) also showed that in the same conditions, the temperature profile is given by (see Eq. (29) in his paper)

$$T^4(m^*) = \frac{3 T_{\text{int}}^4}{4} \left[\frac{2}{3} + \kappa_{\text{th}} m^* \right] + \bar{f} \frac{3 T_{\text{irr}}^4}{4} \left[\frac{2}{3} + \frac{\kappa_{\text{th}}}{\kappa_{\text{vis}}\sqrt{3}} + \left(\frac{\kappa_{\text{vis}}}{\kappa_{\text{th}}\sqrt{3}} - \frac{\kappa_{\text{th}}}{\kappa_{\text{vis}}\sqrt{3}} \right) e^{-\kappa_{\text{vis}} m^* \sqrt{3}} \right]. \tag{1.96}$$

One can see that, in the absence of stellar radiation, the usual Eddington profile is recovered, and the temperature at $\tau_{\text{th}} = \kappa_{\text{th}} m^* = 2/3$ is equal to T_{int}. This also shows that for $\kappa_{\text{vis}}/\kappa_{\text{th}} > 1$, a temperature inversion can occur at low pressures, which is due to the direct thermal heating of the atmosphere by the incoming radiation. Placing ourselves in a zone fulfilling the first condition ($\kappa_{\text{vis}} m^* \gg 1$), and choosing a reference pressure, our boundary condition is then given by

$$T_{\text{atm}}^4 = \frac{3 T_{\text{int}}^4}{4} \left[\frac{2}{3} + \frac{\kappa_{\text{th}}}{g} P_{\text{atm}} \right] + \bar{f} \frac{3 T_{\text{irr}}^4}{4} \left[\frac{2}{3} + \frac{\kappa_{\text{th}}}{\kappa_{\text{vis}}\sqrt{3}} \right]. \tag{1.97}$$

We can see from this relation than therefore depends on three parameters, i.e. T_{int}, T_{irr} and the gravity g[24].

For typical values of

$$\kappa_{\text{vis}} \approx 10^{-3} - 10^{-4} \, \text{m}^2.\text{kg}^{-1}$$

and

$$\kappa_{\text{th}} \approx 10^{-2} \, \text{m}^2.\text{kg}^{-1},$$

$T_{\text{int}} \approx 200$ K, $T_{\text{irr}} \approx 2000$ K and $\bar{f} = 1/4$, Eq. (1.96) yields a nearly isothermal zone between 1 and 100 bar. Then, this zone is nicely fitted to contain our boundary. Fig. 1.4 shows the value of T_{atm} for $P_{\text{atm}} = 10$ bar. We can see that irradiation starts to play a significant role for $T_{\text{irr}} \gtrsim T_{\text{int}}$, and will therefore have a diminishing impact with the mass of the irradiated planet, as we will see in Chapter 2.

---

[24]Note that if the $T_{\text{atm}} = \text{func}(P_{\text{atm}})$ relation does depend on g, at given mass, g itself depends on the radius of the object which is determined by the integration, and thus by the boundary conditions. In other words, g is not a *free parameter* for our structure model. In practice some iterative process is needed to ensure that the $(P_{\text{atm}}, T_{\text{atm}})$ used are consistent with the structure found.

Redistribution factor and advection

With this model, we can also make an attempt to make a more *educated* guess of the redistribution factor. Indeed, taking into account an horizontal, conservative and efficient enough advection of energy at depth, Guillot (2010) also shown that, even with a non-uniform insolation described by Eq. (1.79), the temperature becomes mostly longitudinally and latitudinally homogeneous at high pressures, and is given by

$$\overline{T^4} = \frac{3\,T_{int}^4}{4}\left[\frac{2}{3} + \frac{\kappa_{th}}{g}P\right] + \frac{3\,T_{irr}^4}{16}\left[\frac{2}{3} + \frac{2}{3}\frac{\kappa_{th}}{\kappa_{vis}}\right]. \tag{1.98}$$

Comparing Eqs. (1.97) and (1.98), I find that in this model,

$$\bar{f} = \frac{1}{4}\frac{1 + \frac{\kappa_{th}}{\kappa_{vis}}}{1 + \frac{\sqrt{3}}{2}\frac{\kappa_{th}}{\kappa_{vis}}} \;\Rightarrow\; \boxed{\frac{1}{4} \leqslant \bar{f} \leqslant \frac{1}{2\sqrt{3}} \approx 0.29,} \tag{1.99}$$

where the lower and upper boundaries are respectively given by for $\kappa_{th}/\kappa_{vis} \ll$ or $\gg 1$ (the typical values of the opacity mentioned above yielding $\kappa_{th}/\kappa_{vis} \approx 10^{1-2}$),

Figure 1.4: Atmospheric boundary temperature (T_{atm}; Eq. (1.97)) at the 10 bar level ($P_{atm} = 10$ bar) as a function of the internal flux (parametrized by T_{int}) and incoming stellar flux (parametrized by T_{irr}) for a redistribution factor $\bar{f} = (2\sqrt{3})^{-1}$ (see text).

which is, as expected, larger than 1/4th. **This shows that, in this simple model, because the energy redistribution at depth is rather efficient, averaging the incoming flux over the whole planet is more justified than averaging over the dayside only. Indeed, taking a redistribution factor of 1/2 overestimates the irradiation term in Eq. (1.97) by a factor $\sqrt{3} \approx$ 1.7 to 2.**

While the differences yielded by such a factor are modest in comparison with other uncertainties, especially on opacities, the accurate determination of the redistribution factor is at least of theoretical importance as it gives us some insight on the efficiency of horizontal energy transport inside exoplanets. Let me conclude by noting that, of course, the above estimation is very rough, and such an issue should be addressed with numerical Global Circulation Models (GCM) taking properly into account both radiative transfer and hydrodynamics, and maybe magneto-hydrodynamics.

Chapter 2

Evolution & stellar irradiation: A lid on the boiling kettle

Il faudra revoir vos estimations à l'aune de la mécanique rationnelle.

Lord Kelvin au sujet de l'estimation de l'âge de la Terre

Lord Kelvin a donné une limite supérieure de l'âge de la Terre, sous la condition qu'on ne découvre pas de source de chaleur nouvelle. Cette possibilité prophétiquement annoncée, c'est précisément notre sujet d'aujourd'hui, le radium ! Voyez ! Le vieil homme me gratifia d'un sourire.

Sir Ernest Rutherford

Contents

In this chapter, the first goal will be to review some standard results of the theory of planetary evolution (see § 2.1). To that purpose, I compute new grids of numerical planetary models. I will also discuss possible definitions to distinguish planet from brown dwarfs.

Then, in § 2.2, I analyze these grids of planetary models to show what they can tell us about the interior mechanical structure of extrasolar planets. In particular, I show that the internal $T - P$ profile of a giant planet is well approximated by a polytrope throughout the deep interior, and that this gives us some insight on the behavior of the equation of state in the various regime considered. As a result, I show that the whole mechanical structure can be characterized by a single quantity, namely an effective *polytropic index*, and that the variation of this polytropic index with the mass of the planet can directly be seen on the slope of the *mass-radius relationship*. The results of this sections were published in the article *Distorted, non-spherical transiting planets: impact on the transit depth and on the radius determination* (Leconte et al. 2011c).

in § 2.3, I address the problem of the bloated giant exoplanets, and review the major propositions made to explain it. I show how taking into account the stellar irradiation allows us to decrease the discrepancy. Doing so, I first estimate the impact of the stellar irradiation on the internal structure, for example on its effective polytropic index (see § 2.4.2), and then, in § 2.4.3, quantify more precisely the *radius anomaly* as was done in *The radius anomaly in the planet/brown dwarf overlapping mass regime* (Leconte et al. 2011b). I will defer the discussion of some of the physical mechanisms proposed to explain this radius anomaly, such as semi-convection and tidal heating, to Chapter 4 and 5.

Finally, in § 2.5, I will show how the mass-radius diagram can be used to constrain the composition of extrasolar planets (§ 2.4.4), and help us distinguish giant planets from mini brown dwarfs in the favorable cases (§ 2.5). This method is also described in *Structure and evolution of the first CoRoT exoplanets: probing the brown dwarf/planet overlapping mass regime* (Leconte et al. 2009).

Planetary

EVOLUTION IS A LONGSTANDING PROBLEM. If observational data concerning the current internal structure of a planet are already sparse, fewer are the one on its early state and evolution. It is therefore extremely difficult to predict accurately the properties of a celestial body at a given age, or simply to date its formation. This problem is well illustrated by the controversy that raged during more than 200 years about the age of the Earth. Between Aristotle theory that the Earth has been there from the beginning of times, and the christian thesis dating the creation between 3483 and 6984 BC, physical arguments came to heat up the debate during 18th century.

On one side, Edmond Halley in 1715, followed by Henri Gautier, and nearly one century later, by Charles Darwin, proposed geological arguments demonstrating that the Earth should be older than a few hundred years. Darwin will propose more than 300 million years, which seems in agreement with his theory of a slow natural selection. This possibility was supported by Leonahrd Euler and William Herschel who noted that because light is moving at a finite speed, as has been demonstrated by Römer in 1676, its travel from distant stars could take longer than a few million years. On the other side, Buffon in 1778 and Lord Kelvin in 1862 claimed that the Earth could not be so old. If, as they think, the planet was initially molten, the time that it needed to solidify and cool down to its current temperature should not exceed 100 million years. Later on, with the german physicist Hermann Ludwig Ferdinand von Helmholtz, Kelvin estimated the time needed by the sun to radiate its gravitational energy (defining at the same time the Kelvin-Helmholtz timescale) and lowered down his estimate of the age of the Earth formation to 20 million years. At this point, it seemed impossible to reconcile physicists and geologists.

We will have to wait until the end of the 19th century, and the discovery of a new energy source, radioactivity, to relieve the tension. After Henri Becquerel's discovery, Ernest Rutherford, Lord Rayleigh and others reassessed the age of the Earth, which started to increase until it reached its currently accepted value of 4.55 billion years.

Amusingly, nearly 300 years later, history seems to repeat itself ! Other worlds have been found, and while their parent star seems old, some of them exhibit a surprisingly high radius (i.e. a large thermal energy content), which is usually a sign of youth. However, before starting to look for an extra energy source, it is primordial to accurately quantify this so-called *radius anomaly*.

2.1 Isolated planets

Let us start with *isolated* objects, i.e. objects for which the incident stellar flux can be neglected. As was discussed in Fig. 1.4, this condition can be reformulated as $T_{irr} \ll T_{int}$ for which the evolution of the planet is determined only by its own properties, without any assumption on the parent star. In this section, we will make use of this simpler case to derive some general features of the structure and evolution of planets. This will also provide us with a reference case to compare with when we will consider close in objects.

2.1.1 Adiabaticity

One of the first question that arises is how energy is transported within the object, and consequently, whether the interior is convectively stable or not. We have seen in § 1.1.4, that the stability criterion is given by

$$\nabla_{\mathrm{d}} < \nabla_{\mathrm{ad}}. \tag{2.1}$$

For smaller diffusive gradients, radiative forcing is to weak and all the flux can be carried out by both radiation and conduction. For stronger forcing, however, convection sets in and very efficiently transport a large fraction of the flux (see Chapter 4 for more details).

In the outer layers, the adiabatic gradient can be easily estimated from the classical perfect gas approximation. Indeed, differentiating logarithmically Eqs. (1.69) and (1.70) at constant specific entropy, we see that

$$\frac{2}{7} \lesssim \nabla_{\mathrm{ad}} \lesssim \frac{2}{5}, \tag{2.2}$$

where the first value is derived for a diatomic perfect gas (H_2 for example), and the second for a monoatomic one (He ; see § 1.4.1).

For the radiative gradient[1], which reads

$$\nabla_{\mathrm{rad}} \equiv \frac{3}{16} \frac{\bar{\kappa} P}{T^4} \frac{T_{\mathrm{int}}^4}{g}, \tag{2.3}$$

the problem is much more complex. Even if T_{int} and g can be considered constant in the outer part of the object, the problem lies in the fact that ∇_{rad} depends on P and T, but that the $T - P$ profile itself depends on the integral of ∇_{rad} in a radiative zone[2]. To grasp the difficulty, let us consider a very simple model where the opacity follows a law of the type

$$\bar{\kappa} = \kappa_0 T^{b_T} P^{b_P}. \tag{2.4}$$

Then, an integration of Eq. (2.3) yields

$$T^{4-b_T} = \frac{4-b_T}{1+b_P} \frac{3}{16} \frac{\kappa_0 T_{\mathrm{int}}^4}{g} (P^{1+b_P} + \mathrm{cst}), \tag{2.5}$$

and in the limit of the high pressures, the radiative gradients tends to

$$\nabla_{\mathrm{rad}} = \frac{1+b_P}{4-b_T}, \tag{2.6}$$

which is completely independent of κ_0 (Kippenhahn and Weigert 1990). Thus the transition from a radiative zone to a convective one is not determined by the value of the opacity[3], but by its variation with the temperature and pressure (or density), which is difficult to model analytically. This is confirmed by our simple atmospheric radiative transfer model discussed in § 1.5.2. Indeed, in this model, $\bar{\kappa}$ is constant ($b_T = 0, b_P = 0$), and we can easily see from Eq. (1.96), that $\nabla_T \to 1/4$ in the high pressure limit. Note that, according to the Schwarzschild criterion and Eq. (2.2), this radiative gradient is insufficient to trigger convection.

---

[1]As we are considering the outer layers of the object, thermal conductivity of the electron can be neglected with respect to the radiative diffusivity.

[2]Provided that the diffusion approximation holds. If not, as is the case in the upper atmosphere, the whole radiative transfer must be calculated, still worsening the problem.

[3]Contrarily to the transition from a convective zone toward a radiative one, where the $T - P$ profile is determined by the adiabatic gradient independently of the opacity, and where the criterion for the existence of a *radiative window* can be formulated under the form of a κ_0 threshold (see Guillot et al. 1994 for details).
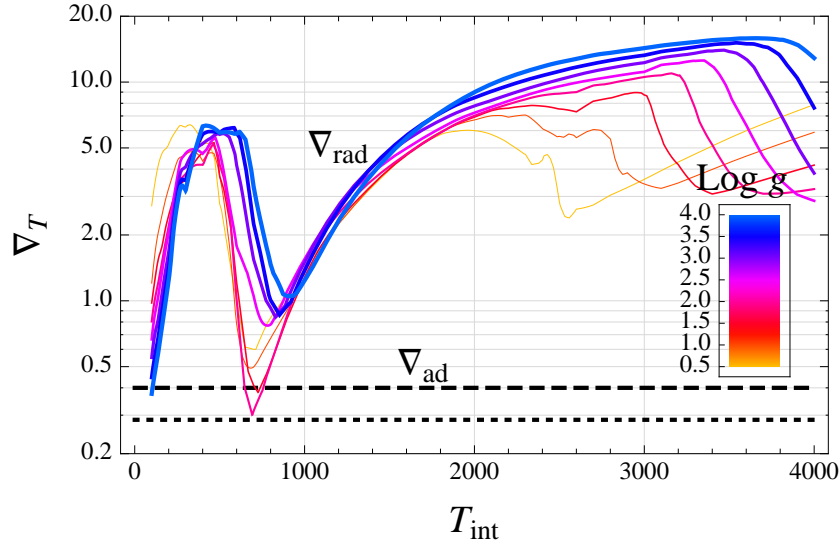
Figure 2.1: Radiative gradient (∇_{rad}) just below the atmosphere ($\bar{\tau}_{\mathrm{atm}} = 100$) as a function of the internal outgoing flux T_{int} for different surface gravities (g ; log g increases by 0.5 dex from 0.5 (thin orange) to 4 (thick blue)). The $T - P$ profiles are taken from Allard and Hauschildt (1995). The adiabatic gradients of mono- (dashed) and diatomic (dotted) perfect gases are also shown for comparison.

Therefore, in order to determine the main transport mechanism at play, **I have used the $T - P$ profiles obtained by Allard and Hauschildt (1995) by solving non grey radiative transfer for an atmosphere in radiative and hydrostatic equilibrium, and computed the value of ∇_{rad} just below the atmospheric boundary level (i.e. at an optical depth of $\bar{\tau}_{\mathrm{atm}} = 100$) with the opacities from § 1.4.2. The results are shown in Fig. 2.1.** We can see that at this optical depth, the medium is always convectively unstable for $T_{\mathrm{int}} \gtrsim 50 - 100\,\mathrm{K}$, the radiative zone being confined to smaller optical depth/pressures. For lower effective temperatures, and thus for older objects, the radiative zone eventually extends deeper down because of the lower radiative forcing, and the object tends toward an isothermal sphere.

Whether the medium remains convectively unstable deeper down can however depend on the physical conditions. It has indeed been proposed by Guillot et al. (1994) that an opacity gap near 1000-2000 K could open a *radiative window* in solar system giant planets. If this possibility seems now improbable as the opacity gap is filled by metal spectral lines, it is still possible in hotter and/or irradiated objects (Burrows et al. 1997).

Because convection is very efficient in gaseous planets, giant planets like Jupiter which are far from their star, or single brown dwarfs follow a nearly adiabatic $T - P$ profile. Hence, $\tilde{S}$ is constant in the interior, which involves a powerful simplification of the equations. Indeed, neglecting nuclear reactions, the luminosity equation can be integrated to give

$$
\begin{aligned}
l(m) &= -\int_0^m T \frac{\partial \tilde{S}}{\partial t}\, \mathrm{d}m \\
&= -\int_0^m T \, \mathrm{d}m \frac{\partial \tilde{S}}{\partial t} \\
&\equiv -\bar{T}(m) \frac{\partial \tilde{S}}{\partial t},
\end{aligned}
\tag{2.7}
$$

where $\bar{T}(m)$ is the mean internal temperature interior to m, with $\bar{T}_1 \equiv \bar{T}(M_1)$. In addition, because ∇_{ad} is independent of the actual luminosity profile, the $T - P$ profile can be integrated from the values of

the temperature and pressure at the atmospheric boundary. Therefore the luminosity affects the structure only by its impact on the boundary conditions (see § 1.5.2).

2.1.2 Parametrization

Now that we have set up our model, let us review the independent parameters on which depend the global structure of the object. The first one is obviously the value of our integration variable m at the boundary, i.e. the mass of our object M_1. As we have seen in § 1.5.2, the upper boundary consists in two parameters, P_{atm} and T_{atm}, where the first one is mostly conventional, and serves to define precisely the radius, and the second one can be calculated by modeling the atmosphere and depends on the internal (T_{int}) and incoming (T_{irr}) luminosities.

For an object with a given mass and in a given environment[4], we are therefore left with at least *one* degree of freedom, namely the *effective temperature* T_{int}. This is rather fortunate ! Indeed, we have to let the liberty to our planets to evolve with time. **To see how the structure of the planet depends on this parameter, I have simulated *isolated* solar composition H/He gaseous spheres ($T_{irr} = 0$) with mass ranging between approximately $10 M_\oplus$ and $2 M_{Jup}$ with the numerical code CHESS (see Appendix J).** Results are shown in Fig. 2.2.

As discussed above, all these objects are mainly adiabatic, and the specific entropy ($\tilde{S}$) is constant throughout the interior. As expected from Eqs. (1.70) and (1.97), once a reference isobar is chosen, bijective relations exist between T_{atm}, T_{int} and $\tilde{S}$ (which all evolve in the same direction), and any of these quantities can be used indifferently to parametrize the tracks in Fig. 2.2. Following a given track from right to left, we can see that, thanks to the adiabatic condition, the internal temperature also decreases when the external layers of the planet get colder (panel c). Hence, at a given pressure level, the decreasing thermal pressure support of the ions must be counteracted by an increase of the density (panel d) and of the degeneracy of the electrons (panel f). In turn, this local and global increase of the density causes a shrinkage of the radius (panel b) and, because of the hydrostatic condition, an increase of the central pressure (panel a).

The problem is thus to solve the luminosity equation to find the evolution of the effective temperature with time $T_{int}(t)$. Indeed, in the adiabatic case, Eq. (1.59) is decoupled from the rest of the system and can be rewritten

$$\frac{\partial}{\partial t}\left[\tilde{S}(T_{int})\right] = -4\pi\,\sigma_{SB}\,\frac{R_1^2(T_{int})\,T_{int}^4}{\bar{T}_1(T_{int})}. \tag{2.8}$$

While our evolutionary code directly solve the whole set of equations, Eqs. (1.57-1.60), this relation could in principle be directly integrated following any track in Fig. 2.2.

However, we can see on Fig. 2.2.d that these models are not totally representative of Solar System giant planets, Jupiter and Neptune[5]. Indeed both planets are denser (and by a large factor for Neptune) than the models of the same mass and effective temperature. This tells us that there is at least another free parameter that we did not yet considered. If this free parameter is not obvious in our set of structure equations, we already encountered it in § 1.4.1. Indeed, to model a planet, one needs to specify the material it will be made of, and use the relevant equation of state. For the moment we only consider gaseous spheres with a solar composition, but the discrepancy stated above is a first clue that dense materials (called heavy elements) must be present inside Solar System giant planets, and giant planets in general. This issue will have to wait until § 2.4.4.

---

[4]Here, the environment is simply defined by the type of the host star and by the orbital configuration which determine the spectral and temporal characteristics of incoming energy received. To simplify the discussion, we will consider that only the average flux, and thus T_{irr}, matters. In this section, however, we consider only isolated object, yielding $T_{irr} = 0$.

[5]While it is not shown here, the same conclusions hold for Saturn and Uranus.

(a) Central pressure

(b) Radius

(c) Central temperature

(d) Mean density

(e) Specific entropy

(f) Degeneracy parameter
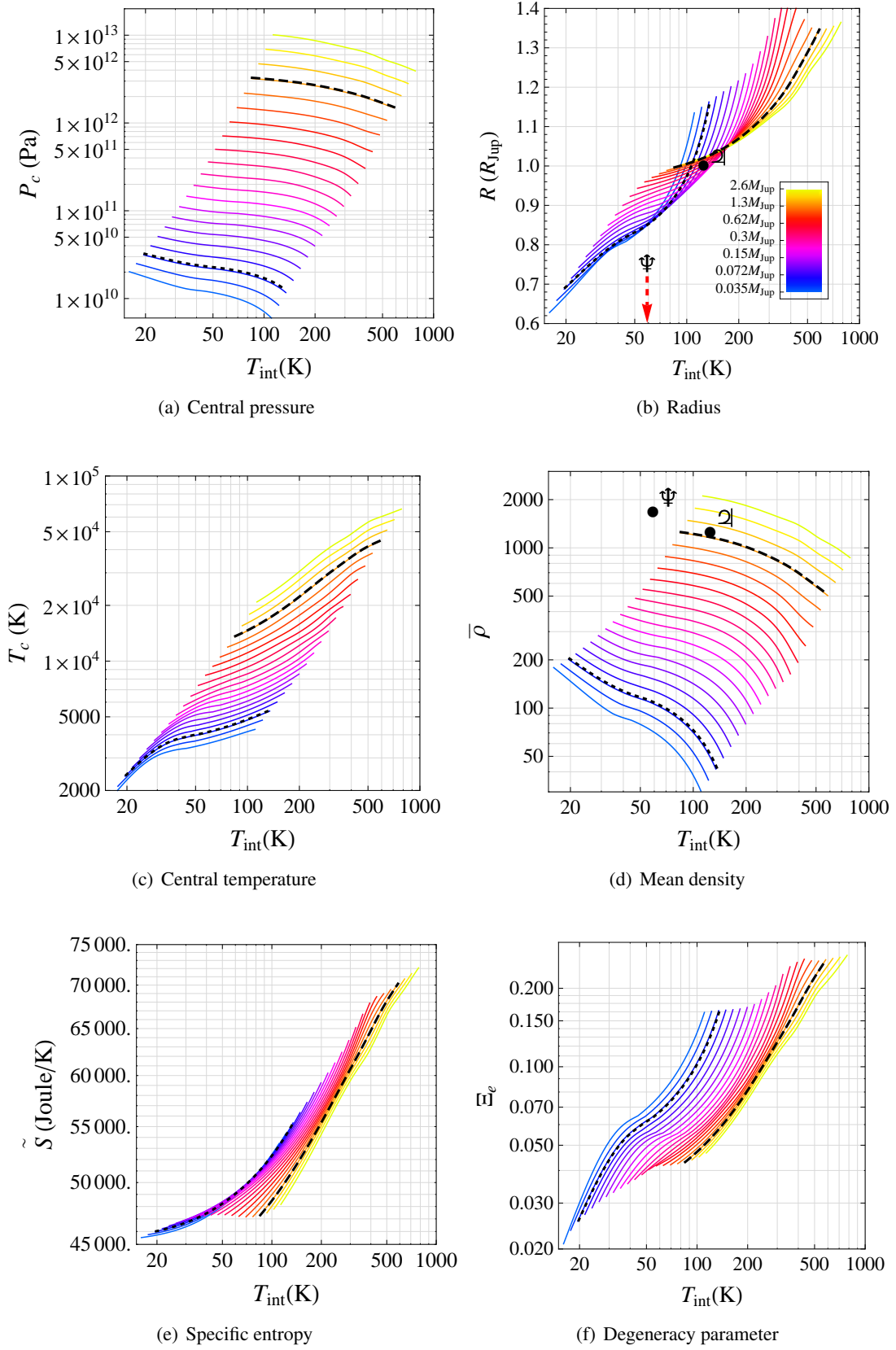
Figure 2.2: Evolutionary tracks parametrized by T_{int} for different masses. The dashed and dotted curves represent respectively the $1M_{\text{Jup}}$ and $1M_{\text{\male}}$ case. The black dots represent the actual Jupiter ($T_{\text{int}} = 125$ K, R_1=71 492 km) and Neptune (T_{int}=59 K, R_1=24 552 km).

2.1.3 Evolution and energy budget

Now that we have all the ingredients needed to compute evolutionary tracks, it is time to use our numerical model to predict the behavior of the various physical quantities describing our objects, and to extract some general features. in order to show the similarities and differences arising between the various mass regimes in the substellar and stellar domain, I computed a grid of models of H/He gaseous spheres covering $M_1 \in \left[1 M_{\text{Jup}}, 100 M_{\text{Jup}}\right]$. Some of these evolutionary tracks are shown in Fig. 2.3. We can clearly distinguish 3 domains

- $M_1 < M_{2\text{HBMM}}$, solid curves in Fig. 2.3 ; The object is not massive enough for its interior to reach sufficiently high central pressures and temperatures, and nuclear reactions never ignite. The internal entropy is radiated away, but the energy lost does not only come from gravitational contraction has it is often said, but also (and sometimes mainly) from the thermal component. To disentangle both contributions, let us consider the energy budget of the object. As we have seen in § 1.2.2, thanks to the Virial theorem,

$$E_{\text{grav}} + \zeta E_{\text{int}} = 0, \tag{2.9}$$

where ζ is a characteristic of the equation of state defined through $E_{\text{int}} \equiv \frac{3}{\zeta} \int \frac{P}{\rho} \mathrm{d}m$, and

$$L_{\text{int}} = -\dot{E}_{\text{grav}} - \dot{E}_{\text{int}} = (\zeta - 1) \dot{E}_{\text{int}} = \left(\frac{1-\zeta}{\zeta}\right) \dot{E}_{\text{grav}}. \tag{2.10}$$

We have seen in § 1.4.1 that either in the classical or degenerate domain, a monoatomic gas is described by $\zeta = 2$. Hence,

$$L_{\text{int}} = \dot{E}_{\text{int}} = -\frac{1}{2} \dot{E}_{\text{grav}}. \tag{2.11}$$

At early ages, we can see on Fig. 2.3.d that the central degeneracy parameter of the electrons is roughly close or bigger than unity. In this classical regime, Eq. (2.11) simply tells us that half of the energy released by the gravitational contraction is radiated away, the remaining half going into the internal energy of the particles. Until $\Xi_e \lesssim 1$, the particles are classical, $E_{\text{int}} \propto k_B T$, and this causes an increase of the temperature which can be seen for $M_1 = 3, 5$ and $10 M_{\text{Jup}}$ curves of Fig. 2.3.c.

Later on, degeneracy sets in and the gas consists of degenerate free electrons mixed with still classical ions. Thus, the internal energy is also split between an electronic and a ionic part (E_e and E_i), the latter being small because $T/T_F = \Xi_e \ll 1$. Because $E_{\text{grav}} \propto 1/R_1 \propto \rho_1^{1/3}$, the very dependence of the Fermi energy with respect to the density ($E_e \propto \rho_1^{2/3}$) gives

$$\frac{\dot{E}_e}{E_e} \approx 2 \frac{\dot{E}_{\text{grav}}}{E_{\text{grav}}}. \tag{2.12}$$

Substituting this into the Virial relations finally yields

$$\dot{E}_e = 2 \frac{E_{\text{int}} - E_i}{E_{\text{grav}}} \dot{E}_{\text{grav}} \approx 2 \frac{E_{\text{int}}}{E_{\text{grav}}} \dot{E}_{\text{grav}} = -\dot{E}_{\text{grav}}$$
$$L_{\text{int}} = -\dot{E}_i \propto -k_B \dot{T}. \tag{2.13}$$

The contraction is thus mainly used to increase the zero point Fermi energy of the electrons, while most of the luminosity is provided by the slow thermal cooling of the ions, as seen on the right

part of Fig. 2.3.c (Guillot 2005). Of course, this result which is nearly exact in the white dwarf domain is here only approximate because of (i) the partial degeneracy, meaning that E_i is not completely negligible, (ii) the Coulombian correlation effects which cannot be neglected in the planetary domain.

Interestingly, during their whole lives, the effective temperature of these objects monotonously decreases with time, and can be seen as a proxy for time. At a given mass, an object will thus follow the corresponding track in Fig. 2.2 from right to left.

- $M_{2\text{HBMM}} < M_1 < M_{\text{HBMM}}$, dotted curves in Fig. 2.3 ; During the early phase, the aforementioned conclusions hold: the object is classical and heats up during contraction. However, at some point, the central pressure and temperature are sufficient to ignite deuterium burning (around $T_c \sim 4.5 \times 10^5 \, \text{K}$[6], and this energy source temporarily counteracts contraction. Unfortunately, because the primordial $^2\text{H}/\text{H}$ ratio is very small ($\sim 2 \times 10^{-5}$; Chabrier and Baraffe 2000), and that its reaction rate is very short, all the available fuel is consumed in $\sim 10^{6-8}$ yr. After that, the standard evolution described above resumes. Note that the beginning and the duration of this phase is highly dependent on the mass of the object. For more massive objects, higher temperature and pressures are reached earlier, so that the reaction starts quickly and have a shorter lifetime.

- $M_1 > M_{\text{HBMM}}$, dashed curves in Fig. 2.3 ; Like the deuterium burning objects, these young contracting *protostars* heats up until they reach $T_c \sim 3 \times 10^6 \, \text{K}$, temperature at which thermonuclear reactions start. In low mass stars ($M_1 < 0.7 M_\odot$), 99% of the fusion of Hydrogen into Helium is ensured by the PPI chain

$$\text{H} + \text{H} \to {}^2\text{H} + e^+ + \nu_e \, ; \quad \text{H} + {}^2\text{H} \to {}^3\text{He} + \gamma \, ; \quad {}^3\text{He} + {}^3\text{He} \to {}^4\text{He} + 2\,\text{H}, \qquad (2.14)$$
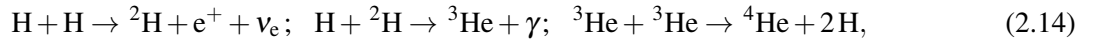
which produces enough energy to stop the contraction (Chabrier and Baraffe 1997, 2000). Hence, the object will only evolve because of its slowly varying chemical composition. The object has reached the so-called *zero age main sequence*. A star is born !

2.1.4   Giant planet or mini brown dwarf ?

Note that, while from the point of view of the evolution I distinguished two different mass regimes in the substellar domain, I took care not call planets the least massive bodies ($M_1 < M_{2\text{HBMM}}$), and brown dwarfs the most massive ones which are able to fuse deuterium ($M_1 > M_{2\text{HBMM}}$). This choice is motivated by several facts. First, if we call deuterium burning objects brown dwarfs, why not give different names to objects burning lithium or other compounds ? Second, the deuterium burning limit itself is not completely well defined, as it depends on various parameters (e.g. Helium and initial Deuterium mass fraction, metallicity) and on the criterion used to identify Deuterium burning (Spiegel et al. 2011). Finally, note that most of the actual objects with $M_1 > M_{2\text{HBMM}}$ are too old to burn deuterium anymore !

In this thesis, I thus chose to assume the following definitions

- *Planet*[7]*: celestial body that formed in the disk of a star.*

- *Brown dwarf: celestial body that formed through gravitational collapse of a dense molecular cloud and that cannot sustain proton fusion.*

---

[6]More massive object are also able to burn Lithium when they reach $T_c \sim 2.5 \times 10^6 \, \text{K}$, around $M_1 \sim 60 M_{\text{Jup}}$.

[7]From Greek *planētēs*, "wanderer". A complete definition should include more constraints, such as a hydrostatic equilibrium condition, in order to differentiate planets from planetesimals or asteroids. Here, as we only concern ourselves with the distinction between planets and brown dwarfs, we mainly focus on the characteristics that differ between these two classes of objects.

(a) Radius

(b) Effective temperature

(c) Central temperature

(d) Central degeneracy
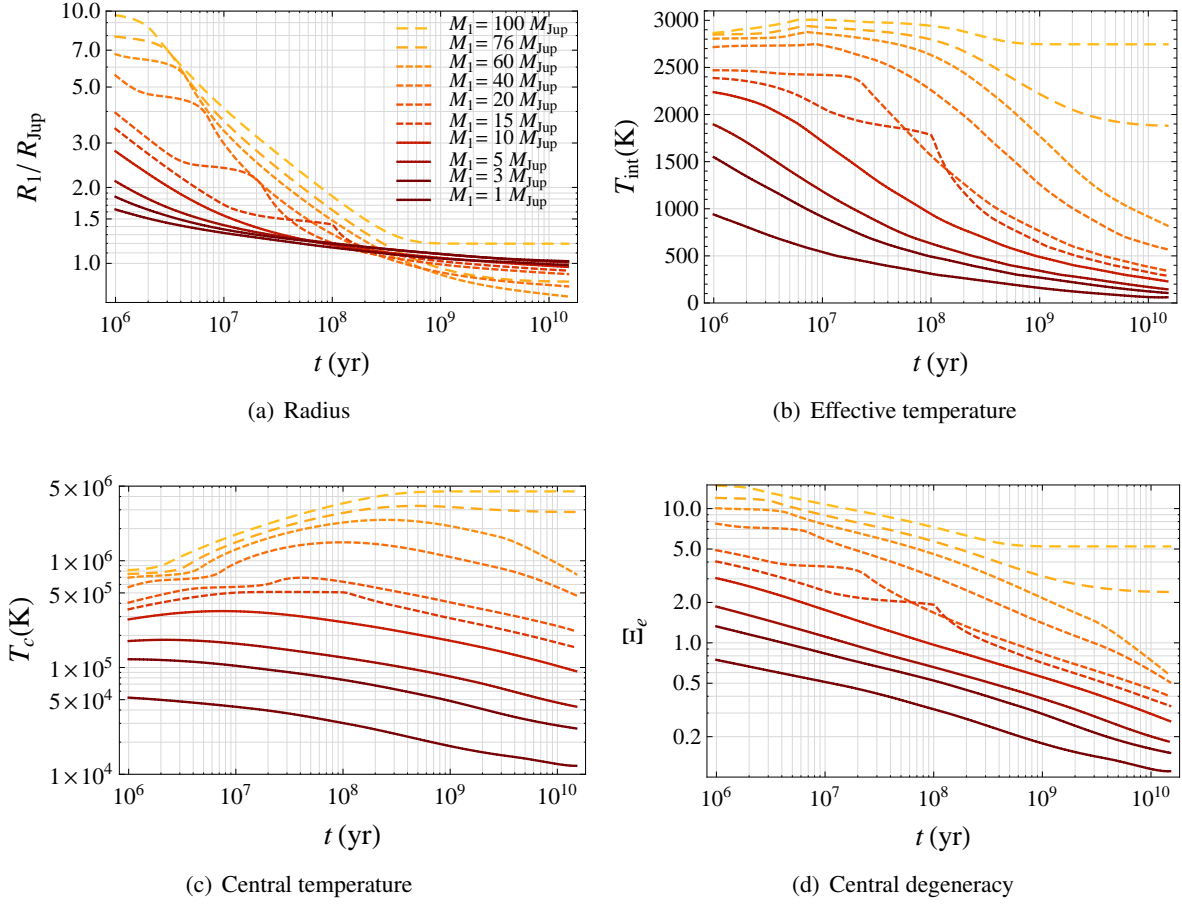
Figure 2.3: Evolution of the radius (panel a), effective and central temperature (panel b and c) and central degeneracy (panel d) with respect to time for different masses. Dashed curves are used to represent object massive enough to sustain Hydrogen nuclear fusion ($M_1 > M_{\mathrm{HBMM}} \approx 75 M_{\mathrm{Jup}}$), and dotted curves for objects burning deuterium ($M_1 > 12.5 M_{\mathrm{Jup}}$).

It directly follows that planet can be massive enough to burn deuterium and also, in principle, hydrogen. The possibility of hydrogen burning planets, though, does not seem to me a serious problem of this more physical definition based on the formation mechanism. Brown dwarf are somehow failed stars that formed just the same way that these latter while not accreting enough mass, and planets form later on, in the dusty gaseous disk formed by the material falling onto the protostar.

However, this definition also implies an underlying ambiguity. Studies of low mass stars and brown dwarfs in young clusters suggest a continuous mass function down to $\sim 6 M_{\mathrm{Jup}}$ (Caballero et al. 2007), indicating that the same formation process responsible for star formation can produce objects down to a few Jupiter masses. Analytical theories of star formation (Padoan and Nordlund 2004, Hennebelle and Chabrier 2008) also show that gravoturbulent fragmentation of molecular clouds produces, with the same processes, stars and brown dwarfs down to a few Jupiter-masses in numbers comparable to the observationally determined distribution. And just like there are binary stars, these brown dwarfs can form near, or be captured by, a more massive star. On the other side, according to current models of planet formation which include migration (Alibert et al. 2005), giant planets can form by core accretion with masses up to $\sim 30 M_{\mathrm{Jup}}$ (Mordasini et al. 2008, 2009). "Mini" brown dwarfs and "super giant" planets

thus overlap in mass, stressing the need for identification criteria enabling the distinction between these two types of astrophysical bodies, but we will come back on this issue in § 2.5.

2.1.5 Initial conditions

There is still a problem that is inherent to the resolution of any set of partial derivative equations, and that we omitted until now. We did not yet specify what are our initial conditions $(T_{int}(t_0))$, or even simply what we call t_0. This problem is complex and cannot be solved without considering consistently the transition between the phase where the object is still forming, and its isolated phase. This is particularly critical to model young bodies, for which the energy content is still determined by the initial amount of energy deposited by the in-falling matter during formation, and should drastically change between a planet embedded in the protoplanetary disk and a brown dwarf.

Fortunately, for younger objects, the typical evolution timescale, which is given by the Kelvin-Helmholtz timescale derived in § 1.2, $\tau_{KH} = GM_1/R_1L_{int}$, is shorter because of the larger luminosity and radius. Numerical simulations give values around $\tau_{KH} \sim 10^{5-6}$ yr for objects up to 20-30 M_{Jup} and $\tau_{KH} \sim 10^{6-7}$ yr for more massive bodies. This is shown on Fig. 2.4, where we see that τ_{KH} can be also seen as the timescale on which the system looses the memory of its initial conditions. Indeed, all the curves that started with a higher initial radius than a given one are nearly confounded after $2 - 3\,\tau_{KH}$. Hence, even if we start from an arbitrarily high entropy state, or *hot start*, we know that the predictions given by our calculations start to be accurate after a few Kelvin-Helmholtz timescales.

The subtle point, however, is that because the object can start from a very low entropy state (Marley et al. 2007), to be conservative, we must use the *longest* possible τ_{KH}, i.e. the one yielded by the coldest possible initial state. Then, considering the lowest curves in each panel of Fig. 2.4, we see that the system can keep the memory of its initial conditions for up to 10^{7-9} yr, which confirms the results of Marley et al. (2007).

To get a better accuracy at younger ages, one needs to know the specific entropy content left into the planet through its formation process. A first attempt into that direction has been done by Marley et al. (2007), which follows the planet trough several stages (see Pollack et al. 1996 for details).

1. Dust particles in the solar nebula form planetesimals that accrete into a solid core surrounded by a very low mass gaseous envelope. When few planetesimals are left in the feeding zone of the planet, the accretion luminosity drops, and gas accretion is enhanced.

2. When the mass of the core and of the envelope become equal, a runaway gas accretion starts, and the planet quickly grows. At this stage, the planet fills its whole Hill sphere and the gas can flow smoothly from the disk. This is called the Nebular stage.

3. At some point, the growing need of the planet for gas cannot be fulfilled by the surrounding nebula. Because of the slow contraction of the object, the radius of the latter becomes smaller than its Hill radius, and a gap opens between the disk and the planet. As a result, the accreting gas falls *hydrodynamically* onto the object.

4. Finally, accretion stops and the planet enters the isolation stage, where its evolution is described by our aforementioned model.

However, as stated by Marley et al. (2007), the most crucial problem is to treat correctly the hydrodynamical accretion that occurs in stage 3. This raises two major issues, namely, (i) the morphology of the accretion, i.e. whether gas falls homogeneously onto the surface or predominantly onto the equator, (ii) the thermal energy left into the accreting gas. Indeed, as shown by Stahler et al. (1980), the gas should
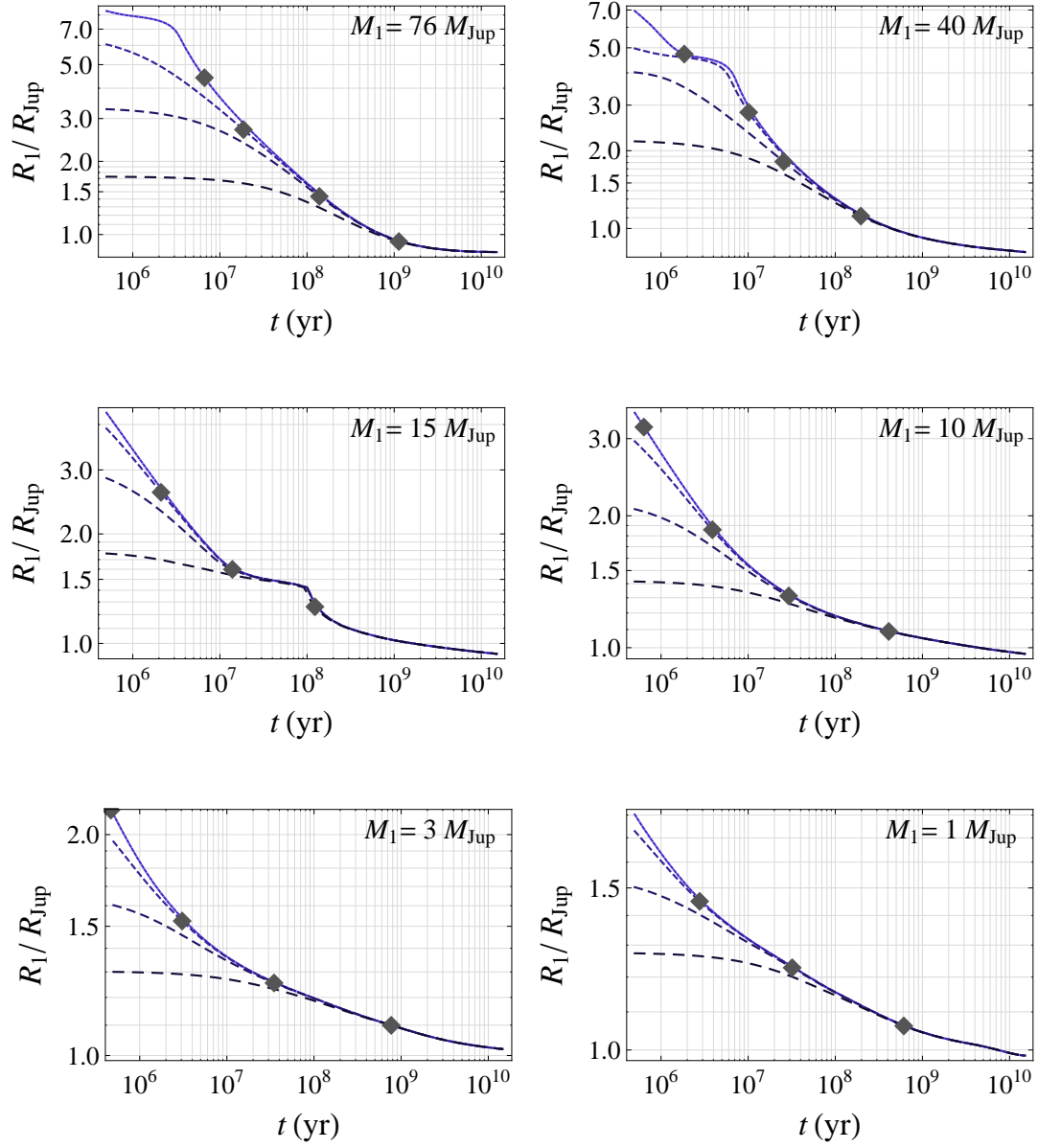
Figure 2.4: Evolution of the radius of a H/He gaseous sphere with respect to time for different initial radii (in each panel), and for different masses (different panels). On each curve, the gray diamond is located at $t = 2\,\tau_{\mathrm{KH}}$, where τ_{KH} is computed at the initial time of the simulation ($t = t_0$). We can see that for any given curve (with an initial radius R_0), for $t \gtrsim 2 - 3\,\tau_{\mathrm{KH}}$, $R_1(t, R(t_0) > R_0) \approx R_1(t, R_0)$.

undergo a shock before reaching the planet surface. Because Marley et al. (2007) assume that this shock is super-critical and that all the gravitational energy of the infalling gas is radiated away, they predict a very *cold start* in which the initial luminosities and radii of the planet can be up to, respectively, 1000 and 2 times smaller than in the hot start model. As expected, after a few τ_{KH}, these differences vanish. If it is often assumed that the accretion shock is super-critical, one should keep in mind that it is not necessarily true and remains to be explored by numerical radiation hydrodynamics calculations.

2.2   The mass-radius relationship

In our yet simple modeling, the properties of an isolated planet (radius, surface temperature, luminosity, spectral colors, etc...) are completely determined by its mass and its age (or equivalently its effective temperature). To constrain the model and knowledge of the internal structure of these bodies, we must measure separately at least three of these physical quantities.

Age can often be inferred from the characterization of the central star. This method becomes rather uncertain for main sequence stars older than a few hundred million years, but at least allows us to identify the objects that are expected to be *old* and *cold*. Thanks to direct detection methods, the luminosity, and even spectra of young planets and brown dwarfs can be obtained. But because neither the radius nor the mass can be directly measured[8], these observations cannot constrain the models.

In the past decade, this is then the successful combination of Doppler measurements and transit light curves that bore the most constraints on our knowledge of internal structure. The observables are thus the masses and radii of transiting bodies.

Figure 2.5: Mass-radius relationship of gaseous objects at 5 (solid), 1 (long dashed), 0.5 (dashed) and 0.1 Gyr (dotted). Observational data points are also shown.

This is why this section is devoted to the study of the ways to use the *mass-radius diagram*. Fig. 2.5 shows the mass-radius relationship computed with the numerical models described above for H/He gaseous spheres with several different ages. It is shown along with observational data from planetary transit surveys, observation of eclipsing binaries, and interferometric observations.

2.2.1   Linking macroscopic features and microscopic properties: the polytrope

One of the striking feature of this relationship is its *non-monotonicity*. To easily understand why it is so, and how this is related to the behavior of the equation of state, I will turn to a simple analytical model, the *polytropic sphere*. As we have seen in § 1.4.1, at least in the ideal and fully degenerate gas,

---

[8]Because of the inherent difficulty to image companions close to their host star, directly imaged substellar companions are generally too far from their host star to transit or to be detected with radial velocimetry methods.

the equation of state of our medium can be written as a polytrope,

$$P = K\rho^{1+1/\tilde{n}}, \tag{2.15}$$

where K and $\tilde{n}$ are called the polytropic *temperature* and *index* respectively, and are constant throughout the configuration. In addition, as I will show later on, even for a realistic equation of state, the $P - \rho$ profile in an actual object can be approximated by a relation of the form given by Eq. (2.15) with well chosen $(K, \tilde{n})$. This provides us with a powerful simplification, as the whole mechanical structure can be captured in a single parameter, $\tilde{n}$, and that mechanical properties such as the gyration radius - r_{gyr} which characterizes the moment of inertia of the body, C_1, and is defined through

$$C_1 \equiv \frac{2}{5} M_1 (r_{\text{gyr}} R_1)^2, \tag{2.16}$$

- the central over mean density ratio $(\rho_{\text{c}}/\bar{\rho}_1)$, and even the linear response to a perturbing potential (k_2, see Chapter 3) can be tabulated as a function of $\tilde{n}$ alone (Chandrasekhar 1939 ; Lai et al. 1993 ; Leconte et al. 2011c). For sake of completeness, a summary of the formalism and of the variables describing polytropic spheres (Chandrasekhar 1939), as well as the well known *Lane-Emden* equation is given in Appendix C.

Thanks to this formalism, we can obtain an analytical mass-radius relationship

$$M_1^{\frac{\tilde{n}-1}{\tilde{n}}} R_1^{\frac{3-\tilde{n}}{\tilde{n}}} = \frac{K}{G} \frac{\tilde{n}+1}{(4\pi)^{1/\tilde{n}}} \xi_{\tilde{n}}^{\frac{\tilde{n}+1}{\tilde{n}}} |\tilde{\theta}'_{\tilde{n}}|^{\frac{\tilde{n}-1}{\tilde{n}}}. \tag{2.17}$$

Of course, as will be shown in the next section, K and $\tilde{n}$ are also functions of the mass of the object, so that the mass-radius relationship is not a power law in the whole mass range. But if we consider that K and $\tilde{n}$ are only slowly varying, we will see in the next section that the slope of the mass-radius relation is directly related to the polytropic index that describes the equation of state in the mass regime considered.

2.2.2 Effective polytropic index

To derive realistic polytropic indices, I fitted the pressure-density profile of each model of the previous grid of planetary models by a polytropic equation of state (Eq. (2.15)) at each time step. An example of the result of such a fit is shown in Fig. 2.6. Note that the disagreement between the actual $P - \rho$ profile and the polytrope in the lower left area of Fig. 2.6 is both expected and needed: This low-density region (the first 5% in mass below the atmospheric boundary surface) has a different effective polytropic index than the planetary interior. In order to capture the bulk mechanical property of the planet, we weight each shell in the internal structure profile by its mass during the fitting procedure. **This provides us with a grid tabulating the polytropic index of the planet, $\tilde{n} \equiv \tilde{n}(M_1, t)$ (plotted in Fig. 2.7).** All the other polytropic functions (r_{gyr}, ...) can be derived by integrating the Lane-Emden equation. These functions, along with other quantities (R_1, T_{int}, ...), are tabulated and can be found in Leconte et al. (2011c).

As shown in Fig. 2.7, we recover qualitatively the results of Chabrier et al. (2009): except for the early stages of the evolution, the (dimensionless) isothermal compressibility of the hydrogen/helium mixture is a monotonically increasing function of the polytropic index, $\tilde{\chi} = \frac{\partial \ln \rho}{\partial \ln P}\Big|_T = \frac{\tilde{n}}{1+\tilde{n}}$, and thus of the mass of the object. In the high mass regime, n slowly increases as the relative importance of ionic Coulomb effects compared with the degenerate electron pressure decreases, and approaches the $\tilde{n} = 3/2$ limit, the expected value for a fully degenerate electron gas, when M_{p} approaches the hydrogen burning minimum mass ($\approx 70 M_{\text{Jup}}$), as can be seen in Fig. 2.7.b. Thus, in this regime, Eq. (2.17) yields $R_1 \propto M_1^{-1/3}$. Toward lower masses, the compressibility decreases with the mass because the repulsive
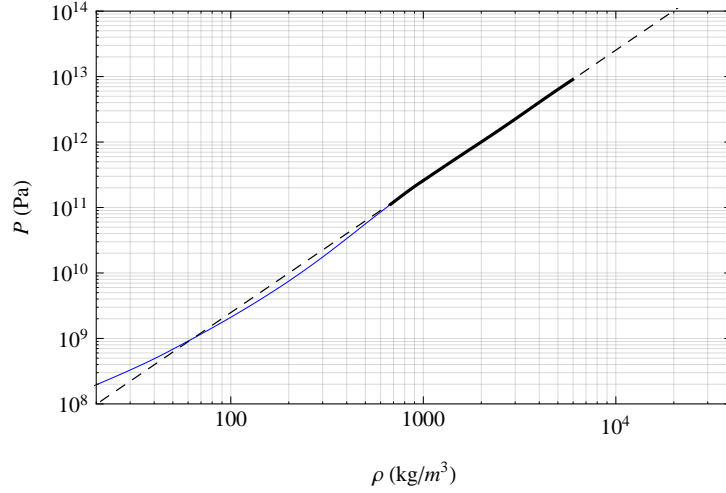
Figure 2.6: The internal pressure-density profile of a $1.8M_{\mathrm{Jup}}$ planet (solid line). The dashed line represents the best-fit polytropic equation of state. The pressure-density range covered in the inner part of the body (95% in mass) is represented by the thicker part of the solid curve, which is well modeled by a polytropic EOS. As the thin part of the $P - \rho$ curve represents only 5% in mass of the body it is disregarded by the fit. *Figure from Leconte et al. (2011c).*

Coulomb potential between the ions, and thus the ionic electrostatic energy becomes dominant. The transition between the two regimes occurs near 2-3 M_{Jup}, where the polytropic index is close to unity. Thus $R_1 \propto M_1^{(1-\tilde{n})/(3-\tilde{n})} \propto$ cst, the mass-radius relationship reaches a maximum and is nearly flat. Ultimately, electrostatic effects dominate, leading eventually to $\tilde{\chi} \approx \tilde{n} \approx 0$ for solid, terrestrial planets. As expected for incompressible matter, we tend toward $R_1 \propto M_1^{1/3}$.

A new feature highlighted by the present calculations is the non-monotonic behavior occurring between 1 - 3 M_{Jup} at early ages. This occurs when the central regions of the planet, of pressure P_{c} and temperature T_{c}, previously in the atomic/molecular regime, become pressure-ionized, above 1-3 Mbar and 5000 - 10 000K (Chabrier et al. 1992 ; Saumon et al. 1992, 1995)**, and the electrons become degenerate. An effect more consequential for the lowest mass objects, whose interiors encompass a larger molecular region. This stems from the fact that** (Chandrasekhar 1939)

$$P_{\mathrm{c}} > \frac{GM_1^2}{8\pi R_1^4}, \quad \text{and} \quad \frac{GM_{\mathrm{Jup}}^2}{8\pi R_{\mathrm{Jup}}^4} \approx 2 - 3\,\mathrm{Mbar} \approx P_{\mathrm{ionization}}. \tag{2.18}$$

Older (with smaller R_1) and more massive ($M_1 \gtrsim 2M_{\mathrm{Jup}}$) objects have $P_{\mathrm{c}} > 10\,P_{\mathrm{ionization}}$ and the ionization extends all the way up to the outermost layers of the gaseous envelope, which then contains too small a mass fraction of molecular hydrogen to significantly affect the value of the polytropic index. This contrasts with younger objects around 1 - 3 M_{Jup}, whose external molecular hydrogen envelope contains a significant fraction of the planet's mass, leading to a larger value of the polytropic index, as molecular hydrogen is more compressible than ionized hydrogen (see e.g. Fig. 21 of Saumon et al. 1995). Once again, for these latter objects, the interior structure would be better described by using two different polytropes, but such a significant complication of the calculations is not needed at the presently sought level of accuracy.

To evaluate the uncertainty in the determination of the polytropic index, I use an alternative method to derive $\tilde{n}$. Since our numerical simulations provide both the radius, $R_1(M_1, t)$, and the central density of the object, $\rho_{\mathrm{c}}(M_1, t)$, we can invert Eqs. (C.9) and (C.11) to compute K and $\tilde{n}$. This new determination of
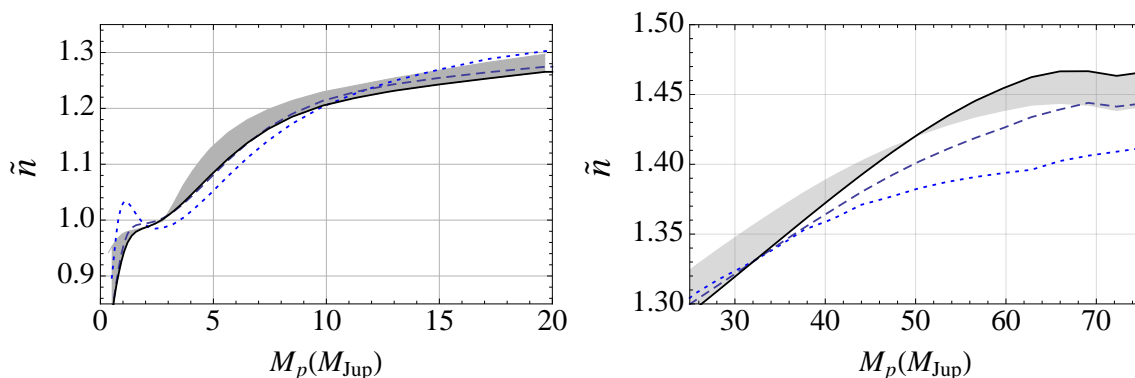
Figure 2.7: Left: Polytropic index for non-irradiated planets as a function of the planet's mass $M_{\rm p}$ at 100 Myr (Dotted), 1 Gyr (Dashed) and 5 Gyr (Solid) in the low mass regime. The shaded area represents the uncertainty on the polytropic index for the 5 Gyr case (see text). *Figure from Leconte et al. (2011c).* Right: Idem but for massive substellar objects. As expected, because the Coulomb effects diminish as the object tends toward the hydrogen burning limit, the gas becomes a perfect electron gas and its polytropic index tends toward $3/2$.

the polytropic index is compared with the previous one, obtained by fitting the $P - \rho$ profile, in Fig. 2.7 for the 5 Gyr case: the new $\tilde{n}$ value corresponds to the upper envelope of the shaded area. Fig. 2.7 shows that the two approaches yield very similar results, the average uncertainty lying around 5 %.

Moreover, as shown in detail in Leconte et al. (2011c), this *effective* polytropic index does not simply explain the behavior of the mass-radius relationship of substellar objects, but also encompasses much information about the internal mechanical structure of the object. Indeed, numerical estimates of the moment of inertia and the tidal response function (i.e. the Love number) of the body, among other quantities, are well approximated by the ones computed for a distorted polytrope, provided that an accurate polytropic index, as the one presented here, is used (Leconte et al. 2011c).

2.3 The bloating problem

If the small discrepancy between the theoretical predictions and the data points at the high mass end of Fig. 2.5 can be explained ($M_1 \gtrsim 20\,M_{\rm Jup}$; Chabrier et al. 2007a), this is not so for lower masses. Indeed, a large fraction of giant planets seem larger than predicted by the models. While this feature was already identified with the first detected transiting planet, HD 209 458 b (Henry et al. 2000), the mechanism(s) responsible for this *bloating* has not been completely identified yet.

In order to express the problem in mathematical terms, let us consider the luminosity equation (Eq. (1.59)) in its integrated form

$$\bar{T}_1 \frac{\partial \tilde{S}}{\partial t} = \int (\dot{\varepsilon}_{\rm nuc} + \dot{\varepsilon}_{\rm ext})\,{\rm d}m - L_{\rm int}. \tag{2.19}$$

This simply means that the internal entropy evolution depends on the balance between the energy supplied to the interior by an external source and the radiative losses. As we have seen in previous sections, in the general case, $\dot{\varepsilon}_{\rm nuc} + \dot{\varepsilon}_{\rm ext} \approx 0$, and the object contracts because R_1 is an increasing function of $\tilde{S}$. In order to keep a larger radius, the planet thus needs to conserve its entropy, and because there are two

terms on the right hand side of Eq. (2.19), there are two principal means to achieve this. These two types of mechanisms can be stated as follows

- Heating sources. This class encompass all the processes that provide a source term $\dot{\varepsilon}_{ext}$ to counterbalance the radiative losses. $\tilde{S}$ decreases at a slower pace, or even increase, and the planet ends up bigger than in the standard model. Proposed scenarios include, among others, tidal heating (Bodenheimer et al. 2001 ; see Chapter 5), downward transport of kinetic energy by stellar irradiation driven winds(Showman and Guillot 2002), or ohmic dissipation (Batygin and Stevenson 2010).

- Inefficient cooling. The same effect can be achieved by simply impeding the transport of energy, either in the interior or in the atmosphere. These include, extension of the radiative zone due to the stellar irradiation (Guillot et al. 1996), enhancement of the radiative opacity decreasing radiative losses (Burrows et al. 2007), and inefficient large-scale convection due to a composition gradient (Chabrier and Baraffe 2007 ; which is also studied in Chapter 4).

Naturally, the first chronological idea, which was proposed *a priori* by Guillot et al. (1996), was linked to the fact that transiting planets are at close orbital distance from their star, and receive a far stronger flux than any of solar system giant planets. Even if other processes are at play to inflate Hot Jupiters, the impact of stellar irradiation cannot be neglected, and I will thus dedicate the following section to its study.

2.4 Effect of stellar irradiation

At first sight, the fact that I classified stellar irradiation among the "inefficient cooling" scenarios can seem a little counter intuitive. Indeed, one might think that such an energy input (sometimes more than a hundred times the internal luminosity of the planet) could heat the whole body. However, as we will see, this heating does not penetrate very deeply into the interior, and incoming energy is rapidly reradiated toward outer space. This is not the energy input which is important, but rather the way the atmosphere is heated *from above*, and the consequences that it implies for the boundary conditions.

2.4.1 The radiative zone

As was discussed in § 1.5.2, the energy density linked to the incoming visible radiation decreases into the atmosphere as $e^{-\sqrt{3}\kappa_{vis}P/g}$, and is nearly completely absorbed at the 0.1-1 bar level, as shown on Fig. 2.8. This level can even be displaced higher in the atmosphere if strong visible absorber are present at low pressures, like TiO and VO, possibly leading to temperature inversions (Hubeny et al. 2003 ; Fortney et al. 2008). As a consequence, the stellar flux does not reach the inner convective zone of the planet, is rapidly reradiated, and does not participate to the energy budget of the planet.

As can be seen on Fig. 2.8, when the atmosphere is heated from above, the nearly isothermal region which is present above the 10 mbar level in the non irradiated case (solid curve) is pushed downward (up to a few hundred bars). This is because the atmosphere is hotter in average, and thus needs a smaller temperature lapse rate to transport the energy by radiation. As a result, the thermal gradient, $\nabla_T = \frac{d\ln T}{d\ln P}$, is smaller. Even if the location of the radiative-convective boundary cannot be determined in this simple model[9], we see that the depth at which the fluid will eventually become convectively unstable according to the Schwarzschild criterion will be pushed deeper. This simple analysis is confirmed by

---

[9]Indeed, as discussed in § 2.1.1, this is the way $\bar{\kappa}$ varies with temperature and pressure that determines if a radiative-convective transition occurs. At constant $\bar{\kappa}$, like this is assumed in Guillot (2010), $\nabla_T \rightarrow 1/4 < \nabla_{ad}$.

fully consistent non gray radiative transfer numerical calculations (see Barman et al. 2001 for a detailed discussion).

The question is now to see how this can affect the observed radius of a giant planet. One of the first idea that comes to mind is just that as a planet is moved inward, its external layers will extend in size as they are heated as discussed above. In order to quantify this effect, let us consider that the height of the atmospheric layer is roughly given by the pressure scale height

$$H_P \equiv -\frac{dr}{d\ln P}, \tag{2.20}$$

which is the typical length scale on which pressure is subject to a significant change. From Eqs. (1.57) and (1.58), and using the perfect gas law which is valid at low pressures, we can show that

$$H_P = \frac{P}{g\rho} = \frac{k_B T}{\mu m_H g}. \tag{2.21}$$

If we further assume that the atmosphere is nearly isothermal with the 1-10 bar temperature shown in Fig. 2.8 (i.e. $\sim 300\,$K for $T_{irr} = 0\,$K and $\sim 2300\,$K for $T_{irr} = 2000\,$K), we get an evolution of the atmospheric scale height from $\sim 50\,$km to $\sim 380\,$km. The atmosphere height still represents less than $\sim 0.5\%$ of the radius of the planet. This is thus clearly insufficient to explain the

Figure 2.8: Atmospheric $T - P$ profile computed with Eq. (1.96) for a Jupiter analog with $T_{int} = 200\,$K and T_{irr} varying between $0\,$K (black solid) and $2000\,$K (yellow dashed) by steps of $200\,$K. For this example, $\kappa_{vis} = 10^{-3}\,$m^2.kg^{-1} and $\kappa_{th} = 10^{-2}\,$m^2.kg^{-1} (see § 1.5.2).

observed bloating. In other words, if we keep the entropy in the inner convective zone constant while moving the planet inward, the temperature of the atmosphere will increase, but the actual radius of the planet will change only by a small amount. The mapping between R_1 and $\tilde{S}$ discussed in § 2.1.2 is only mildly changed by the irradiation (Burrows et al. 2000 ; Chabrier et al. 2004).

To understand how irradiation can significantly affect the radius of a close in planet, one must account for the thermal evolution of the planet. Once again, let us take a planet at long orbital distance from the star, and use our mind to move it quickly close to the star, quickly meaning in a time which is negligible in front of the Kelvin-Helmholtz timescale so that the internal structure of the object does not have the time to significantly thermally evolve[10]. Thus the internal isentrope is left unchanged, and so is the $T - P$ profile in the convective zone. This is roughly equivalent to keeping the couple (T_{atm}, P_{atm}) constant in a region where the incoming stellar irradiation cannot penetrate. Then, let us consider the evolution of the ability of the atmosphere to transport the internal energy and cool down the planet with the degree of irradiation. Isolating T_{int} in Eq. (1.97), we get

$$T_{int}^4 = \left[\frac{4\,T_{atm}^4}{3} - \bar{f}\,T_{irr}^4 \left(\frac{2}{3} + \frac{\kappa_{th}}{\kappa_{vis}\sqrt{3}} \right) \right] \Big/ \left[\frac{2}{3} + \frac{\kappa_{th}}{g} P_{atm} \right]. \tag{2.22}$$

So, as T_{irr} increases, T_{int} decreases. This simply translates the fact that, as temperature lapse rates are decreased, the radiative transport energy is significantly hampered, and because convection is very efficient in the interior, the overall flux is completely determined by the atmospheric energy escape rate. This simple explanation is once again supported by the radiative transfer calculations of Barman et al. (2001).
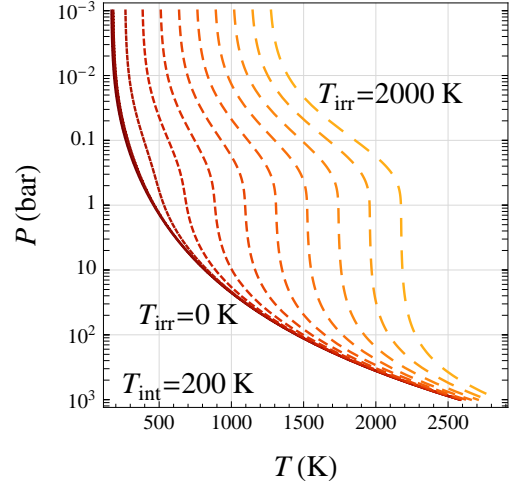
---

[10]Thermodynamically speaking, this can be seen as a quasi static and adiabatic transformation of the planet

Thus, if the mapping between R_1 and $\tilde{S}$ does not change, the relations that link these parameters to the effective temperature depends on T_{irr}. The irradiation plays a role only on the evolution. When T_{irr} is increased, the outgoing flux escaping the planet is decreased, and so is the variation of the internal entropy, which is kept at a higher value for a longer period of time. To summarize, the stellar irradiation impedes the release of the internal gravo-thermal energy of the object, slows down its cooling, and retards the evolution (Baraffe et al. 2003).

2.4.2 Polytropic index of irradiated objects
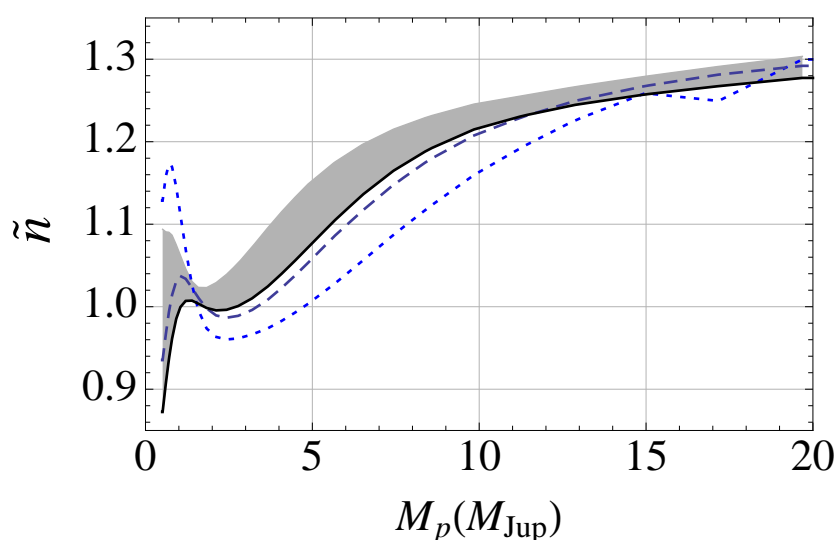
Figure 2.9: Polytropic index for irradiated planets as a function of the planet's mass M_{p} at 100 Myr (Dotted), 1 Gyr (Dashed) and 5 Gyr (Solid). The shaded area represents the uncertainty on the polytropic index for the 5 Gyr case (see text). As the irradiated atmosphere impedes the radiative cooling of the objects, it retards its contraction. Therefore, the non-monotonous behavior observed at the early ages in the non-irradiated case (Fig. 2.7) is enhanced, even at a later epoch. The bump at the high mass end of the 100 Myr curve is caused by deuterium burning (see text). *Figure from Leconte et al. (2011c).*

Analogously to § 2.2.2, I also computed a grid of evolution models of gaseous giant planets with solar composition for $M_{\mathrm{p}} \in [0.35 M_{\mathrm{Jup}}, 20 M_{\mathrm{Jup}}]$ and an incoming stellar flux $F_{\mathrm{inc}} = 4.18 \times 10^6\,\mathrm{W.m^{-2}}$. As seen on Fig. 2.9, a strong irradiation enhances the features described in § 2.2.2: the evolution is delayed because the irradiated atmosphere impedes the release of the internal gravo-thermal energy. This yields a slower contraction, thus a lower central pressure (and lower central temperature) for a longer period so that the object enters the ionization regime at a later epoch. The bump at the high mass end of the 100 Myr isochrone is due to deuterium burning which also occurs later for a given mass, because of the cooler central temperature (see above). At 100 Myr, the 20 M_{Jup} has already burned a significant amount of its deuterium content and starts contracting again, whereas lower mass planets are still burning some deuterium supply, leading to a less compact and thus less ionized structure. This leads to the non-monotonic behavior on the high-mass part of the $\tilde{n} - M$ diagram at 100 Myr, which reflects a similar behavior in the mass-radius relationship.

2.4.3   Radius anomaly

It is now well established that a large number of transiting giant exoplanets are more inflated than predicted by the standard cooling theory of irradiated gaseous giant planets (see Udry and Santos 2007 ; Baraffe et al. 2010 for reviews). As we have seen above that stellar irradiation can help prevent the cooling of such planets, it is time to estimate the remaining discrepancy. Because the radius of a gaseous giant planet is not set only by its mass, but strongly depends also on the object's composition, age and irradiation history, the mass-radius diagram (see Fig. 2.5) only gives a limited view of the constraints offered by the observation of transiting systems. **In order to quantify the *radius anomaly* of many "Hot Jupiters" and study the possibility of such an anomaly for the more massive objects, I computed the radius predicted by our standard irradiated model (R_{irr}) for transiting planets with $M_p > 0.3 M_{Jup}$ (about a Saturn mass). I define the *radius excess* as the difference between the observed radius and that predicted by the model at the estimated age of the system, denominated R_{irr}.** Results are summarized in Fig. 2.10.

In the low mass range, the existence of objects above the $R_1 = R_{irr}$ tells us that the effect of stellar irradiation alone is still unable to explain the mean properties of transiting planets. As seen in § 2.3, this is evidence that some physical mechanism is yet missing in our modeling. A more thorough study of two of these mechanisms, namely the double diffusive convection and the tidal heating, are carried out in Chapter 4 and 5 respectively. Interestingly, Laughlin et al. (2011) showed that the radius anomaly of planets in the 0.1-10 M_{Jup} mass range are correlated to the irradiation temperature, with a best fit dependence, $R_1 - R_{irr} \propto T_{irr}^{1.4 \pm 0.6}$. This seems to favor mechanisms involving an interaction between the star and the planet. However, if the correlation seems robust, the constraints on the exponent are not strong enough yet to disentangle between the various types of possible star-planet interactions, as they all depend on the orbital distance (and thus on T_{irr}).
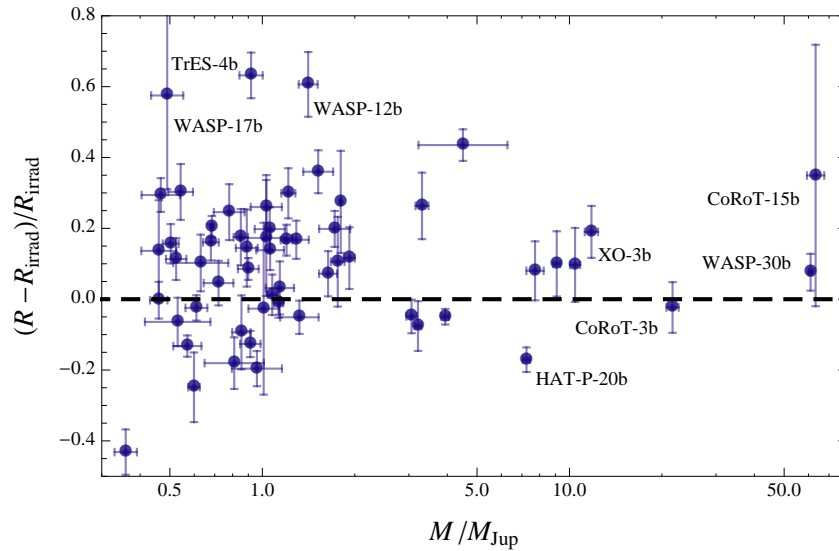
Figure 2.10: Relative radius excess between the observationally and the theoretically determined values for 57 transiting systems. Objects significantly above the dashed line are considered to be anomalously bloated compared with the prediction of the regular evolution of an irradiated gaseous planet. All the objects below this line can be explained by a heavy material enrichment in the planet's interior (Baraffe et al. 2008 ; Leconte et al. 2009, 2010a, 2011b). *Figure from Leconte et al. (2011b).*

2.4.4   Heavy element content

On the other hand, the existence of objects below the $R = R_{\mathrm{irr}}$ shows that there is at least another free parameter that we did not yet considered. This could already be seen in Fig. 2.2.d where our $R_1(T_{\mathrm{int}})$ tracks where not quite representative of Solar System giant planets, Jupiter and Neptune[11]. Indeed both planets are denser (and by a large factor for Neptune) than the models of the same mass and effective temperature. If this free parameter is not obvious in our set of structure equations, we already encountered it in § 1.4.1. To model a planet, one needs to specify the material it will be made of, and use the relevant equation of state. For the moment, we only considered gaseous spheres with a solar composition, but the discrepancy stated above shows us that dense materials (called heavy elements) are present in a significant amount inside giant planets, both inside and outside our Solar System (Hubbard and Marley 1989 ; Chabrier et al. 1992 ; Baraffe et al. 2006 ; Fortney et al. 2007 ; Burrows et al. 2007 ; Baraffe et al. 2008 ; Leconte et al. 2009, 2010a).

Unfortunately, the chemical composition of a planet cannot be encompassed in a single parameter. Even a simple parametrization in terms of mass fractions of Hydrogen (X), Helium (Y) and heavy elements (Z) already gives us two additional free parameters[12], and splitting our heavy materials in *volatiles* (or "ices") and *silicates* (or "rocks" ; see § 1.4.1), adds another one. In addition, the precise location of heavy materials, and whether they are mixed in the gas component or differentiated in a dense core, is still unknown (see Chapter 4). This creates a degeneracy that cannot be removed by the knowledge of mass and radius alone, which is one of the main limitation to the determination of the heavy element content of exoplanets (Baraffe et al. 2008). **In the following, in order to make a simple estimate of the global enrichment inside extrasolar giant planets, I will simply assume that our planet is separated in two well defined regions, (i) a dense core composed exclusively of heavy materials (either ices or silicates) of mass M_{c}, (ii) a gaseous envelope composed of a primordial mixture of hydrogen, helium and metals presenting solar abundances ($Z_{\mathrm{env}} \approx 0.02$).** In this case, I also refer to the total heavy element mass,

$$M_Z = M_{\mathrm{c}} + Z_{\mathrm{env}}\left(M_{\mathrm{p}} - M_{\mathrm{c}}\right), \tag{2.23}$$

or the total mass fraction,

$$Z \equiv M_Z / M_{\mathrm{p}}. \tag{2.24}$$

For this class of objects, **one can infer an upper limit for the content of heavy material by determining the** *maximum mass of heavy elements consistent with the lower observational error bar*, **as done in** Leconte et al. (**2009**). **In the case of CoRoT-4b, I showed that models with less than $10\,M_{\oplus}$ of water remain within the observational error box**, as illustrated by the dash-dotted curve in Fig. 2.11. This corresponds to a total mass fraction of heavy elements $Z \lesssim 15\%$. For such low enrichment, adopting rock as the main heavy element or a mixture of water and rock will barely change this value. For this type of transit planet population, the bulk composition can thus be constrained with reasonable accuracy. Note that the non-irradiated model represented by the solid curve is completely unable to reproduce the measured radius of the planet at the current epoch, showing that the effect of the stellar irradiation must be taken into account when trying to predict the internal properties of the object.

One may argue that since a physical process is missing in the modeling of some close-in planets this upper limit for heavy material enrichment could be underestimated, *if* such a process occurs in all transiting planets. An additional heat source, for instance, will yield a larger planet's inflation at a given age, allowing for a larger maximum amount of heavy material consistent with the observational error

---

[11]While it is not shown in Fig. 2.2, the same conclusions hold for Saturn and Uranus.

[12]By definition $X + Y + Z = 1$.
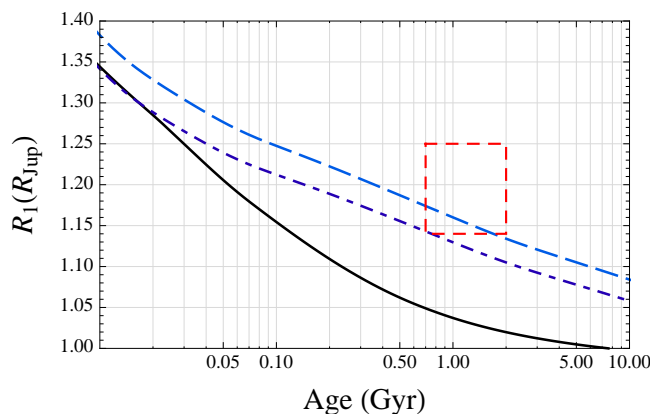
Figure 2.11: CoRoT-4b: evolution of the radius as a function of age. *Solid line*: standard cooling sequence of an isolated $0.72\,M_{\mathrm{Jup}}$ gaseous sphere with solar composition. *Long-dashed line*: irradiated case. *Dash-dotted line*: Irradiated case with a $10\,M_{\oplus}$ water core. *Red box*: observational 1σ error bar. *Revised figure from* Leconte et al. (2009).

box. The exact nature of such additional heating mechanisms being still a subject of debate the wisest (and simplest) assumption is not to invoke missing physics when it is not required. One should bear in mind, however, that, given the remaining limitations in our present understanding of planet structure and evolution, these heavy element enrichment determinations retain some degree of uncertainty. This *maximum mass* should rather be seen as the maximum enrichment consistent with the observed 1σ error bar, according to the present theoretical models.

Using that estimation we can show that, because most of the objects significantly below the R_{irr} line are in the $0.3 \lesssim M_1 \lesssim 1 M_{\mathrm{Jup}}$ region, they can be explained with a $M_Z/M_{\mathrm{p}} \gtrsim 0.10$ heavy material enrichment (Baraffe et al. 2008 ; Leconte et al. 2009). Pushing further Guillot et al. (2006) and Guillot (2008) also showed that in this mass range, a correlation exists between the enrichment of the planet and the metallicity of the star. All these conclusions seems to be in good agreement with predictions of the core-accretion scenario for planet formation (Baraffe et al. 2006 ; Mordasini et al. 2009 ; Alibert et al. 2011). However, some extreme cases exist, such as CoRoT-13 b (Cabrera et al. 2010), a $1.3\,M_{\mathrm{Jup}}$ planet with a $0.9\,R_{\mathrm{Jup}}$ radius. Indeed, with a density of $2\,340\mathrm{kg.m}^{-3}$, this planet is one of the densest in this range of mass, favoring the presence of around 100-300 $M_{\oplus}$ of heavy material in its interior (i.e. $Z \approx 0.75$), depending on the equation of state chosen. The formation mechanism of such a strongly enriched Jupiter like planet ($Z \sim 0.25 - 75$) yet remains an open question.

2.5   Distinguishing super giant planets from mini brown dwarfs in their overlapping mass domain

The discovery of "super" Jupiters, with masses $\gtrsim 10 M_{\mathrm{Jup}}$, in close orbit to a central star, raises questions about their nature: planet or brown dwarf ? CoRoT-3 b (see Fig. 2.10) is a perfect example of such an ambiguity. As discussed in § 2.1.4, brown dwarfs and planets overlap in mass, stressing the need for identification criteria enabling the distinction between these two types of astrophysical bodies. The presence of strongly non-solar atmospheric abundances, as observed in the atmosphere of the giant planets of our Solar System, may provide signatures of a planetary formation process in a protoplanetary disk. Such a signature, however, is difficult both to observe and to characterize at the present time (Chabrier et al. 2007b) and may not apply to irradiated planets, with radiatively stable outer layers.

A more robust signature of the planet formation process, as expected from the core accretion model, is the presence of a significant amount of heavy material in the interior. ***Observed radii significantly smaller than predicted for solar or nearly-solar metallicity objects reveal the presence of such a significant average amount of heavy material*** ; a major argument in favor of the core-accretion planet formation process. On the opposite, if a physical mechanism is missing in current planet cooling models, as discussed in the previous sections, observed radii *larger* than predicted do not necessarily imply an absence or a small amount of heavy material. For such cases, the nature of the object remains ambiguous, if only based on the knowledge if its mean density.
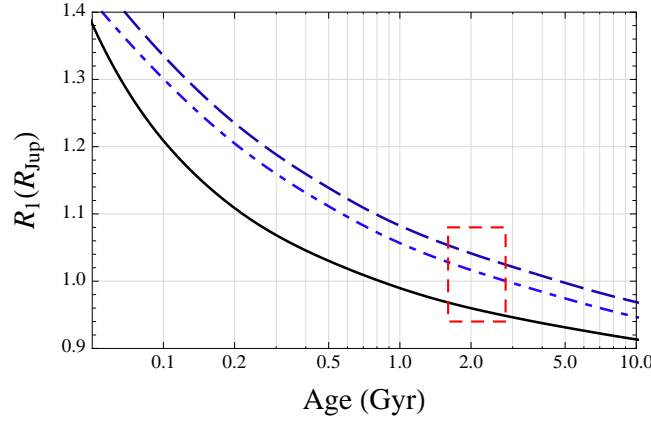
Figure 2.12: CoRoT-3 b. *Solid line*: standard cooling sequence of an isolated $21.66\,M_{\rm Jup}$ brown dwarf with solar composition. *Long dashed line*: irradiated case. *Dash-dotted line*: Irradiated case with a $272\,M_{\oplus}$ core of water. *Red box*: observational 1σ error bar. *Revised figure from Leconte et al. (2009)*.

I first focused on the most massive transiting object in the CoRoT sample, CoRoT-3 b. To examined whether its radius determination enables us to identify its very nature, I computed evolutionary tracks corresponding to several different scenarios and compared it to the data. As shown in Fig. 2.12, the observed radius of CoRoT-3 b can be matched by the model of an *irradiated* brown dwarf of $21.6\,M_{\rm Jup}$ with solar composition (long-dashed line). This is by itself an encouraging confirmation of the theoretical prediction of the age-mass-radius relationship in the brown dwarf regime (Chabrier and Baraffe 1997 ; Baraffe et al. 1998). Note that, given the small orbital distance, the effects of irradiation are not negligible, even for such massive objects. Accounting for irradiation on the atmospheric profile, and thus on the object's cooling history, is thus mandatory to provide consistent comparison between models and observations, when the radius is determined at this level of accuracy ($\sim 7\%$). The present radius error bars, however, are still too large to infer or exclude the presence of a significant amount of heavy material in the interior of this object.

As done in § 2.4.4, I determined the maximum amount of heavy material allowed by the error bar on the radius determination. I found an upper mass limit for the core of about $800\,M_{\oplus}$ (i.e. $Z \lesssim 12\%$). However, we have to see if this *maximum* enrichment compatible with the actual error bars is possible with our current understanding of planet formation. According to current models of planet formation which include migration (Alibert et al. 2005), up to $\eta_{\rm acc} \sim 30\%$ of heavy elements contained in the protoplanetary disk can be incorporated into forming giant planets (Mordasini et al. 2008, 2009). The maximum mass of available heavy material that can be accreted to form planets is thus

$$M_Z \approx \eta_{\rm acc} \cdot Z \cdot (f \cdot M_\star), \tag{2.25}$$

where $f \cdot M_\star$ is the maximum mass for a stable disk ($\lesssim 0.1 M_\star$) and Z is the metal mass fraction of the

star[13]. For CoRoT-3 b, which is orbiting a $1.37 M_{\odot}$ F star with near solar metallicity, at most $M_Z \approx 270 M_{\oplus}$ of heavy material can thus be accreted to form the planet. This (admittedly crude) upper limit derived from current planet core accretion formation models yields a planet contraction consistent with today's observations, as seen in Fig. 2.12 [14].

Therefore, given the present uncertainties in the radius determination, neither the brown dwarf nor the planet possibility can be assessed or excluded for CoRoT-3 b, whose nature remains ambiguous. A comparison between the predicted radius of a (irradiated) solar-metallicity brown dwarf (dashed line) and of a planet with the aforedetermined massive core, which represents only a $\sim 4\%$ metal enrichment (dash-dotted line) in Fig. 2.12, shows that a radius accuracy $\lesssim 3\%$ is required to resolve the ambiguity, according to the present models. In any event, this demonstrates the promising powerful diagnostic provided by mass-radius determinations to distinguish massive planets from low-mass brown dwarfs, providing adequate observational accuracy.
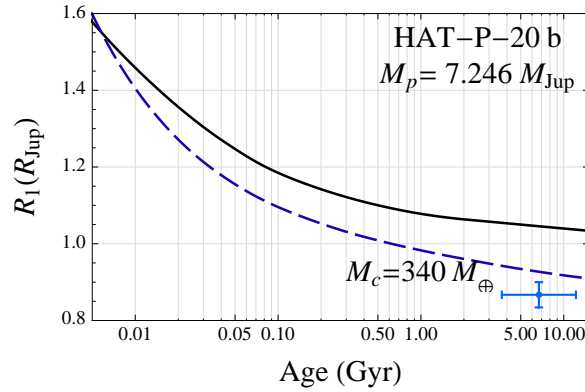
Figure 2.13: Hat-P-20b. *Solid line*: Cooling sequence of an irradiated $7.25 M_{\mathrm{Jup}}$ brown dwarf. *Dashed line*: Irradiated case with a $340 M_{\oplus}$ icy core. *Blue Cross*: observational 1σ error bar. *Figure from Leconte et al. (2011b)*.

Among the few known massive planetary-mass objects, there is at least one example for which such a radius measurement provides the identification of its nature. This is the case of Hat-P-20 b, a $7.25\ M_{\mathrm{Jup}}$ mass object, closely orbiting a K type star (Bakos et al. 2010)[15]. **As illustrated in Fig. 2.13, the evolutionary track that I computed for the irradiated brown dwarf model (long-dashed line) overestimates the radius by $\sim$ 10-15%. Consistently with Eq. (2.25), models including a $340 M_{\oplus}$ core mass of ices[16] can nearly explain the measured radius (dashed line).** The discrepancy would be even smaller if we considered the presence of rocks. Although this amount of heavy material is about the limit of what is available for planet formation, according to current core-accretion models (as estimated from Eq. (2.25) for the HAT-P-20 system ; see also Mordasini et al. 2009), the presence of such a metal enrichment ($Z \lesssim 15\%$) provides the simplest plausible explanation for the observed radius of HAT-P-20 b, according to the present theory. As mentioned earlier, this $340 M_{\oplus}$ core for HAT-P-20 b should be seen as a rough estimate of the upper limit for the available heavy material in the system, but

---

[13]For a more accurate determination, one should take care of the fact that only the *condensed* volatiles and silicates (the so-called *dusts*) can participate to the formation of planetesimals.

[14]Note that, as discussed in Baraffe et al. (2008) for HAT-P-2b, this heavy material does not need to be accreted into one single object, as very massive planets, in particular short-period ones, may result from smaller planet collisions.

[15]In Leconte et al. (2009), we discussed the case of Hat-P-2 b, and not Hat-P-20 b, a $8\ M_{\mathrm{Jup}}$ mass object, closely orbiting an F type star (Winn et al. 2007b), but a more recent analyses of the data showed that the radius had been underestimated in the discovery paper (Pál et al. 2010). What will Hat-P-200 b be like ? Future should tell.

[16]Note that this amount of heavy material does not necessarily need to be in a core but could be distributed all over the planet.

this analysis shows that the currently observed *low* radius of this object cannot be explained without a substantial enrichment.

It would certainly be interesting to see whether planet models from other groups yield or not similar determinations. Given the fact that these various planet models share many common physics inputs (in particular the H/He and heavy element EOS), it would be surprising that they reach severely different conclusions. While keeping in mind the remaining uncertainties in planet cooling theory, **the present analysis provides - with the parameters observed so far - a confirmation of the validity of the core-accretion model, and makes Hat-P-20 b the first confirmed *7-8 $M_{\rm Jup}$ genuine planet* formed by core-accretion in a proto-planetary disk** (Leconte et al. 2009, 2011b).

2.6 Conclusion

In this chapter, I have shown that, even taking into account the impact of the stellar irradiation on the atmosphere of extrasolar giant planets is not sufficient to explain their observed *large* radius. **Then, by modeling numerically all the transiting exoplanets that were known to date, I quantified the remaining *radius anomaly*** (Leconte et al. 2011b).

Doing so, I also showed that **the mechanical structure of both *isolated* and *irradiated* giant planets can be well characterized by an effective polytropic index, for which I gave numerical estimates** (Leconte et al. 2011c). This also confirmed that the principal effect of stellar irradiation is not the direct bloating of the outer layers, but the slowing down of the usual gravo-thermal evolution.

Then, I showed how the mass-radius diagram can be used to constrain the enrichment of observed transiting planets. In particular, **I find that the *mean density* determination, while inconclusive in the case of CoRoT-3 b, is discriminant in the case of Hat-P-20 b, which is thus the first confirmation of the possibility to form massive planets by core accretion (possibly with subsequent collisions) up to $M_1 \gtrsim 8 M_{\rm Jup}$** (Leconte et al. 2009). This analysis shows that, according to the present models, a typical $\lesssim 5$ % accuracy on the radius determination must be achieved in future space-based or ground based transit detections to clearly distinguish planets from brown dwarfs in their overlapping mass domain.

Chapter 3

Probing the deep interior: Theory of planetary figures

Contents

Because the *theory of figures* is the basis of the modeling of Solar System giant planets and of the theory of equilibrium tides that will be explored in the following chapters, the first section of this chapter is dedicated to the definition of the main variables and to the introduction of the main concepts needed (§ 3.1). For completeness, the full development of the general linear theory of Sterne (1939) and of the axisymmetric third order theory of Zharkov and Trubitsyn (1980) (that will be used in Chapter 4) are carried out in Appendix D and E[a] respectively.

Then, in § 3.2, I show how the response in *shape* and in *potential* of giant exoplanets and brown dwarfs to the *combined* effect of rotational and tidal distortion can be computed from the knowledge of the *potential Love number* (k_2) alone. To make the use of these formulae possible, I give numerical estimates for the *Love number* of these objects, and discuss what these values tell us about the mechanical structure of gaseous substellar objects.

I also investigate the impact of heavy element enrichment on the tidal response of giant planets, and demonstrate on a test case how one could take advantage of these models to infer a core mass from k_2 measurements (§ 3.3).

In § 3.4, I show one of the limitation of the numerical theory, and how it can be overcome, at least in the linear regime, by an analytical theory when stronger assumptions are made. Finally, in § 3.5, using this model, I discuss the implications of the tidal distortion of close in planets on the parameters that are measured from their light curve. In particular, I demonstrate that the equilibrium radius of strongly distorted objects can be larger than the measured radius, inferred from the area of the (smaller) cross section presented to the observer by the planet during the transit ; systematic bias in the radius determination which still enhances the aforementioned radius anomaly.

The results presented in § 3.2 to 3.5 led to the publication of *Distorted, non-spherical transiting planets: impact on the transit depth and on the radius determination* (Leconte et al. 2011c).

---

[a]Some typos found in Zharkov et al. (1973) and Zharkov and Trubitsyn (1980) are also corrected.

While

WE USUALLY IMAGINE STARS AS BIG LUMINOUS PERFECT GLOBES moving through empty space, those are spheres only in first approximation. If the sphere is indeed the lowest energy state of an isolated, gravitationally bound, collection of particles at rest[1], there is no such thing as a completely isolated or motionless celestial body ! Through conservation of angular momentum during the gravitational collapse of a dense interstellar cloud and its following contraction, a very small initial velocity inhomogeneity can be sufficient to imprint a quite rapid rotation to the newborn star. Part of this momentum, being kept by the protoplanetary disk, can then be transferred to the young forming planets, in form of both orbital and internal angular velocity. Thus, all planets and stars are rotating, even if sometimes *slowly*, and no longer spherical. Moreover, when another massive body is cruising nearby, the effect of its gravitational pull also changes the macroscopic equilibrium state of our assembly of particles.

This large scale perturbation of the equilibrium of a non rigid body has many dynamical consequences. The most important one, which more or less encompasses all the others, being that a non spherical distribution of matter breaks the shell theorem demonstrated by Sir Isaac Newton (1687) in his *Philosophiae naturalis principia mathematica* ; i.e., the gravitational force that it exerts on external massive particle does not follow the usual inverse square law, and can have a non axial component. As a result, the trajectory of a particle moving under the sole attraction of such a mass distribution will depart from the ellipse that was first anticipated by Johannes Kepler (1609) in his *Astronomica nova*. Speaking in terms of osculating elements[2], the shape and orientation of the orbit that best describes the motion of the particle over time could change both periodically and secularly. If one seeks to predict the orbital evolution of a given set of self-gravitating objects in mutual interaction, the problem of the determination of the gravitational field created by each body, and thus of their shape, arises.

The question of the figure of a self-gravitating body, first formulated for the Earth during the Antiquity, is a long standing problem. Since Parmenides[3], for aesthetic and geometrical reasons, and Plato[4], who based his reasoning on the observation of the Earth shade during lunar eclipses, the Earth was thought to be spherical. This was only, as often through new observations made during the seventeenth century, that the sphericity of the Earth started to be questioned scientifically. On one side, by analogy with Jupiter, whose oblateness has been measured by Giovanni Domenico Cassini in 1666 and has rapidly been thought to be related to the rapid rotation of the planet (as first acknowledged in Philosoph-

---

[1]in a macroscopic sense

[2]From the Latin verb *osculare*, to kiss, the osculating elements at an instant t are the six orbital elements - semi-major axis (a), eccentricity (e), inclination (I), argument of pericenter (ϖ), longitude of the ascending node (Ω) and time of pericenter passage (τ) - that completely define the shape and orientation of the orbit that our two bodies would follow if the perturbing force were to disappear at that instant (Murray and Dermott 1999). In the unperturbed two body problem, those elements are constant over time. In practice, the osculating elements can be computed by knowing the position and velocity of one of the bodies in any reference frame at any given time, and their temporal evolution can calculated by integrating a set of differential equations, commonly known as Lagrange planetary equations. An example of such equations is presented in Chapter 5.

[3]515-450 BC.

[4]428-348 BC.

ical Transactions 1665), it was natural to think that the Earth could also have an ellipsoidal shape. On the other side, during a travel to Cayenne in 1672, Jean Richer discovered that the length of the seconds pendulum, that is a pendulum with a swing of one second, was 2.8 millimeters shorter in Guyana than in Paris, showing that the gravity was smaller near the equator. This rapidly led Newton and Christian Huyghens to formulate a first theory of the gravity of the Earth (Huyghens 1690). However, the modern theory of the figure of celestial bodies in hydrostatic equilibrium, which is detailed hereafter, is first due to Colin Maclaurin and Alexis Clairaut (1743), and was subsequently pursued by Pierre Simon Laplace, Jean-Charles Rodolphe Radau, George Darwin (1899) and Aleksandr Mikhailovich Lyapunov (1903), among others. This is only thanks to these developments that the equilibrium theory of tides could emerge (see Chapter 5).

Conversely, it is possible to measure the gravitational field created by a celestial body and its departure from sphericity. This can be done either directly with orbiting spacecrafts, when the object is nearby, or by monitoring its dynamical interactions with other bodies when the first option is not available. Then, these constraints on the figures of the body considered can be used to constrain some of its internal properties, as has been successfully achieved for, e.g. giant planets in our solar system (see Zharkov and Trubitsyn 1980 and reference therein, Hubbard and Marley 1989 ; Chabrier et al. 1992, large satellites (de Sitter 1914), binary stars (Sterne 1939 ; Kaula 1964), etc...

3.1 Theory of figures

3.1.1 Problem statement

The basic problem of the *theory of figures* is as follows. We are given some amount of self-gravitating matter under the influence of an external perturbation, and for which we have an Equation of State (EOS), and we wish to know what is the distribution of the matter in space when hydrostatic equilibrium is achieved. As we have seen in Chapter 1, a body is in hydrostatic equilibrium when the pressure gradient (∇P) balances the other forces, yielding

$$\nabla P = -\rho \nabla \left(V_G + V_{\text{ext}} \right), \tag{3.1}$$

where V_G is the gravitational self potential, and V_{ext} a perturbing potential. The hydrostatic balance directly implies that isobaric surfaces and equipotentials are identical. Because the equation of state ($P(\rho)$) is known, isodensity surfaces also have the same shape, so the problem reduces to that of finding the shape of the equipotentials, that will also be called *level surfaces* in the following.

In general, no exact analytical solution can be found to the problem stated above. Because we are considering *small* perturbations, in a sense that remains to be defined, the departure of the final equilibrium configuration from sphericity is also weak, and all expansions can be used. The order at which the perturbative development has to be carried out then directly depends on amplitude of the perturbation considered, and on the degree of accuracy sought on the observables. On one side, the precision of the transit observations of exoplanets is not yet high enough to justify the use of high order theories in this context. On the other hand, a high order scheme is necessary to fully take advantage of the accuracy of gravitational moments measurements in our solar system to constrain the composition of our giant planets interiors, as done in Chapter 4. However, such a theory is too cumbersome to be easily usable in a general context.

3.1.2 Summary

Because of the functional form of the gravitational potential of a point mass, which goes as the inverse of the distance, expansions of the total potential naturally involve Legendre polynomials. Then it seems natural to postulate that the final shape of the equipotentials can be expressed in terms of those Legendre polynomials (which are generalized by spherical harmonics in the non axisymmetric case), as first did Maclaurin and Clairaut (1743). This approach, which has been repeatedly criticized because of a divergence of the Legendre expansion in a small region between the sphere and the level surfaces, has however been demonstrated to be correct by Lyapunov (1903). Thus, matter organizes itself in concentric shells, whose shape is a combination of spherical harmonics, and the values of the density, pressure, potential and figure functions (the coefficients affecting the various spherical harmonics) on these shells, depend on a unique *level* variable labeling the surface (see § 3.1.5 for examples of different level variables).

With that in mind, in order to derive usable equations, we follow five different steps that will be considered in that order hereafter.

- We formally compute the gravitational potential created at a point $\mathbf{r}$ by an arbitrary mass distribution ($\rho(\mathbf{r}')$), which is not yet necessarily in equilibrium (§ 3.1.3). The potential is then expressed in terms of spherical harmonics ($Y_n^m(\theta, \phi)$), whose coefficients are expressed through integrals of the density field weighted by the aforementioned spherical harmonics (hereafter, the mass integrals, D_n^m).

- Various possible perturbing potentials (V_{ext}) are then considered and projected onto spherical harmonics. We also define a dimensionless coefficient (m_{ext}), which measures the amplitude of the perturbation compared to the restoring force, i.e. the self gravity (see § 3.1.4).

- Then, in § 3.1.5, we expand the shape of each level surface on the same spherical harmonic basis. To do so, we have to chose the *level* variable (l) and consequently the set of figure functions that we will use ($l_n^m(l)$). At that point, depending on the set of functions and the variable chosen, some preliminary relations can be derived (see either § D.2 or E.2).

- Knowing, at least formally, the mass distribution - meaning that the density field is constrained to verify $\rho(\mathbf{r}') = \rho(l)$, where the latter function is still arbitrary for the moment - we can derive formal expressions for the mass integrals which now involve only this one dimensional density profile and the figure functions (§ D.3 or E.3).

- The coefficients of the expansion of the *total potential on each level surface* on the $Y_n^m(\theta, \phi)$ can then be expressed in terms of algebraic combinations of the mass integrals and figure functions. Because level surfaces are equipotentials by construction, all but one of these terms must be identically equal to zero, which provides us with a sufficient number of integro-differential equations to be solved to obtain the figure functions. Finally the radial term provides us with an expression for the perturbed gravity field to use in solving hydrostatic equilibrium (§ D.4 or E.4).

Of course, we did not detail yet what prescription should be taken for $\rho(l)$. Indeed, if this seems an input in the above procedure, it directly results from the integration of the hydrostatic equilibrium equation which is one of the output of the calculation. It is then understood that an iterative process will be needed, where a first prescription is given for the stratification, allowing a computation of the figure functions and an update of the density profile, this procedure being repeated until some convergence criterion is met. However, thanks to the fact that the perturbation is often... well... only a perturbation, the density profile that would be obtained in the unperturbed spherical case gives a good first guess, and can even be left unchanged, depending on the accuracy sought.

3.1.3 Self gravitational potential

As mentioned above, the main reason why celestial bodies are nearly spherical is that the sphere is the minimum energy shape of self gravitating isolated particles, and that we are considering massive enough objects for self gravity to dominate. Thus, self gravity is the restoring force in our problem, and we must concern ourselves with the computation of this gravitational potential for an arbitrary mass distribution in space $\rho(\mathbf{r}')$. It can be shown that the gravitational potential created at the point $\mathbf{r}$ by this mass distribution reads

$$V_G(\mathbf{r}) = -\frac{G}{r} \sum_{n=0}^{\infty} \sum_{m=-n}^{n} \left(r^{-n} D_n^m + r^{n+1} \bar{D}_n^m \right) Y_n^m(\theta, \phi), \tag{3.2}$$

$$D_n^m(r) = (2 - \delta_{m,0}) \frac{(n-m)!}{(n+m)!} \int_{r'<r} \rho(\mathbf{r}') \, (r')^n \, Y_n^m(\theta', \phi') \, \mathrm{d}^3\mathbf{r}', \tag{3.3}$$

$$\bar{D}_n^m(r) = (2 - \delta_{m,0}) \frac{(n-m)!}{(n+m)!} \int_{r'>r} \rho(\mathbf{r}') \, (r')^{-n-1} \, Y_n^m(\theta', \phi') \, \mathrm{d}^3\mathbf{r}', \tag{3.4}$$

defining the internal (D_n^m) and external ($\bar{D}_n^m$) mass integrals[5,6]. For compactness, we have introduced spherical harmonics defined by

$$Y_n^m(\theta, \phi) \equiv \begin{pmatrix} \cos|m|\phi \\ \sin|m|\phi \end{pmatrix} P_n^{|m|}(\cos\theta), \tag{3.5}$$

where the P_n^m are the usual associated Legendre polynomials. The cos (sin) corresponds to positive (negative) values of m. As advertised, this shows that the gravitational potential can be projected onto spherical harmonics weighted by the mass integrals.

These mass integrals are not purely mathematical entities. Indeed, considering a point exterior to the object, $\bar{D}_n^m = 0$, and D_n^m is constant. Then the gravitational field reads

$$V_G(\mathbf{r}) = -\frac{G}{r} \sum_{n,m} r^{-n} D_n^m Y_n^m(\theta, \phi) \equiv -\frac{GM_1}{r} \sum_{n,m} \left(\frac{R_{\text{eq}}}{r} \right)^n C_n^m Y_n^m(\theta, \phi), \tag{3.6}$$

where we see that the *gravitational moments* are the dimensionless counterparts to the mass integrals

$$C_n^m = D_n^m / (M_1 R_{\text{eq}}^n). \tag{3.7}$$

While these expressions are not yet usable, we will see in § D.3 and E.3, that further constraining the density field yields major simplifications of these relations.

3.1.4 Perturbing potentials

If only the gravitational potential is considered, we know that the body takes a spherical shape in hydrostatic equilibrium. It is now time to consider in more detail the various perturbations that can break this symmetry, and to define the dimensionless quantities measuring the amplitude of these perturbations.

Centrifugal potential

If a mean rotation of the fluid composing the planet occurs, the centrifugal acceleration, which is alway perpendicular to the mean rotation axis, causes a flattening of the body. However, axial and

---

[5]When no confusion can occur, $\delta_{i,j}$ is assumed to be the Kronecker symbol which is equal to 1 if i = j and 0 otherwise.

[6]In the following, $\sum_{n=0}^{\infty} \sum_{m=-n}^{n}$ will be abbreviated by $\sum_{n,m}$.

North/South symmetries remain. For simplicity, we place ourselves in the frame rotating with the planet (assumed in solid body rotation) at the angular speed ω_1. In this frame, the centrifugal potential reads

$$
\begin{aligned}
V_{\text{rot}}(\mathbf{r}) &= -\frac{1}{2}\omega_1^2 r^2 \sin^2\theta \\
&= -\frac{1}{3}\omega_1^2 r^2 \left(1 - P_2(\cos\theta)\right).
\end{aligned}
\tag{3.8}
$$

To evaluate the deformation, we define the dimensionless parameter m_{rot} as the ratio of the centrifugal acceleration over the gravitational one at the surface

$$
m_{\text{rot}} = \frac{\omega_1^2 \bar{R}_1^3}{GM_1},
\tag{3.9}
$$

where $\bar{R}_1$ is the mean radius of the external surface of the planet (see § 3.1.5 for details)[7]. This parameter estimate the relative importance of the rotational deformation over the restoring gravitational force.

For Jupiter and saturn, the values for m_{rot} are on the order of 0.1, justifying our use of a perturbative theory, where equations can be expanded with regard to the (small) parameter m_{rot} (or generally m_{ext} as defined in Eq. (3.15)). However, because errors yielded by a theory of order i[8] will be on the order of m_{rot}^{i+1}, one can see that high order developments will be needed to develop accurate enough models of our giant planets. On the contrary, for close in giant exoplanets, as will be discussed in detail in § 3.5, the slow rotation induced by the tidal pseudo-synchronization yields typical values of m_{rot} ranging from a few percent to 10^{-5}. Coupled to the yet limited accuracy of transit observations, this justifies the use of low order developments (see § 3.5 for details).

Tidal potential

When an external object is present (called the secondary in the following), the non uniform gravitational potential that it creates also disturbs the equilibrium structure of our deformable body. As we will see, this "Tidal potential" also conserve axial symmetry, but the axis of symmetry then lies along the vector joining the center of mass of the two objects.

To calculate the potential created by this external object, we should in principle solve the equations for its internal structure, as detailed hereafter, and then compute its resulting external field using Eq. (3.2). As this external object is itself disturbed by the primary body, we would then have to solve iteratively for the structure of each of these objects until some convergence is reached. To simplify the problem, we will assume that the secondary keeps its spherical symmetry. This is justified as long as we keep our calculations to the quadrupole order, meaning that only linear terms are considered[9].

Let the secondary lie at the location $\mathbf{r}_\star$ in the coordinate system centered on our primary, with a mass M_2. Considering a spherically symmetric body, the value of the potential at the location $\mathbf{r}$ writes

$$
V_{\text{tid}}(\mathbf{r}_\star, \mathbf{r}) = -\frac{GM_2}{|\mathbf{r}_\star - \mathbf{r}|}.
\tag{3.10}
$$

---

[7]In the literature, one can also find a slightly different normalization and definition $q = \frac{\omega_1^2 R_{\text{eq}}^3}{GM_1}$, where R_{eq} is the equatorial radius of the external surface of the object. Note that to high orders, this leads to differences in the figures equations.

[8]Meaning, in the following, a theory for which all the terms proportional to m_{rot}^{i+1} and smaller are neglected.

[9]It might seem a little counter intuitive to speak about the quadrupolar term in the tidal potential as the *linear* term. In the following, the term *linear* always refer to the first non vanishing order of the perturbation, and thus to all the terms that are proportional to m_{ext}.

Because we are interested in the value of this potential in the neighborhood of the primary, we can expand the fraction into Legendre polynomials. We thus have

$$V_{\text{tid}}(\mathbf{r}_\star, \mathbf{r}) = -\frac{GM_2}{r_\star} \sum_{n=0}^{\infty} \left(\frac{r}{r_\star}\right)^n P_n(\cos\psi), \tag{3.11}$$

where ψ is the angle between $\mathbf{r}$ and $\mathbf{r}_\star$. The first term is just a constant and the second gives rise to the usual Keplerian acceleration and need not be considered. Keeping only the quadrupolar term, we are left with the usual tidal potential

$$V_{\text{tid}}(\mathbf{r}_\star, \mathbf{r}) = -\frac{GM_2}{r_\star^3} r^2 P_2(\cos\psi). \tag{3.12}$$

A small parameter corresponding to the tidal disturbance can be defined analogously to Eq. (3.9),

$$m_{\text{tid}} = -\frac{M_2 \bar{R}_1^3}{M_1 r_\star^3}. \tag{3.13}$$

Note the negative sign, which is just a statement that, along the axis of symmetry of the perturbation, the disturbed body is elongated and not flattened.

Considering the Roche limit, r_R[10], as the smallest possible orbital distance between two self gravitating bodies, for a Jupiter like planet orbiting a sun like star, $|m_{\text{tid}}| \lesssim 0.05$. While solid satellites happen to be closer to the planet than the fluid Roche limit in the solar system, this figure shows us that the linear approximation remains satisfying when computing the tidal deformation to be used in Chapter 5.

Arbitrary perturbation

To lowest order the body response is linear and the total deformation is the sum of the response to each term of the decomposition of the perturbing potential. Thus, in order to derive the equations in a rather general way, we only need to consider a term a perturbing potential of the form

$$V_{\text{ext}}(r, \theta, \phi) = \mathbf{c}_n^m r^n Y_n^m(\theta, \phi), \tag{3.14}$$

where $\mathbf{c}_n^m$ is a constant which defines the amplitude of the perturbation (Sterne 1939). The reference axis defining θ and ϕ may change from one term to the other. For example, the rotation axis is best suited to treat rotational distortion and the line connecting the center of mass of each body is better to describe the tidal distortion.

Analogously to Eq. (3.13), a small dimensionless parameter can be defined as

$$m_{\text{ext}} = \frac{\mathbf{c}_n^m \bar{R}_1^{n+1}}{GM_1} = \frac{3}{4\pi} \frac{\mathbf{c}_n^m \bar{R}_1^{n-2}}{G\bar{\rho}_1}. \tag{3.15}$$

One can see that this form is not completely general. For example the first term of the centrifugal potential in Eq. (3.8) cannot be reproduced. This is due to the fact this term produce a net, isotropic, outward centrifugal force, and thus do not affect the shape of the body, but only its mean equilibrium radius. However, in the linear regime, there is no coupling of these different effects, which can then be addressed separately. Restricting the perturbing potentials that we will consider to those that can be described by Eq. (3.14) is thus justified in this limit[11].

---

[10]In the perfect fluid case, the Roche limit of a secondary of mean density $\bar{\rho}_2$, around a primary of mean density and radius, $\bar{\rho}_1$ and $\bar{R}_1$, respectively, is given by $r_R \approx 2.423 \bar{R}_1 (\bar{\rho}_1/\bar{\rho}_2)^{1/3}$

[11]While we will keep the aforementioned definition of m_{rot} to be consistent with Zharkov and Trubitsyn (1980), we remind the reader that for the linear rotational perturbation, only the second term of Eq. (3.8) can be treated, and using Eq. (3.15) yields $m_{\text{ext}} = m_{\text{rot}}/3$. As expected, for the tidal perturbation $m_{\text{ext}} = m_{\text{tid}}$.

3.1.5 Level surfaces

In the spherical case, equipotential surfaces are surfaces of constant radius. For small departure from sphericity, as was first hinted by Maclaurin and later demonstrated by Lyapunov (1903), the equation describing the equipotentials, or level surfaces, can be expanded in a series of spherical harmonics as follows

$$r(l, \theta, \phi) = l \left[1 + \sum_{n, m} \mathbf{l}_n^m(l) Y_n^m(\theta, \phi) \right], \tag{3.16}$$

where l is a characteristic length (radius) of the level surface, or *level variable*, and the $\mathbf{l}_n^m(l)$, or *figure functions*, characterize the shape of each level surface. Intuitively, we see that the figure functions, which would be equal to zero in the unperturbed case, are directly related to the amplitude of the perturbation (quantified by the small parameter m_{ext}), and should be small corrections. More rigorously, it can be shown that, apart from n $= 0$, $\mathbf{l}_n^m \propto m_{\text{ext}}$ (Lyapunov 1903).

As discussed in Zharkov and Trubitsyn (1970), many variables can be chosen as our variable l. However, there is a possibility which somewhat simplifies the figure equations. This variable is the *mean radius $\bar{r}$* which is implicitly defined by

$$\frac{4}{3}\pi \bar{r}^3 = \frac{1}{3} \int_0^\pi \mathrm{d}\cos\theta \int_0^{2\pi} \mathrm{d}\phi \; r^3(\bar{r}, \theta, \phi), \tag{3.17}$$

where $r(\bar{r}, \theta, \phi)$ is given by Eq. (3.16). Indeed, an equipotential labeled by $\bar{r}$ encloses the same volume that the sphere of radius $\bar{r}$, justifying the term of mean radius. Subsequently, the mean radius of the object is defined to be the mean radius of the surface enclosing the mass M_1 and is noted $\bar{R}_1$. Substituting l by this *mean radius* and renaming the $\mathbf{l}_n^m$, $\mathbf{s}_n^m$ in Eq. (3.16) implies that for any $\bar{r}$,

$$4\pi = \int_0^\pi \mathrm{d}\cos\theta \int_0^{2\pi} \mathrm{d}\phi \left[1 + \sum_{n, m} \mathbf{s}_n^m(\bar{r}) Y_n^m(\theta, \phi) \right]^3. \tag{3.18}$$

This provides us with the first of the needed figure equations. To convince ourselves that this variable simplifies the equations, let us consider a first order perturbation. Then, $\mathbf{s}_n^m \mathbf{s}_{n'}^{m'} \propto m_{\text{ext}}^2 \approx 0$, and Eq. (3.18) rewrites $\mathbf{s}_0^0 = 0$. Thus, to this order, the *hydrostatic equilibrium* equation does not involve the $\mathbf{s}_n^m$, as is shown in Appendix D. For this reason, we will use the variable $\bar{r}$, and note $\bar{R}_1$ the mean radius of the 1 bar equipotential of the object considered. For figure equations derived using either the equatorial or polar radius, the reader is referred to Zharkov and Trubitsyn (1970).

Which radius ?

Before going further, it is important to summarize the differences between the various radii that can be defined. Note that, in the literature, the term "radius" is used loosely, even for non-spherical objects. Importantly enough, this can lead to discrepant normalizations throughout different studies and published values of transit radius measurements when, for example, radii are shown in units of Jupiter radii (R_{Jup}) without precisely defining the latter.

For any distorted object, one can define a_1, a_2 and a_3 as the distances between the center and any given isobaric surface along the three principal axes of inertia[12]. If axial symmetry holds (e.g. for a

---

[12]For a fluid object in a binary, the three directions along which the principal axes are measured are, respectively, the line connecting the center of mass of the two components, its normal contained in the orbital plane and the direction of the orbital angular momentum vector.

rotating fluid body), we have $a_1 = a_2 \equiv r_{\text{eq}}$, defining the equatorial radius of the isobar, and $a_3 \equiv r_{\text{pol}}$ its polar radius. In this case, for the 1 bar surface, $r_{\text{eq}} \equiv R_{\text{eq}}$ and $r_{\text{pol}} \equiv R_{\text{pol}}$ by definition. One must be aware that only the external value of a_1, a_2 and a_3 (reducing to R_{eq} and R_{pol} for axisymmetric bodies) can be measured directly and are *not* model dependent. This is why we define R_{Jup} as the equatorial radius of Jupiter at the 1 bar level $R_{\text{Jup}} \equiv R_{\text{eq,J}} = 7.1492 \times 10^7 \,\text{m}$, Guillot 2005 and reference therein).

Equilibrium radius

Finally, we can define R_1, the radius of the spherical shape that the fluid body would assume if it was isolated and at rest in an inertial frame (the limiting case for which all the mentioned radii would be equal). While this definition is purely theoretical, it has some importance, as $R_1(t)$ is the radius computed in usual 1D numerical evolution calculations, and the one that we have used throughout the previous chapters. In general $R_1 \neq \bar{R}_1$ because the centrifugal force has a net outward component that increases the volume of the object. Therefore, if one is not only interested by the shape, but also by the absolute radius of the object, as it will be the case hereafter, one needs to find a relation between R_1 and $\bar{R}_1$. Numerically, this can be handled by integrating hydrostatic equilibrium with the centrifugal force, but requires a numerical integration for each object and each value of the perturbation m_{rot}. However, as we will show in § 3.4, approximate analytical formulae can be used to correct this.

3.1.6 Total potential

The goal of the theory of figures is to express the total potential on the level surfaces using only $(\bar{r}, \theta, \phi)$. In practice, we will replace the r's that appear in the expression of the gravitational potential and in the mass integrals, Eqs. (3.3) and (3.4), by their spherical harmonics decomposition, given by Eq. (3.16). We can then decompose the total potential on spherical harmonics following

$$
\begin{aligned}
V_{\text{tot}}(\bar{r}, \theta, \phi) &= V_G + V_{\text{ext}} \\
&= -\frac{4}{3}\pi G \bar{\rho}_1 \bar{r}^2 \sum_{n,m} \hat{V}_n^m(\bar{r}) Y_n^m(\theta, \phi).
\end{aligned}
\tag{3.19}
$$

Because the $\bar{r} = $cst surfaces are equipotentials by construction, our set of equations on the figure functions we be given by Eq. (3.18) and

$$
\boxed{\left\{ \hat{V}_n^m(\bar{r}) = 0 \right\}_{n \neq 0,\, |m| \leqslant n}.}
\tag{3.20}
$$

The $n = 0$ term provides the equation for the hydrostatic equilibrium,

$$
\boxed{\frac{1}{\rho}\frac{\partial P}{\partial \bar{r}} = -\frac{\partial V_{\text{tot}}}{\partial \bar{r}} = \frac{4}{3}\pi G \bar{\rho}_1 \frac{\text{d}}{\text{d}\bar{r}}\left[\bar{r}^2 \hat{V}_0^0(\bar{r})\right].}
\tag{3.21}
$$

Beyond this stage, the actual form of these equations directly depends on the order of the development carried out. In order not to introduce to much technical discussions, the general first order theory developed by Sterne (1939), and that will be used hereafter, can be found in Appendix D. To summarize, it is found that the shape of each isodensity surface can be characterized by the quantity $\eta_n(\bar{r}) = \frac{\bar{r}}{s_n^m(\bar{r})}\frac{\text{d}s_n^m}{\text{d}\bar{r}}$, which can be obtained by integration of a first order integro-differential equation, Eq. (D.21).

For those interested in a higher order, but axisymmetric theory, based on the work of Zharkov and Trubitsyn (1980), they are referred to Appendix E.

3.2   The figure of (extrasolar) giant planets

Using the linear theory of Sterne (1939) (see Appendix D), once the density profile has been obtained by integrating the hydrostatic equilibrium equation, and the figure functions by the integration of Eq. (D.21), we have all the information needed to completely describe the distribution of matter in our object. But this distribution is not, in general, directly observable. We thus need to concern ourselves with the computation of observable quantities such as the external shape, and the external gravitational potential.

Fortunately, as we use a linear theory, the amplitude of the response of the body is directly proportional to the amplitude of the perturbation. In our context, these *transfer functions* are called the *Love numbers*, and capture all the equilibrium response of the body. **In this section, I will show how these quantities can be computed, and present numerical estimations of their values for giant planets.**

3.2.1   External shape: ellipticity and level Love Numbers
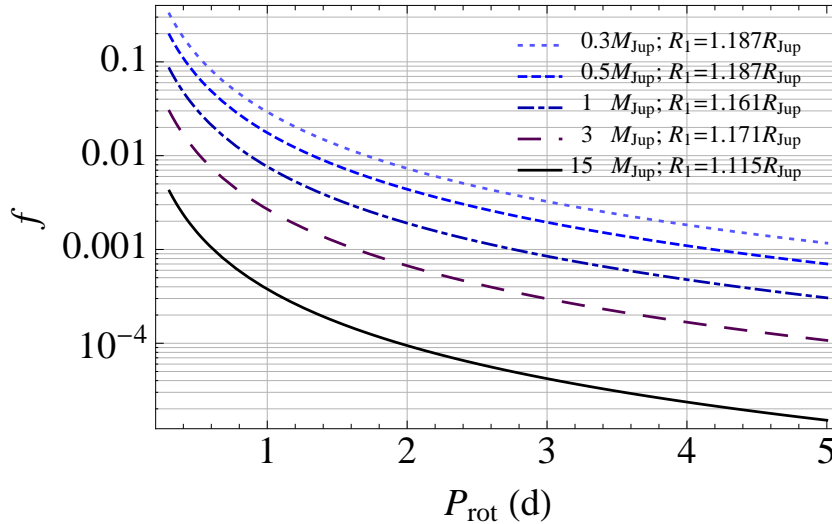
Figure 3.1: Oblateness given by Eq. (3.25) as a function of the rotation period (in days) at 1 Gyr for planets of mass: $0.3 M_{\rm Jup}$ (dotted), $0.5 M_{\rm Jup}$ (dashed), $1 M_{\rm Jup}$ (dash-dotted), $3 M_{\rm Jup}$ (long dashed), $15 M_{\rm Jup}$ (solid). The oblateness decreases when the mass of the planet increases because massive objects are more compressible (see § 2.2.2), have a more intense self-gravity field and are thus less subject to perturbations. *Figure from Leconte et al. (2011c).*

Once, $\hat{\eta}_{\rm n} = \eta_{\rm n}(\bar{R}_1)$ has been obtained by numerical integration of Eq. (D.21), we can show by setting $\tilde{s} = \bar{r}/\bar{R}_1 = 1$ in Eq. (D.18), that the external shape of our body (i.e. the value of the figure function at the surface) is given by

$$\mathbf{s}_{\rm n}^{\rm m}(\bar{R}_1) = -\frac{2{\rm n}+1}{{\rm n}+\hat{\eta}_{\rm n}} m_{\rm ext}. \tag{3.22}$$

As expected, the deformation is linear with respect to the amplitude of the perturbing potential ($m_{\rm ext}$). Because, the strength of the perturbation can vary with time, it is customary to refer to the proportionality constant in Eq. (3.22), which is an intrinsic characteristic of the deformable body itself. This constant of

the object, defined as

$$\mathbf{s}_n^m(\bar{R}_1) Y_n^m(\theta, \phi) \equiv -h_n \frac{V_{\text{ext}}(\bar{R}_1, \theta, \phi)}{g\bar{R}_1} \implies \mathbf{s}_n^m(\bar{R}_1) = -h_n m_{\text{ext}}, \tag{3.23}$$

where g is the unperturbed surface gravity acceleration, is the *level Love number* (h_n), which is therefore given by

$$h_n = \frac{2n+1}{n+\hat{\eta}_n}. \tag{3.24}$$

For an isolated, rotating object, an observable quantity is provided by the dynamical flattening, also called ellipticity or oblateness ($f \equiv \frac{R_{\text{eq}} - R_{\text{pol}}}{R_{\text{pol}}}$), which is given by

$$f = -\frac{3}{2}\mathbf{s}_2^0 = \frac{3}{2}h_2 m_{\text{ext}} = \frac{h_2}{2}m_{\text{rot}}. \tag{3.25}$$

Attempts have been made to constrain the oblateness and thus the rotation period of transiting planets by using the solar system planets as test cases (Carter and Winn 2010a,b). Because of the wide variety of exoplanets, it is important to have the ability to predict the flattening of fluid planets for a wider range of parameters than encountered in the solar system. **Fig. 3.1 shows the oblateness predicted by my numerical code for various planet masses as a function of the rotational period $P_{\text{rot}} = 2\pi/\omega_1$. The values of the *level* Love number are deduced from the *potential* Love number (k_2) as explained in the following section.**

Because the radius weakly depends on the mass of the object in the $1 - 30 M_{\text{Jup}}$ mass range, at fixed angular velocity, m_{rot} decreases when mass increases. *Massive object, which have a much stronger gravity, are thus less subject to perturbations.* However, the main limitation to the detection of the oblateness of transiting objects is that close in planets are expected to quickly pseudo synchronize because of the tidal friction. To get an idea of the timescales involved, with the dissipation rates inferred in Chapter 5, a Jupiter like planet around a Sun like star must be on an orbit with a period longer than 20 days to maintain a fast rotation for more than a Gyr. Below that limit, the rotation period will be mostly determined by the orbital period and will hardly be much shorter than a day. Above, only few objects are available, and observation will take time as an orbital revolution takes longer. In this case, the longer transit duration may be favorable.

3.2.2 External potential: gravitational moments and potential Love numbers

Because the gravitational potential naturally expands on a basis of Legendre polynomials, as shown in § 3.1.3, the external field is often written

$$V_G(r > \bar{R}_1, \theta, \phi) = -\frac{GM_1}{r} \sum_{n,m} \left(\frac{R_{\text{eq}}}{r}\right)^n C_n^m Y_n^m(\theta, \phi), \tag{3.26}$$

where θ is the colatitude and ϕ the longitude of the body considered[13]. For rotating fluid bodies, for which the symmetry with respect to both the rotation axis and the equator plane[14], only the even har-

---

[13] A more conventional notation is

$$V_G(r > \bar{R}_1, \theta, \phi) = -\frac{GM_1}{r} \sum_{n=0}^{\infty} \sum_{m=0}^{n} \left(\frac{R_{\text{eq}}}{r}\right)^n (C_n^m \cos m\phi + S_n^m \sin m\phi) P_n^m(\cos\theta),$$

but this would lead to possible confusion with the mass integrals S_n^m from § D.4, which have a slightly different normalization. By construction, $C_0^0 = 1$.

[14] Meaning that the other perturbation, such as tidal deformation, can be neglected.

monics with a zero azimuthal number remain and the most common notation reads

$$V_G(r > \bar{R}_1, \theta, \phi) = -\frac{GM_1}{r} \left[1 - \sum_n J_{2n} \left(\frac{R_{\text{eq}}}{r} \right)^{2n} P_{2n}(\cos\theta) \right]. \tag{3.27}$$

The gravitational moments, C_n^m or J_n, are directly related to the mass integrals defined in § D.4 by

$$C_n^m = \hat{D}_n^m / (M_1 R_{\text{eq}}^n), \tag{3.28}$$

or

$$J_n = -\hat{D}_n^0 / (M_1 R_{\text{eq}}^n), \tag{3.29}$$

where $\hat{D}_n^m = D_n^m(\bar{R}_1)$, the value of the integral at the surface. Hence, they encompass all the information on the density profile needed to compute the external field. A major consequence of that, is that measurement of the gravitational field of a planet will allow us to estimate only the mass integrals and not directly the density field. In principle, because spherical harmonics are a complete basis, the information contained in all the C_n^m, or equivalently the J_n in the axisymmetric case, should allow us to retrieve exactly the density field. However, as the order of the harmonic (n) increases, the value of C_n^m usually decreases, and only the first harmonics are measured to date[15]. These measurements can thus only constrain the internal state of giant planets, but is sufficient to rule out some compositions and equation of states (Chabrier et al. 1992 ; Saumon and Guillot 2004 ; Guillot 2005)

In our case, we know from Eq. (D.13) that the gravitational potential at the surface of the sphere of radius $\bar{R}_1$ can be expressed through the *dimensionless* mass integrals (Eq. (D.12)), many of them being equal to zero, and reads

$$V_G(\bar{R}_1, \theta, \phi) = -\frac{GM_1}{\bar{R}_1} \left[S_0^0(\bar{R}_1) + S_n^m(\bar{R}_1) Y_n^m(\theta, \phi) \right]. \tag{3.30}$$

Because $S_0^0(\bar{R}_1) = 1$, evaluating Eq. (D.14) at $\tilde{s} = 1$ yields $S_n^m(\bar{R}_1) = s_n^m(\bar{R}_1) + m_{\text{ext}} = (1 - h_n) m_{\text{ext}}$. Then, solving the Dirichlet problem yields the potential outside the sphere

$$V_G(r > \bar{R}_1, \theta, \phi) = -\frac{GM_1}{r} \left[1 - (h_n - 1) \frac{\bar{R}_1^n}{r^n} m_{\text{ext}} Y_n^m(\theta, \phi) \right], \tag{3.31}$$

where the non spherical part is the potential induced by the deformation, V_{ind}. For the same reasons that in § 3.2.1, we can define the *potential Love number*, k_n, as the linear response coefficient

$$V_{\text{ind}}(\bar{R}_1, \theta, \phi) = k_n V_{\text{ext}}(\bar{R}_1, \theta, \phi), \tag{3.32}$$

which yields[16]

$$k_n = h_n - 1 = \frac{n+1-\hat{\eta}_n}{n+\hat{\eta}_n}. \tag{3.33}$$

Thus, for this perturbation

$$C_n^m = -\frac{n+1-\hat{\eta}_n}{n+\hat{\eta}_n} m_{\text{ext}} = -k_n m_{\text{ext}} \tag{3.34}$$

(a) Isolated objects

(b) Irradiated objects
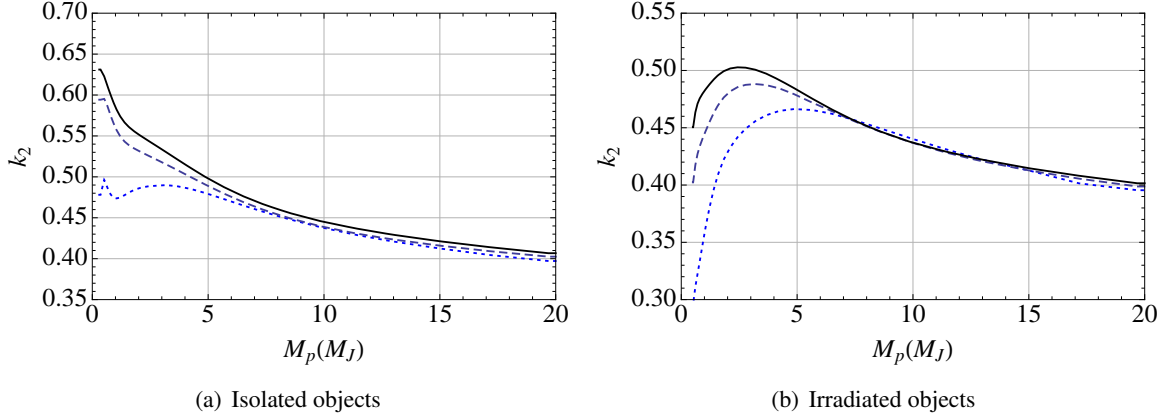
Figure 3.2: Left: *Potential* Love number for isolated planets as a function of the planet mass (M_p) at 100 Myr (dotted), 1 Gyr (dashed) and 5 Gyr (solid). Right: idem for strongly irradiated objects ($F_\mathrm{inc} = 4.18 \times 10^6\,\mathrm{W.m^{-2}}$). As contraction proceeds, the density contrast between the outer layers of the planet and the center decreases, and thus k_2 increases. Note the change in the y scale between panels. As irradiation retards the evolution, irradiated objects show the same behavior than the young isolated object (dotted curve in the left panel).

and $C_{\mathrm{n}'}^{\mathrm{m}'} = 0$ for $\mathrm{n}' \neq \mathrm{n}$ or $\mathrm{m}' \neq \mathrm{m}$[17].

In order to provide a numerical estimates of the response of an actual planet, I thus integrated these equations numerically on a full set of solar metallicity planetary models. The results are summarized in Fig. 3.2. *I find that the value of the Love number tends to decrease when mass increases mass above 1 M_Jup. This is due to the fact that more massive objects are (i) more compressible and thus more centrally condensed (See § 2.2.2), (ii) denser, with a larger surface gravity.* Below this mass, the k_2 of isolated objects also increases when mass decreases. This is expected as we slowly tend toward the incompressible limit ($\tilde{n} = 0$; see § 2.2.2) for which $k_2 = 3/2$, as shown in Appendix D.

For irradiated objects, however, the value of k_2 starts to shrink at lower masses. This has two causes. Most importantly, as already mentioned, irradiation retards the evolution. Like young isolated objects, irradiated planets are more centrally condensed and less subject to perturbation. In addition, as discussed in Chapter 2, the strong stellar irradiation heats up and thus slightly inflates the external layers of the body. While there is not much mass in this zone, this is where a perturbation has the most important effect[18].

---

[15]For Uranus and Neptune, measurements made by the various flyby missions are significant up to J_4, and up to J_6 for Jupiter and Saturn.

[16]Note, that the $k_\mathrm{n} = h_\mathrm{n} - 1$ holds only because our body is in hydrostatic equilibrium without any elastic stress.

[17] For a purely rotational distortion, $\mathbf{c}_2^0 = \omega_1^2/3$ implying $m_\mathrm{ext} = m_\mathrm{rot}/3$, and

$$J_2 = k_2\, m_\mathrm{ext} = \frac{k_2}{3} \frac{\omega_1^2 \bar{R}_1^3}{GM_1} = \frac{k_2}{3}\, m_\mathrm{rot}. \tag{3.35}$$

By extension, one can define J_2 for a tidal perturbation by a secondary of mass which leads to

$$J_2 = k_2\, m_\mathrm{tid} = -k_2 \frac{M_2}{M_1} \left(\frac{\bar{R}_1}{r_\star} \right)^3, \tag{3.36}$$

but the reference axis is the line connecting the two center of mass and not the rotational axis. Note that, in this case, J_2 is negative, because the body is elongated along the symmetry axis, and not flattened.

[18]In other words, like the gravitational moments, the Love number is more sensitive to the density distribution in the outer layers (Guillot 2005).

As shown in Fig. **3.3**, numerical simulations that I performed with my numerical code CHESS **also show that, at constant mass, a small enrichment in heavy elements toward the center (possibly in a core) acts to decrease the value of k_2.** In general, redistributing mass from the external to the internal layers, which are less sensitive to the disturbing potential, decreases the response of the body to an exciting potential, which translates into a lower k_2. **However, when the core is large enough to reach the outer layer of the body, k_2 starts to increase again.** Calculations are stopped around $M_c/M_1 \approx 0.96$ for numerical stability reasons. In principle, in the $M_c = M_1$ limit, k_2 should be larger than for the completely gaseous object as is hinted by the large slope. This is due to the fact that gas is much more compressible than ices or rocks. It will however not reach 3/2 value reached for truly incompressible matter[19] as the ANEOS equation of state does predict a small compressibility for high pressure "ices" (Thompson and Lauson 1972).

Figure 3.3: Love number as a function of the core mass for a 11 $M_\oplus$ planet, for various effective temperature (T_{int} from 20 to 120 K by steps of 20 K ; more and more spaced dashing).

While it is tempting to use these formula to compute, for example, the response of the deformable body to all the successive terms of the tidal disturbance and to add them linearly, one must be aware that this approach is not fully justified due to the fact that we have neglected all the cross correlation terms throughout the calculation. The precision that we would gain by adding the contribution of a higher harmonic would be lost by our poor description of the response to the lower order harmonics. Such cases require a higher order theory like the one presented in Appendix E. It is however perfectly justified to use this approach to compute the response of a body to a sum of disturbing potential having different axes of symmetry but being of the same importance. Such an example is presented hereafter.

3.2.3 Application to close binaries: Combined effect of tidal and rotational disturbances

Because our theory is linear, the calculation of the equilibrium shape of an object undergoing several different perturbations at the same time reduces to the problem of finding the response to each separate perturbing potential and adding them linearly[20]. However, if this seems correct to add Eqs. (3.35) and (3.36) to obtain the total J_2 of a body in a close binary, we must remember that the tidal and rotational deformations do not have the same axis of symmetry in general.

In order to correctly add these contribution, as presented in Leconte et al. (2011c), I thus had to carry out a change of coordinates. Taking θ as the colatitude and ϕ as the longitude of the body considered, the quadrupole moment of the external gravitational potential (Eq. (3.26)) in the linear approximation, is

---

[19]Because we intuitively picture incompressible objects as being solid (like terrestrial planets), it seems a little counter intuitive that k_2 reaches its maximum in this limit. We must remember, however, that this remains true only in the hydrostatic case, i.e. when the cohesion is ensured by gravity alone. For terrestrial planets, the elastic modulus of the bulk imposes a lower tidal response ($k_2 \approx 0.33$ for the Earth). This also reminds us that our formalism does not apply to such low mass terrestrial planets for which hydrostatic equilibrium is not fully achieved.

[20]This linear behavior as been verified with the analytical polytropic model of Lai et al. (1993) and Leconte et al. (2011c), for which calculating the response to a sum of perturbations or adding the response to each perturbation yields exactly the same result.

given at the surface by

$$-\frac{GM_1}{\bar{R}_1}\sum_{m=0}^{2}C_2^m Y_2^m(\theta,\phi) = k_2\bar{R}_1^2\left(\frac{\omega_1^2}{3}P_2^0(\cos\theta) - \frac{GM_2}{r_\star^3}P_2^0(\cos\theta')\right), \tag{3.37}$$

where θ' is the angle between the current point and the line connecting the two center of mass (also called the substellar point for a planet). For the coplanar case where the tides raising object orbits in the equatorial plane of the distorted body, $\cos\theta' = \sin\theta\cos\phi$ and thus

$$\begin{aligned}P_2^0(\cos\theta') &= \frac{3}{4}\sin^2(\theta)\cos(2\phi) + \frac{3\sin^2(\theta)}{4} - \frac{1}{2}\\ &= \frac{1}{4}\cos(2\phi)P_2^2(\cos\theta) - \frac{1}{2}P_2^0(\cos\theta).\end{aligned} \tag{3.38}$$

Thus

$$J_2 = -C_2^0 = k_2\left[\frac{1}{3}\frac{\omega_1^2\bar{R}_1^3}{GM_1} + \frac{1}{2}\frac{M_2}{M_1}\left(\frac{\bar{R}_1}{r_\star}\right)^3\right] = k_2\left[\frac{m_{\mathrm{rot}}}{3} - \frac{m_{\mathrm{tid}}}{2}\right], \tag{3.39}$$

and

$$C_2^2 = -k_2\frac{1}{4}\frac{M_2}{M_1}\left(\frac{\bar{R}_1}{r_2}\right)^3 = k_2\frac{m_{\mathrm{tid}}}{4}. \tag{3.40}$$

All the other moments are equal to 0. Similar decompositions can be used to infer the precise shape of the surface from a sum of perturbing fields. This gives

$$\frac{r(\bar{R}_1,\theta,\phi)}{\bar{R}_1} = 1 - h_2\left(\frac{1}{2}m_{\mathrm{tid}} + \frac{1}{3}m_{\mathrm{rot}}\right)Y_2^0(\theta,\phi) + \frac{h_2}{4}m_{\mathrm{tid}}Y_2^2(\theta,\phi), \tag{3.41}$$

and thus, at the surface,

$$\begin{aligned}\frac{a_1}{\bar{R}_1} &= 1 + h_2\left(\frac{m_{\mathrm{rot}}}{6} + \frac{7\,m_{\mathrm{tid}}}{4}\right),\\ \frac{a_2}{\bar{R}_1} &= 1 + h_2\left(\frac{m_{\mathrm{rot}}}{6} - \frac{5\,m_{\mathrm{tid}}}{4}\right),\\ \frac{a_3}{\bar{R}_1} &= 1 - h_2\left(\frac{m_{\mathrm{rot}}}{3} + \frac{m_{\mathrm{tid}}}{2}\right).\end{aligned} \tag{3.42}$$

Note that to use these relations, one must already know the *mean* radius of the object. In general, if rotation is present, this requires to solve numerically the hydrostatic equilibrium of the body for each value of the rotational perturbation (m_{rot}), and is thus very computationally intensive. *To overcome this limitation, when a high precision is not needed, we can however rely on a completely analytical model such as the one that I will describe in § 3.4, and use in § 3.5 (Leconte et al. 2011c).*

3.3   Gravitational sounding of extrasolar planets

As already mentioned in § 2.4.4, characterizing precisely the composition of a giant planet requires many parameters. In addition, because the large thermal expansion coefficient of the gas cannot be neglected, the age of the object must also be known, and *this degeneracy prevents a precise determination of the composition from the position of the planet in the mass-radius diagram alone* (Adams et al. 2008). However, we can still roughly constrain the composition from the knowledge of (M_1, R_1, t) if

- we reduce the parameter space describing the composition of the planet (e.g. by assuming the object to be composed of a Solar abundance H/He gaseous mixture surrounding a homogeneous core of a given material).

- we assume that no bloating mechanism is at work (see § 2.4.4 for details).

If one wants to go further and relax one or the other of these assumptions, new observables must be measured. As will be detailed in Chapter 4, in the Solar System, these additional constraints are provided by *in situ* measurements of the composition and atmospheric thermal profile, and the determination of the gravitational moments (J_2, J_4, ...). While it was thought that such measurements would remain out of reach for exoplanets, it has been shown that tides in the planet (whose amplitude is proportional to k_2) can lead to characteristic quasi-equilibrium orbital states in multi-planet systems (Mardling 2007), and transit timing variations (Ragozzine and Wolf 2009), making possible the determination of k_2.

In particular, as discussed by Ragozzine and Wolf (2009), values of the Love number on the order the one found in § 3.2.2 could be measured through the precession rate of very Hot Jupiters on eccentric orbits. Such measurements could be carried out by *Kepler* for WASP-12 b analogs with an eccentricity $> 3 \times 10^{-4}$ (most favorable case) or Tres-3 b analogs with an eccentricity $> 2 \times 10^{-3}$ (for $k_2 \approx 0.3$) and lower eccentricities for higher Love number values, and should reach a precision of a few percents. On the other side, if the accuracy of the method proposed by Mardling (2007) is limited if the distant companion is not transiting, With 170 multi-transiting planet system candidates announced recently by Borucki et al. (2011), our ability to measure exoplanets tidal response should soon reach an unprecedented precision.

(a) k_2 maps

(b) M_c constraints
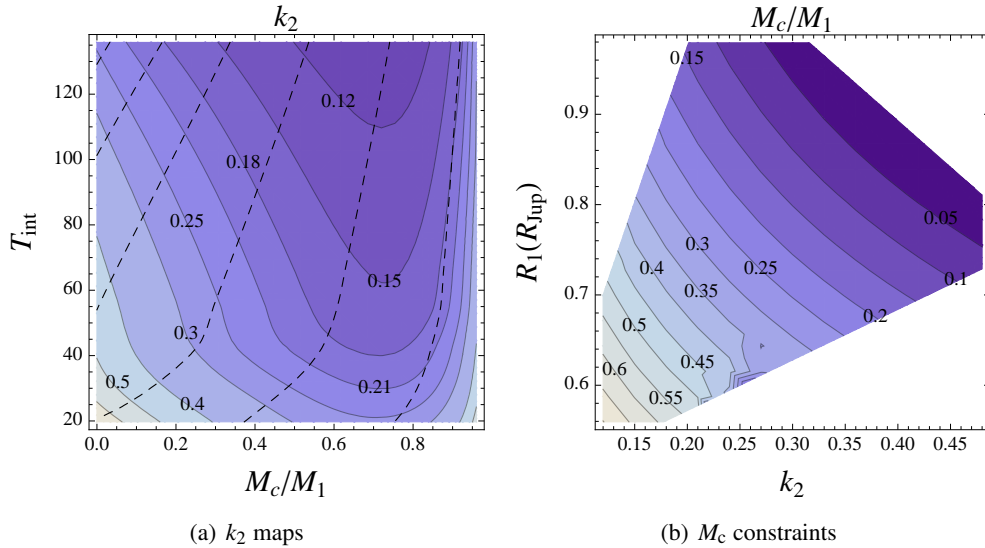
Figure 3.4: (a) Mapping of the Love Number as a function of the effective temperature (T_{int}) and mass of a water core (M_c) for a Neptune mass planet. The dashed lines are the iso-radii curves. (b) Mass fraction of water core (M_c/M_1) retrieved for a given (R_1, k_2). The parameter space that is not covered by the grid is left blank.

While this is only a *work in progress*, in Fig. 3.4, I attempt to outline the possible yields of a measurement of k_2 on our knowledge of an exoplanet structure. **In this example, I relax the assumption on the evolution while still considering a simple 2-layer planetary model.** The planet structure is then entirely determined by three parameters, namely its mass, effective temperature and core mass fraction. **I thus used my numerical code to compute a large grid of structure models covering this parameters**

space and estimate several mechanical characteristics of the object modeled, such as the radius and k_2. Fig. 3.4.a shows an example of such maps for a Neptune mass planet.

Because iso-radii and iso-k_2 contours are not parallel in most of the parameter space, the knowledge these two quantities makes the determination of both T_{int} (constraining the age of the object) and M_c/M_1 possible (as shown in Fig. 3.4.b, where only the core mass is shown). For large core masses, however, both contours follow the same direction. This is because the thermal expansion coefficient of the core is much smaller than the one of the envelope, as can be inferred from the fact that iso-radii curves are mostly vertical in Fig. 3.4.a. The structure only weakly depends on T_{int} and, as a result, this parameter cannot be retrieved. On the other hand, in this limit, the core mass fraction can more easily be linked to the mean density.

Then, ultimately, it will be possible to include additional constraints, such as the age of the system, to get more information about the internal composition. Of course, let us conclude by noting that, because of the highest number of free parameters in the final, more realistic model, and of the observational uncertainties, such constraints on the interior composition will have to be inferred in a statistical sense.

3.4 An analytical model: ellipsoidal polytropes

As mentioned in § 3.2.3, one of the limitations of the numerical approach developed previously is that the final *mean* radius cannot be computed from the spherical equilibrium radius by these relations alone. This is particularly critical when one is interested in predicting the absolute radius that an observed object would have if it were isolated and at rest. Indeed, this is the *equilibrium radius R_1* that needs to be compared to the output of evolutionary codes when, for example, trying to quantify the radius anomaly of observed transiting planets.

To overcome that limitation, in Leconte et al. (2011c), I modeled giant planets by self similar ellipsoidal polytropes, as first done by Lai et al. (1994) for white dwarfs and neutron stars, **and showed that this analytical model yields rather accurate results provided that the effective polytrope index of the object ($\tilde{n}$; see § 2.2.2) be known.** This theory is based on the minimization of the total energy of the binary

$$E_{tot} = U_1 + U_2 + W_1 + W_2 + T + W_{1 \rightleftarrows 2}, \tag{3.43}$$

where U and W are the internal and self gravitational energy of each component, T is the total kinetic energy (including both the orbital motion and the spin of each object), and $W_{1 \rightleftarrows 2}$ the gravitational interaction between the objects.

As this total energy can be easily expressed as a function of both the shape and the mean radius, the minimum energy principle directly yields an approximate formula for these. In addition, because it is easy to cut off the perturbation in these formulae, we also have access to the *equilibrium radius (R_1)*. As shown in Lai et al. (1994), to first order in m_{rot} and m_{tid}[21]

$$\frac{a_1}{R_1} = 1 + \frac{1}{4}\frac{5+\tilde{n}}{3-\tilde{n}}q_{\tilde{n}}m_{rot} + \frac{5}{2}q_{\tilde{n}}m_{tid}$$

$$\frac{a_2}{R_1} = 1 + \frac{1}{4}\frac{5+\tilde{n}}{3-\tilde{n}}q_{\tilde{n}}m_{rot} - \frac{5}{4}q_{\tilde{n}}m_{tid}$$

$$\frac{a_3}{R_1} = 1 - \frac{1}{2}\frac{5-3\tilde{n}}{3-\tilde{n}}q_{\tilde{n}}m_{rot} - \frac{5}{4}q_{\tilde{n}}m_{tid}, \tag{3.44}$$

---

[21]To first order, it is equivalent to use the *mean* or the *equilibrium* radius in defining m_{rot} (or m_{tid}).

where $q_{\tilde{n}}$ is a function of the polytropic index defined in Leconte et al. (2011c). This implies that

$$\frac{\bar{R}_1}{R_1} = 1 + \frac{2}{3}\frac{\tilde{n}}{3-\tilde{n}} q_{\tilde{n}} m_{\text{rot}} \qquad (3.45)$$

As expected, to first order, the tides do not change the volume (and thus the mean radius $\bar{R}_1 = \sqrt[3]{a_1 a_2 a_3}$) of our ellipsoid, and only the rotation has a net effect. As expected, the volume variation also vanishes for an incompressible object ($\tilde{n} = 0$).

While these expressions necessitate a stronger level of approximation than the mere hydrostatic equilibrium used in the complete theory of figures, **I have shown in Leconte et al. (2011c) that, considering our poor knowledge of the metal enrichment of extrasolar gas giant planets (particularly about the presence or not of a differentiated central core), such a simplified model is satisfactory to infer the impact of the shape of close-in exoplanets on their transit light-curve, as done below.** *In addition, these formulae are more accurate than the one yielded by a Roche approximation, as the retroaction of the distortion of each body on the gravitational field is taken into account* (Zahn et al. 2010).

3.5 Distorted exoplanets: Implications for observations

Because the tidal bulge raised by a star on its low mass companion is aligned with respect to the axis joining the two objects, when planet transits across the stellar disc, we expect to see the *smaller* cross section of its actual ellipsoidal shape so that the depth of the transit is *decreased* with respect to the expected signal for a spherical object. *This implies that the radius inferred from the light curve analysis, derived under the assumption of spherical planet and star, should **underestimate** the real equilibrium radius of the object.* This bias needs to be corrected for a proper comparison with theoretical 1D numerical simulations of the structure and evolution of extrasolar planets and enhances the actual discrepancy between theory and observation for the so called "bloated" planets. **This is why, in the following section, I will quantify the impact of the non sphericity of the planet and star on the depth of the light curve, and the resulting bias on the radius determination.**
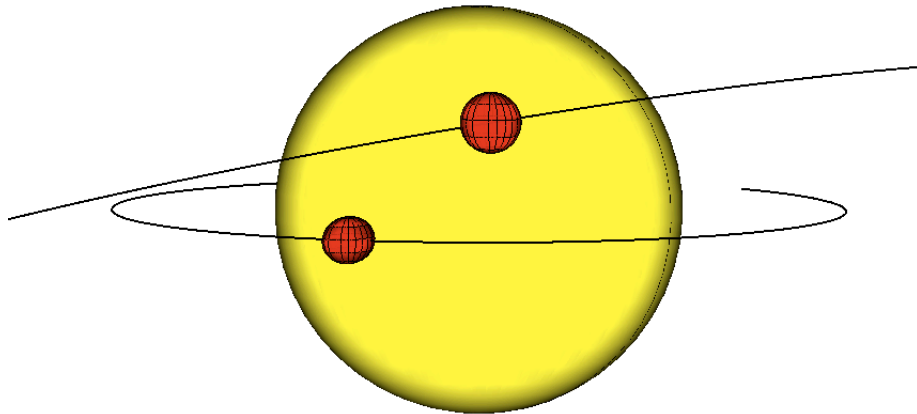
Figure 3.5: Schematic representation of the impact of the non-spherical shape of the planet on its cross section. For the same equilibrium radius, the close in planet is seen smaller during transit.

3.5.1 Transit depth variation

When limb darkening is ignored, the depth of a transit is given by the ratio of the planetary and stellar projected areas. When both bodies are spherical, this simply reduces to $\delta L_\star / L_\star \propto (R_p / R_\star)^2$. For close-in planet-star systems, however, both tidal and rotational deformations yield a departure from sphericity, so that what is measured is no longer the mean radius but an *effective* "transit radius" defined such that the cross section of the planet is equal to $\pi R_{tr,p}^2$ and similarly for the star. Thus the transit depth reads

$$\frac{\delta L_\star}{L_\star} = \left(\frac{R_{tr,p}}{R_{tr,\star}} \right)^2. \tag{3.46}$$

In general, the projected area of an ellipsoid can be computed for any orientation and then at each point of the orbit, as demonstrated in Appendix F. Figure 3.6 shows the projected area of the planet ($\pi R_{tr,p}^2$) as a function of its anomaly (ϕ) normalized to the spherical case (πR_p^2). When the planet is seen from its "side" ($\phi/\pi = 0.5$), the observer sees a bigger planet because the rotation of the latter on itself tends to increase its volume. The possibility to measure these effects from the light curve is discussed in Ragozzine and Wolf (2009) and Carter and Winn (2010a).
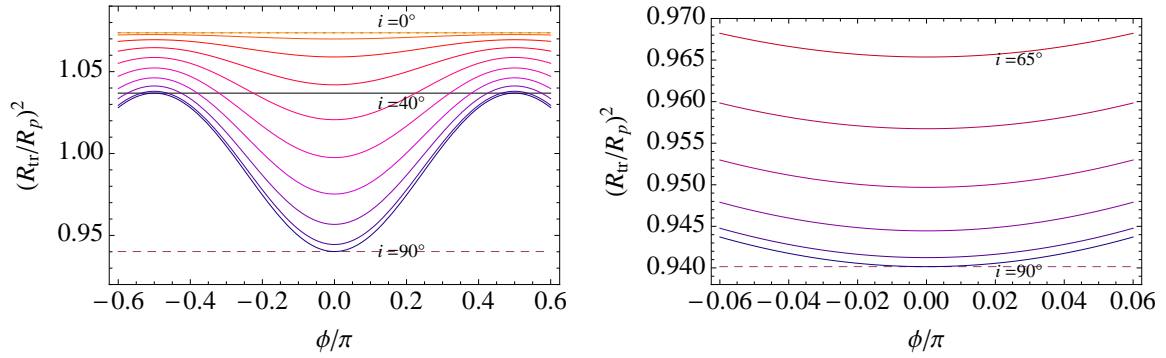
Figure 3.6: Normalized projected area of the planet as a function of its anomaly (ϕ) for inclinations of the orbit going from $i = 90°$ to $i = 0°$ by steps of $10°$ for a WASP-12 b analog on a circular orbit. Top: For the full orbit. Bottom: zoom on the (primary or secondary) transit (i changes by steps of $5°$). The ordinates of the dotted, solid and dashed horizontal lines are respectively $a_1 a_2 / R_p^2$ (face-on orbit), $a_1 a_3 / R_p^2$ and $a_2 a_3 / R_p^2$. *Revised figure from Leconte et al. (2011c).*

For the simple case of an edge-on orbit at mid transit ($\phi = 0$), since the observer, the planet and the star are aligned with the long axis of the tidally deformed ellipsoid[22,23], $R_{tr,p} = \sqrt{a_{2,p} a_{3,p}}$ and $R_{tr,\star} = \sqrt{a_{2,\star} a_{3,\star}}$ (see § 3.1.5 for the definition of the a_i). Therefore,

$$\frac{\delta L_\star}{L_\star} = \frac{a_{2,p} a_{3,p}}{a_{2,\star} a_{3,\star}} \equiv \left(\frac{R_p}{R_\star} \right)^2 \cdot (1 + \text{TDV}), \tag{3.47}$$

where R_p and $R_\star$ are the respective radii the planet and the star would have in spherical equilibrium (the R_1 defined above) and TDV *is by definition the transit depth variation induced by the ellipsoidal shape*

---

[22]This is still verified to first order in ϕ and $i - \frac{\pi}{2}$ as only second order terms appear.

[23]In the following, the variables have the same meaning as earlier with p indices when referring to the planet and $\star$ to the star

of the components relative to the transit depth in the spherical case. This is given by

$$\text{TDV} = \frac{a_{2,\text{p}} a_{3,\text{p}}}{R_\text{p}^2} \frac{R_\star^2}{a_{2,\star} a_{3,\star}} - 1, \tag{3.48}$$

where the a_i/R_1 are given by Eq. (3.44) which depend (through $m_{\text{rot,p}}$ and $m_{\text{rot},\star}$) on $r_\star$, ω_p and $\omega_\star$. However, most of the planet hosting stars have a low rotation rate compared to the orbital mean motion. This entails that the rotational deformation is negligible compared to the tidal one and can generally be neglected. As discussed in Chapter 5, hot Jupiters should be pseudo synchronized early in their evolution[24]. Therefore, we will assume such an approximation in our calculations in order not to introduce any other free parameter. Under such an approximation,

$$\text{TDV} = -\frac{1}{3} q_\text{p} (1+p) m_{\text{rot,p}} \left[\frac{5}{4} \left(\frac{7+p}{1+p} \right) - \left(\frac{4\tilde{n}_\text{p}}{3-\tilde{n}_\text{p}} \right) \right]$$
$$+ \frac{5}{2} q_\star p \frac{R_\star^3}{r_\star^3}, \tag{3.49}$$

where the parameter p now denotes the mass ratio $M_\text{p}/M_\star$, and q_p and $q_\star$ are equal to q_n for $\tilde{n} = \tilde{n}_\text{p}$ and $\tilde{n} = \tilde{n}_\star$, respectively. The first line in the above equation represents the contribution of the planet, which is always negative (for reasonable values of $\tilde{n}_\text{p}$). Our line of sight follows the long axis of the tidal bulge and we see the minimal cross section of the ellipsoid.

The contribution of the star is positive and, in most cases, negligible compared the planet's contribution because

$$\frac{R_\star^3}{R_\text{p}^3} \frac{p^2}{1+p} \ll 1,$$

for a typical system (10^{-3} for a Jupiter-Sun like system). As a consequence, the results presented hereafter do not depend on $q_\star$ as long as realistic values of $\tilde{n}_\star \in [1.5, 3]$ are taken.

Figure 3.7 portrays the relative transit depth variation computed with Eq. (3.49) for several planet masses as a function of the orbital distance, for a Sun-like parent star. While I computed all the curves for an age of 1 Gyr, they do not change much for older ages because both the radii and the polytropic indices remain nearly unchanged after 1 Gyr (see Fig. 2.7). Given the accuracy of the radius determination achieved by the latest observations (1 to 10%), **the transit depth variation is significant for Saturn mass objects ($M_\text{p} \approx M_{\text{Jup}}/3$) closer than 0.04 AU and Jupiter mass objects closer than 0.02-0.03 AU.** Because the equations are derived to first order, the value of TDV derived from the analytical model should be taken with caution when TDV $\gtrsim 0.1 - 0.3$ (and are clearly not meaningful for TDV $\gtrsim 1$). In this regime, corresponding to the upper left region of Fig. 3.7, one should use the theory of planetary figures to higher order, but then numerical calculations become necessary, loosing the advantage of our simple analytical expressions.

Figure 3.7 also displays the transit depth variation computed for the most distorted known transiting exoplanets, with the observationally measured parameters. The error bars reflect the uncertainties in the model and in the measured data.

3.5.2 Radius determination bias

Unfortunately, transit measurements only give access to the projected opaque cross section of the planet ($\equiv \pi R_{\text{tr,p}}^2$) defining a "transit radius" which depends on the shape of the planet, its orientation

---

[24] If the rotation of the object is synchronous with the orbit, then $\omega_1^2 = G(M_1+M_2)/r_\star^3$, and $m_{\text{rot}} = (1+M_1/M_2)m_{\text{tid}}$.
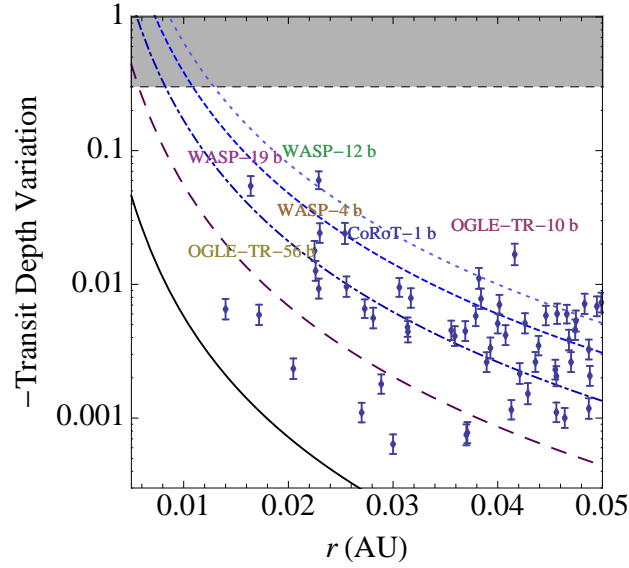
Figure 3.7: Relative transit depth variation TDV computed with Eq. (3.49) as a function of the semi-major axis at 1 Gyr for planets of mass: $0.3M_{\text{Jup}}$ (dotted), $0.5M_{\text{Jup}}$ (dashed), $1M_{\text{Jup}}$ (dash-dotted), $3M_{\text{Jup}}$ (long dashed), $15M_{\text{Jup}}$(solid). The shaded area shows the zone where higher order terms become non-negligible. The decrease of the transit depth due to tidal interactions is smaller when the mass of the planet increases because massive objects are denser and more compressible (see §4) and thus less subject to non-spherical deformations. *Figure from Leconte et al. (2011c).*

during the observation and the wavelength used. To convert this transit radius inferred from the observations ($R_{\text{tr,p}}$) to the spherical radius (R_{p}) - that can be compared to 1D numerical models - one must eliminate $\delta L_\star / L_\star$ from Eqs. (3.46) and (3.47). As shown above, the stellar impact on TDV is negligible compared to the planet's contribution ($R_{\text{tr},\star} \approx R_\star$). Then, using the first term in Eq. (3.49) and expanding the expression giving the definition of $R_{\text{tr,p}}$, one gets

$$R_{\text{p}} \approx R_{\text{tr,p}} \cdot \left(1 - \frac{\text{TDV}}{2} \right). \tag{3.50}$$

For the most distorted known planets, the relative variation between the transit radius and the equilibrium radius

$$\Delta R / R \equiv (R_{\text{p}} - R_{\text{tr,p}}) / R_{\text{tr,p}} \approx -\text{TDV}/2$$

is positive and amounts to 3.00% for WASP-12 b, 2.72% for WASP-19 b, 1.21% for WASP-4 b, 1.20% for CoRot-1 b, 0.89% and OGLE-TR-56 b [25].

To conclude, through this analysis, I showed that the departure from sphericity of the transiting planets produces a distortion of their transit light curves from which many of their parameters

---

[25]Of course, since TDV $\propto (R_{\text{p}}/r_\star)^3$, Eq. (3.50) is an implicit equation on R_{p}. To obtain R_{p} to the sought accuracy, a perturbative development in powers of $\text{TDV}_{\text{tr}} = \text{TDV}(R_{\text{p}} = R_{\text{tr,p}})$ can be obtained using recursively Eq. (3.50)

$$\frac{R_{\text{p}}}{R_{\text{tr,p}}} \approx 1 - \frac{\text{TDV}(R_{\text{p}})}{2} \approx 1 - \frac{\text{TDV}_{\text{tr}}}{2} + \frac{3\,\text{TDV}_{\text{tr}}^2}{4} - \frac{3\,\text{TDV}_{\text{tr}}^3}{2} + \mathcal{O}(\text{TDV}_{\text{tr}}^4). \tag{3.51}$$

However, terms of order TDV_{tr}^2 are of the same order than the second order corrections to the shape that we have neglected throughout.

are measured. In particular, the radius inferred from the light curve analysis always underestimates the real equilibrium radius, possibly by up to 5% for the closest planets detected so far ($\lesssim 0.05$ AU), enhancing the aforementioned radius anomaly.

3.6 Conclusion

Because of the large variety of exoplanetary systems presently discovered, with many more expected in the near future, and the increasing accuracy of the observations, it is important to take into account the changes in the dynamical and observable properties of exoplanets arising from their non-spherical deformation, due to rotational and/or tidal forces. Indeed, such deformations not only yield a decrease of the transit depth, but also perturbs the orbital evolution of the system, possibly leading to a measurement of the tidal response. In order to correct for, or take advantage of these properties, it is primordial to be able to compute either *numerically* (§ 3.2) or *analytically* (§ 3.4 ; see also Leconte et al. 2011c) the shape and potential of planets and stars in any configuration from the knowledge of only their mass, orbital separation and one single parameter describing their internal structure (either the *Love number k_2*, or the *effective polytropic index*, $\tilde{n}$, that was discussed in Chapter 2). *The main problem being to have an accurate value for one or the other of these quantities.*

To that purpose, I performed numerical simulations to calculate the *Love number* of substellar object for a wide range of masses (from a saturn mass to the Hydrogen burning minimum mass), ages and irradiations. As for the determination of the effective polytropic index in Chapter 2, the inferred values of k_2 presented in § 3.2 give us insight on the way the mechanical structure of gaseous substellar objects changes with age and mass. **Using my numerical code CHESS, I also started to investigate the impact of heavy element enrichment on the tidal response of giant planets, and demonstrated on a test case how one could take advantage of these models to infer a core mass from k_2 measurements (§ 3.3).**

In § 3.4, I showed however that, inferring the absolute *mean* radius of a given object from its equilibrium radius cannot be done with the knowledge of k_2 alone, but that this limitation can be overcome with an analytical model based on homologously distorted polytropes (Leconte et al. 2011c). I find that this analytical model can easily be used to determine the impact of the absolute shape of the planet on its phase curve and on the shape of the transit light curve itself (Carter and Winn 2010a). It can also be used to model ellipsoidal variations of the stellar flux that are now detected in the CoRoT and Kepler light curves (Welsh et al. 2010).

Finally, in § 3.5, using this analytical model, I also showed that departure from sphericity of the transiting planets produces a bias in the determination of the radius. For the closest planets detected so far ($\lesssim 0.05$ AU), the effect on the transit depth is of the order of 1 to 10% (see Fig. 3.7), by no means a negligible effect. The equilibrium radius of these strongly distorted objects can thus be larger than the measured radius, inferred from the area of the (smaller) cross section presented to the observer by the planet during the transit. Combining the analytical formulae presented in Leconte et al. (2011c), and the characteristic polytropic index values derived in § 2.2.2 for various gaseous planet masses and ages, allows to easily take such a correction into account. Interestingly, since this equilibrium radius is the one computed with the 1D structure models available in the literature, the bias reported here still enhances the magnitude of the puzzling radius anomaly (see Fig. 2.10) exhibited by the so-called bloated planets.

Chapter 4

A new perspective on heat transport in the interior

Contents

While conventional interior models for Jupiter and Saturn are based on the simplistic assumption of a solid core surrounded by a homogeneous gaseous envelope, in this chapter, I derive new models with an inhomogeneous distribution of heavy elements, i.e. a gradient of composition, within these planets. Such a compositional stratification hampers large scale convection which turns into double-diffusive convection, yielding an inner thermal profile which departs from the traditionally assumed adiabatic interior, affecting these planet heat content and cooling history.

To address this problem, after a brief review of the onset of the double diffusive instability in § 4.1, I develop an analytical formalism of layered double-diffusive convection based on the mixing length theory, and derive analytical asymptotic solutions for the convective efficiency and the super-adiabaticity in the medium (§ 4.2). By simple considerations, I also derive analytical constraints on the range of possible values for the size of the convective/diffusive cells (§ 4.3).

Then, in § 4.5, I apply this formalism to Solar System giant planet interiors. These models satisfy all observational constraints and yield a metal enrichment for our gaseous giants up to 30 to 60% larger than previously thought. As the heavy elements tend to be redistributed within the gaseous envelope, the models predict smaller than usual central cores inside Saturn and Jupiter, with possibly no core for this latter.

These models open a new window and raise new challenges on our understanding of the internal structure of giant (solar and extrasolar) planets, in particular the determination of their heavy material content, a key diagnostic for planet formation theories.

The results of this chapter have been accepted for publication in *A new vision on giant planet interiors: The role of double diffusive convection* (Leconte and Chabrier 2012).

Traditionally, GIANT PLANET MODELS have always been based on two major specific assumptions concerning their inner profile, essentially for reasons of simplicity in the planet's modeling (see e.g. Stevenson 1985). It is conventional to assume (i) that the inner structure of our giants consists of a few - generally 2 to 3 - superposed, well separated, *homogeneous* regions, namely, going from the planet's center to the surface, a central solid rocky/icy core, and a surrounding largely dominantly H/He gaseous envelope, often split into an inner metallic region and an outer atomic/molecular one ; the more dense components are always supposed to have quickly settled into the central core under the action of gravity ; (ii) that planetary interiors are adiabatic, based on the fact that the giant planet heat flow must be transported by convection (Hubbard 1968). All the present determinations of the internal - chemical, mechanical and thermal - structures of the Solar system planets, including their heavy material content, are derived assuming such homogeneously stratified, adiabatic interiors (Saumon and Guillot 2004 ; Fortney and Nettelmann 2010).

Giant planet interiors, however, might depart from this conventional, simplified description, because of complex processes for which we lack an accurate description but which may very well be at play in real situations (Stevenson 1985). In this paper, we derive interior models for Jupiter and Saturn which relax the aforementioned preconceptions. Instead of the homogeneous layer assumption, we explore the possibility of a mixed, *inhomogeneous* solid-gas interior composition, leading to a heavy material gradient throughout the planet. This in turn tends to suppress large scale convection which, due to the double diffusive instability (see § 4.1), can turn into either turbulent enhanced diffusion or layered convection. As both these heat transport mechanisms are fairly inefficient compared to usual convection, this compositional gradient thus leads to significant departure from global adiabaticity in the interior. As shown below, these models do fulfill the planet observational constraints while leading to (i) a significantly larger metal content and (ii) significantly larger internal temperatures than the one inferred from homogeneously stratified adiabatic models.

This opens a new vision on planet structure, evolution and formation efficiency. Such inhomogeneous interior profiles for Solar System giant planets had briefly been suggested several decades ago by Stevenson (Stevenson 1985) but no attempt has ever been made to derive consistent models and to verify whether such models would be consistent with the planet various observational constraints. This scenario has been revived recently in the context of extrasolar planets and has been shown to provide a possible or at least complementary explanation for the anomalously large observed radii of many of these bodies (Chabrier and Baraffe 2007). Indeed, as mentioned above, not only an inhomogeneously stratified interior yields a different interior structure and global metal content, but it decreases heat transport efficiency throughout the planet's interior and thus affects its cooling, thus its mass-radius relationship at a given age, a crucial diagnostic to understand (transiting) extrasolar planet structure and evolution. Since, as mentioned earlier, only loose constraints on the object's internal composition are accessible for gaseous exoplanets, it is crucial to verify whether such unconventional internal structures are a viable possibility for our own giants. Furthermore, determining the maximum possible amount of heavy elements in Jupiter and Saturn and their distribution within the planet are important diagnostics to understand how our own Solar System giants formed.

4.1   The double diffusive instability

In order to introduce the various relevant quantities in a simple way, I first derive the criterion for the presence of overturning convection and the onset of the double diffusive instability.

4.1.1   Adiabatic criterion

It is well known that, when thermal diffusivity and viscosity can be neglected, an homogeneous medium is stable against convective motion if the *Schwarzschild* stability criterion (or *Schwarzschild Härm* criterion) is fulfilled, i.e. if

$$\boxed{\nabla_{\mathrm{ad}} > \nabla_T,}$$
(4.1)

where $\nabla_T \equiv \frac{\mathrm{d}\ln T}{\mathrm{d}\ln P}$ is the thermal gradient, and $\nabla_{\mathrm{ad}} \equiv \left.\frac{\partial \ln T}{\partial \ln P}\right|_{\mathrm{ad}}$ is called the adiabatic gradient. However, concerning the criterion to use in presence of a compositional gradient, there is still a debate. If Schwarzschild and Härm (1958) proposed to keep on with the *Schwarzschild stability criterion*, Sakashita and Hayashi (1959), for example, suggested a new criterion, initially proposed by Ledoux (1947), stating that the (destabilizing) super adiabaticity in the medium must be large enough to counteract the stabilizing effect of a mean molecular weight gradient. In mathematical terms, the *Ledoux* criterion reads

$$\boxed{\nabla_{\mathrm{ad}} > \nabla_T - \frac{\alpha_\mu}{\alpha_T}\nabla_\mu} \quad \text{or} \quad \boxed{\nabla_{\mathrm{ad}} - \frac{\chi_\mu}{\chi_T}\nabla_\mu > \nabla_T,}$$
(4.2)

where $\alpha_T \equiv -\left.\frac{\partial \ln \rho}{\partial \ln T}\right|_{P,\mu}$, $\alpha_\mu \equiv \left.\frac{\partial \ln \rho}{\partial \ln \mu}\right|_{P,T}$, $\chi_\mu \equiv \left.\frac{\partial \ln P}{\partial \ln \mu}\right|_{T,\rho}$ and $\chi_T \equiv \left.\frac{\partial \ln P}{\partial \ln T}\right|_{\rho,\mu}$[1]. In general, areas which are both *Ledoux stable* and *Schwarzschild unstable* are called *semi-convective* zones. If no convective mode can seem to grow in these zones in our basic picture, it is not so when finite thermal and solute diffusivities are taken into account. Our modeling is too simple. We thus have to rely on a more complex stability analysis.

4.1.2   General linear stability analysis of the double diffusive instability

To have a better description of the onset of the double diffusive instability, we will carry a linear analysis similar to the one described by Stern (1960) ; Stevenson (1979a). For brevity, as we will only consider a mono dimensional approach of convection, we will not concern ourselves with rotation or magnetic field, even if these two ingredients have a significant influence on convection (Busse 1976). We consider an infinite medium in a rotating frame in which the unperturbed state is at rest. The mean field is characterized by a uniform gravity field **g**. The velocity, pressure, temperature and density perturbations are denoted by $\delta\mathbf{v}$, δp, δT and $\delta\rho$. In addition, we can have a chemical composition perturbation, $\delta\mu$. In practice, $\delta\mu$ can be the mean molecular weight change due to a chemical concentration change (and not due to ionization which is already taken into account into the equation of state) or the mass fraction of the constituent under consideration, but any other dimensionless parameter describing the chemical

---

[1]For a perfect gas, all these thermodynamic derivatives are equal to 1 (except $\chi_\mu = -1$). In the following, this is the values that we will use in our numerical examples when needed.

composition can be used. The linearized Boussinesq equations are then

$$\nabla \cdot \delta \mathbf{v} = 0, \tag{4.3}$$

$$\partial_t \delta \mathbf{v} = -\frac{1}{\rho} \nabla \delta p + \frac{\delta \rho}{\rho} \mathbf{g} + \nu \nabla^2 \delta \mathbf{v}, \tag{4.4}$$

$$\partial_t \delta T = \kappa_T \nabla^2 \delta T + \delta \mathbf{v} \cdot \hat{\mathbf{z}} (\nabla_T - \nabla_{\rm ad}) \frac{T}{H_P}, \tag{4.5}$$

$$\partial_t \delta \mu = D \nabla^2 \delta \mu + \delta \mathbf{v} \cdot \hat{\mathbf{z}} \nabla_\mu \frac{\mu}{H_P}. \tag{4.6}$$

D, κ_T and ν are the solute, thermal and cinematic viscosities (or diffusivities, in $m^2 s^{-1}$). $\hat{\mathbf{z}}$ is the vertical unit vector directed upward (such as $\mathbf{g} = -g\hat{\mathbf{z}}$), and $H_P \equiv -\frac{\mathrm{d}z}{\mathrm{d}\ln P}$ is the pressure scale height. A closure equation is provided by the equation of state which yields for the density perturbation

$$\frac{\delta \rho}{\rho} = \left(\alpha_\mu \frac{\delta \mu}{\mu} - \alpha_T \frac{\delta T}{T} \right). \tag{4.7}$$

Let us search for plane waves solutions of the form $\delta \mathbf{v} \propto e^{i\mathbf{k}\cdot\mathbf{r}+\sigma t}$, and introduce it in the previous equations[2]. After some vectorial algebra, this yields

$$\mathbf{k} \cdot \delta \mathbf{v} = 0, \tag{4.8}$$

$$(\sigma + \nu k^2)\delta \mathbf{v} = -i\frac{\mathbf{k}}{\rho}\delta p + \frac{\delta \rho}{\rho}\mathbf{g}, \tag{4.9}$$

$$\delta T = \frac{(\nabla_T - \nabla_{\rm ad})}{\sigma + \kappa_T k^2} \frac{T}{H_P} \delta \mathbf{v} \cdot \hat{\mathbf{z}}, \tag{4.10}$$

$$\delta \mu = \frac{\nabla_\mu}{\sigma + D k^2} \frac{\mu}{H_P} \delta \mathbf{v} \cdot \hat{\mathbf{z}}. \tag{4.11}$$

Eliminating all the variables but the velocity perturbation and taking the cross product of Eq. (4.9) with $\mathbf{k}$ we have

$$\left(\sigma + \nu k^2\right)\mathbf{k} \times \delta \mathbf{v} = \frac{\delta \rho}{\rho}\left(\mathbf{k} \times \mathbf{g}\right). \tag{4.12}$$

Defining the following frequencies[3] $\boxed{N_T^2 \equiv \frac{g}{H_P}\alpha_T\left(\nabla_T - \nabla_{\rm ad}\right)}$ and $\boxed{N_\mu^2 \equiv \frac{g}{H_P}\alpha_\mu\nabla_\mu\,,}$ we get

$$\left(\sigma + \nu k^2\right)\mathbf{k} \times \delta \mathbf{v} = \left(\frac{N_T^2}{\sigma + \kappa_T k^2} - \frac{N_\mu^2}{\sigma + D k^2}\right)(\delta \mathbf{v}\cdot\hat{\mathbf{z}})(\mathbf{k}\times\hat{\mathbf{z}}). \tag{4.13}$$

This rewrites $\mathbb{A}\cdot\delta\mathbf{v} = 0$ with

$$\mathbb{A} = (\sigma + \nu k^2)\begin{pmatrix} 0 & -k_z & k_y\left(1 - \frac{\left(\frac{N_T^2}{\sigma+\kappa_T k^2} - \frac{N_\mu^2}{\sigma+Dk^2}\right)}{\sigma+\nu k^2}\right) \\ \\ k_z & 0 & -k_x\left(1 - \frac{\left(\frac{N_T^2}{\sigma+\kappa_T k^2} - \frac{N_\mu^2}{\sigma+Dk^2}\right)}{\sigma+\nu k^2}\right) \\ \\ -k_y & k_x & 0 \end{pmatrix}. \tag{4.14}$$

---

[2]Note that, with this definition, if σ is real and positive (negative), the perturbation grows (is damped) exponentially. If σ is complex, the perturbation oscillates, but its amplitude can still grow if the real part, $\mathrm{Re}(\sigma)$ is positive. In the following, the term *growth rate* will refer to $\mathrm{Re}(\sigma)$.

[3]But remembering that this refers to a true frequency only if $N_T^2 < 0$. In this case, $N_T = iN_{\rm BV}$ where $N_{\rm BV}$ is the well known Brunt-Väisälä frequency.

Finally **Det** $\mathbb{A} = 0$ yields the dispersion relation

$$\sigma + vk^2 = \frac{k_\perp^2}{k^2} \left(\frac{N_T^2}{\sigma + \kappa_T k^2} - \frac{N_\mu^2}{\sigma + Dk^2} \right), \tag{4.15}$$

where $k_\perp$ is the horizontal part of the wave vector ($k_\perp = k_x + k_y$). It can be shown that, in this case, the most unstable mode always occurs when the vertical wavenumber is equal to zero, i.e. when $k_\perp = k$ (Walin 1964). This corresponds to an elevator mode, which is not surprising as all the forcing follows the vertical direction. Then restricting ourselves to this case, we get

$$\boxed{(\sigma + vk^2)(\sigma + \kappa_T k^2)(\sigma + Dk^2) - N_T^2(\sigma + Dk^2) + N_\mu^2(\sigma + \kappa_T k^2) = 0.} \tag{4.16}$$

There are several possibilities to non-dimensionalize this equation. Anticipating the length scale of the fastest growing modes, we will use the thermal diffusion scale

$$d = \sqrt{\kappa_T / N_T}, \tag{4.17}$$

and the diffusion time, $d^2/\kappa_T = N_T^{-1}$. Then using $k = \tilde{k}/d = \tilde{k}\sqrt{N_T/\kappa_T}$ and $\sigma = N_T\tilde{\sigma}$, we get

$$\boxed{(\tilde{\sigma} + \tilde{k}^2)(\tilde{\sigma} + Pr\,\tilde{k}^2)(\tilde{\sigma} + \tau_{\mathrm{d}}\tilde{k}^2) - (\tilde{\sigma} + \tau_{\mathrm{d}}\tilde{k}^2) + R_\rho^{-1}(\tilde{\sigma} + \tilde{k}^2) = 0,} \tag{4.18}$$

where

$$Pr \equiv v/\kappa_T, \tag{4.19}$$

is the *Prandlt* number,

$$\tau_{\mathrm{d}} \equiv D/\kappa_T, \tag{4.20}$$

is the solute to thermal diffusivity ratio (or inverse *Lewis* number), and

$$R_\rho \equiv \left(N_T/N_\mu \right)^2 = \frac{\alpha_T}{\alpha_\mu} \frac{\nabla_T - \nabla_{\mathrm{ad}}}{\nabla_\mu}, \tag{4.21}$$

is the so-called *density ratio* (Rosenblum et al. 2011).

In the *diffusive case*[4], i.e. for a fluid exhibiting a *positive* molecular weight gradient ($\nabla_\mu > 0$), and at fixed Pr and τ_{d}, there are three different regimes that are summarized in Fig. 4.1

- $R_\rho^{-1} < 1$; the cubic Eq. (4.18) have three real roots, two being positive for small enough values of the wavenumber. The instability can grow and overturning convection sets in, as was already predicted by the *Ledoux* criterion. Because the maximum growth rate is obtained for a vanishing wavenumber, this analysis cannot provide us with the typical lengthscale of the fastest growing mode.

---

[4]In the case both the mean molecular weight (due e.g. to a higher concentration of salt in salty water) and the temperature increase with height (∇_μ and ($\nabla_T - \nabla_{\mathrm{ad}}) < 0$), the compositional gradient is destabilizing while the temperature gradient is stabilizing. This case is referred to as the *fingering case*. In that case, convective instability develops when $R_\rho < 1$, which is equivalent to the *Ledoux instability criterion*. But even if $1 < R_\rho < 1/\tau_{\mathrm{d}}$, the *double-diffusive* instability develops and leads to the formation of salt fingers, and sometimes of thermo-compositional staircases, as observed in some parts of the oceans and in laboratory experiments (Turner 1967).

(a) Overturning convection   (b) Double diffusive convection   (c) Stable system
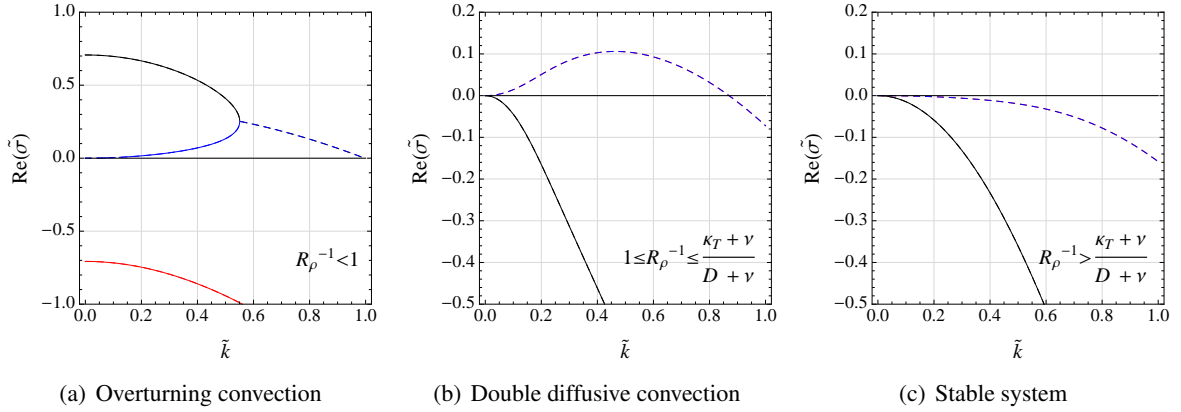
Figure 4.1: Growth rate of the modes described by Eq. (4.18) with respect to the wavenumber for $Pr = \tau_d = 0.3$ in the three different regimes (see text). Solid curves stand for real roots (unstable modes if positive) and dashed curves for their real part when the roots are complex (overstable modes).

- $1 \leqslant R_\rho^{-1} \leqslant \frac{Pr+1}{Pr+\tau_d}$; the real root of Eq. (4.18) is negative and the instability cannot grow as above. However, one of the complex roots exhibits a positive growth rate, so that an oscillating overstable mode can grow. This corresponds to the situation where a hotter rising eddy looses its thermal energy efficiently enough to be colder when it is brought back to its position by its increased mean molecular weight. Thus, during its downward motion, the eddy will sink deeper, and increase the amplitude of the oscillations.

- $R_\rho^{-1} > \frac{Pr+1}{Pr+\tau_d}$; the growth rates of all the roots are negative. The system is stable against convection.

In the double diffusive mode, we can even go further. By maximizing the real part of $\tilde{\sigma}$ over all wavenumbers, we can find the most unstable mode in the system. Fig. 4.2 shows its wavenumber and growth rate for $Pr = \tau_d = 0.3$. By and large, the most rapidly growing mode has a wavelength of the order of $12\,d$ regardless of R_ρ^{-1} for the parameters selected. As advertised, the length scale of the fastest growing mode is on the same order of magnitude than the diffusive length scale.

Thus, this simple linear analysis shows that the Ledoux criterion is not sufficient to decide of the stability of an inhomogeneously stratified medium. However, *we cannot predict the finite amplitude that the perturbation will reach when the instability is fully developed,* and the exact nature of double diffusive convection if it occurs - homogeneous oscillatory convection or layered convection (i.e. uniformly mixed convective layers separated by thin diffusive interfaces characterized by a steep jump in the mean molecular weight) - remains uncertain.

Analytical arguments (Radko 2003) and recent 3D hydrodynamical simulations (Rosenblum et al. 2011 ; Mirouh et al. 2011), however, seem to suggest the picture presented in Fig. 4.3. When the mean molecular weight gradient ($\propto R_\rho^{-1}$) decreases in a stable medium, homogeneous oscillatory con-
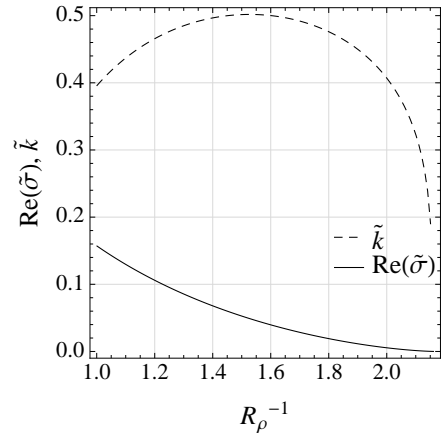
Figure 4.2: Dimensionless wavenumber ($\tilde{k}$; dashed) and growth rate ($\mathrm{Re}(\tilde{\sigma})$; solid) of the fastest growing overstable mode with respect to the inverse density ratio (R_ρ^{-1}). The length scale of the fastest growing mode is about $12\,d$.

vection, also called turbulent diffusion, first appears for

$$R_{\min}^{-1} \leqslant R_\rho^{-1} \leqslant \frac{Pr+1}{Pr+\tau_{\mathrm{d}}} \text{ (oscillatory convection)}, \tag{4.22}$$

while well defined thermo/compositional layers start to develop when

$$1 \leqslant R_\rho^{-1} \leqslant R_{\min}^{-1} \text{ (layered convection)}. \tag{4.23}$$

$R_{\min}^{-1}$ corresponds to the point where the solute to heat buoyancy flux ratio ($\equiv \gamma^{-1}$) stops decreasing when R_ρ^{-1} increases (see Radko 2003 for details). Its exact value, however, depends on the characteristics of the medium in a non trivial way and is difficult to estimate (Rosenblum et al. 2011 ; Mirouh et al. 2011). For smaller ∇_μ gradients, the medium is unstable according to the Ledoux criterion, and the thermal forcing is strong enough to force large scale overturning convection.

Various arguments seem to support, or at least not to exclude, the existence of layered convection under planetary conditions (Chabrier and Baraffe 2007). Conducting 3D hydrodynamics calculations over a wide domain of parameter space (Prandlt number and atomic to thermal diffusivity ratio) *including the regime relevant for planetary interiors*, Mirouh et al. (2011) always find a domain where γ^{-1} decreases with R_ρ^{-1}, a necessary and sufficient condition for the layering instability, thus layer formation to occur. A central question is then the size of the layers ; this will be examined in § 4.3. In any event, both homogeneous double-diffusive convection or layered convection - generically denominated as "semi-convection" in the following - are found to yield thermal and compositional fluxes that are significantly smaller than that expected from standard convection. Indeed, the presence of diffusive interfaces strongly decreases the efficiency of heat transport compared with large-scale, adiabatic convection, leading in planet interiors to a significant departure from the usual adiabatic profile, as quantified below.
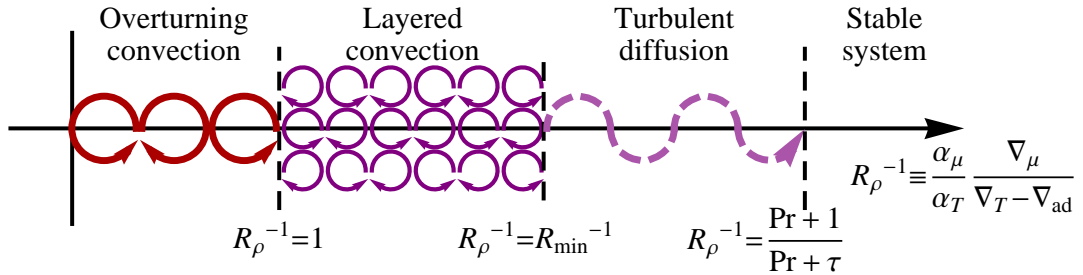
Figure 4.3: Stability diagram for a medium presenting a destabilizing temperature gradient and a stabilizing solute gradient, as a function of increasing R_ρ^{-1} (decreasing R_ρ). The usual instability Ledoux criterion corresponds to $R_\rho^{-1} \leqslant 1$.

4.2 A mixing length theory for layered convection

In order to investigate the impact of such strongly hampered convection on giant planet internal structure, I developed a simple, but completely analytical sub-grid model of layered convection.

As illustrated on Fig. 4.4 and found in simulations (Rosenblum et al. 2011), we consider that a semi convective zone consists of a large number, N_{l}, of well mixed convectively unstable layers of size l, separated by thin diffusive interfaces of *thermal* thickness δ_T, within which the large stabilizing compositional gradient completely inhibits convective motions.
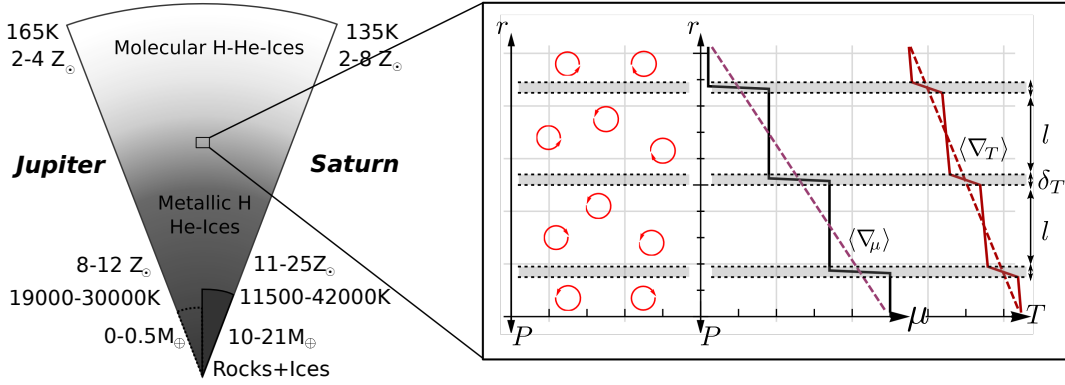
Figure 4.4:   Schematic representation of the interiors of Jupiter and Saturn, according to the present study, and of layered convection, with the resulting compositional and thermal radial profiles. The abundance of metals is constant within the well mixed convective cells of size l, and undergoes a steep variation within the diffusive interfaces of thermal size δ_T (grey regions). Thanks to this steep gradient, these interfaces are stable against convection and energy and matter are transported therein by diffusive processes. Because the size of these diffusive layers is very small compared with the size of the planet, the mean thermal and compositional gradients ($\langle \nabla_T \rangle$ and $\langle \nabla_\mu \rangle$) can be used in good approximation to infer the global planet structure.

In § 4.2.1 and § 4.2.2, I will first derive the equations describing separately the energy transport in the diffusive and in the convective layers. Then, in § 4.2.3, I will show how these formulas can be used to derive the mean properties of a stack of convective/diffusive cells. Finally, considering some physical limits that must apply to semi-convection inside giant planets, I will derive analytical limits on the possible range of sizes for the convective/diffusive cells (§ 4.3).

4.2.1   Convective layers

Within each convective layer, the fluid is expected to follow the dynamics found in turbulent *Rayleigh-Bénard* convection within a cell of typical height equal to the size of the layer, l. By analogy with the mixing length formalism (see details in Appendix G), we define a dimensionless mixing length parameter by dividing l by the pressure scale height, $\alpha \equiv l/H_P$.

In a laboratory or a numerical experiment, the efficiency of the convection is characterized by the thermal *Nusselt* number,

$$Nu_T \equiv \frac{F_{\text{int}} - F_{\text{d}}^{\text{ad}}}{F_{\text{d}} - F_{\text{d}}^{\text{ad}}}, \tag{4.24}$$

where by definition the total *intrinsic* flux (F_{int}), the flux transported by diffusive processes (F_{d}), and the diffusive flux that would be present in a completely adiabatic zone (F_{d}^{ad}) are given by (Cox and Giuli 1968 ; Hansen and Kawaler 1994)

$$\begin{pmatrix} F_{\text{int}} \\ F_{\text{d}} \\ F_{\text{d}}^{\text{ad}} \end{pmatrix} \equiv \kappa_T \frac{\rho \, c_P T}{H_P} \begin{pmatrix} \nabla_{\text{d}} \\ \nabla_T \\ \nabla_{\text{ad}} \end{pmatrix}, \tag{4.25}$$

where c_P is the heat capacity at constant pressure. It is found that, for large Rayleigh numbers, the Nusselt number follows a law of the type

$$Nu_T = C_L Ra_\star^a, \tag{4.26}$$

where $Ra_\star$ is a *modified Rayleigh* number[5], which is the ratio of the strength of the thermal forcing to the one of the radiative losses

$$Ra_\star \equiv \frac{\alpha_T \, g H_P^3}{\kappa_T^2} \, \alpha^4 \left(\nabla_T - \nabla_{\mathrm{ad}} \right) = \left(N_T^2 l^4 / \kappa_T^2 \right). \tag{4.27}$$

Here, g is the local gravity acceleration, and N_T the Brunt-Väisälä frequency.

As convection at very high Rayleigh numbers is difficult to study either experimentally or computationally, it is difficult to give precise values for a and C_L. For the bounded Rayleigh-Bénard problem, theoretical models suggest that the exponent of the convective flux law, a, could be equal to 1/3 (Garaud et al. 2010)[6]. However, experiments done by Krishnamurti (1995) tend to show that this exponent could be smaller, and as low as $a = 0.2$. On the other hand, for homogeneous Rayleigh-Bénard convection (without boundaries), Garaud et al. (2010) showed that the regime predicted by the mixing length theory, i.e. $Nu_T = Ra_\star^{1/2}$ ($C_L = 1$, $a = 1/2$; see Appendix G), is recovered. In the following, we will thus consider $0.2 \leqslant a \leqslant 0.5$ and $C_L = 1$.

Eq. (4.26) is sufficient to calculate the flux transported by convection once the super adiabaticity is known. To compute this latter, however, we must first define a quantity which can be computed *a priori* from the local thermodynamical properties of the medium and the total internal energy flux to be transported. Following Hansen and Kawaler (1994), this *convective forcing* can be defined by

$$\Phi \equiv Nu_T \times Ra_\star. \tag{4.28}$$

Introducing $\varepsilon_{\mathrm{d}} \equiv \nabla_{\mathrm{d}} - \nabla_{\mathrm{ad}}$, we rewrite Eq. (4.28) as $\Phi \equiv \Phi_0 \, \alpha^4 \, \varepsilon_{\mathrm{d}}$ where

$$\Phi_0 \equiv \left(\frac{\alpha_T g H_P^3}{\kappa_T^2} \right). \tag{4.29}$$

It is clear from Eq. (4.28) that Φ_0 is a local constant of the medium, which characterizes its ability to transport energy by convection, independently of the mixing length or of the flux to be transported ($\propto \varepsilon_{\mathrm{d}}$).

Then, from Eqs. (4.26) and (4.28), one sees that in a region where convection remains efficient enough,

$$\Phi = Nu_T \times Ra_\star = C_L Ra_\star^{1+a} \; \Rightarrow \; Ra_\star = \left(\frac{\Phi}{C_L} \right)^{1/(1+a)}, \tag{4.30}$$

which yields the super adiabaticity,

$$\varepsilon_T \equiv \nabla_T - \nabla_{\mathrm{ad}} = \left(\frac{\varepsilon_{\mathrm{d}}}{Nu_T} \right) = \left(\frac{\varepsilon_{\mathrm{d}}}{C_L \Phi_0^a \alpha^{4a}} \right)^{1/(1+a)}. \tag{4.31}$$

The range of super adiabaticity in the convective layers implied by this equation for the various possible exponents a is shown in Fig. 4.5 (pale red area). As seen, the uncertainty on a leads to a large dispersion

---

[5]Indeed, in the astrophysical context, it is convenient to use $Ra_\star = Pr \times Ra$, where Ra is the usual Rayleigh number.

[6]Although the simulations presented by Rosenblum et al. (2011) seem to support exponent values smaller than 1/3, suggesting that interfaces act as impermeable boundaries, it should be noticed that the height of the layers present in their simulations is small compared to a pressure scale height. Their conclusion may thus not be valid for larger layers.

on this super adiabaticity. In this high convective efficiency regime, we can further compute the mean convective flux which, by definition, is given by

$$F_{\text{conv}} = \kappa_T \frac{\rho c_P T}{H_P} (\nabla_T - \nabla_{\text{ad}}) \times Nu_T. \tag{4.32}$$

As mentioned above, this scaling law only applies to the vigorous convection regime, i.e Φ or $Ra_\star \gg 1$. Thus, in terms of the layer height, convection remains efficient as long as $\alpha \gg \alpha_{\text{crit}}$, where α_{crit} is defined such that $Ra_\star(\alpha_{\text{crit}}) = 1$, and, from Eq. (4.27), the critical layer size is

$$l_{\text{crit}} = \left(\kappa_T^2 / N_T^2 \right)^{1/4} = d\,Pr^{-1/4}, \tag{4.33}$$

where d is the lengthscale of the fastest growing mode of the linear instability, $d \equiv (\nu \kappa_T / N_T^2)^{1/4}$ (e.g. Baines and Gill 1969). Analytical and numerical arguments show that the size of the fastest growing layers is equal to 10-100 $d \gtrsim l_{\text{crit}}$ (Radko 2003 ; Rosenblum et al. 2011). The efficient convection regime is thus appropriate in the planetary domain, where $Pr \sim 10^{-2} - 10^{-1}$ (Chabrier and Baraffe 2007).

For conditions prevailing in the interior of the actual Jupiter (Saturn), the mean thermal diffusivity is $\kappa_T \sim 5 \times 10^{-5}\,\text{m}^2.\text{s}^{-1}$ (Potekhin 1999), Φ_0 is equal to $\Phi_0 \approx 3 \times 10^{33}$ (9×10^{32}) and $\varepsilon_d \approx 10$ (10 ; see also Fig. 4.7), so that $\alpha_{\text{crit}} = 2 \times 10^{-9}$ (3×10^{-9}). In the following, all the order of magnitude estimates done throughout the text will use these values.

4.2.2 Interfaces

In the interfaces of thermal size δ_T, overturning convection is inhibited by the strong jump in molecular weight. However, these regions do not need to be in the fully diffusive regime ($R_\rho^{-1} > (Pr+1)/(Pr+\tau_d)$), but can also be in the oscillatory convection regime characterized by Eq. (4.22). Indeed, as shown by Radko (2005) the condition $R_I^{-1} > R_{\min}^{-1}$, where R_I^{-1} is the inverse density ratio within the interface, is a sufficient criterion not only to ensure the stability of the interface itself, but also of the whole stack of layers which would otherwise merge into one homogeneous layer (see § 4.3.1 for details).

Therefore, the interface is very likely either in a stable diffusion state, or in a state of weakly turbulence enhanced diffusion. Rosenblum et al. (2011) show that in this regime $Nu_T \lesssim 2$, meaning that most of the energy is transported by pure diffusion. We will thus assume that the thermal gradient to be used in these regions is given by the gradient needed to transport the whole outgoing energy flux by diffusion:

$$\nabla_d \equiv \frac{1}{\kappa_T} \frac{H_P}{\rho c_P T} F_{\text{int}}. \tag{4.34}$$

The thermal diffusivity κ_T encompasses the contribution of all diffusive processes. If diffusion is ensured by photons, as generally in most astrophysical objects, the diffusive thermal gradient reduces to the so-called radiative gradient, ∇_{rad} (e.g. Hansen and Kawaler 1994). However, in the deep interior of giant planets and in degenerate bodies, density can be high enough for the electrons to become degenerate enough to efficiently conduct thermal energy (see Stevenson and Salpeter (1977a) and Chabrier and Baraffe (2007) for the characteristic radiative and conductive opacities under jovian planet conditions). Along this paper, we will use the generic denomination ∇_d for the diffusive temperature gradient, keeping in mind that diffusion is now due to electronic or atomic motions, with a characteristic thermal diffusivity κ_T. In the present calculations, we use the conductive thermal diffusivities calculated by Potekhin (1999).

4.2.3 Mean thermal gradient

Once we have calculated the thermal gradient in the convective zones of size l, and in the diffusive interfaces of size δ_T, we need to determine the *mean* properties of a whole stack of convective-diffusive cells. As discussed in Chabrier and Baraffe (2007), since the convective plumes must be fed by the diffusive interfaces, the thermal convective (N_T^{-1}) and diffusive (δ_T^2/κ_T) time scales should be similar in each respective layer. Therefore

$$\left(\delta_T/l \right) = \left(\kappa_T/l^2 N_T \right)^{1/2} = Ra_\star^{-1/4} = \left(\Phi/C_L \right)^{-\frac{1}{4(1+a)}}. \tag{4.35}$$

Not surprisingly, the size of the interface, δ_T, is related to the lengthscale of the most unstable mode of the linear instability by $\delta_T = d/Pr^{1/4}$. In addition, comparing the mean kinetic energy of an upwelling eddy with the potential energy barrier created by the negative buoyancy in the diffusive interface, we see that the above condition also entails that convective overshooting can be neglected (see Chabrier and Baraffe 2007 for details).

Knowing δ_T/l enables us to compute the *mean* thermal gradient to be used to compute the planet's structure (see § 4.4.1)

$$\langle \nabla_T \rangle \equiv \frac{\delta_T}{l + \delta_T} \nabla_d + \frac{l}{l + \delta_T} \nabla_T. \tag{4.36}$$

Substituting ∇_T and δ_T/l by their expressions in Eqs. (4.31) and (4.35), and developing the mean gradient to first non vanishing order, we find that

$$\langle \nabla_T \rangle \approx \nabla_{ad} + (\nabla_d - \nabla_{ad}) \left(\frac{1}{Ra_\star^{1/4}} + \frac{1}{Nu_T} \right) + \mathcal{O} \left(\frac{1}{Ra_\star^{1/2}}, \frac{1}{Nu_T Ra_\star^{1/4}} \right), \tag{4.37}$$

or equivalently

$$\langle \nabla_T \rangle - \nabla_{ad} \approx (\nabla_d - \nabla_{ad}) \left[\left(\Phi/C_L \right)^{-\frac{1}{4(1+a)}} + \left(\Phi C_L^{1/a} \right)^{-\frac{a}{(1+a)}} \right]. \tag{4.38}$$

As expected, two terms appear in the mean super adiabaticity, which is shown in Fig. 4.5 (dark grey region). The first one is due to the temperature jumps at each interface and is controlled by the convective overturning timescale which determines the size of these interfaces. The second one is due to the super adiabaticity in the convective layers themselves, which is enhanced by their small size. The relative contributions of these two terms only depend on the properties of the convection, characterized by the exponent a.

Interestingly, if the impact of a on the super adiabaticity in the convective layers (pale red area in Fig. 4.5) is significant, the impact on the *mean* super adiabaticity of the whole stack of layers, $\langle \nabla_T \rangle - \nabla_{ad}$ (dark gray region), is rather small. This can be understood as follows: for the smallest value of the exponent considered here, $a = 0.2$, convection is very inefficient and most of the mean super adiabaticity is contained in the convective layers (upper contour of the grey region). In that case, Eq. (4.36) is dominated by the second term, $\langle \nabla_T \rangle \approx \nabla_T$.

When the exponent is increased, the super adiabaticity in the convective layers ($\propto \Phi^{-a/(1+a)}$) drops dramatically, but this entails a growth of the convective timescale, and thus of the thickness of the interfaces (see Eq. (4.35)). For efficient convection, $a \geqslant 1/4$, this effect eventually dominates, and the mean super adiabaticity increases again with a. This yields a rather narrow region for the mean super-adiabaticity within the considered range of exponent variation.
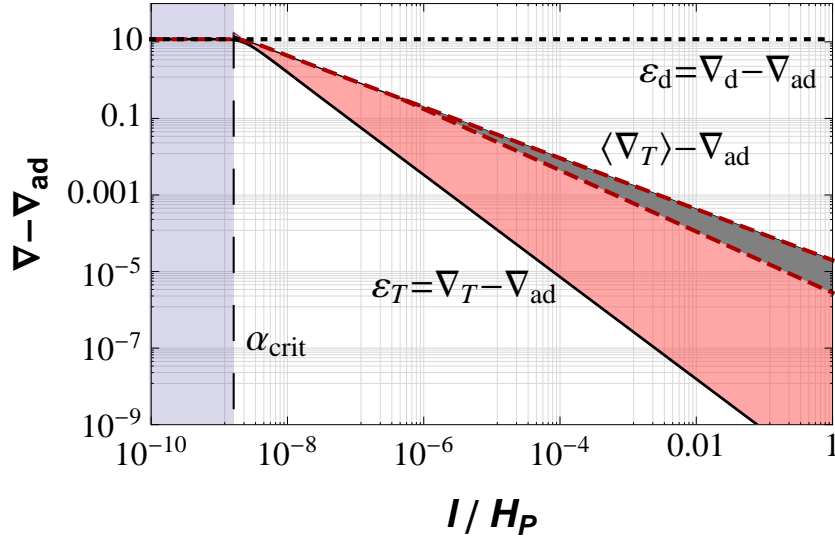
Figure 4.5: Range of mean super adiabaticity ($\langle \nabla_T \rangle - \nabla_{ad}$) of a semi-convective medium as a function of the mixing length parameter $\alpha = l/H_P$, for $0.2 \leqslant a \leqslant 0.5$ (gray area between the red dashed curves; $\Phi_0 = 3 \times 10^{33}$; $\varepsilon_d = 10$; $C_L = 1$). For comparison, the super adiabaticity in a convective (pale red area; same parameters) and in a diffusive cell (dotted curve) are also shown. As expected a smooth transition between the convective and diffusive regimes occurs near α_{crit} (see Appendix G; here $\alpha_{crit} \approx 2 \times 10^{-9}$).

Interestingly, to first order, the $a = 1/2$ and $a = 0.2$ cases, i.e. the two extreme values considered here, yield the same mean superadiabaticity. *Therefore, the model presented here for semi-convection depends only weakly on the precise prescription chosen for convection.* In the following, we will show results obtained with the mixing length theory, i.e. $C_L = 1$ and $a = 1/2$, while keeping in mind that for $\alpha \gg \alpha_{crit}$ these results would be the same as the one obtained in the $a = 0.2$ case.

4.2.4   Mean solute gradient and flux

Disregarding convective overshoot, the solute flux (F_Z) is determined by the transport at each interface. As for heat, the turbulent transport of solute is expected to be very inefficient, and we will assume purely diffusive processes (see § 4.2.2). The impact of a more efficient transport will be discussed in the next section. In this regime, the solute flux is thus given by

$$F_Z = -\rho \, D \nabla Z_I, \tag{4.39}$$

where the subscript I describes quantities determined within the interface, indicating that the solute flux F_Z is determined by the element fraction variation rate at each interface. Neglecting the small inhomogeneities in the convective layer, the interfacial and mean gradients are related by

$$\nabla_{\mu,I} = \frac{l + \delta_Z}{\delta_Z} \langle \nabla_\mu \rangle \quad \text{or} \quad \nabla Z_I = \frac{l + \delta_Z}{\delta_Z} \langle \nabla Z \rangle, \tag{4.40}$$

where $\langle \nabla Z \rangle$ describes the mean gradient of heavy element mass fraction, i.e. the value of dZ/dr averaged over several convective/diffusive cells, and δ_Z is the length over which compositional jump occurs. To constrain the value of δ_Z, two limiting arguments can be used. On one side, equating the diffusive

timescales for heat and solute leads to

$$\frac{\delta_Z}{\delta_T} \approx \sqrt{\frac{D}{\kappa_T}}. \tag{4.41}$$

On the other hand, considering that the compositional jump must cover the whole interface to ensure its mechanical stability, one would expect that

$$\delta_Z \approx \delta_T. \tag{4.42}$$

The present paper focuses on the impact of double-difffusive convection on the planet mechanical and thermal *structure*. The impact on the evolution will be addressed in a forthcoming study (see § 4.6). Therefore, this uncertainty on the heavy element flux, discussed in the next section, does not have a significant impact on the results presented in the present study. Determining more precisely the solute transport properties in the regime of layered convection, however, will be of central importance to evolutionary calculations, and 3D hydrodynamical simulations in a realistic parameter range are strongly needed (Mirouh et al. 2011).

The term $\nabla_{\mu,I}$, which is the relevant quantity when computing the equilibrium condition of the interface, is given by

$$\nabla_{\mu,I} = -\frac{l + \delta_Z}{\delta_Z} H_P \left.\frac{\partial \ln \mu}{\partial Z}\right|_{P,T} \langle \nabla Z \rangle. \tag{4.43}$$

The precise value of $\left.\frac{\partial \ln \mu}{\partial Z}\right|_{P,T}$ depends on the precise chemical composition of the considered heavy element, but is typically around unity ; this is the value we will use in numerical estimates below. We will also use $D \approx 10^{-7} - 10^{-8} \, \text{m}^2.\text{s}^{-1}$ (i.e. $\tau_d \approx 10^{-2} - 10^{-1}$), appropriate for giant planet interior conditions Stevenson and Salpeter 1977a).

4.3 Layer size: analytical point of view

4.3.1 Existence of an equilibrium height

The determination of the size of the layers, when layered convection is occurring, is a complex task. The problem is rendered even more difficult by the fact that the small layers that initially form tend to merge into larger layers. The question is then to know *if* and *when* layer merging ends.

In the fingering case, i.e. when the solute is the destabilizing actor, Radko (2005) derived a criterion for the linear stability of thermo-compositional staircases against merging. In this picture, an initially inhomogeneous medium starts forming layers if its density ratio (R_ρ) is smaller than the density ratio, $R_{\min}$, for which the heat to solute buoyancy flux ratio ($\equiv \gamma$) stops decreasing when R_ρ increases. Then, layers are unstable and merge as long as the density ratio within the interface between them (R_I) is smaller than $R_{\min}$. Then, as R_I increases with the layer height (under some conditions), it eventually reaches $R_{\min}$ and the merging process stops. At this stage, an *equilibrium height* is reached by the convective layers and the staircase is fully equilibrated.

The linear stability analysis of Radko (2005) can be redone in the diffusive case, by simply accounting for the fact that the signs of the various density and temperature differences and of the fluxes must be changed. Then, after some lengthy but straightforward algebra, one can show that layers are unstable and merge when

$$\left.\frac{\partial \gamma^{-1}}{\partial R_\rho^{-1}}\right|_{R_\rho^{-1}=R_I^{-1}} < 0 \Leftrightarrow R_I^{-1} < R_{\min}^{-1}, \tag{4.44}$$

which defines $R_{\min}^{-1}$. As for the fingering case, this linear stability analysis shows that, *if layers form, their merging will stop when their height reaches a finite equilibrium value.*

4.3.2 Global constraints

Although precisely estimating this equilibrium value is difficult, some strong limits on the layer size can be derived theoretically. Let us consider a stack of layers extending over a zone of size L, and define a global gradient $\langle \nabla Z \rangle \approx -\Delta Z/L$, where ΔZ is the difference between the mass ratios of heavy element at the bottom and at the top of the semi-convective zone.

On one hand, the mean molecular weight gradient in *all* the interfaces, $\nabla_{\mu,I}$, must be high enough to satisfy the stability criterion discussed in sections 4.1.2 and 4.2.2. This implies

$$\frac{\alpha_\mu}{\alpha_T} \nabla_{\mu,I} > R_{\min}^{-1} \times (\nabla_d - \nabla_{ad}). \tag{4.45}$$

Substituting $\nabla_{\mu,I}$ by its expression in Eq. (4.43) and δ_Z by using Eqs. (4.41) and (4.35), the criterion (4.45) for a planetary scale ($L \approx R_p$) semi-convective zone reads

$$\alpha^{1/(1+a)} > \alpha_{\min}^{1/(1+a)} \equiv \frac{\alpha_T}{\alpha_\mu} \sqrt{\frac{D}{\kappa_T}} \frac{R_{\min}^{-1}(\nabla_d - \nabla_{ad})^{1 - \frac{1}{4(1+a)}}}{(\Phi_0/C_L)^{\frac{1}{4(1+a)}} \Delta Z \left. \frac{\partial \ln \mu}{\partial Z} \right|_{P,T}}, \tag{4.46}$$

where $\alpha_{\min}$ denotes a lower limit for the layer size. Under the present conditions in the interiors of our gas giants (see end of §4.2.1 and Table 4.1), this yields $\alpha_{\min} \approx 2 \times 10^{-9} \times (R_{\min}^{-1})^{1+a}$, with the less restrictive constraint being obtained for $R_{\min}^{-1} = 1$, as summarized in Table 4.1. However, as the existence of layers allows $R_{\min}^{-1}$ to be as high as $(1+Pr)/(\tau_d + Pr) \approx 10^1 - 10^2$, these constraints could be severely tightened, as showed in Table 4.1. This simply confirms that, *in order for layered convection to be stable, convective cells must remain larger than the diffusive interfaces, and the medium is always in the convective regime,* $\alpha \gg \alpha_{crit}$.

Table 4.1: Numerical constraints on the layer height in the two limiting cases of convection ($a = 0.2$ and 0.5; $C_L = 1$) for the following conditions (representative of Jupiter interior): $\Phi_0 = 3 \times 10^{33}$, $\varepsilon_d = 10$, $\kappa_T = 5 \times 10^{-5}$ m^2.s^{-1}, $D = 5 \times 10^{-7}$ m^2.s^{-1}.

	constraint		$a = 0.2$	$a = 0.5$
$\alpha_{\min}$	stability	$R_{\min}^{-1} = 1$	2.4×10^{-9}	2.4×10^{-9}
		$R_{\min}^{-1} = \frac{1+Pr}{\tau_d + Pr}$	6.0×10^{-7}	2.4×10^{-6}
$\alpha_{\max}$	homogeneization	$Nu_\mu = 1$	1.0×10^{-4}	1.4×10^{-3}
		$Nu_\mu = 3$	2.5×10^{-5}	2.6×10^{-4}
$\alpha_{\min}$	observational	Jupiter		3×10^{-5}
	constraints*	Saturn		4×10^{-6}

* See §4.5

On the other hand, the solute gradient within the planet will be homogenized within a typical timescale

$$t_Z \approx \frac{\rho \, \Delta Z R_p}{|F_Z|}. \tag{4.47}$$

Using Eq. (4.39), (4.40) and (4.41), and taking $\langle \nabla Z \rangle \approx \Delta Z / R_p$, Eq. (4.47) becomes

$$t_Z \approx \frac{R_p^2}{D} \frac{\delta_Z}{l} \approx \frac{R_p^2}{\sqrt{\kappa_T D}} \left(\frac{\Phi}{C_L} \right)^{-\frac{1}{4(1+a)}} \propto \alpha^{-1/(1+a)}. \tag{4.48}$$

Therefore, in order to avoid a complete homogenization of giant planet interiors in less than 5 Gyr, their present age, α must be smaller than $\alpha_{max} \approx 1 \times 10^{-4}$ for $a = 0.2$ and 1.4×10^{-3} for $a = 0.5$. Note however that, as mentioned in Rosenblum et al. (2011), turbulent transport due to the double-diffusive instability can yield compositional Nusselt numbers, Nu_μ[7], around 2-4, yielding even stronger constraints, as summarized in Table 4.1. These small values of α justify a posteriori the approximation of continuous thermal and heavy element profiles when considering the planet's entire internal structure. Note, however, that layered inhomogeneities could be dynamically regenerated over time. In that case, layered convection will be an ongoing process in the planet's interior.

Considering the possibility that the ratio of the compositional to the thermal size of the interface does *not* scale as the square root of the ratio of the diffusivities, and therefore using Eq. (4.42) instead of Eq. (4.41), yields an increase of both α_{min} and α_{max} by a factor $\sqrt{\kappa_T/D}^{1+a} \approx 10$.

This analysis shows that, for the age of the Solar System and for the conditions prevailing in gas giant interiors, there exists a range of layer sizes for which ongoing layered convection is a viable mechanism. According to our estimate, this range is relatively large and corresponds to :

$$10^{-9} - 10^{-6} \lesssim \alpha \lesssim 10^{-4} - 10^{-2}. \tag{4.49}$$

The uncertainty on the lower and upper bounds are respectively due to our poor knowledge of the behavior of R_{min}^{-1}, and of the solute flux at low Prandlt number. Even given these uncertainties, the fact that convection is always in a regime of relatively high Rayleigh number appears to be robust prediction. To make an attempt to overcome these limitations, we examine in § 4.5 how observational data can narrow this possible domain of α, by further constraining the degree of super adiabaticity, and thus the size of the layers, in our Solar System gas giants.

4.3.3 An alternative scenario

We stress that the aforementioned constraints apply only to *layered* convection, and does not preclude the possibility that, under some conditions, double diffusive convection may manifest itself under the form of *homogeneous* double diffusive convection and act like a *turbulent diffusion* (Rosenblum et al. 2011). However, for this to happen, the criterion (4.45) must be verified in the *inefficient convection* regime, $\delta_T \gg l$ (see Appendix G). The following criterion must then hold

$$-H_P \langle \nabla Z \rangle \approx \Delta Z \frac{R_p}{L} \gtrsim R_{min}^{-1} \times (\nabla_d - \nabla_{ad}). \tag{4.50}$$

As $\Delta Z \leqslant 1$ and $R_{min}^{-1} \geqslant 1$, by definition, a zone of turbulent diffusion cannot extend over the *entire planet's scale* unless $\nabla_d \lesssim \nabla_{ad}$, i.e. if the whole object is nearly diffusive in the first place.

In an object with a heat flux high enough to be convectively unstable, the semi-convective zone must then be confined to a *fraction of the planet*, in particular, but not necessarily, near an immiscibility region or a phase transition for instance. In this case, the total size of the zone must verify $L/R_p \leqslant \varepsilon_d^{-1}$ ($\sim 1/10$ in Jupiter), condition for which a large enough jump in the heavy element mass fraction can be sufficient to stabilize the whole zone against convection and open a *diffusive buffer* in the interior (where $\nabla_T \approx \nabla_d$). From the global point of view of the planet, this would act as a composition, temperature

---

[7]Analogously to the thermal Nusselt number, the flux of heavy elements, for a given Nu_μ, is given by $F_Z \equiv -Nu_\mu \times \rho D \nabla Z$.

and entropy nearly discontinuity. This possibility for the existence of such a diffusive-like buffer in the interior of our gas giants, as a consequence of double-diffusive instability, must be kept in mind.

In the following, however, we will not consider this scenario any further, and we will only consider the effect of a planetary scale layered-convection zone.

4.4 Internal structure models of Jupiter and Saturn

In the analytical analysis derived in the previous section, I have shown that semi-convection is theoretically possible in giant planet interiors for the aforementioned range of α values. **To get further constraints from the observational data measured for our Solar System gas giants, we need to determine the area of the *super adiabaticity/composition* parameter space for which we can derive internal structure models that match these measurements.**

This is the goal of the following sections. I first explain the methodology used to find such structure models (§ 4.4.1) and use it to derive reference homogeneous models of Jupiter and Saturn (§ 4.4.2). Finally, in § 4.5, I present new semi-convective inhomogeneous models of our gas giants, and discuss the implications of these models for their heavy element contents and temperature profiles.

4.4.1 Method

Solar System giant planets are rapidly rotating bodies (the period of rotation is about 10 hours), with the centrifugal potential representing about 10% of the gravitational potential. As extensively discussed in Chapter 3 and Appendix E, this modifies the hydrostatic equilibrium condition between the pressure gradient and the gravitational force in the interior which now writes

$$\nabla P = -\rho \, \nabla (V_G + V_{\text{rot}}), \tag{4.51}$$

where

$$V_G(\mathbf{r}) = -G \int \frac{\rho(\mathbf{r}')}{|\mathbf{r} - \mathbf{r}'|} \, \mathrm{d}^3 \mathbf{r}' \quad \text{and} \quad V_{\text{rot}}(r, \theta) = -\int_0^\xi \omega_{\text{p}}^2(\xi') \xi' \, \mathrm{d}\xi' \tag{4.52}$$

denote respectively the gravitational and centrifugal potentials, with differential rotation $\omega_{\text{p}}(\xi)$, where ξ is the distance from the position $\mathbf{r}$ to the rotation axis, and G the gravitational constant. In the present study, ω_{p} is assumed to be constant and given by the magnetospheric rotation rate. Because of the symmetry of the centrifugal potential with respect to both the rotation axis and the equatorial plane, surfaces of equal densities for these objects are supposed to be generalized ellipsoids of revolution whose exact shape is given by

$$r(\bar{r}, \theta) = \bar{r} \left[1 + \sum_n s_{2n}(\bar{r}) P_{2n}(\cos\theta) \right], \tag{4.53}$$

where $\bar{r}$ is the mean radius of the equipotential, P_{2n} are the usual Legendre polynomials, θ is the colatitude and the s_{2n} are a set of figure functions. These latter can be derived using the theory of figures for rotating bodies detailed in Appendix E, and must be solved iteratively with the set of *perturbed* 1D hydrostatic

equilibrium equations

$$\frac{\partial P}{\partial m} = -\frac{1}{4\pi}\frac{Gm}{\bar{r}^4} + \frac{\omega_p^2}{6\pi\bar{r}} + \varphi_\omega(s), \tag{4.54}$$

$$\frac{\partial s}{\partial m} = \frac{1}{4\pi\bar{r}^2\rho}, \tag{4.55}$$

$$\frac{\partial T}{\partial m} = \frac{T}{P}\frac{\partial P}{\partial m}\nabla_T, \tag{4.56}$$

where m is the mass enclosed in the equipotential of mean radius $\bar{r}$, and $\varphi_\omega(\bar{r})$ is a second order correction due to the centrifugal potential, which depends on the figure functions (see Eq. (E.17)). As discussed in § 4.2, the thermal gradient is determined by the energy transport process which is relevant in the zone considered.

The departure from sphericity of the iso-density surfaces results in a perturbation of the external gravity field $V_G(r, \theta)$ that writes

$$V_G(r, \theta) = -\frac{GM_1}{r}\left\{1 - \sum_{i=1}^{\infty}(\frac{R_{eq}}{r})^{2i}J_{2i}P_{2i}(\cos\theta)\right\}, \tag{4.57}$$

$$J_{2i} = -\frac{1}{M_1 R_{eq}^{2i}}\int_V \rho(r, \theta)\, r^{2i}P_{2i}(\cos\theta)\, d^3\mathbf{r}, \tag{4.58}$$

where r is the radial distance from the center of the planet, M_1 the mass of the planet, R_{eq} the equatorial radius, θ the colatitude, P_{2i} are Legendre polynomials and J_{2i} denote the gravitational moments, that can be computed once the figure equations have been solved. The measured gravity moments provide stringent constraints on the density profile and the possible layering within these planets.

As, in practice, Legendre polynomial expansions are truncated at a given order n, a closure equation is provided by the equation of state (EOS) of the mixture along the planet's interior profile. Such an EOS is generally given by the so-called ideal volume law for the mixture:

$$\frac{1}{\rho} = \frac{X}{\rho_X} + \frac{Y}{\rho_Y} + \frac{Z}{\rho_Z}, \tag{4.59}$$

where X, Y and Z denote the mass fractions of H, He and heavy elements, respectively. For the H/He fluid, the most widely used EOS is the Saumon-Chabrier-vanHorn EOS (Saumon et al. 1995 ; SCvH). For the heavy material, I have used the "Rock" EOS of (Hubbard and Marley 1989) for silicates and the "Ice" ANEOS equation of state (Thompson and Lauson 1972) for volatiles (CH$_4$, NH$_3$, H$_2$O). The impact of the differences between various EOS's on exoplanet structure and evolution has been explored in (Baraffe et al. 2008).

Once such equations of states, $P[\rho(X_i)]$, are specified, structure models with various compositions are calculated by solving iteratively the aforementioned hydrostatic equilibrium condition for a rotating body and the third-order level-surface theory (Zharkov and Trubitsyn 1978) to obtain a model which reproduces the observed values of the radius, R_{eq}, and gravitational moments J_2 and J_4 measured by the Pioneer and Voyager missions (see Table 4.2).

4.4.2 Homogeneous reference models

In conventional giant planet models, the abundances of heavy elements are chosen to be constant in the gaseous H/He envelope, with a possible discontinuity at the transition between the molecular and

Table 4.2: Observed characteristics of Solar System gaseous giants (Guillot 2005 and references therein ;
the numbers in parentheses are the uncertainty in the last digits of the value).

	Jupiter	Saturn
M_{p} [10^{26}kg]	18.986112(15)	5.684640(30)
R_{eq} [10^7m]	7.1492(4)	6.0268(4)
R_{pol}[10^7m]	6.6854(10)	5.4364(10)
P_{rot}[10^4s]	3.57297(41)	3.83577(47)
T_{1bar} [K]	165.(5)	135.(5)
F_{int} [W.m^{-2}]	5.44(43)	2.01(14)
$J_2 \times 10^2$	1.4697(1)	1.6332(10)
$J_4 \times 10^4$	-5.84(5)	-9.19(40)
$Z_{\mathrm{atm}}/Z_\odot$	2-4	2-8
$(Y/(X+Y))_{\mathrm{atm}}$	0.238(50)	0.215(35)

metallic regions (Chabrier et al. 1992). In the absence of a compositional gradient and under the actual
conditions found in Jupiter and Saturn,

$$\nabla_{\mathrm{ad}} < \nabla_{\mathrm{d}}, \tag{4.60}$$

so that the medium is always convectively unstable with respect to the Schwarzschild criterion. As
discussed in Appendix G, convection is very efficient the structure can be solved by setting $\nabla_T = \nabla_{\mathrm{ad}}$ in
the energy transport equation given by Eq. (4.56).

**In order to have a reference case, I use the formalism described in § 4.4.1 to derive *homoge-
neous*, adiabatic interior models representative of the usual 2-layer composition.** As the interpolated
SCvH EOS is used, I do not consider the effect of a Plasma Phase Transition, and only two free parame-
ters remain, namely the core mass (M_{c}) and the metal mass fraction in the gaseous envelope (Z_{env}). The
temperature, density and pressure profiles of the best representative homogeneous models of Jupiter and
Saturn are shown in Fig. 4.6 (solid curves). **These are composed of a solid core of mass $M_{\mathrm{c}} = 3.9$ and
$25.6 M_\oplus$ surrounded by a H/He gaseous envelope with a *constant* metal fraction $Z_{\mathrm{env}} = 0.11$ and
$Z_{\mathrm{env}} = 0.05$ for Jupiter and Saturn, respectively (these results are summarized in Table 4.3). These
reference models yields interior enrichment that are consistent previous determinations (Chabrier
et al. 1992 ; Saumon and Guillot 2004 ; Guillot 2005).**

4.5   Inhomogeneous interiors

I now turn to inhomogeneous models. In the present calculations, in contrast to all previous models,
the mass fraction of heavy material $Z(m)$ at a depth $r(m)$ within the planet (i.e. at the depth of the iso-
density surface enclosing a mass m of the planet) is *continuously* decreasing from the core to the surface,
producing a compositional gradient within the gaseous envelope of the planet,

$$\nabla_Z \equiv \frac{\mathrm{d}\ln Z}{\mathrm{d}\ln P} = \frac{\mathrm{d}r}{\mathrm{d}\ln P}\frac{\mathrm{d}Z}{\mathrm{d}r} \equiv -H_P \nabla Z. \tag{4.61}$$

.

Figure 4.6: Pressure (black), temperature (red) and density (blue) profiles as a function of depth (expressed by the Lagrangian coordinate, i.e. the mass m), for the reference adiabatic (solid curves) and semi-convective (dashed curves) cases for Saturn (a) and Jupiter (b). The increased thermal gradient due to the inefficient heat transport in the semi-convective case (with $N_l = 10^{4.5}$ for Jupiter and $10^{5.4}$ for Saturn) strongly increases the internal temperature. This causes a partial redistribution of the core material within the gaseous envelope.
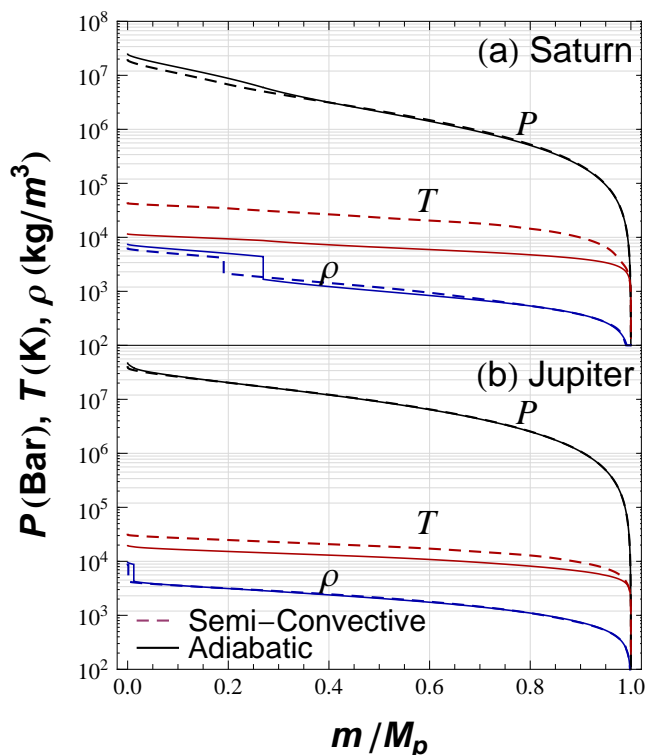
4.5.1   Compositional gradient origin

The possible origin of such a compositional gradient is an open question (Stevenson 1985 ; Chabrier and Baraffe 2007). In the conventional scenario, all the accreted planetesimals are assumed to directly sink to the core and not to evaporate in the envelope, for sake of simplicity. In reality, however, incomplete mixing of large planetesimals or dissolution of a substantial fraction of volatiles and rocks from small solid bodies could occur in the envelope during the phase of planetesimal accretion on the nascent planet ; a substantial amount of ice could as well remain in the envelope (Iaroslavitz and Podolak 2007 ; Hori and Ikoma 2011).

The gradient might also stem from an only partial redistribution by small scale convective motions of stably layered (soluble) constituents released by core erosion in the gas-rich envelope during the planet's evolution (Stevenson 1982 ; Guillot et al. 2004), as seems to be supported for water by recent numerical simulations (**?**). This could be enhanced by the immiscibility (phase separation) of an abundant enough material (e.g. helium, water) in the dominantly metallic-hydrogen envelope (Stevenson and Salpeter 1977b). This would change the dynamical properties of (double diffusive) convection near the regions of immiscibility and add complexity to the problem. Therefore, to avoid extra complication, we only consider the occurence of this process for soluble material in the present paper.

At last, rapid rotation and/or strong magnetic fields, necessarily present in Jupiter and Saturn interiors[8], are known to hamper large-scale convection (Chabrier et al. 2007a), possibly leading to imperfect mixing of heavy elements in part of the envelope.

---

[8]The zonal flows observed in Jupiter's atmosphere might indeed reveal the presence of convective *rolls* at deeper levels, a consequence of the impact of rotation on convective motions, according to the Taylor-Proudman theorem (Busse 1976).

4.5.2   Numerical results

I now derive semi-convective, inhomogeneous interior models for Jupiter and Saturn. I stress that *all these models are consistent, within the observational uncertainties, with the measured gravitational moments of Jupiter and Saturn* (see Table 4.2 ; Campbell and Synnott 1985 ; Campbell and Anderson 1989).
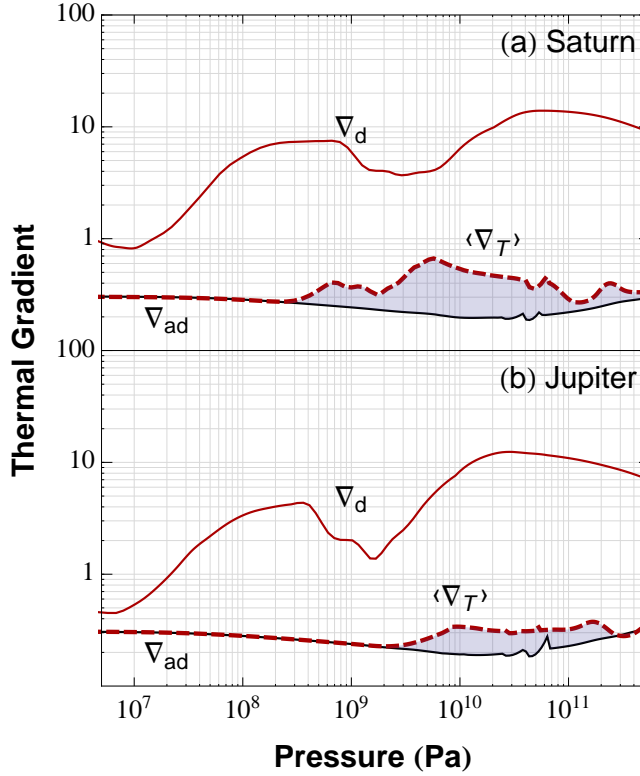
Figure 4.7: Conductive (top red curves) and adiabatic (bottom black curves) thermal gradient profiles for Jupiter and Saturn. The dashed curves correspond to the mean thermal gradient for models with $10^{4.5}$ and $10^{5.4}$ layers for Jupiter and Saturn, respectively. The shaded area represents the allowed range of super adiabaticity in presence of semi-convection, consistent with the observational constraints.

An additional constraint on the outermost value of the compositional gradient is provided by the surface abundance of heavy elements in the planets measured by the 1995 Galileo Entry Probe mission. Indeed, elemental abundances of the atmospheres of solar giant planets are observed to differ significantly from each other and from the solar composition, being enriched by a factor $\sim 2-4$ and $\sim 2-8$ with respect to the Sun's atmosphere for Jupiter and Saturn, respectively, as shown in Table 4.2 (Guillot 2005). Moreover, the planet's total mean abundances of H and He ($\bar{X}$ and $\bar{Y}$)) must recover the values of the protosolar nebula, i.e. $\bar{Y}/(\bar{X}+\bar{Y}) \approx 0.275$.

In the present calculations, the adjustable parameters to fulfill all these constraints are chosen to be the mass of the core (M_c), the mean heavy element mass fraction in the gaseous envelope ($\bar{Z}_{env}$), and the global compositional variation in the envelope (ΔZ_{env}, the difference between the metal mass fraction just above the central core and the one in the atmosphere). To assess the robustness of the results with respect to the equation of state chosen to describe the thermodynamics of the heavy material, I derived several sets of models for which the composition of the core varies from pure ice to pure rock.

Number of layers

From a macroscopic point of view, an important quantity describing layered convection is the number of convective-diffusive layers, N_l. This number is roughly equal to the ratio of the size of the semi-convective zone, comparable to the planet's radius, R_p, if this zone extends over the whole planet, to

Figure 4.8: Metal abundance profiles as a function of depth (expressed by the Lagrangian mass m) for Saturn (a) and Jupiter (b) for different numbers of layers. The abundance increases with the number of layers, to keep the density profile unchanged when convection becomes inefficient. The extreme cases ($10^{5.4}$ layers for Saturn and $10^{4.5}$ layers for Jupiter) correspond to the semiconvective profiles portrayed in Fig. 4.6.
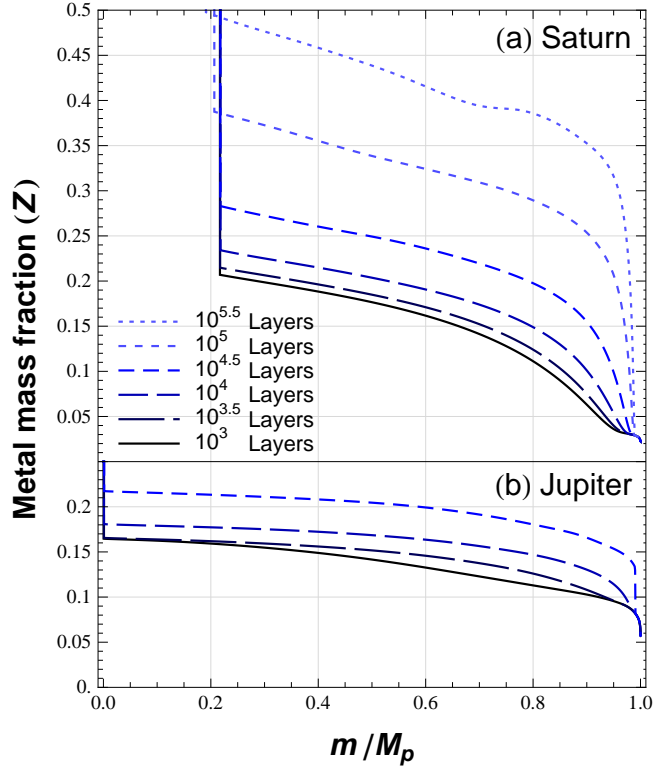
the height of a typical convective/diffusive cell, $l + \delta_T$. As shown in § 4.3, in the regime of interest, $l + \delta_T \approx l$, and $N_{\mathrm{l}} \approx R_{\mathrm{p}}/l$. Because $H_P \approx R_{\mathrm{p}}$ in the deep interior, the number of layers in the planet is thus approximately equal to $N_{\mathrm{l}} \sim \alpha^{-1}$, and in the following we will always refer indifferently to either α or

$$\boxed{N_{\mathrm{l}} \equiv \alpha^{-1} \equiv H_P/l.} \tag{4.62}$$

As shown in § 4.3, N_{l} is constrained to lie within the range $10^{2-4} \leq N_{\mathrm{l}} \leq 10^{6-9}$. Note that, given the small size of the diffusive-convective layers compared with the size of the planet, the discontinuous (staircase-like) temperature and composition profiles can be well approximated by continuous *mean* thermal and compositional gradients ($\langle \nabla_T \rangle$ and $\langle \nabla_\mu \rangle$, respectively) to determine the planet's global structure, as illustrated in Fig. 4.4.

This possible range of numbers of layers is further constrained by the numerical calculations. **I find that, in order to reproduce our giant planet observational constraints, no more than $\sim 2.5 \times 10^5$ layers ($\alpha_{\min} \approx 4 \times 10^{-6}$) can in reality be present in Saturn and $\sim 3 \times 10^4$ ($\alpha_{\min} 3 \times 10^{-5}$) in Jupiter (see Table 4.1). Indeed, a larger number of layers leads to so high temperatures in the interior that the induced mean density decrease can not be counterbalanced by an increase of the heavy element mass fraction compatible with the observed surface abundances.** This is due to the fact that, the larger the number of layers, the smaller the size of each convective cell, reducing the maximum height a convective eddy can travel to transport heat before being stopped by the negative buoyancy present in the diffusive interface. A large number of layers thus decreases convective heat (and composition) transport efficiency. This leads to an increase of the mean super adiabaticity, as portrayed on Fig. 4.7, which in turn immediately implies a rise of the internal temperature, as illustrated on Fig. 4.6. It is important to stress that super adiabaticity is the physical quantity most directly constrained by the data. Thus, *whereas the allowed range of number of layers (or equivalently of mixing length parameter values) may depend*

on the model used to parametrize semi-convection (see § 4.2.3), the allowed range of super adiabaticity displayed in Fig. 4.7 should remain weakly affected.

Enhanced heavy material enrichment

The pressure, density and thermal profiles obtained in the most extreme *semi-convective* case compatible with the observational constraints discussed above are shown in Fig. 4.6 (dashed curves). As seen on the figure, and as expected from the above discussion, the non-adiabatic envelope profile obtained in the semi-convective case yields substantially higher internal temperatures than the usual adiabatic assumption, as heat and material redistributions are partly inhibited by diffusive processes. The pressure and density profiles, on the other hand, remain barely affected, being strongly constrained by the gravitational moments.

Indeed, at basically fixed density profile, a higher temperature profile must be compensated by a larger amount of heavy material within the envelope. This is illustrated in Fig. 4.8, where we show the abundance profiles, as calculated in Appendix H, corresponding to semi-convective models with different numbers of layers. The bottom curve (solid) in each panel corresponds to models with 1000 layers while the other curves correspond to a gradually increasing number of layers.
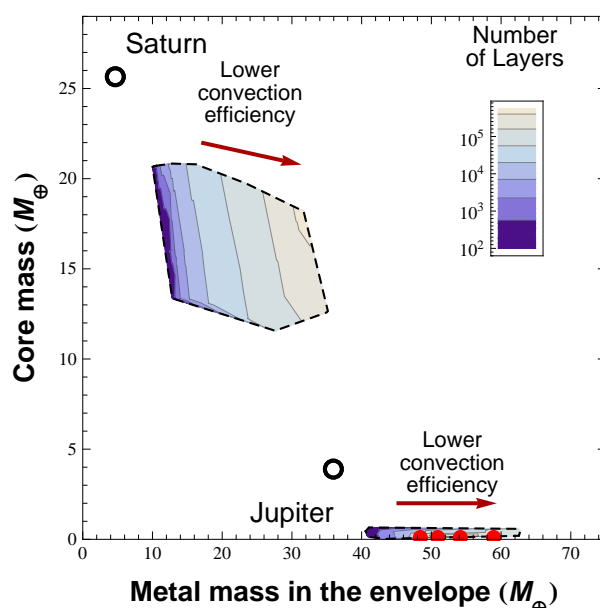
Figure 4.9: Mass range of heavy elements in the core (M_c) and in the envelope ($M_{Z,env}$) consistent with all observational constraints, for different numbers of layers, for Jupiter (bottom right) and Saturn (upper left). The open dots at the upper left of each region correspond to the homogeneous interior models. As the number of semi-convective layers increases, the efficiency of convection decreases, and the heavy element mass fraction increases to counteract the radius increase induced by the planet's higher internal temperature. The metals initially present in the core are then redistributed within the envelope. For Jupiter, solutions with no core at all ($M_c = 0$) can be found for the non adiabatic models (red dots).

Therefore, *in order to compensate the radius increase (density decrease) due to the hotter interior, semi-convection yields a significantly **larger total metal content** compared with conventional homogeneous models.* This can be seen in Fig. 4.9, which shows the amount of heavy elements in the core and envelope for the various cases discussed here, as summarized in Table 4.3. For Saturn, up to $50\,M_\oplus$ of heavy elements could be present in the planet while for Jupiter the heavy material content could reach

63 $M_\oplus$. This corresponds to about 25 and 10 times the solar abundances, respectively[9]. Since these values only depend on the allowed amount of super adiabaticity, they should not strongly depend on our modeling of diffusive/convective transport, as mentioned above. In contrast, the maximum amount of heavy elements compatible with the observational constraints for the homogeneous, adiabatic models, is about $30\,M_\oplus$ for Saturn and $40\,M_\oplus$ for Jupiter, in agreement with previous studies (Saumon and Guillot 2004).

But semi-convection does not only increase the global metal content, it also yields a *completely different* distribution of heavy elements. While the global enrichment of the planet is *increased* in the inhomogeneous models, *the mass of the central core is decreased*, as heavy elements are preferentially redistributed in the gaseous envelope.

In the case of Saturn, the vertical spread in core mass at fixed number of layers observed in Fig. 4.9 is obtained when varying the core composition from pure ice (top) to pure rock (bottom). In Jupiter the inferred core mass is too small for the equation of state to make a significant difference. One could wonder why the homogeneous case is not continuously recovered when α tends toward 1. This slightly counter intuitive effect is due to the fact that, at least when using the SCvH EOS, completely homogeneous models (central core plus a fully homogeneous envelope) cannot in general reproduce both the observed J_2 and J_4 (Chabrier et al. 1992 ; Saumon and Guillot 2004). Thus, if we relax the constant Z condition in the envelope, the presence of a compositional gradient and of a smaller core appears to be the best solution to reproduce observational data, even in the absence of any additional super-adiabaticity.

For Jupiter, models can be found that match the gravitational moments without the presence of a central, completely differentiated core (red dots on the bottom right of Fig. 4.9). Such cases yield an atmospheric metallicity $Z_{atm} \sim 4 - 5\,Z_\odot$. The fact that the possible erosion of the core mass would have been more efficient in Jupiter than in Saturn might stem from the larger energy flux available in Jupiter (Guillot et al. 2004).

Table 4.3: Heavy element content for Jupiter and Saturn inferred from the various models consistent with these constraints within the quoted observational uncertainties.

	Jupiter	Saturn
Region	Amount of heavy elements ($M_\oplus$)	
	Homogeneous model	
Envelope	36	4.7
Core	3.9	25.6
Total	40	30.3
	Semi-convective models	
Envelope	41-63.5	10-36
Core	0-0.5	10-21
Total	41-63	26-50

4.6   Prospect for giant planet evolution

While the aim of present study is to examine and to constrain the properties of transport by semi-convection inside Jupiter and Saturn *at the present time*, the impact of non-adiabatic interiors on the

---

[9] Note that the abundances of heavy elements brought to Jupiter and Saturn, in particular water, could already be enriched compared with the solar value (Gautier et al. 2001)

cooling of these planets, and of giant planets in general, remains to be explored. This requires more cumbersome evolutionary calculations, for which initial conditions will be of crucial importance, as will be explored in a forthcoming study. Note that evolution will add an additional constraint, namely that the planet cooling rates yield the correct properties at the age of the solar system, which will put more stringent constaints on the range of possible layer sizes/numbers. Without going into such detailed calculations, however, the following points can be mentioned.

4.6.1 Merging of the layers

As mentioned in § 4.3, soon after they form, layers are expected to merge, leading to larger layers, until the layer height reaches either the planet size, yielding a standard adiabatic interior, or an equilibrium value, which is the semi-convective case considered here. Numerical simulations by Radko (2005) and Rosenblum et al. (2011) tend to show that the equilibration timescale of the staircase is much shorter than the typical timescale for the evolution of the planet.

Thus, if an equilibrium height is reached, as discussed in § 4.3.1, this rather quick equilibration timescale suggests that the layer size should remain roughly constant during the evolution, or change slowly with the mean properties of the medium (e.g. the mean molecular weight gradient). A precise prescription for the height of the layers being yet lacking and demanding a more precise knowledge of the heat transport properties of layered convection under astrophysical conditions, it seems reasonable, as a first guess, to use a constant size, whose value has been constrained in the afore sections, throughout the evolution.

4.6.2 Initial heavy element distribution

Conventional models based on fully adiabatic thermal profiles notably lead to cooling times about 15% longer than the age of the Solar System for Jupiter (Fortney et al. 2011). In principle, the hotter non-adiabatic internal structures suggested in the present paper will prolong the cooling and thus worsen the problem.

However, in the case of the erosion of an initially large core, part of the gravitational work will be spent eroding the core and mixing the material upward and will thus not contribute to the total luminosity, quickening the cooling. All these effects must be properly accounted for to infer the appropriate cooling timescale.

In addition, if Jupiter and Saturn initial cores were allowed to be relatively large ($\gtrsim 10 M_{\oplus}$), the corresponding high surface density of solids in the protosolar nebula will quicken the formation timescale in the conventional core accretion scenario, helping solving the related formation timescale problem (Pollack et al. 1996). Finally, since, in the present scenario, some of the ablated material from the accreted planetesimals during the planet's early formation stages remains distributed throughout the envelope, this will (i) reduce the heating due to gravitational energy release produced by the infalling planetesimals on the planet embryo and (ii) increase the envelope mean molecular weight. Both effects will cause the protoplanet to contract more quickly, shortening again the planet's formation timescale in the conventional core accretion scenario (Pollack et al. 1996). A correct exploration of the impact of inhomogeneous interiors upon giant planet history thus necessitates to investigate the consequences not only on the thermal evolution but also on the formation process.

4.7 Conclusion and perspective

In this chapter, **I have first developed an analytical approach of layered convection, based on a standard parametrization of convection similar to the MLT formalism.** This formalism allows a quantitative determination of the expected number of diffusive layers, or equivalently of the average characteristic mixing-length parameter, in a semi-convective planet interior characterized by a given total flux and a given thermal (and compositional) diffusivity. Furthermore, **this formalism allows an exact determination of the characteristic thermal gradient in the presence of double-diffusive convection, and thus of the related amount of super-adiabaticity within the planet's interior.**

Using this formalism, **I have computed semi-convective interior models of Jupiter and Saturn. I have shown that a stratified internal structure for Solar System gaseous giants, with a compositional gradient of heavy material extending over a substantial fraction of the planet, is a viable hypothesis**, as such models can fulfill all the observed gravitational and atmospheric constraints for these planets. This new possibility differs from the conventional description of giant planet interiors, assumed to be composed of 2 main superposed, well identified layers of homogeneously distributed material, namely a solid core surrounded by a dominantly gaseous H/He envelope. The consequences of the present giant planet interior description are multiple. Namely,

- **(i) our jovian planets might be significantly more enriched in heavy elements than previously thought**,

- **(ii) their interior temperature, thus heat content, might be much larger than usually assumed,**

- **(iii) the inner temperature profile could significantly depart from the usually assumed adiabatic profile.**

Note that these conclusions do not depend on the precise model used to describe double diffusive convection.

Besides directly affecting our conventional vision of giant planet mechanical, compositional and thermal structures, these results have profound impacts on our understanding of planet formation and cooling properties. Indeed, the revised possible maximum amount of heavy material bears direct consequences on the determination of the efficiency of solid planetesimal accretion during planet formation in the protoplanetary nebula, suggesting an early and efficient capture of planetesimals for our, and probably extrasolar as well, giant planets. Moreover, the larger heat content and the departure from adiabaticity, as well as the possibility of significant core erosion from an initially large core, directly impact the planet cooling histories. Departure from adiabaticity, in particular, implies less efficient heat transport, a direct consequence of the inhibited convective motions due to a persistent compositional gradient, and thus a smaller heat flux output rate than assumed in the conventional approach. These results open a new window, and raise new challenges, on our present understanding of planet structure, formation and evolution. Importantly, the viability of such stratified interior models for our Solar System gas giants directly applies to the case of extrasolar planets, reinforcing the possibility that such a lower heat flux output could at least partly explain the anomalously large radius of several transiting "hot Jupiters" (Chabrier and Baraffe 2007). Indeed, it seems that invoking an extra source of (tidal, kinetic or magnetic) energy dissipation in these object interiors can not completely solve this "radius anomaly" puzzle and that an alternative or complementary process is necessary (Laughlin et al. 2011). Unconventional, inhomogeneous non-adiabatic planetary interiors, as suggested in the this chapter, might provide the missing piece of the puzzle.

Chapter 5

An alternative energy source: Tidal friction

Contents

After examining in detail in § 5.1.2 the relation between the *constant time lag* (Δt) in Hut (1981) model and the usual tidal quality factor (Q) widely used in the literature, in Appendix I, I extend the Hut model to any finite obliquity. Then, in § 5.2, I present analytical solutions of the equations that I derived for two limiting cases. These simple models have two purposes, (i) providing benchmarks for the numerical code that I developed to solve the full set of equations, and (ii) allowing an analytical constraint on Δt from the study of the Galilean satellites with the constant timelag model. In § 5.3, I also update the results of Levrard et al. (2009) by including newly found transiting planets, and find many new stable systems.

In § 5.4 I demonstrate with *analytical arguments* that truncating the tidal equations at 2nd order in eccentricity leads to wrong tidal evolution histories, with sequences drastically differing from those obtained when solving the complete equations. In § 5.5, I compare the full thermal/orbital evolution calculations with similar studies based on a truncated and constant Q tidal model. These numerical comparisons confirm and quantify the conclusions reached in § 5.4, namely that low-order eccentricity models substantially underestimate the tidal evolution timescales for initially eccentric systems and thus lead to incorrect tidal energy contributions to the planet's energy balance. I show for instance that tidal heating cannot explain the radius of HD 209 458 b for the present values of their orbital parameters, contrarily to what has been claimed in previous calculations based on truncated eccentricity models (Ibgui et al. 2009).

Finally I apply my model in § 5.6 to some of the discovered bloated planets. I show that although tidal heating can explain the presently observed radius of some *moderately bloated* Hot Jupiters, as indeed suggested in some previous studies, tidal heating alone cannot explain *all* the anomalously large radii. Indeed, in these cases eccentricity damping occurs too early in the system's tidal evolution (assuming a genuine two-body planetary system) to lead to the present state of the planet's contraction.

The results of this chapter led to the publication of *Is tidal heating sufficient to explain bloated exoplanets ? Consistent calculations accounting for finite initial eccentricity* (Leconte et al. 2010a) and in Leconte et al. (2011a). The results of § 5.2.3 where also used in *Tidal obliquity evolution of potentially habitable planets* (Heller, Leconte & Barnes 2011).

Gravitational

TIDES HAVE MARKED OUT THE HISTORY of science and astrophysics since the first assessment by Seleucus of Seleucia of the relation between the height of the tides and the position of the Moon and the Sun in the second century BC. Modern astrophysics extended the study of gravitational tides in an impressive variety of contexts from the synchronization of the Moon and other satellites to the evolution of close binary stars and even the disruption of galaxies.

The recent discoveries of short period extrasolar planetary systems and the determination of the anomalously large radius of some giant close-in exoplanets revived the need for a theory of planetary tides covering a wider variety of orbital configurations than previously encountered in our own solar system planets. In particular, the orbital evolution of very eccentric systems like HD 80 606 ($e \approx 0.9337$, Naef et al. 2001), or of planets on polar and even retrograde orbits, like HAT-P-7 b (with a stellar projected obliquity $\approx 182.5 \pm 9.4\,\mathrm{deg}$; Pál et al. 2008), cannot be properly treated with tidal models limited to the case of zero or vanishing eccentricity and obliquity.

5.1 Theory of tidal evolution

5.1.1 Tidal potential

Since Kepler (1609), we know that when two spherical body are in gravitational interaction, they undergo - provided that their total mechanical energy is negative - a Keplerian motion consisting in elliptical orbits. It has been shown by Newton (1687) that this behavior stems from the scaling of the gravitational force between the two bodies as the inverse of the square of their separation. Of course, this simplicity of the gravitational potential relies heavily on the assumption of spherical symmetry of the object creating the potential, and breaks when its mass distribution presents non spherical deformations.

These asymmetries can be separated in two classes that have quite a different impact on the dynamical properties of the object.

The permanent or slowly varying asymmetries

Their origin can be very diverse. In rigid or elastic bodies, such as rocky planets and asteroids, the internal stress keeps the structure from evolving toward its minimum energy state, conserving the primordial asymmetries inherited from the formation stage. For small - generally undifferentiated - objects, where self-gravitational energy is still comparable to the internal electromagnetic cohesion forces, this primordial asymmetry can directly come from an inhomogeneous accretion of matter. For more massive objects, including planets, the energy released during mass accretion is sufficient to liquify the bulk material. During this early fluid phase, differentiation takes place and the object is in a state of near hydrostatic equilibrium. As discussed in Chapter 3, in such a phase, the presence of a disturbing potential gives rise to a non-spherical shape that can be crystallized during the cooling and solidification of the
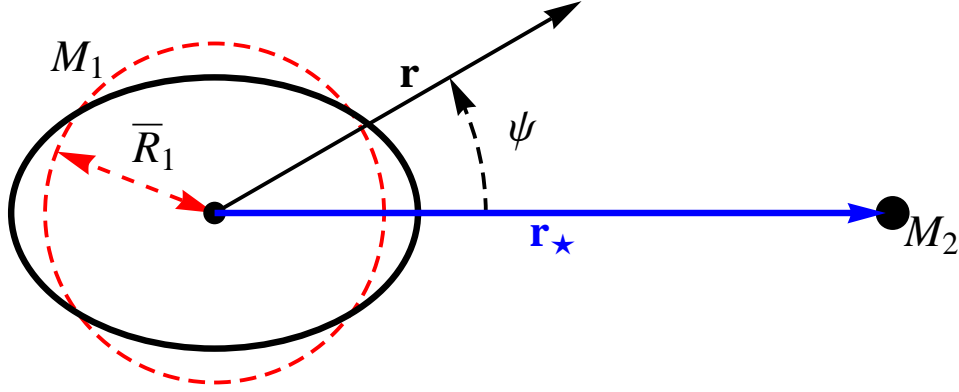
Figure 5.1: External potential created by a deformable body under the influence of a distant companion.

planet. This is thought to be the cause of the flattening observed on our own earth and all other rocky planets in the solar system. For fluid bodies, like giant gaseous planets, a fast rotation also prevents the sphericity of the object.

Up to the quadrupole order, it can be shown that the potential of the object is given by

$$V_G(\mathbf{r}) = -\frac{GM_1}{r} - \frac{G}{r^3}\left[(B-A)\left(\frac{1-3(\hat{\mathbf{r}}\cdot\hat{\mathbf{j}})^2)}{2}\right) + (C-A)\left(\frac{1-3(\hat{\mathbf{r}}\cdot\hat{\mathbf{k}})^2)}{2}\right)\right], \tag{5.1}$$

where A, B, and C are the principal moment of inertia of the body with respect to the axis following $\hat{\mathbf{i}}$, $\hat{\mathbf{j}}$ and $\hat{\mathbf{k}}$, respectively. This perturbation to the gravitational potential causes the precession of the periapsis, and the precession and nutation of the spin of the planet. For perfectly rigid bodies, no energy is dissipated, and these effects are periodic. The precession period for example can be approximated by

$$P_{\mathrm{pr}} = \frac{2\pi}{3}\frac{\omega_1}{n^2\cos\varepsilon_1}\frac{2C}{2C-A-B}, \tag{5.2}$$

where ω_1 is the angular velocity of the body, and ε_1 is its obliquity, i.e. the angle between the rotation and the orbital axis. Because the periods of these processes range from a few days to a few million years, when no resonances arise, the precession-nutation motion can be averaged to compute the secular tidal evolution on a billion years timescale, as discussed later.

The periodic deformations

For an elastic or fluid body, the presence of an external perturbation, like the one created by a secondary body, creates a distortion of both the shape and the gravitational field of the object, as discussed above. As detailed in Chapter 3, the external gravitational field created at the location $\mathbf{r}$ by a deformable body perturbed by a secondary point mass (M_2) located at $\mathbf{r}_\star$ (See Fig. 5.1) is given by Eq. (3.31):

$$V_G(\mathbf{r}, \mathbf{r}_\star) = \frac{GM_1}{r}\left[1 - \sum_{n=2}^{\infty} k_n \frac{\bar{R}^{2n+1}}{r^n r_\star^{n+1}}\frac{M_2}{M_1}P_n(\cos\psi)\right], \tag{5.3}$$

where ψ is the angle between $\mathbf{r}$ and $\mathbf{r}_\star$, $\bar{R}$ is the mean radius of the primary and k_n is the love number of degree n. This perturbed gravitational field also creates periodic variations of the orbital elements. In particular the n = 2 term entails an apsidal precession that can be measured and give direct constraints on the internal structure of the object considered (Sterne 1939).

The major difference with the permanent inhomogeneities discussed above is that the external perturbation varies with time, and so does the shape of the primary (Eq. (3.22)). This of course involves

large scale motions, or "tides", of the fluid composing the latter. The direct consequence of this forced internal motion in the fluid is that the viscosity of the material can act to damp the oscillations. It is of course understood that, in gaseous bodies, the molecular viscosity alone has a negligible effect on these large scales motion (Hubbard 1974) and that some dynamical mechanism are needed to transfer the energy from the large scales to the small scales where it can be dissipated and transferred into internal energy. The exact nature of these mechanisms - gravity waves, inertial waves, elliptical instability, etc... - is still subject to debate (Zahn 1989 ; Zahn and Bouchet 1989 ; Rieutord and Zahn 1997 ; Rieutord 2004 ; Ogilvie and Lin 2007 ; Goodman and Lackner 2009 ; Barker and Ogilvie 2010 ; Cébron et al. 2011).

However, this dissipation is not yet present in Eq. (5.3). Indeed, this equation describe the potential of an object in hydrostatic equilibrium[1], and applies only if the time needed for the body to relax to this equilibrium state is infinitely short compared to the timescale of the orbital motion. In this case, it can be shown that the forces derived from Eq. (5.3) exert no average work over an orbit, and thus do not cause any secular energy dissipation.

5.1.2 Modeling the dissipation

Including the effect of dissipative processes arising inside the deformable body on its orbital dynamics is a rather complicated matter. Indeed, in addition to the various sources of friction in the non ideal medium, the forcing tidal frequencies are not, in the cases of interest, very different from the characteristic frequencies of the various oscillations or waves that can take place in the deformable body. The large scale tidal motion can then excite these waves, and a complete modeling of these dynamical processes coupled with the orbital motion is needed.

The earliest mathematical model for the dynamical effects of tides is due to George Darwin (son of naturalist Charles Darwin). In his pioneering work, he assumed that tidal friction was solely due to viscosity, and developed a linear theory of the *equilibrium tides*, in which the departure of the shape of the deformable body from hydrostatic equilibrium is small and can be related to the strength of the dissipation (Darwin 1880, 1908). In practice, this assumes that the perturbing potential created by the tides raising object can be split in a sum of Fourier components, and that the response of the primary to each of these terms is linear and depends only on its frequency ($\sigma/2\pi$). The direction of each of these tidal bulges is then shifted with respect to the direction of the secondary by an angle $\delta(\sigma)$, and the amplitude of the wave can differ from the equilibrium value. Modern astrophysics generalized and extended Darwin's work to an impressive variety of contexts, from the synchronization of the Moon and other satellites to the evolution of close binary stars (Kaula 1964 ; MacDonald 1964 ; Goldreich and Soter 1966 ; Goldreich 1966 ; Mignard 1978, 1979, 1980 ; Hut 1980, 1981 ; Zahn 1989 ; Zahn and Bouchet 1989 ; Touma and Wisdom 1993, 1994 ; Neron de Surgy and Laskar 1997 ; Eggleton et al. 1998 ; Correia and Laskar 2001 ; Jackson et al. 2008 ; Ferraz-Mello et al. 2008 ; Efroimsky and Williams 2009 ; Levrard et al. 2009 ; Leconte et al. 2010a, 2011b). However, when considering the impact of the dissipative processes on the orbital evolution, all these models still rely on a simple parametrization in terms of lag angles and amplitudes.

Then, the difficulty lies in choosing the best formulation for $\delta(\sigma)$, or equivalently for the phase lag $\varepsilon(\sigma)$[2]. A simple way to link this lag angle to the dissipation is through the specific dissipation function (Q^{-1}), which is defined, at each frequency, as the energy damped over a cycle of flexure divided by the peak energy stored in the system during that time (Goldreich 1963 ; Efroimsky and Williams 2009).

---

[1] Meaning here that there is no motion in the considered frame, but elastic forces can be present and are already accounted for in k_n.

[2] The response to a perturbation proportional to $e^{i\sigma t}$ thus being proportional to $e^{i(\sigma t+\varepsilon)}$. For the usual diurnal tides, both angles are simply related by $2\delta = \varepsilon$.

Efroimsky and Williams (2009) show that

$$Q^{-1}(\sigma) \equiv -\frac{\Delta_{\text{cycle}} E(\sigma)}{2\pi E_{\text{peak}}(\sigma)} = \frac{\tan|\varepsilon(\sigma)|}{1 - (\frac{\pi}{2} - |\varepsilon(\sigma)|)\tan|\varepsilon(\sigma)|}. \tag{5.4}$$

Thanks to this relation, specifying the spectrum of the dissipation, either by equilibrium or dynamical tides, is sufficient to infer the impact of tides on the orbital evolution of the system.

However, to further simplify the model, one of the two following assumptions is often made.

Constant Q approximation

Based on the observation that, for the earth, the specific dissipation function varies by less than one order of magnitude between the Chandler period[3] (~ 440 days) and the periods relative to seismic waves (a few seconds), it is often assumed that the specific dissipation is constant with respect to the forcing frequency ($Q(\sigma) = Q$). The overall dissipation is therefore encompassed in a single number, the tidal Q (or equivalently Q'[4]), or the *constant phase lag ε*. However, this model has two major drawbacks, whose consequences will be more comprehensively discussed in the following sections.

(i) Inverting Eq. (5.4) in the limit of low dissipation, we see that $\varepsilon = \text{sign}(\sigma)/Q$. This model thus introduces a discontinuity at each time that one of the tidal frequency vanishes. This assumption is thus particularly unjustified when considering tides on nearly synchronized objects, as it is thought to be the case for most close in exoplanets.

(ii) Because, one must first decompose the forcing potential in terms with a well defined phase and frequency before lagging them with the chosen lag, perturbative developments of Kepler equations of motion, both in eccentricity and inclination must be used. The resulting equations are then strictly valid only in the low eccentricity and obliquity regime.

Weak friction approximation

As shown by Darwin (1880) and Alexander (1973), the frequency dependence of the phase lag of a purely viscoelastic oscillator is given by

$$\tan(\varepsilon) = \frac{\sigma}{\tau_{\text{v}}(\omega_0^2 - \sigma^2)}, \tag{5.5}$$

where τ_{v} is a viscous damping timescale and $\omega_0/2\pi$ the natural frequency of the oscillator. In an incompressible gaseous body, the restoring force acting against the tidal deformation is the self-gravity of the body. Thus ω_0 can be estimated through the free-fall time as $2\pi/\omega_0 \approx \frac{1}{4}\sqrt{\frac{3\pi}{2G\bar{\rho}_1}} \approx 30$ minutes for Jupiter mean density ($\bar{\rho}_1 \approx 1.33 \times 10^3 \text{kg/m}^3$). For tidal periods of several days $\omega_0 \gg \sigma$ and for weakly viscous fluid, the phase lag reads

$$\varepsilon(\sigma) \approx \frac{\sigma}{\tau_{\text{v}} \omega_0^2}. \tag{5.6}$$

---

[3] Period of the free motion of the of the figure axes of a body around its rotational pole.

[4] Because the efficiency of tidal processes is proportional to the product of the amplitude of the tides (proportional to k_2) with the efficiency of the damping of these tides (inversely proportional to Q), it is customary to introduce the reduced quality factor $Q' = \frac{3}{2}\frac{Q}{k_2}$, so that $Q' = Q$ for an incompressible homogeneous sphere.

In this weak friction approximation, the specific dissipation then scales linearly with the forcing frequency. Each Fourier component is thus delayed by a single *constant time lag*

$$\Delta t \equiv \frac{1}{\tau_v \, \omega_0^2}, \text{ with } \varepsilon(\sigma) \approx \sigma \Delta t. \tag{5.7}$$

While this approximation may overestimate the dissipation for high frequencies ($\sigma \gtrsim \omega_0$), it entails a significant simplification. Indeed, in the frame co-rotating with the deformable body, the tidal forces exerted by the secondary can be calculated by stating that the effect of viscosity is simply to delay the tidal bulge with respect to the tides raising potential by the same *constant time lag* Δt. As shown in Hut (1981), and detailed in Appendix I, thanks to this approximation, the set of equations for the tidal evolution of the orbital elements can be calculated for any eccentricity and inclination of the orbit in terms of closed formulae. Because many exoplanets are very eccentric, and for the reasons described in § 5.4, in the following, I will use this weak friction approximation.

The frequency dependent quality factor then reads,

$$Q(\sigma) \approx \frac{1}{\sigma \Delta t}. \tag{5.8}$$

It is therefore difficult to express a *global* dissipation efficiency. A rough estimate can nonetheless be found in cases for which the excitation spectrum reduces to a small number of frequencies. For non-synchronized circular orbits, semi-diurnal tides, whose frequency is twice the difference between the rotation rate of the primary (ω) and the orbital mean motion (n), dominate and setting $\sigma = 2|\omega - n|$ in Eq. (5.8) yields

$$Q^{-1} \approx 2\Delta t |\omega - n|. \tag{5.9}$$

This formula can be used to estimate the quality factor for non-synchronous bodies, such as the Sun, the Earth or Jupiter, as long as the eccentricity of the orbit is small. As the planet tends toward synchronization, the dissipative effects of the semi diurnal tides vanish with their frequency. Then, the most dissipative tides are the eccentric annual tides ($\sigma = n$) and

$$Q^{-1} \approx \Delta t \, n. \tag{5.10}$$

Apart from these two limit cases, no tidal frequency dominates, and the dissipation is the response of the body to the rich spectrum of exciting tidal frequencies. Thus no simple relation exists between Q and Δt in the general case.

Although it is tempting to use Eq. (5.10) to rewrite the tidal equation and to keep Q' constant instead of Δt as done by, for example, Mardling and Lin (2002), Dobbs-Dixon et al. (2004) and Barker and Ogilvie (2009), one must keep in mind that this procedure is not equivalent either to the constant phase lag (i.e. constant Q) or time lag model. Indeed the frequency dependence of the phase lag is given by $\varepsilon(\sigma) = \sigma/(nQ)$ and is still proportional to the tidal frequency over an orbit as in the constant time-lag model, but with a slope that is changing during the evolution, while no physical change has necessarily occurred inside our bodies.

5.1.3   Secular evolution equations

Having a prescription for the parameters modeling the dissipation in our bodies, in our case a constant *time lag*, we can concern ourselves with the determination of the secular change of the orbital elements of a tidally interacting binary system. We consider a system of two deformable bodies of mass

M_1 and M_2. Note that no approximation will be made on the masses of the two bodies, meaning that the following equations can be used in a large variety of contexts, covering Star-Star, Star-Planet and Planet-Satellite interactions.

The major interest of the *linear* model, i.e. at constant time lag, is that, as demonstrated by Hut (1981), equations can be derived to be valid up to any finite value of the eccentricity. However, his model remained restricted to vanishing obliquities. **In the calculations presented in Appendix I, using a vector representation of the tidal torque, I extend the set of tidal secular evolution differential equations to account for any finite obliquity.**

In fine, the complete equations taking into account tides in both bodies are obtained by computing separately the effects of the tides raised in both objects (as shown in Appendix I) and by adding them up. We are then left with the following set of six coupled, non linear equations of first order

$$\frac{1}{a}\frac{da}{dt} = \frac{4a}{GM_1M_2}\sum_i K_i\left[N(e)x_i\frac{\omega_i}{n} - N_a(e)\right], \tag{5.11}$$

$$\frac{1}{e}\frac{de}{dt} = \frac{11a}{GM_1M_2}\sum_i K_i\left[\Omega_e(e)x_i\frac{\omega_i}{n} - \frac{18}{11}N_e(e)\right], \tag{5.12}$$

$$\frac{dC_i\omega_i}{dt} = -\frac{K_i}{n}\left[\left(1+x_i^2\right)\Omega(e)\frac{\omega_i}{n} - 2x_iN(e)\right], \tag{5.13}$$

$$\frac{d\varepsilon_i}{dt} = \sin\varepsilon_i\frac{K_i}{C_i\omega_i n}\left[(x_i - \eta_i)\Omega(e)\frac{\omega_i}{n} - 2N(e)\right], \tag{5.14}$$

where $x_i = \cos\varepsilon_i$ and η_i is defined by Eq. (I.31). For details about the notations, the reader is referred to Appendix I. The various functions of the eccentricity are

$$N_a(e) = \frac{1 + \frac{31}{2}e^2 + \frac{255}{8}e^4 + \frac{185}{16}e^6 + \frac{25}{64}e^8}{(1-e^2)^{15/2}},$$

$$N_e(e) = \frac{1 + \frac{15}{4}e^2 + \frac{15}{8}e^4 + \frac{5}{64}e^6}{(1-e^2)^{13/2}},$$

$$N(e) = \frac{1 + \frac{15}{2}e^2 + \frac{45}{8}e^4 + \frac{5}{16}e^6}{(1-e^2)^6}, \tag{5.15}$$

and

$$\Omega_e(e) = \frac{1 + \frac{3}{2}e^2 + \frac{1}{8}e^4}{(1-e^2)^5},$$

$$\Omega(e) = \frac{1 + 3e^2 + \frac{3}{8}e^4}{(1-e^2)^{9/2}}. \tag{5.16}$$

The strength of the tides in the body i are parametrized by

$$K_i = \frac{3}{2}k_{2,i}\Delta t_i\left(\frac{GM_i^2}{\bar{R}_i}\right)\left(\frac{M_j}{M_i}\right)^2\left(\frac{\bar{R}_i}{a}\right)^6 n^2, \tag{5.17}$$

where the j index denotes the quantities relative to the other body. Notice here that no assumptions have been made on the masses of the objects studied. In particular, in our notations, the secondary can be the most massive object of the binary. In general, the tides raised in both objects have rather different amplitudes and dissipation timescales and effects. It can thus sometimes be useful to study them separately. In these cases, and when no confusion is possible, the index i will refer to the body on which tides are raised (the primary), and j will stand for the tides raising object (the secondary).

As shown in § I.2.3, for a strongly interacting low mass companion, such as a planet, pseudo synchronization is often achieved. Eqs. (5.13) and (5.14) can thus be replaced by $\varepsilon_\mathrm{p} = 0$ and ω_p equal

$$\omega_\mathrm{eq} = \frac{N(e)}{\Omega(e)} \frac{2x_\mathrm{p}}{1+x_\mathrm{p}^2} n = \frac{N(e)}{\Omega(e)} n. \tag{5.18}$$

In this case, the rate of tidal dissipation which is given by Eq. (I.43) in the general case can be rewritten

$$\dot{E}_\mathrm{tid} = 2K_1 \left[N_a(e) - \frac{N^2(e)}{\Omega(e)} \right]. \tag{5.19}$$

5.2 Some analytical solutions

The above equations are coupled and non-linear and must then be handled numerically in most cases. **For this purpose I developed a code integrating the set of equations by means of a leap-frog integrating scheme. In order to test both the code and the level of numerical error yielded by the integration, I solved the equations in some simple limit cases, which are presented below.** In addition, when the system studied is in the right regime, these analytical solutions can be used directly to have a more flexible model. **As shown in Leconte et al. (2010a) and in § 5.2.2, the model presented below can be used to constrain the dissipation inside Jupiter.**

5.2.1 Small object spiraling in or outward on circular orbits

Let us consider the case of a pseudo synchronized and aligned secondary around a non synchronized (but aligned) primary. This case is not purely ideal, as it can be used to describe the orbital evolution of binaries with large mass ratios, such as a satellite orbiting a planet, or a close in planet orbiting its host star. As we will see, in the first case, the often fast rotation of the planet pushes the satellites away (as for the Earth, Jupiter, Saturn, etc...), whereas the slow stellar rotation causes most exoplanets to spiral inward, and eventually cross the Roche lobe where they are tidally disrupted. In this case, some simplifications occur. Let us take the following initial conditions:

$$\begin{pmatrix} \omega_1(t=0) = \alpha n_0 \\ a(t=0) = a_0 \\ e(t=0) = 0 \end{pmatrix}.$$

Thanks to Eq. (5.12), we can show that if $\alpha < \frac{18}{11}$, $e = 0$ is a stable value for the eccentricity and will not evolve with time. With the same argument we can show that $\varepsilon_\mathrm{i} = 0$ are also stable solutions. As the pseudo synchronization approximation gives $\omega_2 = \omega_\mathrm{eq} = n$, we are left with only two variables and equations to solve simultaneously. Let us highlight that in this configuration, there is no more dissipation in the secondary, and the only tidal effects are due to the tides raised on the primary. Taking the dimensionless variables $\tilde{a}$ counted in units of a_0 and t in units of

$$\tau_\mathrm{in} = \frac{1}{6} \frac{M_1^2}{M_2(M_2+M_1)} \left(\frac{a_0}{\bar{R}_1}\right)^8 \frac{\bar{R}_1^3}{GM_1 k_{2,1} \Delta t_1}, \tag{5.20}$$

the equations read

$$\dot{\omega}_1 = \frac{\tau_\mathrm{in}}{\tau_\mathrm{sync}} \frac{n}{\tilde{a}^6} \left[1 - \frac{\omega_1}{n} \right],$$

$$\dot{\tilde{a}} = -\frac{1}{\tilde{a}^7} \left[1 - \frac{\omega_1}{n} \right]. \tag{5.21}$$

The combination of these equations gives

$$\dot{\omega}_1 = -\frac{\tau_{\text{in}}}{\tau_{\text{sync}}} \frac{\mathring{a}}{\sqrt{\tilde{a}}} n_0$$

and by time integration

$$\frac{\omega_1}{n_0} = \alpha - \tilde{\beta}(\sqrt{\tilde{a}} - 1), \tag{5.22}$$

where the initial conditions have been used and $\tilde{\beta} = 2\tau_{\text{in}}/\tau_{\text{sync}}$. This relation is to be expected as it is simply the expression of the conservation of the total angular momentum of the system[5]. Substituting Eq. (5.22) in Eq. (5.21) yields:

$$\mathring{a} = -\frac{1}{\tilde{a}^7} \left[1 - \tilde{a}^{3/2}(\alpha - \tilde{\beta}(\sqrt{\tilde{a}} - 1)) \right].$$

Therefore, the following integration gives an implicit solution for the semi major axis

$$\boxed{\int_1^{\tilde{a}} \frac{-\tilde{a}^7 \mathrm{d}\tilde{a}}{1 - \tilde{a}^{3/2}(\alpha - \tilde{\beta}(\sqrt{\tilde{a}} - 1))} = \tilde{t}.} \tag{5.23}$$

I computed this analytic solution and compared it with the numerical integration of the full set of equations (including the spin state of the planet). For a given object, the only parameters left are the ratio of initial rotational over orbital angular velocities (α), and the initial semi-major axis (a_0). I decided to consider a system near the critical semi-major axis a_{crit}, as defined in § 5.3, with $a_0 = 1.03\ a_{\text{crit}}$. Therefore, choosing an $\alpha < \alpha_c$ [6] yields an unstable system with a total angular momentum lower than H_{crit}. As shown in figure 5.2, in this case angular momentum is transferred from the orbit to the central object until the merging of the two bodies. For $\alpha > \alpha_c$ the system tends to the closest stable orbital equilibrium available for its angular momentum and the angular momentum is transferred from spin to orbit.

Figure 5.3 shows the discrepancies between the analytical solution derived here and the numerical integration. As the numerical integration dealt with the full set of equations, these discrepancies are due both to the numerical error and to the pseudo synchronization hypothesis for the planet. Further calculations showed that in this case the numerical errors are predominant. This validates the pseudo synchronization hypothesis made for most of the computations involving a star-planet system, as done hereafter.

5.2.2 Constraining the dissipation in Jupiter

In order to use the constant *time lag* model, we must consider many values for Δt. **To constrain the range of values to use in the numerical calculations performed in § 5.5, I follow the analysis of Goldreich and Soter (1966), but with the constant time lag model, and use the Io-Jupiter system to infer an upper limit for $k_{2,\text{p}} \times \Delta t_\text{p}$ in giant extrasolar planets (Leconte et al. 2010a).** As I shown above, because the massive body (hereafter Jupiter) is rapidly rotating, with $\omega_\text{J} > n_\text{S}$, where n_S is the orbital mean motion of any of the satellites of Jupiter, tidal transfer of angular momentum drives the small bodies *outwards*, into expanding orbits. Therefore the presence of Io in a close orbit provides an upper limit for the time lag in Jupiter. Indeed, if Δt_p was too large, the backward evolution of the satellites' orbits would imply their disappearance within less time than the age of the Solar system, i.e. of Jupiter.

---

[5]The angular momentum of the planet can be neglected, which is, here, equivalent to the pseudo synchronization hypothesis.
[6]$\alpha_c \approx 0.995$ in this case.
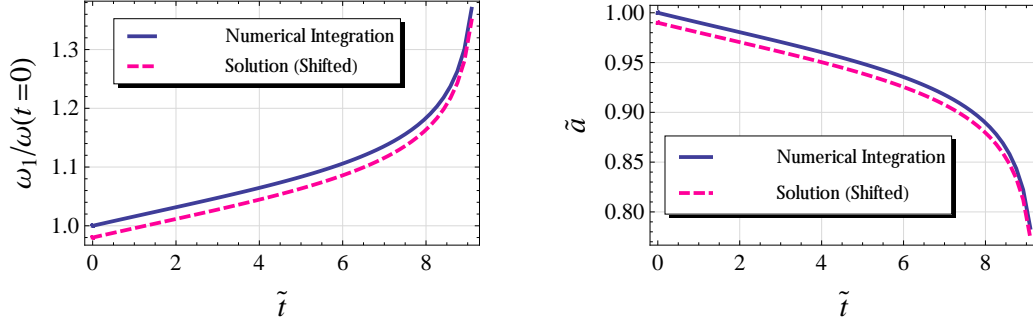
Figure 5.2: Comparison between the exact solution given by Eq. (5.23) for the angular velocity of the primary and the semi-major axis and the numerical integration of the full set of equations. The exact solution has been shifted to be visible (the real relative error is $\lesssim 10^{-6}$). As predicted for $\alpha < 1$ angular momentum is transferred from the orbit to the central object: the primary is spinning up while the semi-major axis is decreasing. As this configuration is not stable ($\alpha < \alpha_{\rm c}$), the two objects will eventually merge at $t \approx 9.3\,\tau_{\rm in}$.

I can thus use the model described above and directly integrate Eq. (5.23). Note that in this context, this integral cannot be performed down to $a = 0$ because the satellite first crosses the co-rotation radius where the integrand tends to infinity, which is an unstable equilibrium state for the system (Hut 1980). For the Io-Jupiter system, taking $t = -4.5 \times 10^9$ yr and $a(t)$ equal to the Roche limit in Eq. (5.23) yields $k_{\rm J}\Delta t_{\rm J} \lesssim 5 \times 10^{-3}$ s. Therefore Eq. (5.9) implies $Q'_{\rm J} \gtrsim 1 \times 10^6$ for the actual Io-Jupiter system, slightly lower than the value derived by Goldreich and Soter (1966). As discussed by these authors, our upper limit on $\Delta t_{\rm p}$ must be multiplied by a factor 5 to 7.5, as Io might have been trapped in a low order commensurability with Europa and Ganymede during part of its evolution, slowing down the expansion of its orbit. **Thus, as discussed in Leconte et al. (2010a), for Jupiter,**

$$\boxed{\mathbf{k_J \Delta t_J \lesssim 2 - 3 \times 10^{-2}\,s.}} \tag{5.24}$$

For the sake of easy comparison, I will refer to the quantity Q'_0, which is the reduced quality factor computed for a reference period of one day:

$$Q'_0 = \frac{3}{2}\frac{Q(2\pi/1\,\text{day})}{k_2} = \frac{3}{2}\frac{1\,\text{day}}{2\pi k_2 \Delta t}. \tag{5.25}$$

The above calculated constraint reads $Q'_{0,\rm p} \gtrsim 1 \times 10^6$. In the calculations presented in the following sections, I will examine two cases for the planet under consideration, namely $Q'_{0,\rm p} = 10^6$ and $Q'_{0,\rm p} = 10^7$ ($k_{2,\rm p}\Delta t_{\rm p} \sim 2 \times 10^{-2} - 2 \times 10^{-3}$), while taking $Q'_{0,\star}$ in the range $10^5 - 10^6$ ($k_{2,\star}\Delta t_\star \sim 2 \times 10^{-1} - 2 \times 10^{-2}$), a typical value for solar-type stars (Ogilvie and Lin 2007).

It is important to stress that if Δt, or its counterpart Q, is poorly known for both planets and stars, its variability from one object or configuration to another is even more uncertain. For instance, the tidal dissipation in planets probably differs significantly from that in brown dwarfs because of a dense core able to excite inertial waves in the convective envelope (Goodman and Lackner 2009). Given the highly non-linear behavior of tidal dissipation mechanisms, the effective tidal dissipation function varies not only with the structure of the object or with the tidal frequency, but also with the amplitude of the tidal potential. For example, $Q'_\star$ values inferred from the circularization of close FGK binary stars (Meibom and Mathieu 2005), may be lower than the actual $Q'_\star$ encountered in star-planet systems (Ogilvie and
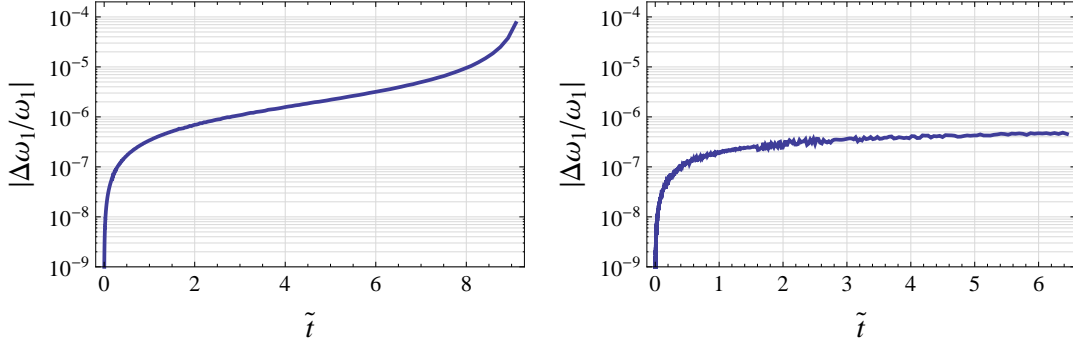
Figure 5.3: Relative error between the exact solution given by Eq. (5.23) and the numerical integration of the full set of equations (right: unstable system, left: stable system). The numerical integration yields correct results down to 10^{-6}. The error grows near the singularity corresponding to the fall of the planet on to the star.

Lin 2007). Consequently, the range of values considered here for both $Q'_\star$ and Q'_p should be seen as mean values and be re-evaluated when considering specific and/or atypical systems (XO-3, HAT-P-2 or CoRoT-3 for example).

5.2.3 The spin state of the low mass companion.

In the previous section we discussed the angular momentum transfer between a massive primary and the orbital motion. To do so, we assumed synchronism between the rotation of the smaller companion and the orbit. For long term evolution, because the synchronization timescale for the planet is very short compared to the one of the orbital evolution, this assumption is justified as discussed in § I.2.1 and verified in § 5.2.1. For the same reason, if we want to look at the evolution of the spin state of the low mass companion, the other orbital parameters can be considered frozen in time because they evolve on a much longer timescale. This is what I attempt to do in this section. This will allow us to verify the coupling between the equations on ω and ε for any eccentricity. Let us take the following initial conditions:

$$\begin{pmatrix} \omega_1(t) = \omega_0 \\ a(t) = a_0 \\ e(t) = e_0 \end{pmatrix}.$$

We are left with only two equations, Eqs. (5.13) and (5.14), for the variables ω_2 and ε_2 to solve simultaneously. The non linearity of these equations with respect to ε_2 and the coupling between the equations prevents any analytical solution to be found in the general case. Therefore we will consider only the linear case, implying $\varepsilon_2 \ll 1$. In addition, we place ourselves in the case where

$$\eta_2 \propto \frac{M_1 + M_2}{M_1} r_{g,2}^2 (\bar{R}_2/a)^2 \ll 1,$$

meaning that the internal angular momentum of the object can be neglected with respect to the orbital one. This assumption is fully justified for a planet, as is confirmed by the numerical integration. Since the eccentricity and the semi-major axis are fixed, it is tempting to use the following dimensionless
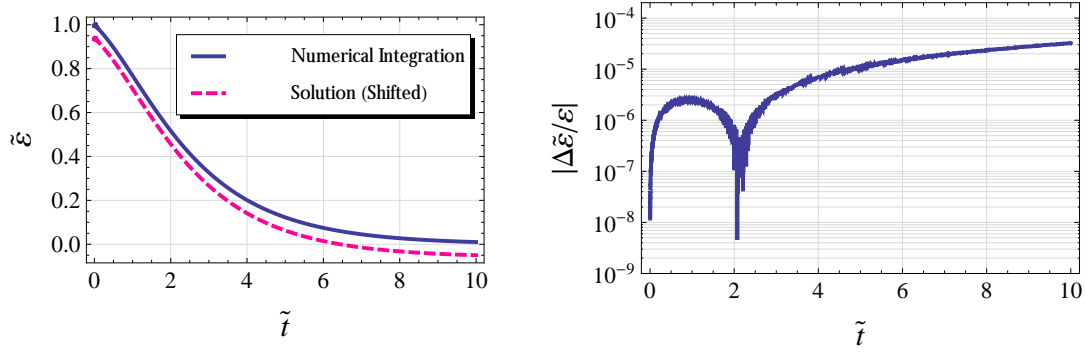
Figure 5.4: Left: Comparison between the exact solution given by Eq. (5.28) for the obliquity obliquity of the planet and the numerical integration of the full set of equations. The exact solution has been shifted to be visible. As predicted the planet pseudo synchronizes and its obliquity is damped to 0. Right: Relative error between the exact solution and the numerical integration. The numerical integration yields correct results down to 10^{-5}. The peculiar behavior of the error is due to the fact that the solution is not convex: the sign of the error changes.

variables,

$$
\begin{cases}
\tilde{t} = t\,\Omega(e)/\tau_{\text{sync}} \equiv t/\tilde{\tau}_{\text{sync}} \\
\tilde{\omega} = \omega_2/\omega_{\text{eq}} \\
\tilde{\varepsilon} = \varepsilon_2/\varepsilon_{2,0}
\end{cases}
,
\tag{5.26}
$$

where ω_2 is normalized to the pseudo synchronization rotation speed and $\varepsilon_{2,0}$ is the initial obliquity of the planet. We finally just need to provide an initial condition for the angular velocity: $\tilde{\omega}(t=0)=\tilde{\omega}_0$. The equations thus read:

$$
\dot{\tilde{\omega}} = 1 - \tilde{\omega},
$$

$$
\dot{\tilde{\varepsilon}} = \tilde{\varepsilon}\left[\frac{1}{2} - \frac{1}{\tilde{\omega}}\right].
$$

Fortunately, the obliquity creates only a second order perturbation of the other equations, and thus our system is no longer coupled. We can then solve our system sequentially. The first equation being similar to the one of a damped twisted pendulum without inertia, we can see that the rotation rate will relax toward its quasi equilibrium value following an exponential decay of the form

$$
\tilde{\omega}(\tilde{t}) = 1 + (\tilde{\omega}_0 - 1)\mathrm{e}^{-\tilde{t}}.
\tag{5.27}
$$

Thus

$$
\ln(\tilde{\varepsilon}(\tilde{t})) = \frac{\tilde{t}}{2} - \int_0^{\tilde{t}} \frac{\mathrm{d}t}{1 + (\tilde{\omega}_0 - 1)\mathrm{e}^{-t}}
$$

$$
\tilde{\varepsilon}(\tilde{t}) = \frac{\tilde{\omega}_0\,\mathrm{e}^{\tilde{t}/2}}{\mathrm{e}^{\tilde{t}} + (\tilde{\omega}_0 - 1)}.
\tag{5.28}
$$

I compared this analytical solution with the numerical integration of the full set of equations in Fig. 5.4. As predicted the planet pseudo synchronizes and its obliquity is damped to zero on a short timescale compared to the global orbital evolution. As can be seen from Eq. (5.14) in the general case, or by differentiating Eq. (5.28) with respect to time, we can see that when the rotation of the object becomes larger than twice the pseudo synchronous rotation rate, the zero obliquity state is no longer stable. **This analytical model has been used to countercheck our numerical results in Heller et al. (2011).**

5.3   Are transiting planetary systems about to merge ?
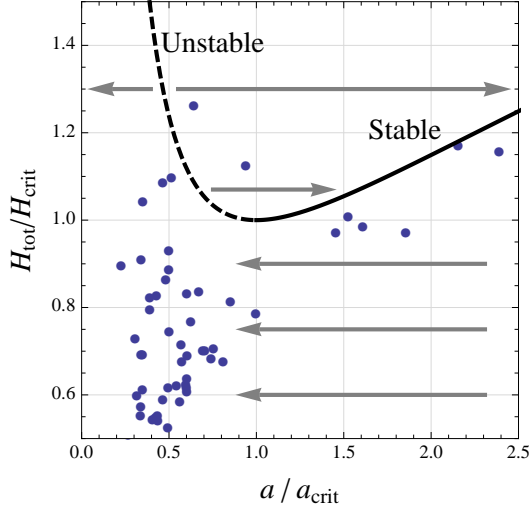
Figure 5.5: $H_{tot}(a)$ for equilibrium states in unit of (a_{crit}, H_{crit}). The solid (dashed) part of the curve represent the (un)stable branch. Gray arrows show the direction followed by $a(t)$ in each part of the diagram. The dots represent observed values for transiting systems. In all the systems with $H_{tot} < H_{crit}$, the planet will eventually merge with its star.

From the equations shown in § 5.1.3, we directly see that a tidal equilibrium is achieved only when the two bodies are in a state of coplanarity ($\varepsilon_i = 0$), circularity ($e = 0$) and co-rotation ($\omega_i = n$). However, this does not tell us whether such equilibrium states exist or can be reached by a given system ! Thanks to Hut (1980) a criterion for the existence of these states can be derived. Indeed, because the total angular momentum of the system is conserved, and tidal friction dissipates mechanical energy, a system with a given angular momentum (H_{tot}) will be able to reach equilibrium only if there is an equilibrium state with the same angular momentum. The stability of the equilibrium can then be deduced from the fact that energy is at a minimum and not a maximum.

Let us then study the angular momentum of equilibrium states, which is given by

$$H_{tot} = H_{orb} + H_1 + H_2. \tag{5.29}$$

Hut (1980) showed that, thanks to the synchronization condition, this rewrites

$$H_{tot} = H_{equ}(a)$$
$$= H_{crit}\left[\frac{3}{4}\left(\frac{a}{a_{crit}}\right)^{1/2} + \frac{1}{4}\left(\frac{a_{crit}}{a}\right)^{3/2}\right], \tag{5.30}$$

where $\boxed{a_{crit} = \sqrt{3\dfrac{(M_1+M_2)}{M_1 M_2}(C_1+C_2)}}$ and $\boxed{H_{crit} = 4\left(\dfrac{G^2(M_1 M_2)^3}{27(M_1+M_2)}(C_1+C_2)\right)^{1/4}}$.

This shows that the angular momentum of a configuration in equilibrium only depends on the semi-major axis. It is easy to see that $H_{equ}(a)$ has a minimum reached for a_{crit}[7] for which the minimum reads H_{crit}[8]. Thus, only systems with $H_{tot} > H_{crit}$ can pretend to reach an equilibrium before the merging of the two components. Unfortunately for most transiting planets, Levrard et al. (2009) showed that because of their short period orbit, only one of the transiting planetary systems known at the time, namely HAT-P-2, had enough angular momentum to fulfill this criterion, all the other planets being doomed to fall onto their parent stars !

To see wether this conclusion still holds, I have performed a similar analysis but including newly found transiting planets. The results are summarized in Fig. 5.5. While most of the transiting systems are found to be unstable, the number of stable systems has significantly increased. For the systems found on the left of the $a = a_{crit}$ line, the stability is just due to the fast rotation of the star, as was the case for HAT-P-2. But this analysis also reveals systems with $a > a_{crit}$ that were not present in Levrard et al. (2009) (some of these with very large a are not shown in Fig. 5.5). For these, stability in

---

[7] For a Star-planet system, $M_\star \gg M_p$ and $R_\star > R_p$, thus $C_\star \gg C_p$ and $a_{crit} \approx \sqrt{3 r_{gyr,\star}^2 \frac{M_\star}{M_p}} R_\star > R_\star$.

[8] Hut (1980) also showed that from the equilibrium states described above, only the $a \geqslant a_{crit}$ branch of the $H_{equ}(a)$ curve is stable, as shown on Fig. 5.5.

ensured by a long orbital period, and thus a large orbital angular momentum. The fact that such transiting objects have been discovered only recently is due to the fact that long period planet have a smaller transit probability and require longer observation run to be detected and confirmed. **However, this reminds us that if many short period planets are about to be engulfed by their host star, exoplanets on wider orbits, many having already been discovered by radial velocity, are safe.**

Note however, that these studies make use of two major assumptions that are not true in general. First, the radii of the components are assumed to be constant. As it is not true, this means that H_{crit} and a_{crit} will change over time. During the early stages of the evolution of the star-planet system where a rapid contraction occurs, the system will move toward the upper right corner of the phase diagram shown in Fig. 5.5. This is a rather good news from the point of view of the stability: As the star spins up during contraction, its co-rotation radius shrinks and the planet has more chances to be outside of this radius, where tides push it outward. On the other hand, because of the stellar magnetic winds, angular momentum is not conserved. This causes a spin down of the star and a downward motion in the $a - H_{\text{tot}}$ diagram. From a theoretical point of view, all the systems will eventually enter the $H_{\text{tot}} < H_{\text{crit}}$ zone, and all the planets will fall onto their parent star. The only remaining question is when ? But as tidal interaction strongly decrease when planets are further away, most long period planets are safe for more than the lifetime of their star.

5.4   On the effect of the quasi circular approximation: Analytical analysis

Following the initial studies of Jackson et al. (2008), all studies exploring the effect of tidal heating on the internal evolution of "Hot Jupiters" (Miller et al. 2009, Ibgui et al. 2009) have been using a tidal model assuming a constant Q value during the evolution. Moreover, in all these calculations the tidal evolution equations are truncated at the 2$^{\text{nd}}$ order in eccentricity (hereafter referred to as the "e^2 model"), even when considering tidal evolution sequences with non-negligible values of e at earlier stages of evolution. **Although such a e^2-truncated model is justified for planets and satellites in the solar system (Kaula 1963 ; Goldreich and Soter 1966), it becomes invalid, and thus yields incorrect results for $a(t)$, $e(t)$ and $\dot{E}_{\text{tides}}$ for finite eccentricity values, as showed in Leconte et al. (2010a).** The main argument claimed for using this simple tidal model is the large uncertainty on the tidal dissipation processes in astrophysical objects. In particular, as detailed by Greenberg (2009), the linearity of the response to the tidal forcing based on the viscoelastic model may not hold in a real object for the large spectrum of exciting frequencies encountered when computing high-order terms in the eccentricity. Although the large uncertainty in the dissipative processes certainly precludes an exact determination of the tidal evolution, it can by no means justify calculations which are neglecting dominant terms at finite e.

Indeed, from a dimensional point of view and *prior to any particular tidal model*, the strong impact of high-order terms in the eccentricity is simply caused by the tidal torque ($\mathbf{N}$) being proportional to $(\omega - \dot{\theta})/r_\star^6$ (θ being the true anomaly) and that over a Keplerian orbit the average work done by the torque is of the form

$$< \mathbf{N} \cdot \dot{\theta} > \propto < \frac{\dot{\theta}^2}{r_\star^6} > = \frac{n^2}{a^6} \cdot \frac{1 + 14e^2 + \frac{105}{4}e^4 + \frac{35}{4}e^6 + \frac{35}{128}e^8}{(1 - e^2)^{15/2}},$$

which is a rapidly increasing function of e (see § I.1.1 for the details of the calculation). This means that although the mean distance between the planet and the star increases with e, the distance at the periapsis strongly *decreases*, and most of the work due to the tidal forces occurs at this point of the orbit. One can see that for $e > 0.32$ the high-order terms dominate the constant and e^2 terms. **This is physical evidence that shows that for moderate to high eccentricity most of the tidal effects are contained in the high-order terms that can therefore not be neglected independently of any tidal model.**

(a) ω/n vs e phase space: complete equations

(b) ω/n vs e phase space: truncated equations

Figure 5.6: Pseudo-synchronization curve (*solid*), the $\dot{a} = 0$ curve (*dashed*) and the $\dot{e} = 0$ curve (*dotted*) for the complete model (left panel) and for the truncated one (right panel) in the ω/n vs e phase space. A pseudo-synchronized planet always follows the $\dot{\omega} = 0$ curve and always lies in the $\dot{a} < 0$ and $\dot{e} < 0$ part of the diagram because the curves do not intersect with the complete equations (left panel). In contrast, in the 2nd-order truncated model the pseudo-synchronization curve intersects the $\dot{a} = 0$ (at $e \sim 0.208$) and $\dot{e} = 0$ lines ($e \sim 0.326$). *Revised figure from Leconte et al. (2010a).*

In this section, as already presented in Leconte et al. (2010a), I quantify this statement more comprehensively. I will demonstrate analytically that

- **in the context of the Hut model, a truncation of the tidal equations at the order e^2 can lead not only to *quantitatively* wrong but to *qualititatively* wrong tidal evolution histories, with sequences drastically differing from those obtained with the complete solution.**

- **the rate of tidal dissipation can be severely underestimated by the quasi circular approximation ($e \ll 1$).**

Furthermore, Q-constant models consider only low-order terms in obliquity (ε_i), and thus cannot address the problem of obliquity tides and energy dissipation produced by this mechanism. For more detailed discussion of this subject, see Levrard et al. (2007) and Barker and Ogilvie (2009).

5.4.1 Expanding vs shrinking orbits

On one hand, considering Eq. (5.11) (with $\varepsilon_i = 0$ for simplification) we can see that for $\omega_i/n \leqslant N_a(e)/N(e)$, the tides raised on the body i lead to a decrease of the semi-major axis, transferring the angular momentum from the orbit to the body's internal rotation. It is easy to show that for a synchronous planet this condition is always fulfilled, because $\frac{\omega_{eq}}{n} = \frac{N(e)}{\Omega(e)} \leqslant \frac{N_a(e)}{N(e)}$ for any eccentricity (respectively solid and dashed curves of Fig. 5.6.a). As a result, the semi-major axis of most short period planets is decreasing.

On the other hand, truncating Eq. (5.11) for the semi-major axis evolution at the order e^2 yields

$$\frac{1}{a}\frac{da}{dt} = \frac{4a}{GM_\star M_p}\left\{K_p\left[(1+\frac{27}{2}e^2)\frac{\omega_p}{n} - (1+23e^2)\right] + K_\star\left[(1+\frac{27}{2}e^2)\frac{\omega_\star}{n} - (1+23e^2)\right]\right\},$$

(5.31)

and the previous condition becomes $\omega_i/n \leqslant (1+23e^2)/(1+\frac{27}{2}e^2)$. Up to 2nd order in eccentricity, the pseudo-synchronization angular velocity is given by $\omega_{eq} = (1+6e^2)n$ [9]. One can see that $\omega_{eq}/n = 1+6e^2 \leqslant (1+23e^2)/(1+\frac{27}{2}e^2)$ only for

$$e \leqslant \frac{1}{9}\sqrt{\frac{7}{2}} \approx 0.208.$$

This means that even for a moderate eccentricity, $e \sim 0.2$, the truncated model predicts that tides raised on a pseudo-synchronous planet lead to a *growth* of the semi-major axis instead of a *decrease*, as obtained by the complete model. Therefore, truncating the tidal equations at the order e^2 for an eccentricity $e \geqslant 0.2$ not only predicts quantitatively wrong but *qualitatively* wrong tidal evolutions. The same arguments for the evolution of the eccentricity show that tides raised on a pseudo-synchronous planet lead to a *growth* of the eccentricity for

$$e \geqslant \sqrt{\frac{7}{66}} \approx 0.326$$
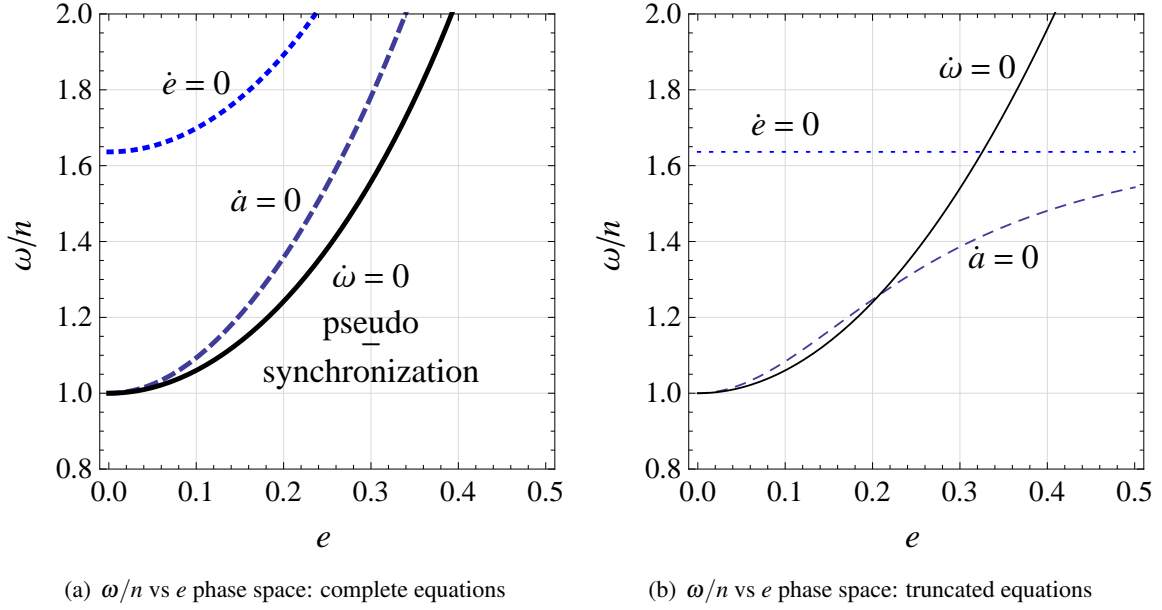
and not to a *decrease*. This is illustrated by Fig. 5.6, which shows the pseudo-synchronization curve (solid), the $\dot{a} = 0$ curve (dashed) and the $\dot{e} = 0$ curve (dotted) for the full model (left panel) and the truncated one (right panel), in the ω/n vs e phase space. As demonstrated before, the pseudo-synchronization curve crosses the $\dot{a} = 0$ and $\dot{e} = 0$ lines in the 2nd order model (Fig. 5.6.b), whereas it does not when solving the complete Hut equations (Fig. 5.6.a). ***As a result, with the truncated model, a pseudo-synchronized planet can erroneously enter the zone of the phase space where its tides act to increase both the semi-major axis and the eccentricity.*** While this behavior is not observed with the constant phase-lag model because it assumes that the star is slowly rotating ($\omega_\star/n \ll 1$) and that the planet is near synchronization ($\omega_p/n \approx 1$) - placing them in the $\dot{a} < 0$ and $\dot{e} < 0$ zone of the phase space - this formal demonstration sets clear limits on the domain of validity of the quasi-circular approximation.

5.4.2 Underestimating tidal heating

The key quantity arising from the coupling between the orbital evolution and the internal cooling history of a planet is the amount of energy dissipated by the tides in the planet's interior, which may compensate or even dominate its energy losses. As a result, tides raised in an eccentric planet can slow down its contraction (Bodenheimer et al. 2001 ; Leconte et al. 2009 ; Baraffe et al. 2010) or even lead to a transitory phase of expansion (Miller et al. 2009 ; Ibgui et al. 2009). Correctly determining the tidal heating rate is thus a major issue in the evolution of short-period planets. The often used formula is (Kaula 1963 ; Peale and Cassen 1978 ; Jackson et al. 2008)

$$\dot{E}_{tid} = 7K_p e^2 = \frac{21}{2}\frac{k_{2,p}}{Q}\left(\frac{GM_\star^2}{R_p}\right)\left(\frac{R_p}{a}\right)^6 n e^2$$

(5.32)

(the $21k_{2,p}/2Q$ is rewritten $63/4Q'$ in Miller et al. (2009)). As already stated by Wisdom (2008), although this formula gives a fair approximation of the tidal dissipation rate for the small eccentricity cases,

---

[9]these equations truncated at the order e^2 agree with equations in §16 of Ferraz-Mello et al. (2008), even though they have been derived with different methods

which are typical in the solar system, it severely underestimates the tidal heating for moderate and high eccentricities. Figure 5.7 illustrates the power dissipated in a pseudo-synchronized planet as a function of the eccentricity. It shows that for $e \gtrsim 0.45$, **the truncated formula used in Miller et al. (2009) and Ibgui et al. (2009) underestimates the actual tidal dissipation rate** *by more than one order of magnitude and by more than a factor* 10^3 *for* $e \gtrsim 0.7$**, an eccentricity value often advocated by these authors to explain the highly inflated planets (see §5.5.3 ; Leconte et al. 2010a, 2011b).**
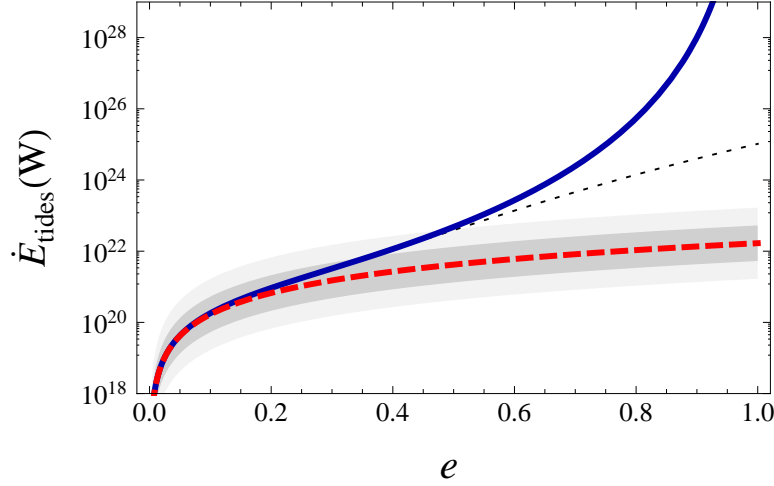
Figure 5.7: Tidal energy dissipation rate in a pseudo-synchronized planet (in Watt) as a function of the eccentricity calculated with Eq. (5.19) (*solid curve*) and with the truncated formula (Eq. (5.32) ; *dashed*). The ratio of the two curves only depends on the eccentricity and not on the system's parameters. For $e = 0.45$, the e^2 approximation (Eq. (5.32)) underestimates the tidal heating by a factor 10. The actual values were derived using HD 209 458 b parameters: $M_{\rm p} = 0.657\,M_{\rm Jup}$, $R_{\rm p} = 1.32\,R_{\rm Jup}$, $M_\star = 1.101\,M_\odot$, $a = 0.047\,{\rm AU}$ (Knutson et al. 2007). $Q' = 10^6$ (see §5.1.2). The *dotted curve* gives the dissipation rate calculated up to e^{10} (Eq. (5.35)). The shaded areas are obtained by varying Q' by one (two) order of magnitude. *Revised figure from Leconte et al. (2010a).*

From a mathematical point of view, the fact that a truncation to $2^{\rm nd}$ order in eccentricity yields such discrepancies is due to the $(1 - e^2)^{-{\rm n}}$ factors in the equations for the tidal dissipation, that are expanded in low order calculations. Fortunately, such expansions can be carried out, as the convergence radius of the series is 1. Indeed, if the power series converges

$$\frac{1}{(1 - e^2)^{\rm n}} = \sum_{{\rm k}=0}^\infty \frac{e^{2{\rm k}}}{{\rm k}!} \prod_{{\rm i}=1}^{\rm k} ({\rm n} - {\rm i}) \equiv \sum_{{\rm k}=0}^\infty a_{\rm k} e^{2{\rm k}}. \tag{5.33}$$

The convergence radius is thus given by

$$e_{\rm conv} = \sqrt{\lim_{{\rm k} \to \infty} \left| \frac{a_{{\rm k}+1}}{a_{\rm k}} \right|} = \sqrt{\lim_{{\rm k} \to \infty} \frac{|{\rm n} - {\rm k}|}{{\rm k} + 1}} = 1. \tag{5.34}$$

However, as already stated by Wisdom (2008), for moderate to high eccentricity this function is poorly represented by the first terms of its polynomial representation. Indeed, the first terms of the energy dissipation rate are given by

$$\frac{\dot{E}_{\rm tid}}{7 K_{\rm p} e^2} = 1 + \frac{54}{7} e^2 + \frac{1133}{28} e^4 + \frac{31845}{224} e^6 + \frac{381909}{896} e^8 + O\left(e^{10}\right). \tag{5.35}$$

The dissipation rate calculated up to e^{10} is plotted in Fig. 5.7 (dotted curve), where it can be compared with the exact result. It is clear that *for $e \gtrsim 0.4$ the polynomial developments of the tidal evolution equations must be done to a much higher degree than in previous studies, or complete calculations like those done in Hut (1981) must be used.* The same argument holds for the evolution of the semi-major axis and the eccentricity. Because Eqs. (5.11) and (5.12) also contain $(1 - e^2)^{-p/2}$ factors, the decrease of a and e is severely underestimated at even moderately high eccentricity when using a 2nd order truncated expansion in eccentricity.

In particular, as discussed in the next section, a high eccentricity ($e \gtrsim 0.6$) cannot be maintained for a few 100 Myr to a few Gyr in a system like HD 209 458 in agreement with the results of Miller et al. (2009) (see Fig. 5.9 below). This is in contrast with Ibgui and Burrows (2009), who find that the radius HD 209 458 b can be matched and that the system can sustain a significant eccentricity up to the observed epoch. These discrepancies between these two studies based on the same tidal model may reveal differences in the implementations of the tidal equations, or a difference in the calculation of interior structures or boundary conditions.

5.5   Tidal friction as an energy source: Implications for Hot Jupiters

As mentioned earlier, tidal heating has been suggested by several authors to explain the anomalously large radius of some giant close-in observed exoplanets. As demonstrated analytically in § 5.4, the previous calculations, which are all based on constant-Q models truncated at the order e^2 yield inaccurate results when applied to significantly (initial or actual) eccentric orbits - a common situation among detected exoplanetary systems. In the following section, I first review the energetic arguments on which this "tidal heating hypothesis" is based. Doing so, in § 5.5.1, **I also develop for the first time an analytical formula bracketing the total energy available for the planet during circularization which is valid to any eccentricity. Then, I investigate the impact of tidal heating on the thermal evolution of the planet on numerical grounds.** As expected from the analytical analysis, and shown in § 5.5.2 and 5.5.3, the numerical comparison of the two models shows that the complete tidal equations lead to a much quicker evolution, and thus to a much higher, but also shorter, tidal heating. Finally, in § 5.6, **I revisit the viability of such a tidal heating mechanism to explain the extensive observed Hot Jupiter radii with the present complete Hut tidal model.** I show that although it indeed provides a possible explanation for some transiting systems, the tidal heating hypothesis fails to explain the radii of extremely bloated planets like - among others - HD 209 458 b, TrES-4 b, WASP-4 b or WASP-12 b, in contrast with some previously published results based on truncated tidal models.

5.5.1   Energy budget

Tidal friction is, by nature a dissipative process. Over time, non ideal effects inside one or the other of the deformable bodies transform macroscopic mechanical energy into microscopic entropy. If this processes are energy sinks when considering the orbital evolution ($\mathrm{d}(E_{\mathrm{orb}} + E_{\mathrm{rot}})/\mathrm{d}t < 0$), from the point of view of the thermal evolution of the object, they represent an energy source ($\dot{\varepsilon}_{\mathrm{tid}}$) which has to be incorporated in the luminosity equation

$$\frac{\partial L}{\partial m} = \dot{\varepsilon}_{\mathrm{nuc}} + \dot{\varepsilon}_{\mathrm{tid}} - T\frac{\partial \tilde{S}}{\partial t}. \tag{5.36}$$

As a large fraction of the objects considered are convective, this equation can be integrated to yield (see Eq. (1.59))

$$L_{\rm p} = -\dot{E}_{\rm nuc} + \dot{E}_{\rm tid} - \bar{T}\frac{\partial \tilde{S}}{\partial t}, \tag{5.37}$$

where the three terms are, respectively, the contribution of the nuclear reactions[10], tidal friction[11] and gravo-thermal energy release (intrinsic luminosity). If an additional source of energy is present, it increases the total outgoing energy flux. Then, the bottom of the atmospheric boundary layer, and thus the adiabat, is slightly hotter in presence of heating than without. This causes an increase of the radius compared to the traditional case, and less gravo-thermal energy, or entropy, is radiated away. This mechanism is very similar to the irradiation of the atmosphere by the star, but here, the energy is deposited at depth (in the convective zone), participates to the energetic budget of the object, and thus, the atmosphere is heated from *below*.

However, for this effect to become significant, the energy injection rate must be comparable to the intrinsic luminosity of the body, and remain so for an extended period of time. To have a first insight into the capacity of tidal friction to increase the radius of giant exoplanets, I will thus estimate the global amount of mechanical energy available for the planet in the system, and the typical timescale on which it will be released, and compare them to the binding energy of the planet and its relevant evolution time.

Synchronization energy

Like Jupiter and Saturn, giant planets are believed to form with a high specific angular momentum, and thus a high initial rotational energy which reads

$$E_{\rm rot} = \frac{1}{2}C_1\omega_1^2 = \frac{1}{5}r_{\rm gyr}^2 M_1\bar{R}_1^2\omega_1^2. \tag{5.38}$$

Because tidal processes tend to synchronize the rotational with the orbital motion, and that, in general, $n \ll \omega_{\rm ini}$, the ratio of the available rotational energy over the internal energy of the body is

$$\frac{E_{\rm rot}}{E_{\rm int}} = \frac{r_{\rm gyr}^2}{5\gamma}\frac{\bar{R}_1^3\omega_1^2}{GM_1} \lesssim \frac{r_{\rm gyr}^2}{5\gamma}, \tag{5.39}$$

where $\gamma = E_{\rm int}R_1/GM_1^2$ and should be of order unity. Within a numerical factor, this is equal to the dimensionless rotation parameter $m_{\rm rot}$ defined in Chapter 3, which cannot be higher than unity because then, gravity at the surface would be to weak too counteract the centrifugal force, and the body would experience high mass losses. For roughly the same reason, the spin of the planet is small compared to the orbital angular momentum, and (pseudo)synchronization occurs on a short timescale compared to the age of the system (see § I.2.1). Therefore, rotational energy is not a sustainable energy source in our context. At most, the early synchronization will provide a small initial energy pulse whose consequences will be visible only during a few Kelvin-Helmholtz timescales.

Obliquity tides

Another way to dissipate energy into the interior is by obliquity tides. For the same reasons than above, if there is no other torque present, the planet obliquity will be damped very quickly. However, as proposed by Levrard et al. (2007) the presence of a secular perturbation of the orbit could trap the

---

[10]Which are important only above 12-13$M_{\rm Jup}$, and at young ages.

[11]Note that contrarily to § 1.1.3, here, I have defined $\dot{E}_{\rm tid} \equiv \int \dot{\varepsilon}_{\rm tid}\,{\rm d}m$ to manipulate positive quantities.

planet into a Cassini state, stabilizing the obliquity. Orbital energy can then be dissipated into the planet trough this channel. If this process can be important for terrestrial planets, it seems rather inefficient in maintaining a large obliquity for a giant planet, as demonstrated by Fabrycky et al. (2007).

Circularization energy

If synchronization happens way to fast to heat the planet at a late epoch, we have seen in §I.2.1 that the timescale needed to circularize a binary system seems to be much more similar to the age of the planets that we currently observe[12]. At first sight, we might be tempted to say that the maximum energy available is simply the total mechanical energy that need to be extracted from the system to decrease the semi-major axis from its initial value (a_{ini}), to the current one (a_{fin}), the latter being necessarily larger than the Roche limit (a_R) under which the planet is disrupted by the tidal forces. Therefore, the mechanical energy available is

$$\Delta E_{\text{orb}} = \frac{GM_1M_2}{2}\left(\frac{1}{a_{\text{fin}}} - \frac{1}{a_{\text{ini}}}\right) > 0. \qquad (5.40)$$

However, this energy can be released in both the star, and the planet. Indeed, if the planet is pseudo synchronized, and that orbit is nearly circular, tides in the planet do not dissipate energy anymore, and all the momentum exchange arise between the star, which is spinning up, and the orbit, which is shrinking. This is why, for Hot Jupiters, which are probably pseudo synchronized, only the circularization period need to be considered to evaluate the energy available (Bodenheimer et al. 2001).

Figure 5.8: Maximum (minimum) tidal energy available in unit of E_{int} as a function of initial eccentricity and observed (initial) semi-major axis. The zone where tidal circularization will not impact the thermal history of the planet is roughly above the $E_{\text{tid}} = E_{\text{int}}$ curve.

During this period, tides in the planet dominate[13]. For a pseudo synchronized object, a combination of Eqs. (5.11) and (5.12) gives us

$$\frac{\dot{a}}{a}\frac{e}{\dot{e}} = \frac{4}{11}\frac{\frac{N^2(e)}{\Omega(e)} - N_a(e)}{\frac{\Omega_e(e)N(e)}{\Omega(e)} - \frac{18}{11}N_e(e)} = -\frac{2e^2}{1-e^2}! \qquad (5.41)$$

Neglecting the dissipation in the star, I can estimate the total energy released during the circularization by

$$E_{\text{circ}} = \int_{e_{\text{ini}}}^{0} \frac{GM_1M_2}{2a}\frac{\mathrm{d}a}{a} = \int_{0}^{e_{\text{ini}}} \frac{GM_1M_2}{a}\frac{e\,\mathrm{d}e}{1-e^2}, \qquad (5.42)$$

which extends the formula given by Bodenheimer et al. (2001) to higher orders. If the integration of the full set of tidal equations is needed to compute precisely the energy released, the latter can be

---

[12]Indeed, most of them orbit around main sequence stars, and are supposed to be between a few 100 Myr and a few Gyr old.

[13]As long as a finite eccentricity remains in the system, the ratio of the planetary over stellar tidal dissipation rates is roughly given by $K_{\text{p}}/K_{\star} = \frac{k_{2,\text{p}}\Delta t_{\text{p}}}{k_{2,\star}\Delta t_{\star}}\left(\frac{M_{\star}}{M_{\text{p}}}\right)^2\left(\frac{R_{\text{p}}}{R_{\star}}\right)^5$, and is ~ 10 for a Jupiter-Sun like system.

bracketed by integrating the above equation for both $a = a_{\text{ini}}$ and $a = a_{\text{fin}}$ (with $a_{\text{ini}} > a_{\text{fin}}$)

$$-\frac{GM_1M_2}{2a_{\text{ini}}}\ln(1-e_{\text{ini}}^2) < E_{\text{circ}} < -\frac{GM_1M_2}{2a_{\text{fin}}}\ln(1-e_{\text{ini}}^2). \qquad (5.43)$$

Note that, contrarily to the estimate given by Bodenheimer et al. (2001), this formula is valid for arbitrarily high eccentricities. Thus

$$\frac{E_{\text{circ}}}{E_{\text{int}}} < -\frac{1}{2\gamma}\frac{M_2}{M_1}\frac{\bar{R}_1}{a_{\text{fin}}}\ln(e_{\text{ini}}^2-1) \approx -\frac{5}{\gamma}\times\left(\frac{M_2}{M_\odot}\right)\left(\frac{M_{\text{Jup}}}{M_1}\right)\left(\frac{\bar{R}_1}{R_{\text{Jup}}}\right)\left(\frac{0.05AU}{a_{\text{fin}}}\right)\ln(e_{\text{ini}}^2-1).$$
$$(5.44)$$

Fig. 5.8 shows the maximum (minimum) circularization energy in unit of the internal energy (with $\gamma = 1$) for a Jupiter-Sun like system as a function of the final (initial) semi-major axis and initial eccentricity. As expected, the importance of the tidal heating will increase as the object starts on a more eccentric orbit, and is closer to the central body. This also shows that the amount of available energy could in principle be sufficient to significantly impact the planet.

5.5.2 Coupled tidal/thermal evolution

However, to know whether this energy is delivered at the right time and at the right pace, one must couple consistently the internal and the orbital evolution as each one will influence the other. I thus implemented the aforementioned module computing the orbital evolution at each time step in the evolutionary code described in Chapter 2. For the moment, the internal evolution of the star is supposed frozen, and its radius is kept constant at its current value during the whole evolution. Regarding the orbital evolution of the system, this hypothesis is valid for two main reasons. First, the tidal heating in the star is too weak compared to the nuclear burning to significantly impact the stellar evolution, and second, the pre main sequence phase, where the star exhibits a radius and an angular velocity which are drastically higher than today, does not last long enough compared to the tidal evolution. Of course, this is no longer possible if one is specifically interested in the evolution of the angular velocity of the star. Indeed, as discussed in § I.2.4, in this case, conservation of the angular momentum during the contraction and stellar winds must be properly taken into account along tidal friction to calculate consistently the evolution.

In our simulations, the evolution of the planet can exhibit three different general behaviors, depending on the initial conditions:

- In the low initial eccentricity regime, the eccentricity is damped to zero in a few Gyr and the semi-major axis decreases until the planet reaches the Roche limit and merges with the star (due to *stellar* tides ; Levrard et al. 2009), because the system does not have enough angular momentum to reach a stable equilibrium (Hut 1980 ; Levrard et al. 2009). In this case, tidal heating is not sufficient to significantly affect the radius of the planet, which keeps shrinking steadily as it cools.

- For higher initial eccentricities, the planet first undergoes a phase of contraction and rapid cooling before the tidal heating due to the high initial eccentricity starts to dominate the energy balance of the object, leading to a phase of radius inflation (as shown by Fig. 5.10 for a test case). This speeds up the damping of the eccentricity and the decrease of the semi-major axis, because $\dot{a}$ and $\dot{e} \propto R_{\text{p}}^5$. When the eccentricity becomes low enough, a "standard" contraction phase begins and lasts until the planet merges with the star or - if enough angular momentum is present in the system - until both tidal and thermal equilibria are achieved. This behavior has already been identified by Miller et al. (2009) and Ibgui and Burrows (2009), but because these authors used truncated tidal

(a) Semi-major axis

(b) Eccentricity

(c) Planetary radius

(d) Tidal energy dissipation
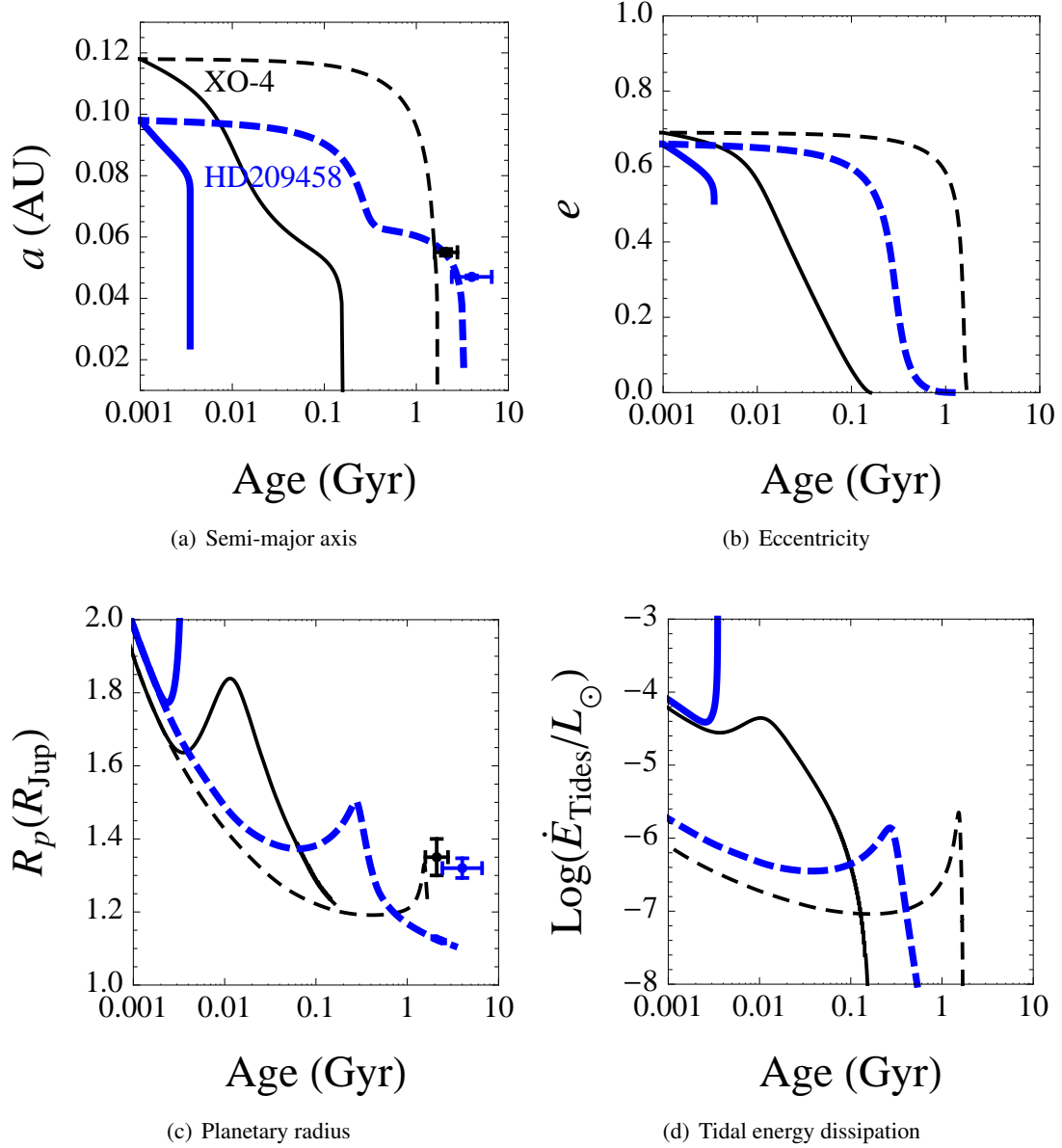
Figure 5.9: Consistent tidal/thermal evolution of XO-4 b (*thin, black*) and HD 209 458 b (*thick, blue*) computed with our constant time-lag model (*solid line*) and with the "e^2 model" (*dashed line*). XO-4 b is a 1.72 M_{Jup} planet orbiting a 1.32 $M_\odot$ star (McCullough et al. 2008). HD 209 458 b is a 0.657 M_{Jup} planet orbiting a 1.01 $M_\odot$ star (Knutson et al. 2007). The dashed curves are comparable to Fig. 8 and 10 of Miller et al. (2009) and were computed with the same parameters ($Q'_p = 10^5$, $Q'_\star = 10^5$). In this high eccentricity regime, using the same quality factor, the "e^2 model" underestimates the tidal dissipation rate by 2 orders of magnitude and thus overestimates the star-planet merging timescale by a factor 10 to 10^3. *Figure from Leconte et al. (2010a).*
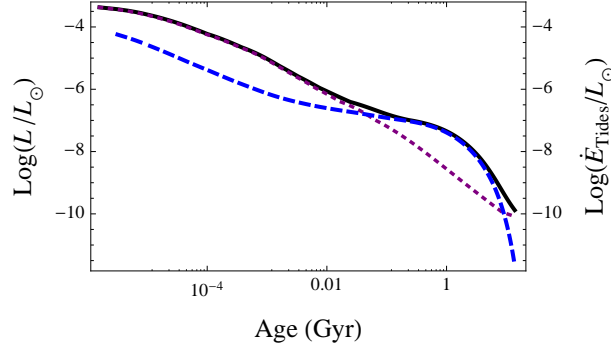
Figure 5.10: Internal energy balance in the evolving planet. *Black solid line*: luminosity of the object with tidal heating. *Purple dotted line*: luminosity of the object without tidal heating. *Blue dashed line*: tidal energy dissipation rate. The object contracts as it cools until the energy input balances its thermal losses and sustains a higher entropy in the gaseous envelop, yielding a larger radius. *Figure from Leconte et al. (2010a)*.

equations, they found that a high eccentricity can be maintained for a few Gyr and kept inflating the planet at a late time, as illustrated in Fig. 5.9 (dashed curves) ; while this is not the case.

- In some extreme cases like HD 209 458, for the initial conditions corresponding to those in Fig. 5.9, the tidal heating can overwhelm the cooling rate of the planet by orders of magnitude and lead to a spectacular inflation of the planet and thus to a rapid merging with the star. This stems from a combination of different effects. First of all, as mentioned above, the expansion of the radius accelerates the tidal evolution and thus the decrease of the orbital distance. Furthermore, the Roche limit ($a_R = \alpha R_p \sqrt[3]{M_\star/M_p}$, where α is a constant which depends on the structure of the body and is equal to 2.422 for fluid objects) increases with the radius of the planet, extending the merging zone.

5.5.3 Effect of the truncation to 2nd order in e: Simulation results

In this section, I present the comparison of the results of the complete model with the "e^2 model". **I calculated evolutionary tracks of the tidal evolution for various transiting systems, coupling the internal evolution of the object either with my tidal model (Leconte et al. 2010a), or with the "e^2 model" used in Miller et al. (2009) and Ibgui and Burrows (2009).** In order to ensure a consistent comparison with these authors, I directly convert their set of tidal parameters. Because our model assumes a constant time lag, and not a constant Q' value, a history track computed with the Q' "e^2 model" with a constant couple ($Q'_p, Q'_\star$) is compared with a history track computed in our model with a constant couple ($k_2\Delta t_p, k_2\Delta t_\star$) given by ($k_2\Delta t_p = \frac{3}{2n_{obs}Q'_p}, k_2\Delta t_\star = \frac{3}{2n_{obs}Q'_\star}$), where n_{obs} is the currently observed value of the mean motion of the planet considered (see § 5.1.2 and Eq. (5.10)). This ensures that - although Δt is held *constant* in our calculations (because n_{obs} is by definition a constant)- the quality factor computed with Eq. (5.10) in the object at the present time is the same as that used in the *Q constant* model.

(a) Semi-major axis

(b) Eccentricity

(c) Planetary radius

(d) Tidal energy dissipation
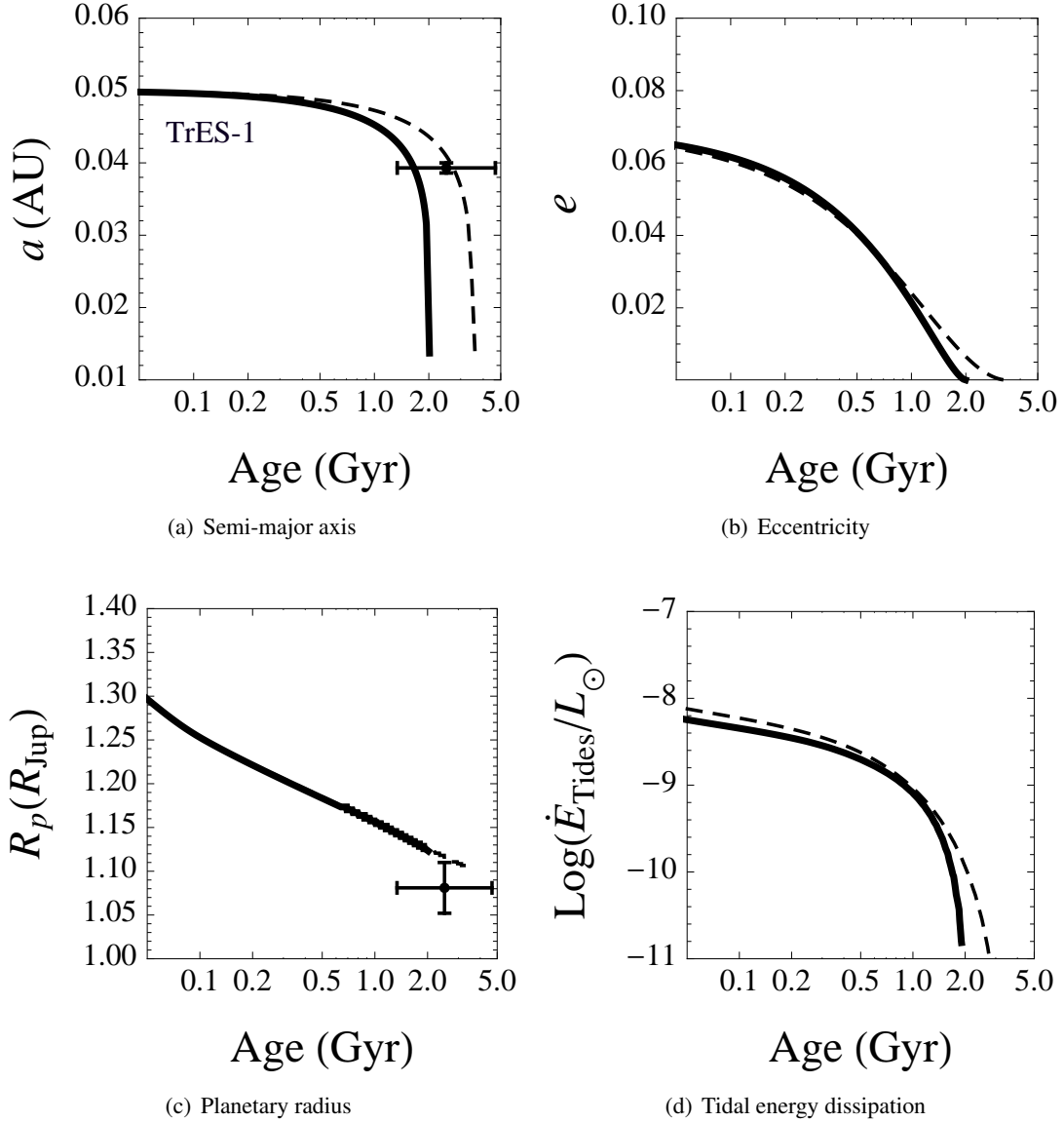
Figure 5.11: Consistent tidal/thermal evolution of TrES-1 b computed with our constant time-lag model (*solid line*) and with the "e^2 model" (*dashed line*). This is a $0.76\,M_{\rm Jup}$ planet orbiting a $0.89\,M_{\odot}$ star (Winn et al. 2007a). The error bars are the measured parameters with the 1σ uncertainty. The dashed curve is comparable to Fig. 7 of Miller et al. (2009) and was computed with the same parameters ($Q'_{\rm p} = 10^{6.5}$, $Q'_{\star} = 10^5$). As expected, in the low e limit the tidal dissipation rate is well approximated by Eq. (5.32) and the two models yield similar evolutions, although the merging time depends on the rheology used. *Figure from Leconte et al. (2010a).*

Calculations at low eccentricity

I first compare the results of the two models on a system which has a zero measured eccentricity and is not inflated, namely TrES-1. Such a system does not require a substantial initial eccentricity for its observed properties to be reproduced and thus provides an opportunity to test the quasi-circular limit, where the "e^2 model" used by Miller et al. (2009) and our model should yield similar results. Figure 5.11 illustrates the results of the integration of the coupled internal/orbital evolution equations with our constant time-lag model (solid curve) and with the "e^2 model" (dashed curve) for an initial eccentricity of 0.07. As expected, in this low eccentricity limit both models yield very similar tracks whose behavior is discussed in § 5.5.2. Note however that although the qualitative behavior of the evolution is the same, the hypothesis made on the rheology of the body can influence the age at which the merging occurs.

Calculations at high eccentricity

In the moderately to highly eccentric regime, the tidal dissipation rate can no longer be approximated by Eq. (5.32) (see § 5.4.2). Instead, Eq. (5.19) must be used and yields - as shown by Fig. 5.7 - a much more important dissipation rate. As a result, tidal evolution takes place on a much shorter time scale, and both the eccentricity damping and the merging with the star occur earlier in the evolution of the planet. For illustration Fig. 5.9 portrays the possible thermal/tidal evolution (for given initial conditions) for XO-4 b (thin black curves) and HD 209 458 b (thick blue curves) computed with the "e^2 model" (dashed) and with our model (solid). The dashed curves are similar to those displayed in Figs. 8 and 10 of Miller et al. (2009). As mentioned above and illustrated in Fig. 5.9.d, the energy dissipation is much larger when fully accounting for the high eccentricity. As clearly illustrated by these calculations, using tidal equations truncated at 2$^{\text{nd}}$ (e^2) order leads to severely erroneous evolutionary tracks for initially moderately ($e \gtrsim 0.2$) or highly eccentric systems. Indeed, the complete tidal model shows that for the initial conditions and Q parameter values chosen by Ibgui and Burrows (2009) and Miller et al. (2009), HD 209 458 b would actually have disappeared ! **As mentioned earlier, the use of this quasi-circular approximation cannot be justified by the uncertainty on the quality factor, as the discrepancy in the characteristic evolution timescales can amount to 3 orders of magnitude in some cases, depending on the initial eccentricity (Leconte et al. 2010a).** Conversely, trying to infer values for the stellar or planetary tidal quality factors Q from tidal evolution calculations performed with the truncated e^2 model will lead to severely inaccurate values.

5.6   Viability of the tidal heating hypothesis

Among the observed objects in the giant planet/mini brown dwarfs mass regime (see § 2.4.3), **I will focus on the most extremely inflated ones to investigate the validity of the tidal heating hypothesis to explain their abnormally low density, as they provide the most stringent cases to examine the viability of this scenario.** Indeed all the planets with radii in the $R_1 \lesssim R_{\text{irr}}$ region of Fig. 2.10 (i.e. with a negative radius anomaly) do not need any additional energy source. Interestingly enough, these do not show any significant eccentricity, so that an evolution without tidal heating can be obtained with a low initial eccentricity. For the sake of simplicity and to avoid introducing further free parameters in our tidal model, and because our aim is to derive an *upper limit* for the radius that a planet can achieve under the effect of tidal heating, I will not consider heavy element enrichment in our calculations.

My calculations proceed as follows:

1. For each of the systems a range of initial semi-major axis ($[a_{\text{min}}, a_{\text{max}}]$) is found by a *backward integration* of the tidal equations from present-day observed values.

2. Evolutionary tracks, which consistently couples the gravo-thermal evolution of the irradiated planet and the tidal heating source (Eq. (5.19)), are then computed for $a_{\rm ini} \in [a_{\rm min}, a_{\rm max}]$ and an initial eccentricity $e_{\rm ini} \in [0, 0.8]$. The plausibility of these initial conditions as a remnant of early planet-disk and/or planet-planet interaction is discussed in Miller et al. (2009). Because total angular momentum is conserved during the tidal evolution, the *initial spin rate* of the star is calculated by satisfying the equality between the initial and the presently observed value of the system's total angular momentum (see § I.2.4 for details). Calculations are performed with $Q'_{0,\star} = 10^5$ and 10^6 and $Q'_{0,\rm p} = 10^6$ and 10^7 (see § 5.2.2 for a detailed discussion).

3. For each evolutionary calculation, the departure from a given measured quantity is defined as $\delta_x(t) = \left(\frac{x(t) - x_{\rm p}}{\sigma_x}\right)$, where x refers to a, e, $R_{\rm p}$, $\varepsilon_\star$ or $\omega_\star$ and σ_x to their measured uncertainty. When no error bar was measured for the eccentricity and $e = 0$ was assumed in the light curve analysis, I took $\sigma_e = 0.05$. I consider that the evolution accurately reproduces the presently measured data if there is a time interval (compatible with the age of the system) within which *all* the δ_x's are smaller than 1, meaning that each one of these parameters agrees with the measured one within 1 σ.
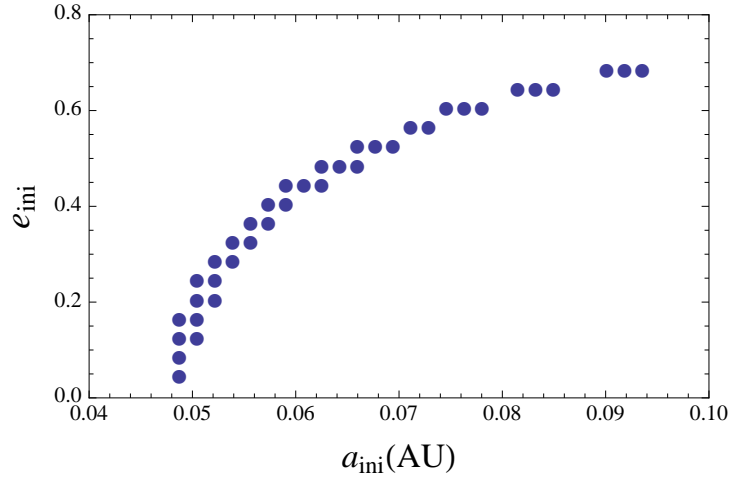
Figure 5.12: Set of initial conditions yielding evolutions consistent with the actual orbital parameters of HD 209 458 b. These runs assume $Q'_{0,\rm p} = 10^6$ and $Q'_{0,\star} = 10^6$. Because high eccentricity speeds up the tidal evolution, the initial semi-major axis must increase when the initial eccentricity of the orbit increases to recover the observed parameters at the age of the system. *Figure from Leconte et al. (2010a)*.

Figure 5.12 portrays a grid of evolution history initial conditions that are found to be consistent with the observed parameters of HD 209 458, at the age of the system. As expected, an initially more eccentric system must have a greater initial separation to end up at the same location. This stems from the fact that $|\dot{a}|$ is a monotonically increasing function of e for a slowly rotating star (as obtained from Eq. (5.11) for $\omega_{\rm p} = \omega_{\rm equ}$ and $\omega_\star/n \ll 1$). **Although I do find evolutionary tracks that lead to the presently observed orbital parameters for these extremely bloated planets,** *none of these solutions can reproduce the presently observed radii, as illustrated in Fig. 5.13 for HD 209 458 b.* Indeed, the major phase of eccentricity damping as given by Eq. (5.12) and discussed in § 5.5.3 occurs too early in the evolution, so that a large fraction of the tidal heating energy dissipated in the planet has been radiated away at the age of the system ($\sim$ a few Gyrs) and can no longer provide enough energy to slow down the gravitational contraction. The same behavior is found for other bloated systems like WASP-12, TrES-4 and WASP-4, whose best evolutionary tracks are shown in Fig. 5.14. For all these systems tidal dissipation occurs too early to reproduce the present values of the planet radii, although a solution matching the presently observed orbital parameters can be found.

(a) Semi-major axis

(b) Eccentricity

(c) Planetary radius

(d) Tidal energy dissipation
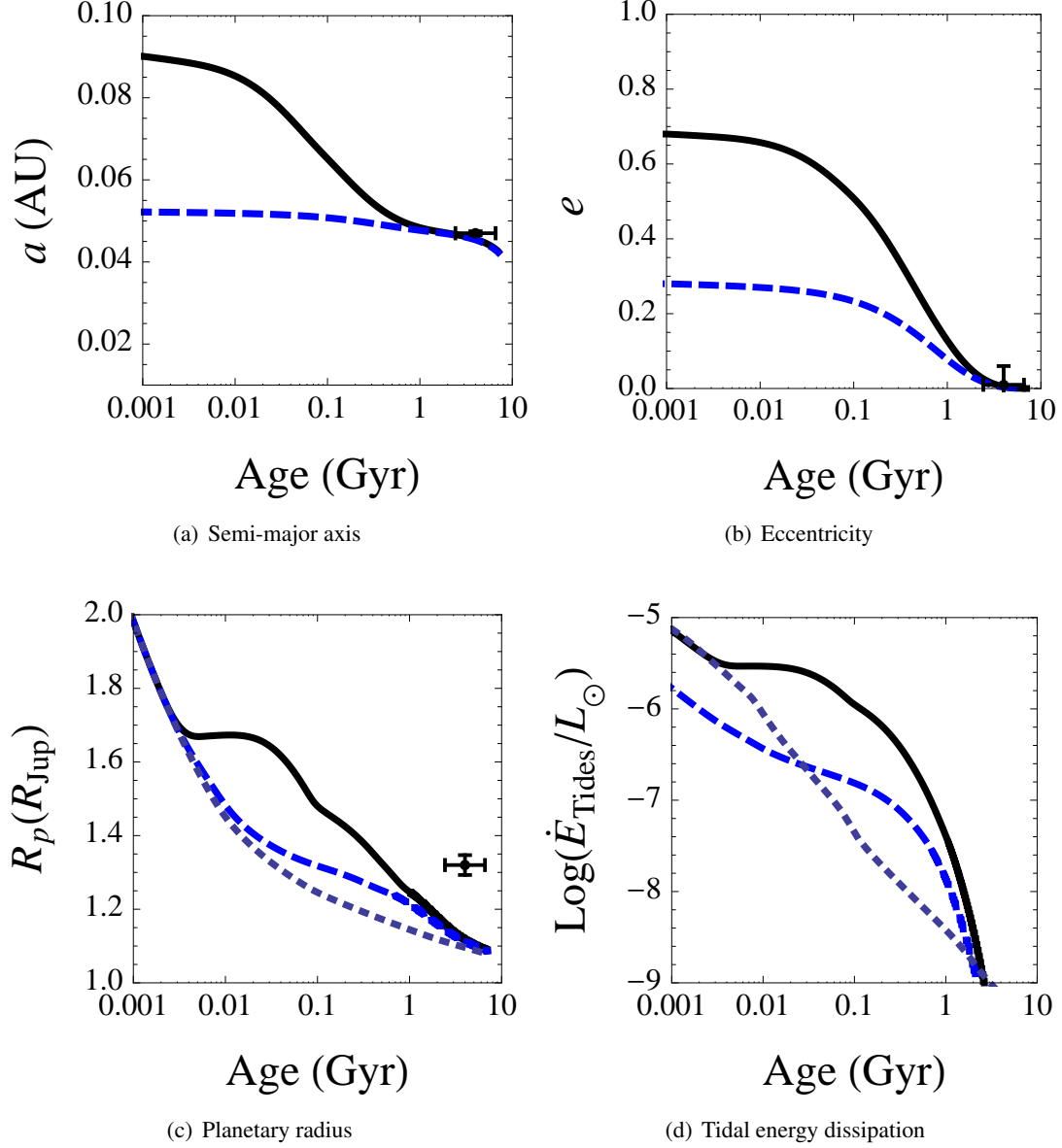
Figure 5.13: Consistent tidal/thermal evolution of HD 209 458 b with different initial conditions (solid and dashed) computed with our constant time-lag model. HD 209 458 b is a 0.657 M_{Jup} planet orbiting a 1.01 $M_\odot$ star (Knutson et al. 2007). These runs assume $Q'_{0,\text{p}} = 10^6$ and $Q'_{0,\star} = 10^6$. For comparison, the radius and luminosity of an isolated planet (no tidal heating) is shown on the lower panels (dotted curves). Even though these evolutions recover the presently observed orbital parameters for the system, the eccentricity damping arises too early during the evolution, leading to insufficient tidal dissipation at present epoch to explain the inflated radius. *Figure from Leconte et al. (2010a).*

(a) Semi-major axis

(b) Eccentricity

(c) Planetary radius

(d) Tidal energy dissipation
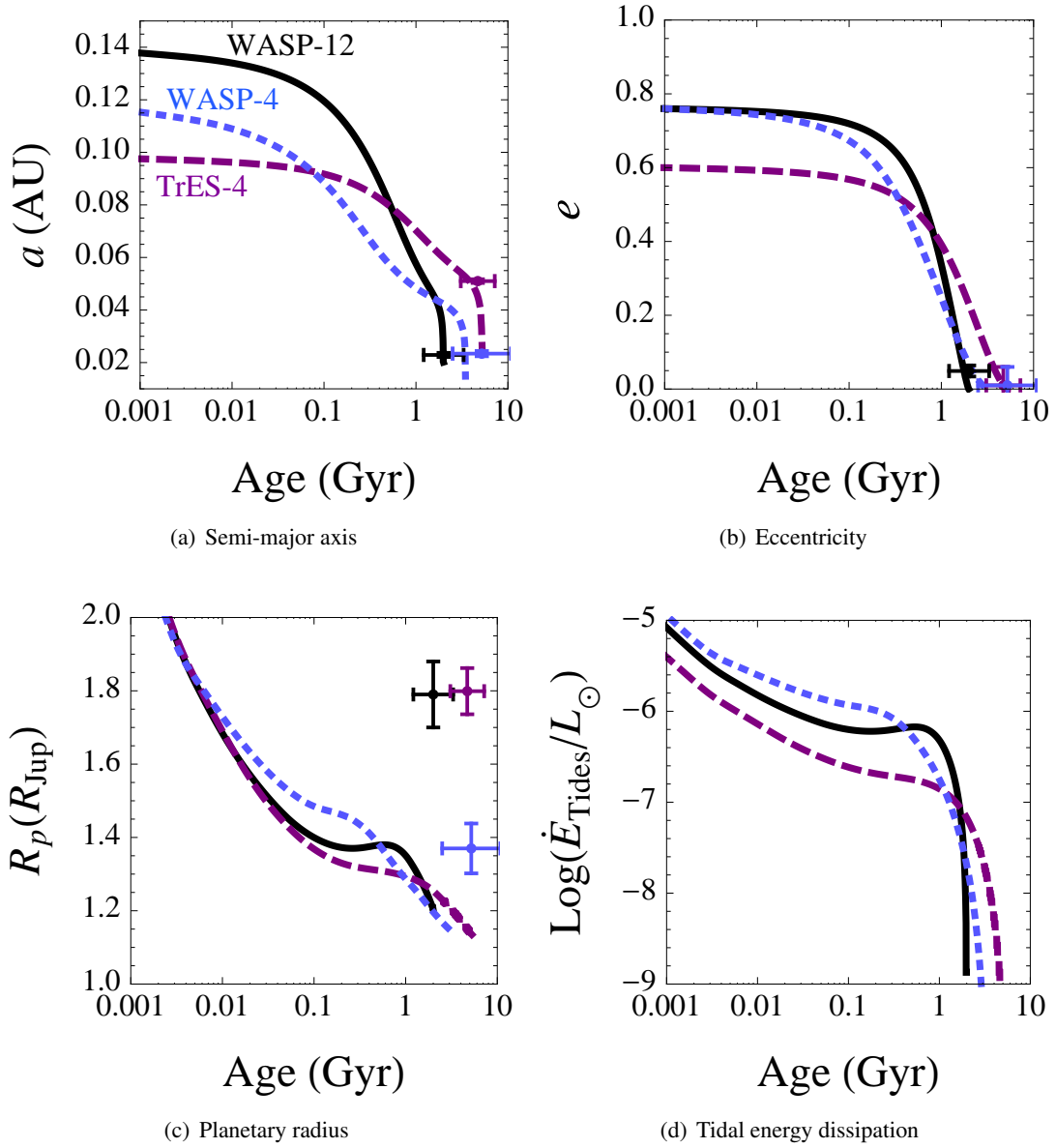
Figure 5.14: Evolutionary tracks for WASP-12 b (solid, Hebb et al. 2009), TrES-4 b (dashed, Daemgen et al. 2009) and WASP-4 b (dotted, Winn et al. 2009) that lead to the best agreement with the observed orbital parameters for these systems. These runs assume $Q'_{0,p} = 10^6$ and $Q'_{0,\star} = 10^6$. Tidal dissipation is not sufficient to sustain the large radii observed for these planets.

These results, based on complete tidal evolution calculations, show that the tidal energy dissipated in the planet's tidal bulges, although providing a viable explanation to the large radius of many short-period planets (like OGLE-TR-211 b shown in Fig. 10 of Leconte et al. 2010a), is not sufficient to explain the radii of the most bloated planets at the age inferred for these systems. In that case, an extra mechanism besides tidal heating must be invoked to solve this puzzling problem. Surface winds driven by the powerful incident stellar flux (Showman and Guillot 2002), converting kinetic energy to heat by dissipation within the tidal bulge and thus reaching deep enough layers to affect the planet's inner isentrope, or inefficient large-scale convection due to a composition gradient (Chabrier and Baraffe 2007) could be the other mechanisms to be considered with tidal dissipation to eventually lead to these large planet radii (see Baraffe et al. 2010 for discussion).

5.7   Summary and prospects

Let us summarize the main results of this chapter.

First, as shown in Appendix I, I developed the secular tidal equations of Hut (1981) to arbitrarily high obliquity. Then, considering the tidal set of equations in various asymptotic regimes, I derived two simple analytical solutions that, to my knowledge, have not been found before. These solutions, presented in § 5.2, were then used to benchmark my numerical integrator, and check numerical calculations from (Heller, Leconte & Barnes 2011). Thanks to these models, **I also derived an upper limit on the tidal dissipation (and thus the time lag) in Jupiter**.

In § 5.3, **I updated the results of Levrard et al. (2009) by including newly found transiting planets**, and showed that, while most of the transiting planetary systems yet discovered do not possess a stable equilibrium end state, this is only due to the detection bias toward short period systems. As this detection bias tends to diminish, the number of long period transiting planets able to reach a stable tidal equilibrium should grow in a near future.

Then, I demonstrated that the quasi-circular approximation ($e \ll 1$, i.e. tidal equations truncated at the order e^2) usually assumed in tidal calculations of transiting planet systems and valid for our Solar system planets, is not valid for the exoplanetary systems that have - or were born with - an even modestly high ($e \gtrsim 0.2$) eccentricity. As shown in sect. 5.4, although the real frequency dependence of the tidal effect remains uncertain, **there are dimensional evidences that for eccentric orbits, most of the tidal effect is contained in the high-order terms and that truncating the tidal equations at 2nd order in eccentricity can overestimate the characteristic timescales of the various orbital parameters by up to three orders of magnitude.** Therefore truncating the tidal equations at the 2nd order can by no means be justified by invoking the large uncertainty in the dissipative processes and their frequency dependence. Accordingly, high-order tidal equations should be solved to derive reliable results for most of the existing exoplanet transiting systems. This need to solve the complete equations is met by any tidal model. In this context, even though no tidal model can claim describing perfectly a two body evolution, I recall that the Hut model is at least exact in the weak friction viscous approximation (see sect. 5.1.2).

In § 5.6, I tested the complete tidal model on several inflated planets to find out whether or not tidal heating can explain the large radius of most of the observed transiting systems. Although this mechanism is indeed found to be sufficient to explain moderately bloated planets like OGLE-TR-211 b (see Fig. 10 of Leconte et al. 2010a), I was *unable* to find evolutionary paths that reproduce both the measured radius and the orbital parameters of HD 209 458 b, WASP-12 b, TrES-4 b, and WASP-4 b (see Figs. 5.13 and 5.14) for their inferred age range. The main reason is the early circularization of the orbit of these systems. As demonstrated in § 5.4, this stems from the non-polynomial terms in eccentricity in the complete tidal equations, which are missing when truncating the equations at small e-order. **The present results, based on complete tidal equations, show that tidal heating, although providing an**

important contribution to the planet's internal heat budget during the evolution, cannot explain *alone* **the observed properties of all exoplanets (Leconte et al. 2010a).**

This is in contrast with some of the conclusions reached in previous studies. Based on truncated tidal models, Ibgui and Burrows (2009) and Ibgui et al. (2009) find evolutionary tracks that match observed parameters for HD 209 458 b, WASP-12 b, and WASP-4 b and thus suggest that the tidal heating is the principal cause of the large radii of Hot Jupiters.

These particular properties of Hot Jupiters, including the extreme cases of the most severely bloated planets, can only be explained if the following explanations/mechanisms occur during the system's lifetimes:

- Early spin-up of the star: simulations of the rotational evolution of solar-like stars (Bouvier et al. 1997) show that after the dispersion of the accretion disk, the rotation rate of the contracting star increases due to angular momentum conservation, until magnetic braking takes over. Considering Eq. (5.12), we see that stellar tides act as an eccentricity source if $\frac{\omega_*}{n} \geqslant \frac{18}{11} \frac{N_e(e)}{\Omega_e(e)}$. Investigating whether the duration of this phase lasts long enough and whether the magnitude of this effect is large enough to drive enough eccentricity requires performing consistent star/planet thermal/tidal calculations and will be investigated in a forthcoming paper.

- Presence of a third body: as proposed by Mardling (2007), a low-mass terrestrial planet can drive the eccentricity of a massive giant planet during up to Gyr timescales. Accurate enough observations are necessary to support or exclude such low-mass companions.

- As mentioned earlier, combining tidal heat dissipation with other mechanisms like surface winds, due to the stellar insolation, dissipating deep enough in the tidal bulges, or layered convection within the planet's interior may provide the various pieces necessary to completely solve the puzzle.

In conclusion, the suggestion that tidal heating is the main mechanism responsible to solve the problem of anomalously large short-period planets, as sometimes claimed in the literature, must be more rigorously reformulated: although providing a non-negligible contribution to Hot Jupiter heat content, tidal dissipation does not appear to provide the whole explanation. Further studies are thus necessary to eventually nail down this puzzling issue.

Summary & Perspectives

During this thesis, I studied various physical processes affecting the internal structure and evolution of both solar, and extrasolar giant planets. Let me summarize briefly the main results that I obtained during this work and that led to the publication of the articles listed in Appendix A.

Evolution & stellar irradiation: A lid on the boiling kettle

First, by comparing the internal structure of gaseous substellar objects predicted by my numerical simulations, and by a simple analytical model, I showed that most features of their mechanical structure can be well captured by a single effective polytropic index. As this index characterizes both the equation of state, and the slope of the mass-radius relationship, this study highlights the existing link between the microscopic and the macroscopic mechanical properties of degenerate gaseous bodies.

Then, I investigated the impact of the intense stellar irradiation received by a close in planet on its subsequent internal evolution. As most transiting planets are very close from their host star, this effect must be taken into account to infer accurate theoretical predictions to be compared with observations. This allowed me to quantify the *radius anomaly* of bloated Hot Jupiters and to constrain their internal composition.

Based on this study, I proposed an observational criterion based on the mean density of the object to distinguish massive giant planets from mini brown dwarfs in their overlapping mass domain. The application of this criterion to several objects in this regime revealed that, with its unusually high density, Hat-P-20 b is probably the first secured planet in this range of masses.

Probing the deep interior: Theory of planetary figures

In this chapter, I used both analytical and numerical models to study the tidal and centrifugal distortion of a fluid planet, and infer its shape. As these models depend on a unique response coefficient (e.g. the Love number), I carried out numerical simulations to provide numerical estimates of this quantity and discussed how these values characterize the mechanical internal structure of giant planets and brown dwarfs.

I also discussed how k_2 measurements could help us to constrain the composition of extrasolar planets. With the more and more precise transit timing measurements, and the large number of newly announced multi transiting planet systems, this opens new possibilities to infer direct constraints on the internal composition of extrasolar planets ; internal composition which remains out of reach of spectroscopic observations.

Finally, thanks to our analytical model, I found that because close in planets are tidally elongated toward the star, they exhibit a smaller cross section, yielding major implications for transit measurements. In particular, this causes a systematic underestimation of the radius which can amount to a few percents. While slightly enhancing the so-called *radius anomaly*, this reminds us that, as transit measurements get more precise, subtler effects must be taken into account into the light curve modeling to extract accurate results.

A new perspective on heat transport in the interior

Here, I developed a completely analytical model to investigate how the presence of double-diffusive convection caused by a heavy elements gradient in the gaseous envelope of a planet can decrease the efficiency of its internal heat transport. This formalism allows an exact determination of the characteristic super-adiabaticity within the planet, and can thus easily be used in planetary structure and evolution numerical models to quantify the global impact of the presence of double-diffusive convection in the interior.

By applying this model to the Solar System gas giants, I found that the metal enrichment for our gaseous giants can be up to 30 to 60% larger than previously thought. As the heavy elements tend to be redistributed within the gaseous envelope, the models predict smaller than usual central cores inside Saturn and Jupiter, with possibly no core for this latter.

These results open a new window, and raise new challenges, on our present understanding of planet structure, formation and evolution. The revised possible maximum amount of heavy material, for example, suggests a greater efficiency of solid planetesimal accretion during giant planet formation than previously thought, both inside and outside our Solar System. The slower cooling entailed by semi-convection may also provide a part of the explanation of exoplanets large radii, and interestingly enough, without requiring any star-planet interaction.

An alternative energy source: Tidal friction

Finally, using an analytical model for the secular tidal evolution which is fit to describe highly eccentric and inclined orbits, I studied the coupling between the orbital and the thermal evolution of a exoplanets arising from the strong star-planet tidal interaction. Such a model is necessary to describe exoplanetary systems which, contrarily to the Solar System, commonly exhibit high eccentricities and obliquities, some planets even being on polar or retrograde orbits.

In particular, I demonstrated that using tidal models based on a quasi circular approximation can lead to quantitatively, and sometimes qualitatively different orbital evolutions, and can overestimate the evolution timescales by orders of magnitude. Subsequently, thanks to this more complete mathematical treatment of eccentric orbits, I found that contrarily to previously published results base on the quasi circular approximation, the circularization (and thus heating) period is too short compared to the age of observed transiting planets for tidal heating alone to be a viable explanation for their large radii.

As presently observed transiting planets are very close to their host stars, tidal interactions are a significant ingredient of their lives, and properly taking these interactions into account is primordial in understanding both the thermal and orbital evolution of exoplanets and their coupling. Coupling which is not only ensured by tidal heating, but also by the secular and seasonal variations of the stellar flux influenced by the orbital and the rotational evolution of the planet. In that context, a general and robust theory, such as the linear model studied here, is strongly needed.

In the decade to come

If the successful combination of Doppler measurements and Transit photometry already taught us a lot about the internal structure of giant planets in a wide variety of physical contexts, things are far from over. Not only these methods will continue to improve, and gain in precision, but new detection methods will soon come to maturity, opening many promising paths for the coming years.

On the transiting planet side, recent observations have proved our ability to detect Earth size objects. But these planets are still too close from a too bright star to be able to sustain liquid water at their surface. At the same time, spectroscopic observations of the primary and secondary transits of giant planets revealed a complex, and possibly out of equilibrium, atmospheric chemistry. But such observations are not precise enough yet to be carried out on an Earth analog orbiting a Sun like star.

Fortunately, most stars in the universe are fainter than the Sun ! Warm planets can thus be found on much closer orbits. And as these stars are also smaller and less massive than our Sun, they offer ideal targets for transit detection and radial velocity follow up, and even make spectroscopic observations of small size objects possible. With ground and space based missions already finding such objects (*MEarth*: Charbonneau et al. 2009 ; *Kepler*: Borucki et al. 2011), the first *characterizable* Earth analog in the habitable zone does not seem so far ahead of us.

However, to prepare upcoming spectrometric observations with *HST*, *Spitzer* or *JWST*, theoretical models of the chemical composition and thermal structure of the atmosphere of terrestrial planets in the relevant range of the parameter space are required. Moreover, as these planets are expected to be (pseudo) synchronized and exhibit a strong day night contrast, the global atmospheric circulation must be properly treated to correctly interpret the transmission spectra which probe very specific regions of the surface. This should soon revive the need for applying 3D Global Circulation Models (GCMs) not only to Hot Jupiters, but also to close in Super Earths for which the atmospheric dynamics and chemistry is yet poorly understood. The potential of this research is immense as it will open the avenue to the detection of bio-signatures.

On the non transiting side, during the last few years, a tremendous amount of work has been devoted to direct imaging of extrasolar planets and brown dwarfs. This resulted on one hand in many successful detections, for example by Chauvin et al. (2004) or Marois et al. (2010) (to cite only a few), and on the other in constraining the population of substellar companions by large surveys (Lafrenière et al. 2007 ; Chauvin et al. 2010 ; Leconte et al. 2010b).

However, while this method is a formidable tool to constrain the atmospheric physics - in particular the presence of molecular absorbers, clouds or non-equilibrium chemistry - of young giant planets and brown dwarfs at large orbital separation, it cannot yet constrain our structure and evolution models. Indeed, as the mass of the object is still unmeasured, this is only through the theoretical mass-luminosity

relationships provided by the aforementioned models that it can be determined. But, as transit and Doppler measurements probe toward longer and longer period objects, and as extremely high angular resolution imaging instruments are being built (*SPHERE*, *GPI*), these techniques should soon overlap.

When this arrives, the possibility to have at the same time, the mass of the body, its bolometric luminosity and its colors in different bands will undoubtedly unravel new families of substellar objects, maybe allowing us to distinguish between their various possible formation mechanisms and to pin down their true nature. Not to mention the possibility to detect such objects at the very first stages of their evolution and even maybe from their formation. Hence, to ready ourselves to these upcoming observations, in addition to a better modeling of planets and brown dwarfs atmospheres, we will have to bridge the gap between formation and evolution models. This of course requires to treat consistently the early solid and gas accretion, the radiative shock that occurs when a gap is opened between the planet and the nebula, and the following evolution in the detached phase. We will thus be able to make more accurate predictions of the observable parameters of substellar objects from their very youngest age, and follow their life from birth to fate.

Let us wager that the next decade will bring us, as always, very challenging findings.

Appendix A

Publication list

A.1   Refereed publications

- **J. Leconte** & G. Chabrier. "A new vision of giant planet interiors: Impact of double diffusive convection". *Astronomy & Astrophysics*, 540 :A20, Avril 2012.

- E. Bolmont, S. N. Raymond & **J. Leconte**. "Tidal evolution of planets around brown dwarfs." *Astronomy & Astrophysics*, 535 :A94, Novembre 2011.

- **J. Leconte**, D. Lai, and G. Chabrier. "Distorted, non-spherical transiting planets : impact on the transit depth and on the radius determination". *Astronomy & Astrophysics*, 528 :A41, April 2011.

- R. Heller, **J. Leconte**, and R. Barnes. "Tidal obliquity evolution of potentially habitable planets". *Astronomy & Astrophysics*, 528 :A27, April 2011.

- **J. Leconte**, G. Chabrier, I. Baraffe, and B. Levrard. "Is tidal heating sufficient to explain bloated exoplanets ? Consistent calculations accounting for finite initial eccentricity". *Astronomy & Astrophysics*, 516 :A64+, June 2010.

- **J. Leconte**, R. Soummer, S. Hinkley, B. R. Oppenheimer, A. Sivaramakrishnan, D. Brenner, J. Kuhn, J. P. Lloyd, M. D. Perrin, R. Makidon, L. C. Roberts, Jr., J. R. Graham, M. Simon, R. A. Brown, N. Zimmerman, G. Chabrier, and I. Baraffe. "The Lyot Project Direct Imaging Survey of Substellar Companions : Statistical Analysis and Information from Nondetections". *The Astrophysical Journal*, 716 :1551-1565, June 2010.

- **J. Leconte**, I. Baraffe, G. Chabrier, T. Barman, and B. Levrard. "Structure and evolution of the first CoRoT exoplanets : probing the brown dwarf/planet overlapping mass regime". *Astronomy & Astrophysics*, 506 :385-389, October 2009.

A.2   Proceedings

- R. Heller, R. Barnes, & **J. Leconte**. "Habitability of Extrasolar Planets and Tidal Spin Evolution". *Origins of Life and Evolution of the Biosphere*, page 37, December 2011.

- **J. Leconte**, G. Chabrier & I. Baraffe. "Uncertainties in tidal theory: Implications for bloated hot Jupiters". In *A. Sozzetti, M. G. Lattanzi, & A. P. Boss, editor, IAU Symposium, volume 276 of IAU Symposium*, pages 248-251, November 2011.

- G. Chabrier, **J. Leconte** & I. Baraffe. "Understanding exoplanet formation, structure and evolution in 2010". In *A. Sozzetti, M. G. Lattanzi, & A. P. Boss, editor, IAU Symposium, volume 276 of IAU Symposium*, pages 171-180, November 2011.

- E. Bolmont, S. N. Raymond, & J. Leconte. "Tidal evolution of planets around brown dwarfs". In *EPSC-DPS Joint Meeting 2011*, held 2-7 October 2011 in Nantes, France. p.588, page 588, October 2011.

- A.-S. Maurin, F. Selsis, F. Hersant, S. N. Raymond, J. Leconte & M. Delbo. "Effects of tides on the infrared light curve of rocky exoplanets". In *EPSC-DPS Joint Meeting 2011*, held 2-7 October 2011 in Nantes, France. p.1351, page 1351, October 2011.

- J. Leconte, G. Chabrier, I. Baraffe, and B. Levrard. "The radius anomaly in the planet/brown dwarf overlapping mass regime". *EPJ Web of Conferences*, 11 :03004, 2011.

- G. Chabrier, I. Baraffe, J. Leconte, J. Gallardo, and T. Barman. "The mass-radius relationship from solar-type stars to terrestrial planets : a review". In E. Stempels, editor, *American Institute of Physics Conference Series*, volume 1094, pages 102-111, February 2009.

Appendix B

Thermodynamic relations

As is well known, for a given material, there exists only three independent thermodynamic derivatives (Callen 1960). Thus, numerical equations of state only provide a set of three such derivatives from which one can find all the others by means of thermodynamic relations. In this appendix, we briefly give general thermodynamic relations that can be used to derive the relations needed, as well as the relations that are most needed when handling the numerical ANEOS and SCVH packages.

B.1   General relations

As can be shown (e.g. Callen 1960), if we have three thermodynamic variables (X, Y, Z), there exists the relation

$$dZ = \left.\frac{\partial Z}{\partial X}\right|_Y dX + \left.\frac{\partial Z}{\partial Y}\right|_X dY,$$ (B.1)

and thus

$$\left.\frac{\partial X}{\partial Y}\right|_Z = -\frac{\left.\frac{\partial Z}{\partial Y}\right|_X}{\left.\frac{\partial Z}{\partial X}\right|_Y}.$$ (B.2)

Sometimes, we also need to compute the derivative of a given function $F(X, Y')$ that we know as a function of (X, Y). We thus need to carry out a change of variable from (X, Y) to (X, Y'). As

$$dY = \left.\frac{\partial Y}{\partial X}\right|_{Y'} dX + \left.\frac{\partial Y}{\partial Y'}\right|_X dY',$$ (B.3)

we have

$$\begin{aligned} dF &= \left.\frac{\partial F}{\partial X}\right|_Y dX + \left.\frac{\partial F}{\partial Y}\right|_X dY \\ &= \left(\left.\frac{\partial F}{\partial X}\right|_Y + \left.\frac{\partial F}{\partial Y}\right|_X \left.\frac{\partial Y}{\partial X}\right|_{Y'}\right) dX + \left.\frac{\partial F}{\partial Y}\right|_X \left.\frac{\partial Y}{\partial Y'}\right|_X dY', \end{aligned}$$ (B.4)

whence

$$\begin{aligned} \left.\frac{\partial F}{\partial Y'}\right|_X &= \left.\frac{\partial F}{\partial Y}\right|_X \left.\frac{\partial Y}{\partial Y'}\right|_X \\ \left.\frac{\partial F}{\partial X}\right|_{Y'} &= \left.\frac{\partial F}{\partial X}\right|_Y + \left.\frac{\partial F}{\partial Y}\right|_X \left.\frac{\partial Y}{\partial X}\right|_{Y'}. \end{aligned}$$ (B.5)

B.2 ANEOS

ANEOS (Thompson and Lauson 1972) was designed to work with the variables (ρ, T), and thus provides the specific thermal capacity at constant volume (density)

$$c_V \equiv \left. \frac{\partial \tilde{U}}{\partial T} \right|_\rho,$$

(B.6)

and two derivatives of the pressure, $\left. \frac{\partial P}{\partial T} \right|_\rho$ and $\left. \frac{\partial P}{\partial \rho} \right|_T$. For convenience, as it was designed to be used in hydrodynamics codes, it also provides directly the sound speed

$$c_s^2 = \left. \frac{\partial P}{\partial \rho} \right|_{\tilde{S}},$$

(B.7)

as well as the radiative opacity ($\bar{\kappa}$). As we have seen in Chapter 1, there are two other derivatives that can be needed, the specific thermal capacity at constant pressure and the adiabatic gradient, that are given by

$$c_P \equiv T \left. \frac{\partial \tilde{S}}{\partial T} \right|_P = -T \frac{\left. \frac{\partial P}{\partial T} \right|_{\tilde{S}}}{\left. \frac{\partial P}{\partial \tilde{S}} \right|_T} = -T \left(\frac{\left. \frac{\partial \rho}{\partial T} \right|_{\tilde{S}}}{\left. \frac{\partial \rho}{\partial \tilde{S}} \right|_T} + \frac{\left. \frac{\partial P}{\partial T} \right|_\rho}{\left. \frac{\partial P}{\partial \rho} \right|_T \left. \frac{\partial \rho}{\partial \tilde{S}} \right|_T} \right) = c_V + \frac{T \left. \frac{\partial P}{\partial T} \right|_\rho^2}{\rho^2 \left. \frac{\partial P}{\partial \rho} \right|_T},$$

(B.8)

where the last transformation uses the usual maxwell relation $\left. \frac{\partial \rho}{\partial \tilde{S}} \right|_T = -\rho^2 \left. \frac{\partial T}{\partial P} \right|_\rho$, and

$$\nabla_{\text{ad}} \equiv \left. \frac{\partial \ln T}{\partial \ln P} \right|_{\tilde{S}} = \frac{P}{T} \left(\left. \frac{\partial P}{\partial T} \right|_\rho + \left. \frac{\partial P}{\partial \rho} \right|_T \left. \frac{\partial \rho}{\partial T} \right|_{\tilde{S}} \right)^{-1} = \frac{P \left. \frac{\partial P}{\partial T} \right|_\rho}{c_V \rho^2 \left. \frac{\partial P}{\partial \rho} \right|_T + T \left. \frac{\partial P}{\partial T} \right|_\rho^2},$$

(B.9)

because

$$\left. \frac{\partial \rho}{\partial T} \right|_{\tilde{S}} = -\frac{\left. \frac{\partial \tilde{S}}{\partial T} \right|_\rho}{\left. \frac{\partial \tilde{S}}{\partial \rho} \right|_T} = \rho^2 \left. \frac{\partial T}{\partial P} \right|_\rho \left. \frac{\partial \tilde{S}}{\partial T} \right|_\rho = \frac{\rho^2 c_V}{T} \left. \frac{\partial T}{\partial P} \right|_\rho.$$

(B.10)

B.3 SCVH

The SCVH equation of state (Saumon et al. 1995) uses the intensive variables (P, T), and provides all the derivatives of the density and entropy, as well as the adiabatic gradient[1]. Then, the sound speed is given by

$$c_s^2 = \left(\left. \frac{\partial \rho}{\partial P} \right|_{\tilde{S}} \right)^{-1} = \left(\left. \frac{\partial \rho}{\partial P} \right|_T + \left. \frac{\partial \rho}{\partial T} \right|_P \left. \frac{\partial T}{\partial P} \right|_{\tilde{S}} \right)^{-1} = \left(\left. \frac{\partial \rho}{\partial P} \right|_T - \left. \frac{\partial \rho}{\partial T} \right|_P \frac{\left. \frac{\partial \tilde{S}}{\partial P} \right|_T}{\left. \frac{\partial \tilde{S}}{\partial T} \right|_P} \right)^{-1}$$

(B.11)

---

[1]Note that the SCVH package gives the decimal logarithm of the thermodynamic quantities, and their logarithmic derivatives ($\left. \frac{\partial \log \rho}{\partial \log T} \right|_P$, $\left. \frac{\partial \log \rho}{\partial \log P} \right|_T$, etc...).

Appendix C

Polytropic spheres

Let us assume that our equation of state is of the form

$$P = K\rho^{1+1/\tilde{n}}, \tag{C.1}$$

where K and $\tilde{n}$ are called the polytropic *temperature* and *index*, and are constant throughout the configuration. Because the temperature does not enter explicitly in our equation of state, we do not need any equation for the energy conservation, nor the energy transport, which are already implicitly contained in Eq. (C.1). We can thus derive a simple equation for the structure of the object (e.g. Chandrasekhar 1939). For brevity, we will only discuss here undistorted polytropic spheres to introduce the classical variables used and have the useful equations at hand.

C.1 Lane-Emden equation

Following Chandrasekhar (1939), combining hydrostatic equilibrium and mass conservation (Eqs. (1.57) and (1.58)), we get

$$\frac{\partial P}{\partial r} = -\frac{G\rho}{r^2} \int_0^r 4\pi r'^2 \rho(r) dr', \tag{C.2}$$

and differentiating this intro-differential equation with respect to r yields

$$\frac{\partial}{\partial r}\left(\frac{r^2}{\rho}\frac{\partial P}{\partial r}\right) = -4\pi G r^2 \rho. \tag{C.3}$$

Substituting P by its expression given by the polytropic equation of state, and introducing the two following dimensionless variables

$$\tilde{\theta}^{\tilde{n}} = \rho/\rho_c \text{ and } \tilde{\xi} = r/R_{\text{LE}}, \tag{C.4}$$

where ρ_c is the central density, and R_{LE} is a yet undetermined scaling factor we finally obtain

$$\frac{(\tilde{n}+1)K\rho_c^{\frac{1}{\tilde{n}}-1}}{4\pi G R_{\text{LE}}^2} \cdot \frac{1}{\tilde{\xi}^2}\frac{d}{d\tilde{\xi}}\left(\tilde{\xi}^2\frac{d\tilde{\theta}}{d\tilde{\xi}}\right) = -\tilde{\theta}^{\tilde{n}}. \tag{C.5}$$

Then, choosing

$$\boxed{R_{\text{LE}}^2 = \frac{\tilde{n}+1}{4\pi G}K\rho_c^{\frac{1}{\tilde{n}}-1},} \tag{C.6}$$

yields the famous *Lane Emden* equation

$$\boxed{\frac{1}{\tilde{\xi}^2}\frac{\mathrm{d}}{\mathrm{d}\tilde{\xi}}\left(\tilde{\xi}^2\frac{\mathrm{d}\tilde{\theta}}{\mathrm{d}\tilde{\xi}}\right) = -\tilde{\theta}^{\tilde{n}}.} \tag{C.7}$$

As it is visible from Eq. (1.57), $\frac{\mathrm{d}\tilde{\theta}}{\mathrm{d}\tilde{\xi}} \propto \frac{m}{\tilde{\xi}^2}$. Near the center, $m \propto \tilde{\xi}^3$, and the boundary conditions are thus

$$\frac{\mathrm{d}\tilde{\theta}}{\mathrm{d}\tilde{\xi}}(\tilde{\xi}=0) = 0 \quad \text{and} \quad \tilde{\theta}(\tilde{\xi}=0) = 1. \tag{C.8}$$

C.2   Global properties

Once the *Lane Emden* equation has been integrated numerically until $\tilde{\theta} = 0$, we are left with the value of $\tilde{\xi}$ and of the derivative of $\tilde{\theta}$ at this point. As these quantities depend on $\tilde{n}$ alone, I will call them $\tilde{\xi}_{\tilde{n}}$ and $\tilde{\theta}'_{\tilde{n}}$ respectively[1]. Using the structure equations, we can derive some global characteristics of our objects. Because of the definition of $\tilde{\xi}$, the radius is obviously given by

$$R_1 = \tilde{\xi}_{\tilde{n}} R_{\mathrm{LE}} = \tilde{\xi}_{\tilde{n}} \sqrt{\frac{\tilde{n}+1}{4\pi G}K\rho_{\mathrm{c}}^{\frac{1}{\tilde{n}}-1}}. \tag{C.9}$$

The mass can be obtained by integrating the density which, by means of the Lane-Emden equation, rewrites

$$M_1 = 4\pi \int_0^r \rho\, r'^2 \mathrm{d}r' = 4\pi\rho_{\mathrm{c}} R_{\mathrm{LE}}^3 \int_0^{\tilde{\xi}_{\tilde{n}}} \tilde{\theta}^{\tilde{n}}\tilde{\xi}^2 \mathrm{d}\tilde{\xi},$$

$$= -4\pi\rho_{\mathrm{c}} R_{\mathrm{LE}}^3 \int_0^{\tilde{\xi}_{\tilde{n}}} \frac{\mathrm{d}}{\mathrm{d}\tilde{\xi}}\left(\tilde{\xi}^2\frac{\mathrm{d}\tilde{\theta}}{\mathrm{d}\tilde{\xi}}\right)\mathrm{d}\tilde{\xi} = 4\pi\rho_{\mathrm{c}} R_{\mathrm{LE}}^3 \tilde{\xi}_{\tilde{n}}^2 |\tilde{\theta}'_{\tilde{n}}|. \tag{C.10}$$

Hence

$$\boxed{M_1 = \frac{\rho_{\mathrm{c}}^{\frac{3-\tilde{n}}{2\tilde{n}}}}{\sqrt{4\pi}}\left(\frac{\tilde{n}+1}{G}K\right)^{3/2}\tilde{\xi}_{\tilde{n}}^2 |\tilde{\theta}'_{\tilde{n}}|.} \tag{C.11}$$

Thanks to Eqs. (C.9) and (C.10), we can also show that the mean density writes

$$\boxed{\frac{\bar{\rho}_1}{\rho_{\mathrm{c}}} = \frac{3\,|\tilde{\theta}'_{\tilde{n}}|}{\tilde{\xi}_{\tilde{n}}}.} \tag{C.12}$$

Defining the dimensionless gyration radius is given by

$$r_{\mathrm{gyr}}^2 = \frac{5}{3}\frac{\int_0^{\tilde{\xi}_{\tilde{n}}} \tilde{\theta}^{\tilde{n}}\tilde{\xi}^4 \mathrm{d}\tilde{\xi}}{\tilde{\xi}_{\tilde{n}}^4 |\tilde{\theta}'_{\tilde{n}}|}, \tag{C.13}$$

which can also be computed for any given $\tilde{n}$. With this definition, r_{gyr} is equal to 1 for an incompressible body ($\tilde{n} = 0$), and to 0 for an object where all the mass in concentrated at the center.

Finally, by eliminating ρ_{c} from Eqs. (C.9) and (C.10), we get the mass radius relationship

$$\boxed{M_1^{\frac{\tilde{n}-1}{\tilde{n}}} R_1^{\frac{3-\tilde{n}}{\tilde{n}}} = \frac{K}{G}\frac{\tilde{n}+1}{(4\pi)^{1/\tilde{n}}}\tilde{\xi}_{\tilde{n}}^{\frac{\tilde{n}+1}{\tilde{n}}} |\tilde{\theta}'_{\tilde{n}}|^{\frac{\tilde{n}-1}{\tilde{n}}}.} \tag{C.14}$$

---

[1]As $\tilde{\theta}'_{\tilde{n}}$ is always negative, we often make use of $|\tilde{\theta}'_{\tilde{n}}|$ to manipulate positive quantities.

Appendix D

First order theory for an arbitrary perturbing potential

In Chapter 3, we introduced the various concepts of the theory of figures. In order for the reader to have all the needed equations at hand, here we outline the method first developed by Sterne (1939).

D.1 Arbitrary perturbation

To lowest order the body response is linear and the total deformation is the sum of the response to each term of the decomposition of the perturbing potential. Thus, in order to derive the equations in a rather general way, we only need to consider a term a perturbing potential of the form

$$V_{\text{ext}}(r, \theta, \phi) = \mathbf{c}_n^m r^n Y_n^m(\theta, \phi),$$ (D.1)

where $\mathbf{c}_n^m$ is a constant which defines the amplitude of the perturbation. The reference axis defining θ and ϕ may change from one term to the other. Analogously to Eq. (3.13), a small dimensionless parameter can be defined as

$$m_{\text{ext}} = \frac{\mathbf{c}_n^m \bar{R}_1^{n+1}}{GM_1} = \frac{3}{4\pi} \frac{\mathbf{c}_n^m \bar{R}_1^{n-2}}{G\bar{\rho}_1}.$$ (D.2)

D.2 Level surfaces

To simplify the figure equations, we choose to use the mean radius $\bar{r}$ defined by Eq. (3.17). Using this *mean radius* implies that to first order, meaning that $\mathbf{s}_n^m \mathbf{s}_{n'}^{m'} \propto m_{\text{ext}}^2 \approx 0$,

$$\frac{4}{3}\pi \bar{r}^3 = \frac{4}{3}\pi \bar{r}^3 (1 + 3\,\mathbf{s}_0^0) \quad \Rightarrow \quad \boxed{\mathbf{s}_0^0 = 0.}$$ (D.3)

For this reason, using the variable $\bar{r}$, instead of r_{eq} or r_{pol}, simplifies the first order equation for the *hydrostatic equilibrium* which thus does not involve the $\mathbf{s}_n^m$ (the dependency in $\bar{r}$ of the $\mathbf{s}_n^m$ being implicitly assumed). Thus, in the following, we will use the variable $\bar{r}$, and note $\bar{R}_1$ the mean radius of the 1 bar equipotential of the object considered. To first order, the shape of our body is a general triaxial ellipsoid, and we have $\bar{R}_1 = (a_1 a_2 a_3)^{1/3}$. For figure equations derived using either the equatorial or polar radius, the reader is referred to Zharkov and Trubitsyn (1970).

As discussed in § 3.1.1, by definition, level surfaces are also isodensity surfaces. This means that the various integrals involving the density can be integrated by using $\rho(\mathbf{r}') = \rho(\bar{r})$.

D.3 Computation of the mass integrals

As we have reduced our density field to a function of $\bar{r}$ alone, we can now express the gravitational potential and the mass integrals, Eqs. (3.3) and (3.4), with algebraic functions of the figure functions. As $\rho(\mathbf{r}')$ is only a function of $\bar{r}$, we must carry out the change of variable from (r, θ, ϕ) to $(\bar{r}, \theta, \phi)$ using Eq. (3.16). The difficulty lies in the limit of the integration domain which is still spherical. It has been shown by Zharkov and Trubitsyn (1980) and Lyapunov (1903) that replacing this domain by the one delimitated by a level surface of the form Eq. (3.16) and enclosing the same volume (the condition therefore reading $\bar{r}' < \bar{r}$ instead of $r' < r$) does not affect the integral, all the terms calculated between the level surface and the sphere compensating one another. This yields

$$
\begin{aligned}
D_n^m &= (2 - \delta_{m,0}) \frac{(n-m)!}{(n+m)!} \int_{r'<r} \rho(\mathbf{r}') (r')^n Y_n^m(\theta', \phi') \, d^3\mathbf{r}' \\
&= (2 - \delta_{m,0}) \frac{(n-m)!}{(n+m)!} \frac{1}{n+3} \times \\
&\quad \times \int_{\bar{r}'<\bar{r}} d\bar{r}' \rho(\bar{r}') \int_{-1}^{1} d\cos\theta' \int_0^{2\pi} d\phi' \frac{d}{d\bar{r}'} [(r')^{n+3}] Y_n^m(\theta', \phi'),
\end{aligned}
$$
(D.4)

$$
\begin{aligned}
\bar{D}_n^m &= (2 - \delta_{m,0}) \frac{(n-m)!}{(n+m)!} \frac{1}{2-n} \times \\
&\quad \times \int_{\bar{r}<\bar{r}'<\bar{R}_1} d\bar{r}' \rho(\bar{r}') \int_{-1}^{1} d\cos\theta' \int_0^{2\pi} d\phi' \frac{d}{d\bar{r}'} [(r')^{2-n}] Y_n^m(\theta', \phi'), \\
\bar{D}_2^m &= (2 - \delta_{m,0}) \frac{(n-m)!}{(n+m)!} \times \\
&\quad \times \int_{\bar{r}<\bar{r}'<\bar{R}_1} d\bar{r}' \rho(\bar{r}') \int_{-1}^{1} d\cos\theta' \int_0^{2\pi} d\phi' \frac{d}{d\bar{r}'} [\ln r'] Y_n^m(\theta', \phi').
\end{aligned}
$$
(D.5)

Replacing r' using Eq. (3.16) we get

$$
\begin{aligned}
D_n^m &= (2 - \delta_{m,0}) \frac{(n-m)!}{(n+m)!} \times \\
&\quad \times \int_0^{\bar{r}} d\bar{r}' \rho(\bar{r}') \frac{\partial}{\partial \bar{r}} \left[\frac{\bar{r}'^{n+3}}{n+3} \int_{-1}^{1} d\cos\theta' \int_0^{2\pi} d\phi' \left(1 + \sum_{n',m'} s_{n'}^{m'} Y_{n'}^{m'}(\theta', \phi') \right)^{n+3} Y_n^m(\theta', \phi') \right].
\end{aligned}
$$
(D.6)

Developing the last term, ignoring terms of order $s_n^m \times s_{n'}^{m'}$, and using the orthogonality relation for the tesseral harmonics, this simplifies to

$$
D_n^m = \frac{4\pi}{2n+1} \int_0^{\bar{r}} d\bar{r}' \rho(\bar{r}') \frac{d}{d\bar{r}'} \left[\bar{r}'^{n+3} s_n^m \right].
$$
(D.7)

Analogously

$$
\bar{D}_n^m = \frac{4\pi}{2n+1} \int_{\bar{r}}^{\bar{R}_1} d\bar{r}' \rho(\bar{r}') \frac{d}{d\bar{r}'} \left[\bar{r}'^{2-n} s_n^m \right].
$$
(D.8)

By coincidence, this equation also works for $n = 2$, even if $\bar{D}_2^m$ involves the derivative of $\ln r'$. There are two special cases:

$$
\begin{aligned}
D_0^0 &= \frac{4\pi}{3} \int_0^{\bar{r}} \rho(\bar{r}') \, d\bar{r}'^3, \\
\bar{D}_0^0 &= \frac{4\pi}{2} \int_{\bar{r}}^{\bar{R}_1} \rho(\bar{r}') \, d\bar{r}'^2.
\end{aligned}
$$
(D.9)

We can see that $D_n^m \propto s_n^m$, therefore they are all first order quantities (except D_0^0 and $\bar{D}_0^0$ which give the zeroth order spherical potential).

D.4   Total potential and equations of figures

Now that we have calculated the coefficients of the spherical harmonics decomposition of both gravitational and perturbing potentials, we can express the total potential as well

$$V_{\text{tot}}(\bar{r}, \theta, \phi) = V_G + V_{\text{ext}}$$
$$= -\frac{4}{3} \pi G \bar{\rho}_1 \bar{r}^2 \sum_{n,m} \hat{V}_n^m(\bar{r}) Y_n^m(\theta, \phi). \tag{D.10}$$

Because the $\bar{r} = \text{cst}$ surfaces are equipotentials by construction, our set of equations on the figure functions we be given by Eq. (D.3) and

$$\left\{ \hat{V}_n^m(\bar{r}) = 0 \right\}_{n \neq 0, |m| \leqslant n}. \tag{D.11}$$

Using the dimensionless variables

$$\begin{cases} \tilde{s} &= \bar{r}/\bar{R}_1 \\ S_n^m &= \frac{3 D_n^m}{4\pi \bar{\rho}_1 \bar{r}^{n+3}} \\ \bar{S}_n^m &= \frac{3 \bar{D}_n^m}{4\pi \bar{\rho}_1 \bar{r}^{2-n}} \end{cases} \tag{D.12}$$

the potential given by Eqs. (3.2) and (D.1) can be expanded onto spherical harmonics, and rewriten (neglecting all the $s_n^m \times s_{n'}^{m'}$ and $s_n^m \times m_{\text{ext}}$ terms)

$$V_{\text{tot}}(\bar{r}, \theta, \phi) = -\frac{4}{3} \pi G \bar{\rho}_1 \bar{r}^2 \times$$
$$\times \left[S_0^0 + \bar{S}_0^0 - m_{\text{ext}} \tilde{s}^{n-2} Y_n^m(\theta, \phi) + \sum_{n' \geqslant 0, m'} \left(S_{n'}^{m'} + \bar{S}_{n'}^{m'} - s_{n'}^{m'} S_0^0 \right) Y_{n'}^{m'}(\theta, \phi) \right]. \tag{D.13}$$

Thus, our set of equations is

$$\boxed{\left\{ \hat{V}_{n'}^{m'}(\tilde{s}) = S_{n'}^{m'} + \bar{S}_{n'}^{m'} - s_{n'}^{m'} S_0^0 - \delta_{n,n'} \delta_{m,m'} \tilde{s}^{n-2} m_{\text{ext}} = 0 \right\}_{n',m'}.} \tag{D.14}$$

Of course, the *mean* hydrostatic equilibrium is provided by the n = 0 term, which reads

$$\frac{\partial P}{\partial \bar{r}} = \frac{4}{3} \pi G \bar{\rho}_1 \frac{\mathrm{d}}{\mathrm{d}\bar{r}} \left(\bar{r}^2 \hat{V}_0^0 \right), \quad \hat{V}_0^0 = S_0^0 + \bar{S}_0^0. \tag{D.15}$$

Substituting S_0^0 and $\bar{S}_0^0$ by their expressions in Eq. (D.9) shows us that the mean equilibrium is left unperturbed

$$\boxed{\frac{\partial P}{\partial \bar{r}} = -\rho \frac{Gm}{\bar{r}^2},} \tag{D.16}$$

meaning that the mean radius of any given equipotential surface is the same in the spherical case or in the real object[1]. This entails that the profiles of all the thermodynamical variables expressed as a function of the mean radius in the distorted object are equal to the radial profile obtained in the unperturbed case ($\rho(\bar{r}) = \rho(r)$). In particular, the density profile yielded by the integration of the zeroth order hydrostatic equilibrium ($\rho(r)$), can be directly used in integrating Eq. (D.19) derived hereafter.

---

[1] As can be seen in Appendix E, this is true only to first order.

D.5   Differential equation on s_n^m

From the set of equations (D.14), we immediately see that all the $s_{n'}^{m'}$ ($n' \neq n$ and $m' \neq m$) are equal to 0. To derive numerically the s_n^m, the integro-differential equation (D.14) can be solved iteratively with the method described in Zharkov and Trubitsyn (1980). The numerical solution after i iterations is given by

$$s_n^m|_i = \frac{1}{S_0^0} \left[S_n^m(s_n^m|_{i-1}) + \bar{S}_n^m(s_n^m|_{i-1}) - \tilde{s}^{n-2} m_{\text{ext}} \right], \tag{D.17}$$

and $s_n^m(\tilde{s})|_0 = 0$ can be used as a first guess. This procedure, which is mandatory to higher order, can however be reduced in the linear case. Indeed, multiplying Eq. (D.14) by $\tilde{s}^{n+3}$, differentiating with respect to $\tilde{s}$, and dividing by $\tilde{s}^{2n}$, we see that s_n^m verifies[2] (Sterne 1939)

$$-\left[\frac{n s_n^m}{\tilde{s}^{n+1}} + \frac{1}{\tilde{s}^n} \frac{d s_n^m}{d \tilde{s}} \right] \int_0^{\tilde{s}} \rho(\tilde{s}) \tilde{s}^2 d\tilde{s} + \int_{\tilde{s}}^1 \rho(\tilde{s}) d \left[\tilde{s}^{2-n} s_n^m \right] = \frac{2n+1}{3} \bar{\rho}_1 m_{\text{ext}}. \tag{D.18}$$

Differentiating once again with respect to $\tilde{s}$ yields

$$\frac{d^2 s_n^m}{d\tilde{s}^2} - \frac{n(n+1)}{\tilde{s}^2} s_n^m + \frac{6}{\tilde{s}^2} \frac{\rho(\tilde{s})}{\bar{\rho}(\tilde{s})} \left(\tilde{s} \frac{d s_n^m}{d\tilde{s}} + s_n^m \right) = 0, \tag{D.19}$$

with

$$\bar{\rho}(\tilde{s}) = \frac{3}{\tilde{s}^3} \int_0^{\tilde{s}} \rho(\tilde{s}') \tilde{s}'^2 d\tilde{s}', \tag{D.20}$$

the mean density interior to $\tilde{s}$, and $\bar{\rho}(1) = \bar{\rho}_1$. Using the variable $\eta_n(\tilde{s}) = \frac{\tilde{s}}{s_n^m(\tilde{s})} \frac{d s_n^m}{d\tilde{s}}$, this rewrites

$$\boxed{\tilde{s} \frac{d\eta_n}{d\tilde{s}} + \eta_n^2 - \eta_n - n(n+1) + 6 \frac{\rho(\tilde{s})}{\bar{\rho}(\tilde{s})} (\eta_n + 1) = 0.} \tag{D.21}$$

As always, the difficult part lies in finding the boundary condition for $\eta_n(0)$. Following Jeffreys (1970), let us assume that $s_n^m \propto \tilde{s}^k$ near $\tilde{s} = 0$ and substitute this solution in Eq. (D.19). Keeping the smallest power in $\tilde{s}$ we get the following equation for k

$$k(k-1) - n(n-1) + 6k + 6 = 0, \tag{D.22}$$

whence

$$k = n-2 \text{ or } k = -n-3. \tag{D.23}$$

The $k = -n-3$ solutions are obviously singular at the center and can be discarded. Thus $s_n^m(\tilde{s}) \propto \tilde{s}^{n-2}$ near $\tilde{s} = 0$, which provides us with the boundary condition for η_n

$$\boxed{\lim_{\tilde{s} \to 0} \eta_n(\tilde{s}) = n-2.} \tag{D.24}$$

For the $n = 1$ case, there still seems to be a singularity at the center. But we can see that in this case, $s_n^m(\tilde{s}) = A \tilde{s}^{-1}$ is an exact solution of Eq. (D.19). Therefore, the radial displacement is given by $\bar{r} \frac{A}{\bar{r}} Y_n^m = A Y_n^m$. This is a rigid body displacement and need not be considered further.

In an idealized case, this equation can be directly solved analytically. Indeed, in the incompressible case, $\rho(\tilde{s}) = \bar{\rho}(\tilde{s}) = \bar{\rho}_1$. Then, for a quadrupolar disturbance ($n = 2$), $\eta_n(0) = 0$ and $\eta_n'(0) = 0$. Because $\eta_n(\tilde{s}) = 0$ is a solution of the differential equation that verifies the boundary conditions, the Cauchy's theorem states that it is the unique solution we are looking for. As explained hereafter, this yields $k_2 = 3/2$ and $h_2 = 5/2$, as expected (Zharkov and Trubitsyn 1980).

---

[2]To involve only the variable $\tilde{s}$ in the following equations, it is implicitly assumed that for any function g, $g(\tilde{s})$ indeed denotes $g(\tilde{s}\bar{R}_1) = g(\bar{r})$.

Appendix E

Third order theory of planetary figures

While the first order theory presented in Chapter 3 can be sufficient to describe system where observational constraints are still weak, it is not accurate enough to describe the major planets of the Solar System. Indeed, the missions that landed, orbited or simply passed by our four gas giants provided high precision measurements of their composition, atmospheric properties and gravitational and magnetic fields (see Guillot 2005 for a review). The gravitational field, in particular, has been measured up to its third harmonic (J_6 ; Campbell and Synnott 1985 ; Campbell and Anderson 1989) providing very valuable information on the deep interior of these planets. To extract this information, we need an accurate theory predicting the structure of the gravitational field of a body in hydrostatic equilibrium to third or higher order as derived in Zharkov and Trubitsyn (1980). However, during the process of re-calculating these high order developments, I found some errors or typos that I wish here to correct.

E.1 Rotational perturbation

Because the tidal distortion is negligible for the giant planets - for Jupiter, the disturbance created by Io gives $|m_{tid}| \approx 2 \times 10^{-7}$ against $m_{rot} \approx 0.1$ due to the fast rotation of the planet - we only focus on the rotational deformation. This directly entails that the shape of planet will be symmetric with respect to both the rotation axis and the equatorial plane (Zharkov and Trubitsyn 1980). As a result, only the m = 0 harmonics need to be considered. For simplicity, we therefore drop these in our notation and superscript indices will only be exponents.

E.2 Level surfaces

E.2.1 Mean radius

Once again, to obtain a set of equations for the figure functions, we must decompose the total potential on spherical harmonics and as a function of the figure functions. Because of the symmetry of the problem, we can reduce our set of spherical harmonics to a set containing only the even Legendre

polynomials[1]. In this case only the $\mathbf{s}_{2n}^0$ terms remain[2]. Eq. (3.16) thus reduces to

$$r(l, \theta, \phi) = \bar{r} \left[1 + \sum_n s_{2n}(\bar{r}) P_{2n}(\tilde{\mu}) \right], \tag{E.1}$$

where $\tilde{\mu} = \cos \theta$, the cosine of the colatitude. Hence, Eq. (3.17) yields

$$2 = \int_{-1}^1 \left[1 + \sum_{n=0}^\infty s_{2n} P_{2n}(\tilde{\mu}) \right]^3 \mathrm{d}\tilde{\mu}. \tag{E.2}$$

To 3$^{\text{rd}}$ order, this yields (with correction of a typo in Zharkov and Trubitsyn 1980)

$$s_0 = - \left(\frac{1}{5} s_2^2 + \frac{2}{105} s_2^3 \right). \tag{E.3}$$

Defining r_{eq} the equatorial radius of a shell of mean radius $\bar{r}$, we also have

$$\frac{r_{\text{eq}}}{\bar{r}} = 1 + \sum_{n=0}^\infty s_{2n} P_{2n}(0)$$

$$= 1 + s_0 - \frac{1}{2} s_2 + \frac{3}{8} s_4 - \frac{5}{16} s_6 + \mathscr{O}(m_{\text{rot}}^4), \tag{E.4}$$

$$\frac{\bar{r}}{r_{\text{eq}}} = 1 - s_0 + \frac{s_2}{2} + \frac{s_2^2}{4} - \frac{3 s_4}{8} - s_0 s_2 + \frac{1}{8} s_2^3 - \frac{3}{8} s_2 s_4 + \frac{5}{16} s_6 + \mathscr{O}(m_{\text{rot}}^4). \tag{E.5}$$

E.2.2 Generalized ellipsoids: e, k and h variables

For an axisymmetric disturbance, one can also search a planetary figure equation in the form of a distorted ellipsoid of revolution. To 3$^{\text{rd}}$ order, this equation writes (Zharkov and Trubitsyn 1980)

$$r(\theta) = r_{\text{eq}} \left[1 - e \cos^2 \theta - \left(\frac{3 e^2}{8} + k \right) \sin^2(2\theta) \right)$$

$$+ \left(\frac{e^3}{2} + h \right) \sin^2 \theta \left(5 \sin^4 \theta - 6 \sin^2 \theta + 1 \right) \right]. \tag{E.6}$$

Converting trigonometric functions into Legendre polynomials and the equatorial radius into the mean radius (using Eq. (E.4)), the comparison of Eq. (E.6) with Eq. (3.16) gives a system of nonlinear equations for e, k, h and the s_n. To solve this set of equations to 3$^{\text{rd}}$ order, one can replace the figure functions by

$$s_{2n} = \sum_{k=n}^\infty s_{2n}^{(2k)} m_{\text{rot}}^k, \quad e = \sum_{k=1}^\infty e^{(k)} m_{\text{rot}}^k, \quad k = \sum_{k=2}^\infty k^{(k)} m_{\text{rot}}^k, \quad \dots \tag{E.7}$$

Because m_{rot} is arbitrary, the coefficients of all the m_{rot}^k (k=1...3) terms must be equal. This provides us with a set of linear equations on the $s_{2n}^{(2k)}$, $e^{(k)}$, ... Regrouping all the terms we get

$$s_0 = - \frac{4}{45} e^2 - \frac{52}{567} e^3 - \frac{32}{315} ek,$$

$$s_2 = - \frac{2}{3} e - \frac{23}{63} e^2 - \frac{8}{21} k - \frac{4}{27} e^3 + \frac{2}{21} h - \frac{152}{315} ek,$$

$$s_4 = \frac{12}{35} e^2 + \frac{32}{35} k + \frac{4}{11} e^3 + \frac{192}{385} h + \frac{32}{105} ek,$$

$$s_6 = - \frac{40}{231} e^3 - \frac{80}{231} h. \tag{E.8}$$

---

[1] The rotational symmetry entails that the shape cannot depend on the longitude, and the symmetry of the planet with respect to the equator plane implies that only even harmonics are not equal to zero.

[2] In this context, the $\mathbf{s}_{2n}^0$ are rewritten s_{2n} and the superscripts are only exponents.

This formula is in agreement with Eq (30.4) of Zharkov and Trubitsyn (1980).

E.3   Mass integrals: S_{2n}

As in § D, we must first compute the mass integrals that appear in the self gravitational potential of the deformable body (Eq. (3.2)). The mass integrals D_{2n} and $\bar{D}_{2n}$ are given by

$$
\begin{aligned}
D_n(\bar{r}) &= \int_0^{2\pi} d\phi' \int_0^{\bar{r}} d\bar{r}' \rho(\bar{r}') \int_{-1}^1 d\tilde{\mu}' (r')^{n+2} P_n(\tilde{\mu}') \\
&= \frac{2\pi}{n+3} \int_0^{\bar{r}} d\bar{r}' \rho(\bar{r}') \int_{-1}^1 d\tilde{\mu}' \frac{d}{d\bar{r}'} [(r')^{n+3}] P_n(\tilde{\mu}'), \\
\bar{D}_n(\bar{r}) &= \frac{2\pi}{2-n} \int_{\bar{r}}^{\bar{R}} d\bar{r}' \rho(\bar{r}') \int_{-1}^1 d\tilde{\mu}' \frac{d}{d\bar{r}'} [(r')^{2-n}] P_n(\tilde{\mu}'), \\
\bar{D}_2(\bar{r}) &= 2\pi \int_{\bar{r}}^{\bar{R}} d\bar{r}' \rho(\bar{r}') \int_{-1}^1 d\tilde{\mu}' \frac{d}{d\bar{r}'} [\ln r] P_n(\tilde{\mu}').
\end{aligned}
\tag{E.9}
$$

Again, we have changed the limit of the integration domain in Eqs. (3.3) and (3.4) from $r' = r$ to $r' = r(\tilde{\mu})$, the additional terms arising from the integration domain contained between the sphere and the level surfaces being equal to zero (Zharkov and Trubitsyn 1980). As usual, the powers of r are expanded in terms of the figure functions using Eq. (3.16). Then, products of Legendre polynomials can be developed and all the angular functions are integrated over $\tilde{\mu}$. Using the dimensionless variables

$$
\begin{cases}
\tilde{s} &= \bar{r}/\bar{R}_1 \\
\delta &= \rho/\bar{\rho}_1 \\
S_n &= \frac{3 D_n}{4\pi \bar{\rho}_1 \bar{r}^{n+3}} \\
\bar{S}_n &= \frac{3 \bar{D}_n}{4\pi \bar{\rho}_1 \bar{r}^{2-n}}
\end{cases}
\tag{E.10}
$$

this gives

$$
S_n = \tilde{s}^{-n-3} \int_0^{\tilde{s}} \delta(z) d[z^{n+3} \phi_n] \quad \text{and} \quad \bar{S}_n = \tilde{s}^{n-2} \int_{\tilde{s}}^1 \delta(z) d[z^{2-n} \bar{\phi}_n],
\tag{E.11}
$$

where

$$
\begin{aligned}
\phi_0 &= 1, \\
\phi_2 &= \frac{3}{5} \left(s_2 + \frac{4}{7} s_2^2 + \frac{2}{35} s_2^3 + \frac{8}{7} s_2 s_4 \right), \\
\phi_4 &= \frac{1}{3} \left(s_4 + \frac{54}{35} s_2^2 + \frac{120}{77} s_2 s_4 + \frac{108}{77} s_2^3 \right), \\
\phi_6 &= \frac{3}{13} \left(s_6 + \frac{40}{11} s_2 s_4 + \frac{24}{11} s_2^3 \right),
\end{aligned}
$$

$$
\begin{aligned}
\bar{\phi}_2 &= \frac{3}{5} \left(s_2 - \frac{1}{7} s_2^2 + \frac{12}{35} s_2^3 - \frac{2}{7} s_2 s_4 \right), \\
\bar{\phi}_4 &= \frac{1}{3} \left(s_4 - \frac{27}{35} s_2^2 - \frac{60}{77} s_2 s_4 + \frac{216}{385} s_2^3 \right), \\
\bar{\phi}_6 &= \frac{3}{13} \left(s_6 - \frac{25}{11} s_2 s_4 + \frac{90}{77} s_2^3 \right).
\end{aligned}
\tag{E.12}
$$

In terms of the e, k and h functions, this reads

$$\phi_0 = 1,$$

$$\phi_2 = -\frac{2}{5}\left(e + \frac{1}{6}e^2 + \frac{4}{7}k + \frac{2}{9}e^3 - \frac{1}{7}h + \frac{4}{3}ek\right),$$

$$\phi_4 = \frac{12}{35}\left(e^2 + \frac{8}{9}k + \frac{1}{3}e^3 + \frac{16}{33}h + \frac{40}{297}ek\right),$$

$$\phi_6 = -\frac{8}{21}\left(e^3 + \frac{30}{143}h + \frac{192}{143}ek\right),$$

$$\bar{\phi}_2 = -\frac{2}{5}\left(e + \frac{9}{14}e^2 + \frac{4}{7}k + \frac{8}{21}e^3 - \frac{1}{7}h + \frac{4}{7}ek\right),$$

$$\bar{\phi}_4 = \frac{32}{105}\left(k + \frac{6}{11}h + \frac{14}{33}ek\right),$$

$$\bar{\phi}_6 = -\frac{80}{1001}\left(h - 4ek\right). \tag{E.13}$$

E.4   3$^{\rm rd}$ order potential

As in the linear theory, once the mass integrals are known, one can express the total potential. Here also, because of the symmetry of the problem, we can reduce our set of spherical harmonics to a set containing only the even Legendre polynomials. The total potential thus writes

$$V(\bar{r}, \tilde{\mu}) = V_G + V_{\rm rot}$$

$$= -\frac{4}{3}\pi G\bar{\rho}_1\,\bar{r}^2 \sum_{n=0}^{\infty} \hat{V}_{2n}(\bar{r})\,P_{2n}(\tilde{\mu}). \tag{E.14}$$

Then the equations to be solved to find the figure functions will be

$$\left\{\hat{V}_n(\bar{r}) = 0\right\}_{n=2,4,6} \tag{E.15}$$

and the hydrostatic equilibrium will read

$$\frac{1}{\rho}\frac{\partial P}{\partial \bar{r}} = -\frac{\partial V_{\rm tot}}{\partial \bar{r}} = \frac{4}{3}\pi G\bar{\rho}_1\frac{\mathrm{d}}{\mathrm{d}\bar{r}}\left[\bar{r}^2\hat{V}_0(\bar{r})\right] = -\frac{Gm}{\bar{r}^2} + \frac{2}{3}\omega_1^2\bar{r} + 4\pi\bar{r}^2\,\varphi_\omega, \tag{E.16}$$

where

$$\boxed{\varphi_\omega(\bar{r}) \equiv \frac{G\bar{\rho}_1}{3\bar{r}^2}\frac{\mathrm{d}}{\mathrm{d}\bar{r}}\left[\bar{r}^2\left(\hat{V}_0 - S_0 - \bar{S}_0 - \frac{m_{\rm rot}}{3}\right)\right].} \tag{E.17}$$

E.4.1   Expression in term of the s_{2n}

To 3$^{\rm rd}$ order, the first terms of Eq. (E.14) are given by

$$\hat{V}_0 = \left(1 + \frac{2}{5}s_2^2 - \frac{4}{105}s_2^3\right)S_0 + \left(-\frac{3}{5}s_2 + \frac{12}{35}s_2^2\right)S_2$$

$$+ \bar{S}_0 + \left(\frac{2}{5}s_2 + \frac{2}{35}s_2^2\right)\bar{S}_2 + \frac{m_{\rm rot}}{3}\left(1 - \frac{2}{5}s_2 - \frac{9}{35}s_2^2\right), \tag{E.18}$$

$$\hat{V}_2 = \left(-s_2 + \frac{2}{7}s_2^2 - \frac{29}{35}s_2^3 + \frac{4}{7}s_2 s_4\right) S_0 + \left(1 - \frac{6}{7}s_2 + \frac{111}{35}s_2^2 - \frac{6}{7}s_4\right) S_2 - \frac{10}{7}s_2 S_4$$
$$+ \left(1 + \frac{4}{7}s_2 + \frac{1}{35}s_2^2 + \frac{4}{7}s_4\right) \bar{S}_2 + \frac{8}{7}s_2 \bar{S}_4 - \frac{m_{\text{rot}}}{3}\left(1 - \frac{10}{7}s_2 - \frac{9}{35}s_2^2 + \frac{4}{7}s_4\right), \tag{E.19}$$

$$\hat{V}_4 = \left(-s_4 + \frac{18}{35}s_2^2 - \frac{108}{385}s_2^3 + \frac{40}{77}s_2 s_4\right) S_0 + \left(-\frac{54}{35}s_2 + \frac{648}{385}s_2^2 - \frac{60}{77}s_4\right) S_2$$
$$+ \left(1 - \frac{100}{77}s_2\right) S_4 + \left(\frac{36}{35}s_2 + \frac{108}{385}s_2^2 + \frac{40}{77}s_4\right) \bar{S}_2 + \left(1 + \frac{80}{77}s_2\right) \bar{S}_4$$
$$- \frac{12}{35}m_{\text{rot}}\left(s_2 - \frac{5}{22}s_2^2 - \frac{95}{66}s_4\right), \tag{E.20}$$

$$\hat{V}_6 = \left(-s_6 - \frac{18}{77}s_2^3 + \frac{10}{11}s_2 s_4\right) S_0 + \left(\frac{108}{77}s_2^2 - \frac{15}{11}s_4\right) S_2 - \frac{25}{11}s_2 S_4 + S_6$$
$$+ \left(\frac{18}{77}s_2^2 + \frac{10}{11}s_4\right) \bar{S}_2 + \frac{20}{11}s_2 \bar{S}_4 + \bar{S}_6 - \frac{10}{33}m_{\text{rot}}\left(s_4 + \frac{9}{35}s_2^2\right). \tag{E.21}$$

These formulae are in agreement with Eq (28.7-9) and (29.4) of Zharkov and Trubitsyn (1980).

E.4.2 3$^{\text{rd}}$ order potential with e, k and h

In term of the e, k and h functions, this writes

$$\hat{V}_0 = \left(1 + \frac{8}{45}e^2 + \frac{64}{315}ek + \frac{584}{2835}e^3\right) S_0 + \frac{2}{5}\left(e + \frac{13}{14}e^2 + \frac{4}{7}k\right) S_2$$
$$+ \bar{S}_0 - \frac{4}{15}\left(e + \frac{19}{42}e^2 + \frac{4}{7}k\right) \bar{S}_2 + \frac{1}{3}m_{\text{rot}}\left(1 + \frac{4}{15}e + \frac{2}{63}e^2 + \frac{16}{105}k\right) \tag{E.22}$$

$$\hat{V}_2 = \left(\frac{2}{3}e + \frac{31}{63}e^2 + \frac{76}{189}e^3 + \frac{88}{315}ek - \frac{2}{21}h + \frac{8}{21}k\right) S_0 + \left(1 + \frac{4}{7}e + \frac{10}{7}e^2 - \frac{16}{35}k\right) S_2$$
$$+ \frac{20}{21}eS_4 + \left(1 - \frac{8}{21}e + \frac{32}{105}k\right) \bar{S}_2 - \frac{16}{21}e\bar{S}_4 - \frac{1}{3}m_{\text{rot}}\left(1 + \frac{20}{21}e + \frac{38}{63}e^2 + \frac{16}{15}k\right) \tag{E.23}$$

$$\hat{V}_4 = \left(\frac{4}{35}e^2 - \frac{172}{1155}e^3 - \frac{32}{35}k - \frac{192}{385}h - \frac{416}{1155}ek\right) S_0 + \left(\frac{36}{35}e + \frac{402}{385}e^2 - \frac{48}{385}k\right) S_2$$
$$+ \left(1 + \frac{200}{231}e\right) S_4 + \left(-\frac{24}{35}e - \frac{4}{55}e^2 + \frac{32}{385}\right) \bar{S}_2 + \left(1 - \frac{160}{231}e\right) \bar{S}_4$$
$$+ m_{\text{rot}}\left(\frac{8}{35}e + \frac{76}{231}e^2 + \frac{32}{55}k\right) \tag{E.24}$$

$$\hat{V}_6 = \left(\frac{8}{231}e^3 - \frac{128}{231}ek + \frac{80}{231}h\right) S_0 + \left(\frac{12}{77}e^2 - \frac{96}{77}k\right) S_2 + \frac{50}{33}eS_4 + S_6$$
$$+ \left(\frac{32}{77}e^2 + \frac{64}{77}k\right) \bar{S}_2 - \frac{40}{33}e\bar{S}_4 + \bar{S}_6 + m_{\text{rot}}\left(-\frac{32}{231}e^2 - \frac{64}{231}k\right) \tag{E.25}$$

E.5   Gravitational moments

As shown in § 3.2.2, the gravitational moments are directly given by the mass integrals, which rewrites here

$$\boxed{J_{2n} = -S_{2n}.}$$ (E.26)

Like in § E.2.2, we can find an algebraic relation between the J and the figure functions. To do so, one can replace the figure functions and the gravitational moments by

$$e = \sum_{k=1}^{\infty} e^{(k)} m_{rot}^k, \ ..., \ J_2 = \sum_{k=1}^{\infty} J_2^{(k)} m_{rot}^k, \ ...$$ (E.27)

in Eqs. (E.23), (E.24) and (E.25). Then, because $\hat{V}_n = 0$ for $n = 2, 4, 6, ...$, and equating all the terms of the same order to zero, we get

$$J_2 = \frac{2}{3}e - \frac{m_{rot}}{3} - \frac{e^2}{3} + \frac{2}{21}e\,m_{rot} + \frac{8}{21}k - \frac{11}{147}e^2\,m_{rot} - \frac{16}{105}k\,m_{rot} + \frac{40}{147}ek - \frac{2}{21}h,$$ (E.28)

$$J_4 = -\frac{4}{5}e^2 - \frac{32}{35}k + \frac{4}{7}e\,m_{rot} + \frac{4}{5}e^3 - \frac{3616}{2695}ek - \frac{22}{49}e^2\,m_{rot} + \frac{208}{385}k\,m_{rot} - \frac{192}{385}h,$$ (E.29)

$$J_6 = \frac{8}{7}e^3 + \frac{128}{77}ek - \frac{20}{21}e^2\,m_{rot} - \frac{160}{231}k\,m_{rot} + \frac{80}{231}h.$$ (E.30)

These expressions correct minor typos in Zharkov et al. (1973).

Appendix F

Projected area of a triaxial ellipsoid

F.1   General case

Let us define two coordinate systems. The first one $(\hat{\mathbf{x}}', \hat{\mathbf{y}}', \hat{\mathbf{z}}')$ is defined by the three main axes of the ellipsoid. In this frame, the equation of the surface of the ellipsoid is

$$\frac{x'^2}{a_1^2} + \frac{y'^2}{a_2^2} + \frac{z'^2}{a_3^2} = 1. \tag{F.1}$$

To compute the projected area of this ellipsoid as it will be seen by the observer, it is easier to put ourselves in another coordinate system defined by the line connecting the center of mass of the system and the observer (toward the observer ; $\hat{\mathbf{x}}$), the projection of the orbital angular momentum on the sky plane ($\hat{\mathbf{z}}$) and a third axis in the sky plane chosen so that $(\hat{\mathbf{x}}, \hat{\mathbf{y}}, \hat{\mathbf{z}})$ follows the right-hand vector sense. The current position vector $(\mathbf{r} = (x, y, z))$ expressed in this frame is thus related to the one expressed in the first coordinate system by a rotation matrix $\mathbb{R}$ such as $\mathbf{r}' = \mathbb{R} \cdot \mathbf{r}$, with $\mathbb{R}^{\text{tr}} \mathbb{R} = \mathbf{1}$. The equation of the ellipsoid in the new system thus writes

$$g(\mathbf{r}) \equiv \mathbf{r}^{\text{tr}} \mathbb{R}^{\text{tr}} \begin{pmatrix} \frac{1}{a_1^2} & 0 & 0 \\ 0 & \frac{1}{a_2^2} & 0 \\ 0 & 0 & \frac{1}{a_3^2} \end{pmatrix} \mathbb{R} \mathbf{r} \equiv \mathbf{r}^{\text{tr}} \mathbb{S} \mathbf{r} = 1. \tag{F.2}$$

The exact value of the matrix $\mathbb{S}$ will depend on the rotation needed and on the angles chosen to represent it. This can be worked out in each specific case. To keep some generality, we will take $\mathbb{S}$ of the form

$$\mathbb{S} = \begin{pmatrix} a & d & f \\ d & b & e \\ f & e & c \end{pmatrix}. \tag{F.3}$$

The symmetry is ensured by the fact that both of our coordinate systems are orthonormal. The equation of the contour of the projected shadow is given by the fact that the normal to the ellipsoid is normal to the line of sight ($\hat{\mathbf{x}}$) there. This assumes a completely opaque body below the isobar chosen to be the surface. This reads

$$0 = \mathbf{grad}[g(\mathbf{r})]^{\text{tr}} \cdot \hat{\mathbf{x}} = 2 \mathbf{r}^{\text{tr}} \mathbb{S} \hat{\mathbf{x}}. \tag{F.4}$$

This shows that these points are located on a plane whose equation is (since $a \neq 0$)

$$x = -\frac{1}{a}(d y + f z). \tag{F.5}$$

Substituting x in Eq. (F.2) by Eq. (F.5) we see that the cross section is an ellipse following the equation

$$(y,z) \begin{pmatrix} b - \frac{d^2}{a} & e - \frac{df}{a} \\ e - \frac{df}{a} & c - \frac{f^2}{a} \end{pmatrix} \begin{pmatrix} y \\ z \end{pmatrix} \equiv (y,z) \, \mathbb{P} \begin{pmatrix} y \\ z \end{pmatrix} = 1. \tag{F.6}$$

It is thus possible to find the rotation in the sky plane needed to reduce the ellipse and find its principal axes (p_1, p_2). If only the cross section $(\pi p_1 p_2)$ is needed, we can use the fact that the determinant of a matrix is independent of the coordinate system so that

$$\pi p_1 p_2 = \frac{\pi}{\sqrt{\mathrm{Det}(\mathbb{P})}}, \tag{F.7}$$

with

$$\mathrm{Det}(\mathbb{P}) = bc - e^2 - \frac{bf^2}{a} - \frac{cd^2}{a} + \frac{2def}{a}. \tag{F.8}$$

In the case of an edge-on orbit at mid transit, no rotation is needed, $\mathbb{R}$ is the identity and thus $a = 1/a_1^2$, $b = 1/a_2^2$, $c = 1/a_3^2$ and $d = e = f = 0$. We retrieve

$$\pi p_1 p_2 = \frac{\pi}{\sqrt{bc}} = \pi a_2 a_3. \tag{F.9}$$

F.2   Coplanar case

If the planet equator and the orbital plane are coplanar, the unit vectors of first coordinate system defined above coincides with the unit vectors defined by the line connecting the two center of mass (from the secondary to the object under consideration ; $\hat{\mathbf{x}}'$), its normal in the orbital plane (in the direction of motion ; $\hat{\mathbf{y}}'$) and the rotation axis of the body ($\hat{\mathbf{z}}'$). If i is the inclination of the orbit with respect to the sky plane and ϕ the true anomaly defined to be 0 at mid transit, the rotation matrix reads

$$\mathbb{R} = \begin{pmatrix} \sin i \cos \phi & \sin \phi & \cos i \cos \phi \\ -\sin i \sin \phi & \cos \phi & -\cos i \sin \phi \\ -\cos i & 0 & \sin i \end{pmatrix}. \tag{F.10}$$

The $\mathbb{S}$ matrix can be computed thanks to Eq. (F.2) giving the a, b, ..., f coefficients and thus the projected area reads

$$\mathscr{A} = \pi \sqrt{a_3^2 \sin^2 i \left(a_1^2 \sin^2 \phi + a_2^2 \cos^2 \phi \right) + a_1^2 a_2^2 \cos^2 i}. \tag{F.11}$$

This gives the projected area of the planet or the star at any given point of the orbit as shown on Fig. 3.6.

Appendix G

The Mixing Length Theory

In order to investigate the impact of strongly hampered convection on giant planet internal structure, I developed a simple sub-grid model based on convection power laws in the efficient convection regime ($Ra_\star \gg 1$). However, this model can easily extended, in some cases, to the low efficiency regime. In order to demonstrate this, and to exhibit some physical evidence in favor of the power laws discussed above, I present here the particular case of the Mixing Length Theory (MLT ; Cox and Giuli 1968 ; Hansen and Kawaler 1994).

G.1 Growth rate

In a homogeneous medium without rotation and magnetic field, the dispersion relation for horizontal waves (corresponding to vertical velocity ; see § 4.1.2) is

$$\boxed{(\tilde{\sigma} + \tilde{k}^2)\,(\tilde{\sigma} + Pr\,\tilde{k}^2) - 1 = 0,}$$ (G.1)

or

$$\tilde{\sigma}^2 + \tilde{\sigma}\,\tilde{k}^2(1 + Pr) + Pr\,\tilde{k}^4 - 1 = 0.$$ (G.2)

A closer look at the determinant of this equation,

$$\Delta = (1 + Pr)^2\tilde{k}^4 - 4(Pr\,\tilde{k}^4 - 1) = 4 + (1 - Pr)^2\,\tilde{k}^4,$$

shows us that is is always positive, so that the roots are real. Then, because the sum of these roots, $-(1 + Pr)\,\tilde{k}^2$, is negative, their product must also be negative so that at least one of them be positive. This entails $Pr\,\tilde{k}^4 \leqslant 1$. Recasting this in term of the well known Rayleigh number

$$\boxed{Ra \equiv N_T^2/(\nu\,\kappa_T k^4) = (Pr\,\tilde{k}^4)^{-1},}$$ (G.3)

this criterion then reads $Ra \geqslant 1$. Hence, not only the super adiabaticity needs to be positive for the medium to be convectively unstable, but it must be large enough to counteract the radiative losses and maintain an overturning convection. The problem that arises, however, is that in an infinite medium, this criterion can always be met by taking a small enough $\tilde{k}$, i.e. a large enough length scale for the perturbation. This problem is at the heart of the MLT formalism. As the fastest growing mode is reached for vanishing wave numbers, the theory cannot predict the typical size of the perturbation. In practice, this implies that the so-called *mixing length*, $l \equiv 1/k$, is a free parameter.

Let us agree for the moment that this mixing length is determined by some exterior constraint. Moreover, one of the fundamental assumptions of the MLT is that our growing wave can be seen as a rising eddy of size l which is described by a velocity $v_{\rm conv}$ and temperature difference ΔT, those being the finite versions of $\delta \mathbf{v}$ and δT defined in § 4.1.2 reached for $t = t_{\rm conv} \equiv 1/\sigma$. Solving Eq. (G.1), we get the growth rate of the convective wave

$$\tilde{\sigma} = \frac{1}{2}\left(\sqrt{4 + (1 - {\rm Pr})^2 \tilde{k}^4} - (1 + {\rm Pr})\tilde{k}^2 \right). \tag{G.4}$$

Following Hansen and Kawaler (1994), we define

$$\boxed{Ra_\star \equiv Ra \times Pr = N_T^2 / (\kappa_T^2 k^4) = \tilde{k}^{-4},} \tag{G.5}$$

which measures the efficiency of the convection. The growth rate of the perturbation then rewrites

$$\boxed{\sigma = N_T\, \tilde{\sigma}(Ra_\star)} \quad \text{with} \quad \boxed{\tilde{\sigma}(Ra_\star) \equiv \frac{1}{2\sqrt{Ra_\star}}\left(\sqrt{4Ra_\star + (1 - {\rm Pr})^2} - (1 + {\rm Pr}) \right),} \tag{G.6}$$

and the convective velocity is then

$$v_{\rm conv} = \sigma\, l = N_T\, l\, \tilde{\sigma}(Ra_\star). \tag{G.7}$$

To find the convective flux, we will need to know what is the temperature difference between a moving eddy and the exterior (ΔT). Using Eqs. (4.10) and (G.1), we have

$$\begin{aligned}
\Delta T &= \frac{(\nabla_T - \nabla_{\rm ad})}{\sigma + \kappa_T k^2}\, \frac{T}{H_P}\, v_{\rm conv} \\
&= (\tilde{\sigma} + Pr\tilde{k}^2)\, \frac{(\nabla_T - \nabla_{\rm ad})}{N_T}\, \frac{T}{H_P}\, v_{\rm conv} \\
&= \frac{1}{2\sqrt{Ra_\star}}\left(\sqrt{4Ra_\star + (1 - {\rm Pr})^2} - (1 - {\rm Pr}) \right) \frac{(\nabla_T - \nabla_{\rm ad})}{N_T}\, \frac{T}{H_P}\, v_{\rm conv},
\end{aligned} \tag{G.8}$$

and the convective flux can be written

$$F_{\rm conv} = \rho\, c_P\, \Delta T\, v_{\rm conv}. \tag{G.9}$$

G.2 Convective efficiency

While we seem to have solved the problem and found the convective velocity, we are still far from a usable solution. Indeed, all along, we have used the Brunt-Väisälä frequency, N_T, as if it were known. However, this depends on the super adiabaticity in the medium which will obviously depend on the efficiency of the convection. As discussed in Chapter 4, in order to find a fixed point to this system, I consider the *Nusselt* number (Nu_T), which is given in general by the ratio of the total flux (diffusive + turbulent) to the diffusive flux in a convective layer. In our context, we use the slightly different definition of Hansen and Kawaler (1994)

$$\boxed{Nu_T \equiv \frac{F_{\rm int} - F_{\rm d}^{\rm ad}}{F_{\rm d} - F_{\rm d}^{\rm ad}} = \frac{\nabla_{\rm d} - \nabla_{\rm ad}}{\nabla_T - \nabla_{\rm ad}}.} \tag{G.10}$$

Hence, with this definition, if convection is efficient, the super adiabaticity will be small and the Nusselt number high. On the other hand, if convection is not present or inefficient, $Nu_T \rightarrow 1$. The interesting property of Nu_T is that, by multiplying it by $Ra_\star$, we can define our convective forcing

$$\Phi \equiv Ra_\star Nu_T = \frac{\alpha_T\, g}{\kappa_T^2} \frac{l^4}{H_P}(\nabla_{\mathrm{d}} - \nabla_{\mathrm{ad}}), \tag{G.11}$$

which can be directly computed once the total flux to be transported (hidden in ∇_{d}) is known. Hence to get our equation on the convective efficiency, we need to manipulate the definition of the Nusselt. Since $F_{\mathrm{int}} = F_{\mathrm{conv}} + F_{\mathrm{d}}$,

$$Nu_T = \frac{F_{\mathrm{int}} - F_{\mathrm{d}} + F_{\mathrm{d}} - F_{\mathrm{d}}^{\mathrm{ad}}}{F_{\mathrm{d}} - F_{\mathrm{d}}^{\mathrm{ad}}} = 1 + \frac{F_{\mathrm{conv}}}{F_{\mathrm{d}} - F_{\mathrm{d}}^{\mathrm{ad}}}. \tag{G.12}$$

Then, using the definition of the convective flux, we can obtain the sought for equation and solve it numerically. By chance, in the context of gaseous bodies, the Prandlt number is often small. In order to derive an analytical theory, we will thus use the $Pr \ll 1$ limit of the equations (Hansen and Kawaler 1994), and will come back later on the implications of this approximation. Then using Eqs. (G.8) and (G.9), the convective flux also takes a more manageable form

$$F_{\mathrm{conv}} = \frac{\rho c_P T N_T}{H_P}(\nabla_T - \nabla_{\mathrm{ad}})\tilde\sigma^3 l^2. \tag{G.13}$$

Hence,

$$\frac{F_{\mathrm{conv}}}{F_{\mathrm{d}} - F_{\mathrm{d}}^{\mathrm{ad}}} = \frac{N_T l^2}{\kappa_T}\tilde\sigma^3 = Ra_\star^{1/2}\tilde\sigma^3, \tag{G.14}$$

and

$$\Phi \equiv Ra_\star \times Nu_T = Ra_\star + Ra_\star^{3/2}\,\tilde\sigma^3, \tag{G.15}$$

where $\tilde\sigma$ now reads

$$\tilde\sigma(Ra_\star) \equiv \frac{1}{2\sqrt{Ra_\star}}\left(\sqrt{1 + 4Ra_\star} - 1\right). \tag{G.16}$$

The general behavior of the solutions to this equation are shown in Fig. G.1.

In the efficient convection regime ($Ra_\star \gg 1$), one can easily show that $\tilde\sigma \rightarrow 1$ and $Nu_T \propto Ra_\star^{1/2}$. This case can be recovered, in this regime, by the more general model presented in § 4.2, by setting $C_L = 1$ and $a = 1/2$, but we show below that the MLT formalism can be extended to the inefficient convection regime.

Indeed, in the $1 \gg Ra_\star \gg Pr$ regime, developing Eq. (G.16) yields $\sigma \approx Ra_\star^{1/2}$. Then, because the convective time is dramatically increased, Eq. (4.35) rewrites in that case

$$\left(\delta_T/l\right) \approx \left(\kappa_T/l^2\,\sigma N_T\right)^{-1/2} \approx Ra_\star^{-1/2} \gg 1. \tag{G.17}$$

The size of the diffusive interfaces thus grows until the convective layers eventually turn into a completely diffusive medium for which $\langle\nabla_T\rangle = \nabla_{\mathrm{d}}$.

Let us now derive some orders of magnitude for large scale convection. Of course we need a prescription for the mixing length. An implicit assumption that was made during our linear analysis was

(a) Convection efficiency

(b) Thermal thickness
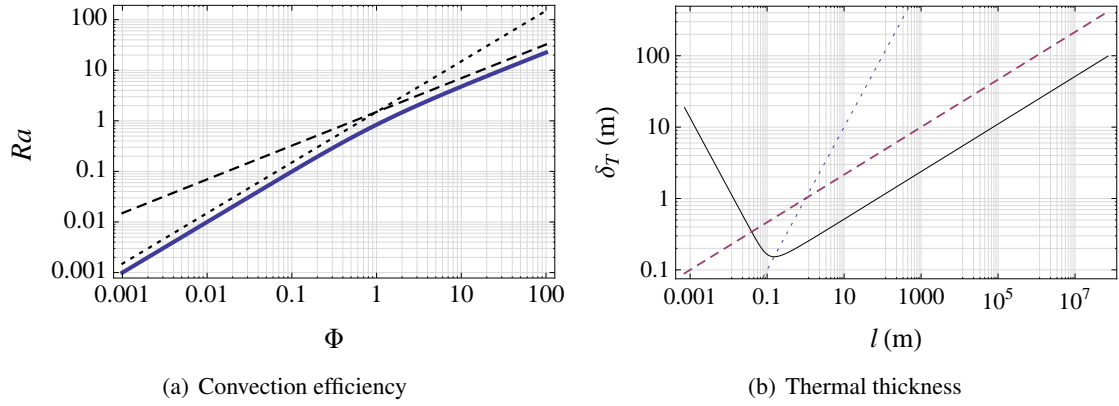
Figure G.1: Left: Modified Rayleigh Number ($Ra_\star$) as a function of the forcing $\Phi = Ra_\star Nu_T$ (Solid curve). The dashed (dotted) line represents the 2/3 (1) power law characteristic of the high (low) efficiency regime. Right: Size of the diffusive layer as a function of the mixing length under Jovian conditions. The dashed and dotted lines are the $l^{1/3}$ and l curves respectively. At the bottom of the curve, we shift from the efficient convection regime (on the right) to the fully diffusive regime (on the left). As expected, this transition occurs when the size of the diffusive and convective regions are equal.

that all the quantities involved should be constant in our medium. In a star or a gaseous body, this is strictly verified only if $l \ll H_P$. It has been shown, however, that in order to reproduce some observed properties of solar like stars, the mixing length should be chosen to be on the order of the pressure scale height. Then, as $H_P \approx R_1$ in most of a gaseous object interior, we find that for condition prevailing in the interior of the actual Solar System giant planets, the super adiabaticity needed to transport the outgoing energy is on the order of $10^{-8} - 10^{-9}$, so that the structure can be solved by setting $\nabla_T = \nabla_{\mathrm{ad}}$ [1].

---

[1]Note that rapid rotation and/or strong magnetic fields, necessarily present in Jupiter and Saturn interiors, are known to hamper large-scale convection. Indeed, the zonal flows observed in Jupiter's atmosphere might reveal the presence of convective *rolls* at deeper levels, a consequence of the impact of rotation on convective motions, according to the Taylor-Proudmann theorem (Busse 1976). However the super adiabaticity needed is still negligible in front of ∇_{ad} (Stevenson 1979b)

Appendix H

Computation of the heavy element content

The mean molecular weight gradient needed to stabilize the fluid against large scale convection can be caused by an inhomogeneous distribution of both helium ($Y(m)$) and metals ($Z(m)$) in the hydrogen ($X(m)$)-rich medium. In practice, both gradients can be present at the same time and either compete or contribute constructively.

In the model, I consider an ideal mixture of heavy elements within a H/He envelope whose H/He mass ratio is kept constant and equal to its value in the protosolar nebula, (H/He)$_{\text{proto}}$. This implies

$$X + Y + Z = 1, \text{ and } \frac{Y}{X+Y} = \left(\frac{\bar{Y}}{\bar{X}+\bar{Y}} \right)_{\text{proto}} \approx 0.275, \tag{H.1}$$

everywhere in the planet's gaseous envelope. Only one degree of freedom thus remains. Following previous calculations (Chabrier et al. 1992), for sake of simplicity and in order to have a flexible determination of the metal enrichment and a thermodynamically consistent EOS in the gaseous phase, the metal mass fraction is approximated by an *effective* helium mass fraction (Y') in the H/He EOS. As for the core, this latter is correctly described by the appropriate water and silicate EOS mentioned in the text.

The various element mass fractions, then the corresponding metal enrichment, are thus inferred from the relation

$$\frac{1}{\rho(P,T,Y')} = \frac{1-Z}{\rho_{(\text{H/He})_{\text{proto}}}(P,T)} + \frac{Z}{\rho_Z(P,T)}, \tag{H.2}$$

which gives Z at each depth along a given model *P-T* profile (Chabrier et al. 1992). The hydrogen and helium mass fractions are then derived using

$$Y = (1-Z) \left(\frac{\bar{Y}}{\bar{X}+\bar{Y}} \right)_{\text{proto}} \tag{H.3}$$

and

$$X = 1 - Y - Z. \tag{H.4}$$

In this simple model, a Z gradient thus necessarily yields a competing inhomogeneous helium distribution within the planet. Because the mean molecular weight of a H/He mixture at fixed temperature and pressure only depends on $Y/(X+Y)$, only the Z variations need to be considered to compute ∇_μ in our simplified model. The $Z(m)$ profile is then integrated to obtain the total amount of heavy elements mixed in the gaseous layers for each planetary model, as portrayed in Fig. 4.9. In the most general case, with an intrinsic inhomogeneity of the helium distribution, caused for instance by its immiscibility in metallic hydrogen, both the Y and Z gradients would have to be properly calculated.

Appendix I

Secular tidal evolution for finite eccentricity and obliquity

Having a prescription for the parameters modeling the dissipation in our bodies, in our case a constant viscosity, we can concern ourselves with the determination of the secular change of the orbital elements of a tidally interacting binary system. We consider a system of two deformable bodies of mass M_1 and M_2. Note that no approximation will be made on the masses of the two bodies, meaning that the following equations can be used in a large variety of contexts, covering Star-Star, Star-Planet and Planet-Satellite interactions. Up to the quadrupolar terms in the tidal deformation, approximation that remains to be explained and justified, the mutual interaction of the tidal bulges is negligible and we can separately consider the effects of the tides raised in each body and sum them up at the end of the calculation. Let us consider the effect of the tides raised in a deformable body (say M_1, hereafter the primary, of mean radius $\bar{R}_1$) in interaction with a point mass (say M_2 the secondary). In these notations, the primary is not necessarily the most massive object of the pair, but always refers to the object whose tides are being considered, and the secondary always refers to the tides raising object. *In fine*, the complete equations are obtained by simply adding the contributions of the tides in both objects, each body playing consecutively the role of primary.

In general, because tidal processes are small perturbations to the mean orbital motion, the standard perturbation method first developed by Lagrange can be used (see e.g. Brouwer and Clemence 1961). However, I will present hereafter a simple and physically more transparent derivation of the equations, based on the formulation of Hut (1981). **Note that I have extended the calculations to be valid for any obliquity.**

I.1   Secular equation to arbitrary obliquity

The demonstration follows three main steps.

1. The orientation of the tidal bulge with time is computed. This yields vector expressions for the tidal force and torque.

2. The variations of the rotation rate, obliquity and orbital angular momentum are obtained thanks to this expression of the torque and using the *total* angular momentum conservation.

3. The evolution of the semi-major axis and eccentricity are obtained from the expression of the work exerted by tidal forces. The total amount of energy dissipated by tides in one of the bodies is a direct product of the calculation.

I.1.1   Trivia

One of the major assumption made here, that remains to be justified, is that the tidal perturbation entails only a small departure of the orbital motion from the unperturbed Keplerian solution. We will thus consider that, over an orbit, our two bodies follow the usual motion, solution of the unperturbed two body problem. This will allow us to average the effect of the tidal forces over the orbital timescale, and to keep only the secular effect of the tidal interaction on the orbital elements, a, e, ω_i and ε_i, respectively, the semi major axis (or the mean motion n), the eccentricity, and the rotation rate and obliquity of the component i.

In order to simplify the following derivation, I briefly recall here some properties of the two body problem solution. The radial distance $r_\star$ between the center of mass of the two objects writes

$$r_\star = a\frac{1-e^2}{1+e\cos\theta}, \tag{I.1}$$

where θ is the true anomaly, defined as the angle between the line connecting the center of mass of the two components and the one connecting the center of mass of the whole system and the perihelion (point of closest encounter).

Over such an orbit, the total orbital energy of the binary is given by

$$E_{\text{orb}} = -G\frac{M_1 M_2}{2a}, \tag{I.2}$$

and the orbital angular momentum by

$$H_{\text{orb}} = \frac{M_1 M_2}{M_1 + M_2}r_\star^2\dot\theta = \sqrt{G\frac{M_1^2 M_2^2}{M_1 + M_2}a(1-e^2)}. \tag{I.3}$$

Because the orbital angular momentum is constant over an orbit, we can compute the variation of the true anomaly and radial distance with respect to the position on the orbit

$$\dot\theta = n\sqrt{1-e^2}\left(\frac{a}{r_\star}\right)^2 = n\frac{(1+e\cos\theta)^2}{(1-e^2)^{3/2}}, \tag{I.4}$$

and differentiating Eq. (I.1) with respect to θ we get

$$\frac{\mathrm{d}r_\star}{\mathrm{d}\theta} = \frac{\dot r_\star}{\dot\theta} = ae(1-e^2)\frac{\sin\theta}{(1+e\cos\theta)^2}, \tag{I.5}$$

and thus

$$\dot r_\star = an\frac{e\sin\theta}{\sqrt{1-e^2}}. \tag{I.6}$$

Thanks to these expressions, it is now easy to compute the average value of any function f, involving a combination of $\dot\theta$, $\dot r_\star$ or $r_\star$, over an orbit. Indeed, one can first express f as a function g of θ alone (with $g(\theta(t)) = f(t)$). Then the average is given by

$$\langle f\rangle \equiv \frac{1}{T_{\text{orb}}}\oint_{\text{orbit}} f(t)\,\mathrm{d}t = \frac{1}{T_{\text{orb}}}\oint_{\text{orbit}} g(\theta)\frac{\mathrm{d}\theta}{\dot\theta(\theta)}. \tag{I.7}$$

In the cases of interest, the function $g(\theta)/\dot\theta$ can be expanded in a finite series of sines cosines functions, and the integral in Eq. (I.7) reduces to a sum of terms of the form

$$I_{\text{n}} = \int_0^{2\pi} \sin^2\theta\cos^{\text{n}}\theta\,\mathrm{d}\theta. \tag{I.8}$$

If n is odd, $I_n = 0$ due to the symmetry. For even values of n,

$$I_{2k} = 4 \int_0^{\pi/2} \sin^2 \theta \cos^{2k} \theta d\theta = 4 \left(\int_0^{\pi/2} \cos^{2k} \theta d\theta - \int_0^{\pi/2} \cos^{2k+2} \theta d\theta \right). \tag{I.9}$$

A recursive process shows that the integrals on the right hand side (also known as Wallis integrals) give[1] $\int_0^{\pi/2} \cos^{2k} \theta d\theta = \frac{(2k-1)!!}{2k!!} \pi/2$ and thus

$$I_{2k} = 2\pi \frac{(2k-1)!!}{(2k+2)!!}. \tag{I.10}$$

I.1.2   Tidal torque

Up to quadrupolar order, the potential created at a location $\mathbf{r}$, by a body being distorted by a secondary located at $\mathbf{r}_\star$, is obtained by truncating Eq. (5.3) up to terms with $n = 2$ which gives

$$V_G(\mathbf{r}, \mathbf{r}_\star) = \frac{GM_1}{r} \left[1 - k_2 \frac{\bar{R}_1^5}{r^2 r_\star^3} \frac{M_2}{M_1} P_2(\cos \psi) \right], \tag{I.11}$$

where ψ is the angle between $\mathbf{r}$ and $\mathbf{r}_\star$, and k_2 is the Love number of degree 2 of the primary.
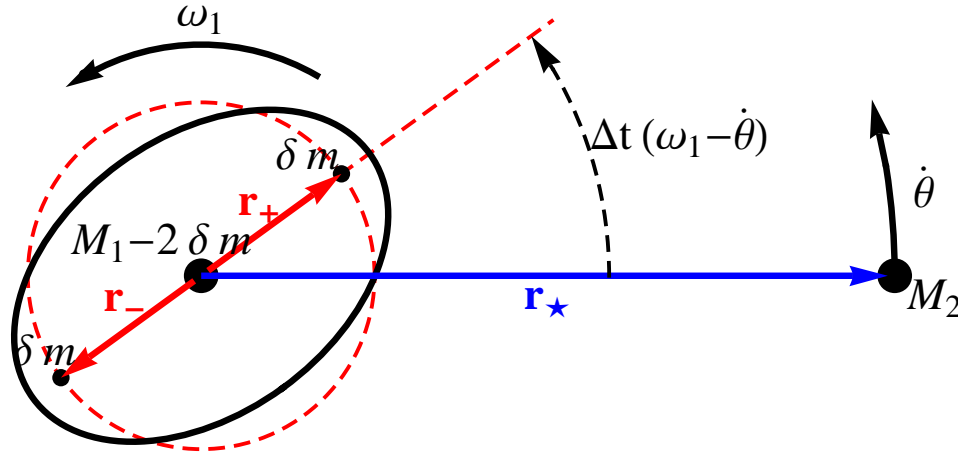
Figure I.1: Point mass approximation of the tidal bulge (in the coplanar case). In this example, $\omega_1 > \dot{\theta}$ so that the tidal bulge is leading in front of the secondary.

To this order, the mass distribution of the primary can be mimicked by a central mass $M_1 - 2\delta m$ and two point masses at the location of the tidal bulges ($\mathbf{r}_+$, $\mathbf{r}_- = -\mathbf{r}_+$; see Fig. I.1) of mass δm with $\|\mathbf{r}_+\| = \|\mathbf{r}_-\| = \bar{R}_1$ the radius of the primary and

$$\delta m = \frac{1}{2} k_2 M_2 \left(\frac{\bar{R}_1}{r_\star} \right)^3. \tag{I.12}$$

Because we consider a *constant* time lag Δt_1 between the deforming potential and the tidal deformation in the frame rotating with the primary, $\hat{\mathbf{r}}_+ = \hat{\mathbf{r}}_\star(t - \Delta t_1)$ ($\hat{\mathbf{r}}_\star$ refers to the unit vector associated to $\mathbf{r}_\star$) in this frame. Let $\dot{\theta}$ be the orbital rotation vector colinear to the orbital angular momentum whose value is

---

[1]By definition, $i!! = i(i-2)(i-4)\dots 1$.

the instantaneous variation rate of the true anomaly θ of the bodies in their Keplerian motion and $\boldsymbol{\omega_1}$ the rotation vector of the primary. Thus, to first order in Δt_1,

$$\hat{\mathbf{r}}_+ = \hat{\mathbf{r}}_\star(t - \Delta t_1) \approx \hat{\mathbf{r}}_\star - \Delta t_1\,\hat{\mathbf{r}}_\star \times (\boldsymbol{\omega_1} - \dot{\theta}). \tag{I.13}$$

The amplitude of the tidal bulges also lags behind the deforming potential and is given by

$$
\begin{aligned}
\delta m(t) &= \frac{1}{2}k_2 M_2 \left(\frac{\bar{R}_1}{r_\star(t - \Delta t_1)}\right)^3 \\
&\approx \frac{1}{2}k_2 M_2 \left(\frac{\bar{R}_1}{r_\star}\right)^3 \left(1 + 3\frac{\dot{r}_\star}{r_\star}\Delta t_1\right).
\end{aligned}
\tag{I.14}
$$

Then, adding the forces exerted by each point mass of the primary on the secondary, the total tidal force exerted on the secondary reads

$$\mathbf{F_{1\to2}} = -\frac{G(M_1 - 2\,\delta m)M_2}{\|\mathbf{r}_\star\|^3}\cdot\mathbf{r}_\star - \frac{GM_2\delta m}{\|\mathbf{r}_\star - \mathbf{r}_+\|^3}\cdot(\mathbf{r}_\star - \mathbf{r}_+) - \frac{GM_2\delta m}{\|\mathbf{r}_\star - \mathbf{r}_-\|^3}\cdot(\mathbf{r}_\star - \mathbf{r}_-). \tag{I.15}$$

Substituting $\mathbf{r}_+$, $\mathbf{r}_- = -\mathbf{r}_+$ and δm by their expressions in Eqs. (I.13) and (I.14), and neglecting terms smaller than $(\bar{R}_1/r_\star)^5$ gives

$$\mathbf{F_{1\to2}} = -\frac{GM_1 M_2}{r_\star^2}\cdot\hat{\mathbf{r}}_\star - 3\frac{Gk_2 M_2^2 \bar{R}_1^5}{r_\star^7}\left\{1 + 3\frac{\dot{r}_\star}{r_\star}\Delta t_1\right\}\cdot\hat{\mathbf{r}}_\star + 3\frac{Gk_2 M_2^2 \bar{R}_1^5}{r_\star^7}\Delta t_1(\boldsymbol{\omega_1} - \dot{\theta})\times\hat{\mathbf{r}}_\star. \tag{I.16}$$

Thus the tidal torque exerted by the tidal bulge on the secondary is given by

$$\mathbf{N_{1\to2}} = 3\frac{Gk_2 M_2^2 \bar{R}_1^5}{r_\star^6}\,\hat{\mathbf{r}}_\star \times \left(\Delta t_1(\boldsymbol{\omega_1} - \dot{\theta})\times\hat{\mathbf{r}}_\star\right). \tag{I.17}$$

I.1.3   Angular momentum transfer

Because the total angular momentum is conserved, we can write

$$\mathbf{N_{1\to2}} = \dot{\mathbf{H}}_{\mathbf{orb}} = -\dot{\mathbf{H}}_\mathbf{1}, \tag{I.18}$$

where $\mathbf{H_{orb}}$ is the orbital angular momentum vector, whose direction follows $\dot{\theta}$, and $\mathbf{H_1} = C_1\boldsymbol{\omega_1}$ the rotational angular momentum of the primary, whose moment of inertia along the rotation axis is C_1. Remember that the secondary is here treated as a point mass, meaning that its angular momentum is an internal degree of freedom, and cannot be transferred to another component for the moment. We can then simply derive the rate of variation of the modulus of the internal angular momentum:

$$\frac{\mathrm{d}}{\mathrm{d}t}(C_1\omega_1) = \dot{H}_1 = \dot{\mathbf{H}}_\mathbf{1}\cdot\hat{\mathbf{H}}_\mathbf{1} = -\mathbf{N_{1\to2}}\cdot\hat{\mathbf{H}}_\mathbf{1}. \tag{I.19}$$

This product can be carried out by projecting in any base. We choose the base defined by $\mathbf{H_{orb}} = (0, 0, h)$ and $\boldsymbol{\omega_1} = (\omega_1\sin\varepsilon_1, 0, \omega_1\cos\varepsilon_1)$ where ε_1 is the obliquity. In this base,

$$\mathbf{N_{1\to2}} = 3\frac{Gk_2 M_2^2 \bar{R}_1^5}{r_\star^6}\Delta t_1\begin{pmatrix}\omega_1\sin\varepsilon_1\sin^2(\theta + \varpi)\\ -\omega_1\sin\varepsilon_1\cos(\theta + \varpi)\sin(\theta + \varpi)\\ \omega_1\cos\varepsilon_1 - \dot{\theta}\end{pmatrix}, \tag{I.20}$$

where ϖ is the longitude of the periapsis. The precession of the periapsis occurring on a much shorter timescale than the tidal migration, we can average the tidal torque over ϖ. This yields

$$\mathbf{N_{1\rightarrow 2}} = 3\frac{Gk_2 M_2^2 \bar{R}_1^5}{r_\star^6}\Delta t_1 \begin{pmatrix} \frac{1}{2}\omega_1 \sin\varepsilon_1 \\ 0 \\ \omega_1 \cos\varepsilon_1 - \dot\theta \end{pmatrix}. \tag{I.21}$$

We can compute the dot product in Eq. (I.19) giving (with $x_1 = \cos\varepsilon_1$)

$$\frac{\mathrm{d}C_1\omega_1}{\mathrm{d}t} = 3\frac{Gk_2\Delta t_1 M_2^2 \bar{R}_1^5}{r_\star^6}\left(x_1\dot\theta - \left(\frac{1+x_1^2}{2}\right)\omega_1\right). \tag{I.22}$$

The mean rotation-rate variation is obtained by averaging over a Keplerian orbit using

$$\Omega(e) \equiv \frac{1}{T_{\mathrm{orb}}}\oint_{\mathrm{orbit}}\left(\frac{a}{r_\star}\right)^6 \mathrm{d}t = \frac{1+3e^2+\frac{3}{8}e^4}{(1-e^2)^{9/2}} \tag{I.23}$$

and

$$N(e) \equiv \frac{1}{T_{\mathrm{orb}}}\oint_{\mathrm{orbit}}\frac{\dot\theta}{n}\left(\frac{a}{r_\star}\right)^6 \mathrm{d}t = \frac{1+\frac{15}{2}e^2+\frac{45}{8}e^4+\frac{5}{16}e^6}{(1-e^2)^6}. \tag{I.24}$$

This reads

$$\boxed{\frac{\mathrm{d}C_1\omega_1}{\mathrm{d}t} = -\frac{K_1}{n}\left[\left(1+x_1^2\right)\Omega(e)\frac{\omega_1}{n} - 2x_1 N(e)\right],} \tag{I.25}$$

where we have introduced a scaling factor which has the dimension of an energy dissipation rate,

$$K_1 = \frac{3}{2}k_2\Delta t_1\left(\frac{GM_1^2}{\bar{R}_1}\right)\left(\frac{M_2}{M_1}\right)^2\left(\frac{\bar{R}_1}{a}\right)^6 n^2. \tag{I.26}$$

As detailed later, this parameter can be used to compare the strength of the tidal dissipation inside each body. As can be seen from Eq. (I.25), for any value of the obliquity and orbital elements, one can find a value of the rotation rate which cancels the mean tidal torque.

The variation of the obliquity can be obtained with

$$\dot{x}_1 = \frac{\mathrm{d}}{\mathrm{d}t}(\hat{\mathbf{H}}_1\cdot\hat{\mathbf{H}}_{\mathbf{orb}}) = \dot{\hat{\mathbf{H}}}_1\cdot\hat{\mathbf{H}}_{\mathbf{orb}} + \hat{\mathbf{H}}_1\cdot\dot{\hat{\mathbf{H}}}_{\mathbf{orb}}. \tag{I.27}$$

Carrying out the differentiation and using Eq. (I.18) yields

$$\dot{x}_1 = \frac{(\hat{\mathbf{H}}_1\cdot\hat{\mathbf{H}}_{\mathbf{orb}})(\mathbf{N_{1\rightarrow 2}}\cdot\mathbf{H_1})}{H_1^2} - \frac{(\mathbf{N_{1\rightarrow 2}}\cdot\hat{\mathbf{H}}_{\mathbf{orb}})}{H_1} - \frac{(\hat{\mathbf{H}}_{\mathbf{orb}}\cdot\hat{\mathbf{H}}_1)(\mathbf{N_{1\rightarrow 2}}\cdot\mathbf{H_{orb}})}{H_{\mathrm{orb}}^2} + \frac{(\mathbf{N_{1\rightarrow 2}}\cdot\hat{\mathbf{H}}_1)}{H_{\mathrm{orb}}}. \tag{I.28}$$

Subsituting Eq. (I.21) for $\mathbf{N_{1\rightarrow 2}}$ we get after simplification

$$\frac{\mathrm{d}\varepsilon_1}{\mathrm{d}t} = \frac{3}{2}\frac{Gk_2\Delta t_1 M_2^2 \bar{R}_1^5}{r_\star^6}\sin\varepsilon_1\left(\frac{x_1}{C_1} - 2\frac{\dot\theta}{C_1\omega_1} - \frac{\omega_1}{H_{\mathrm{orb}}}\right). \tag{I.29}$$

Averaging over an orbit using Eqs. (I.23)-(I.24) gives

$$\boxed{\frac{\mathrm{d}\varepsilon_1}{\mathrm{d}t} = \sin\varepsilon_1\frac{K_1}{C_1\omega_1 n}\left[(x_1-\eta_1)\Omega(e)\frac{\omega_1}{n} - 2N(e)\right],} \tag{I.30}$$

where η_i is the ratio of rotational over orbital angular momentum

$$\eta_i = \frac{M_1+M_2}{M_1 M_2}\frac{C_i\omega_1}{a^2 n\sqrt{1-e^2}}. \tag{I.31}$$

I.1.4 Energy dissipation

To obtain the variation of the semi-major axis and eccentricity, we must compute the work done by the tidal force on the secondary

$$
\begin{aligned}
\langle \dot{E}_{\mathrm{orb}} \rangle_1 &= \frac{1}{T_{\mathrm{orb}}} \oint_{\mathrm{orbit}} \mathbf{F_{1 \to 2}} \cdot \mathrm{d}\mathbf{r} \\
&= \frac{1}{T_{\mathrm{orb}}} \oint_{\mathrm{orbit}} (\dot{r}_\star \mathbf{F_{1 \to 2}} \cdot \hat{\mathbf{r}} + \mathbf{N_{1 \to 2}} \cdot \dot{\theta}) \, \mathrm{d}t,
\end{aligned}
\tag{I.32}
$$

where $\dot{r}_\star \mathbf{F_{1 \to 2}} \cdot \hat{\mathbf{r}}$ is the radial component and $\mathbf{N_{1 \to 2}} \cdot \dot{\theta}$ the normal one. The radial forces in $r_\star^{-2}$ and $r_\star^{-7}$ in Eq. (I.16) are conservative and do not dissipate energy. The radial part of the work is computed using

$$
N_e(e) \equiv 2 \frac{1 - e^2}{e^2} \frac{1}{T_{\mathrm{orb}}} \oint_{\mathrm{orbit}} \left(\frac{a}{r_\star} \right)^8 \left(\frac{\dot{r}_\star}{na} \right)^2 \cdot \mathrm{d}t = \frac{1 + \frac{15}{4} e^2 + \frac{15}{8} e^4 + \frac{5}{64} e^6}{(1 - e^2)^{13/2}}.
\tag{I.33}
$$

The normal component can be written

$$
\mathbf{N_{1 \to 2}} \cdot \dot{\theta} \, \mathrm{d}t = 3 G k_2 \Delta t_1 M_2^2 \bar{R}_1^5 \left(\frac{x_1 \omega_1 - \dot{\theta}}{r_\star^6} \right) \mathrm{d}\theta.
\tag{I.34}
$$

Again, averaging is carried out using Eqs. (I.24)-(I.23). After integration we get

$$
\langle \dot{E}_{\mathrm{orb}} \rangle_1 = 2 K_1 \left[N(e) x_1 \frac{\omega_1}{n} - N_a(e) \right],
\tag{I.35}
$$

where

$$
N_a(e) = \frac{1 + \frac{31}{2} e^2 + \frac{255}{8} e^4 + \frac{185}{16} e^6 + \frac{25}{64} e^8}{(1 - e^2)^{15/2}}.
\tag{I.36}
$$

The variation of semi-major axis due to the tides raised in the primary can be obtained through the fact that

$$
\langle \dot{E}_{\mathrm{orb}} \rangle_1 = -\frac{\mathrm{d}}{\mathrm{d}t} \frac{G M_1 M_2}{2a} = \frac{G M_1 M_2}{2a^2} \dot{a},
\tag{I.37}
$$

which gives

$$
\boxed{ \frac{1}{a} \frac{\mathrm{d}a}{\mathrm{d}t} \bigg|_1 = \frac{4a}{G M_1 M_2} K_1 \left[N(e) x_1 \frac{\omega_1}{n} - N_a(e) \right]. }
\tag{I.38}
$$

Because the orbital angular momentum is given by

$$
H_{\mathrm{orb}} = \sqrt{ G \frac{M_1^2 M_2^2}{M_1 + M_2} a (1 - e^2) },
\tag{I.39}
$$

the variation of the eccentricity can be obtained by differentiating H_{orb} with respect to t:

$$
\frac{2 \dot{H}_{\mathrm{orb}}}{H_{\mathrm{orb}}} = \frac{\dot{a}}{a} - \frac{2 e \dot{e}}{1 - e^2}.
\tag{I.40}
$$

Only *total* angular momentum is conserved, then $\dot{H}_{\mathrm{orb}} = -\mathrm{d}(C_1 \omega_1)/\mathrm{d}t$ and substituting Eq. (I.25), (I.38) and (I.39) in (I.40) gives

$$
\boxed{ \frac{1}{e} \frac{\mathrm{d}e}{\mathrm{d}t} \bigg|_1 = 11 \frac{a}{G M_1 M_2} K_1 \left[\Omega_e(e) x_1 \frac{\omega_1}{n} - \frac{18}{11} N_e(e) \right]. }
\tag{I.41}
$$

Finally, the rate of mechanical energy ($E_{\text{mec}} \equiv E_{\text{orb}} + E_{\text{rot}}$) dissipated by the primary is

$$
\begin{aligned}
\langle \dot{E}_{\text{mec}} \rangle_1 &= \langle \dot{E}_{\text{orb}} \rangle_1 + \langle \dot{E}_{\text{rot}} \rangle_1 \\
&= -\frac{\mathrm{d}}{\mathrm{d}t} \frac{GM_1 M_2}{2a} + \omega_1 \frac{\mathrm{d}}{\mathrm{d}t}(C_1 \omega_1).
\end{aligned}
\tag{I.42}
$$

Thus, substituting Eqs. (I.22) and (I.35) in Eq. (I.42) gives

$$
\boxed{\langle \dot{E}_{\text{mec}} \rangle_1 = -2K_1 \left[N_a(e) - 2N(e)x_1 \frac{\omega_1}{n} + \left(\frac{1+x_1^2}{2} \right) \Omega(e) \left(\frac{\omega_1}{n} \right)^2 \right].}
\tag{I.43}
$$

One can see that the energy dissipated in the body ($\dot{E}_{\text{tid}} \equiv -\langle \dot{E}_{\text{mec}} \rangle_1$) is positive for any value of e and x_1 as expected (Hut 1981) and that it is minimum when the body is pseudo-synchronized. Substituting ω_1 by the pseudo-synchronization rate (Eq. (I.51)), Eq. (I.43) simplifies to Eq. (I.53), which can be used for a close-in gas-giant exoplanet. For rocky planets locked in synchronous rotation by their permanent quadrupolar mass distribution, the heating rate can be estimated setting $\omega_1 = n$ in Eq. (I.43).

I.2 Assumptions, order of magnitudes and timescales

I.2.1 Timescales

Let us summarize the different timescales involved with tidal evolution. We remind here that most of the timescales defined here can change when considering one or the other object of a pair, but we will omit the subscript i for simplicity. The shortest period, is of course the dynamical timescale which we take here to be the period of the orbital motion of a test particle which would be grazing the surface of the primary

$$
P_{\text{dyn}} \equiv 2\pi \sqrt{\frac{\bar{R}_i^3}{GM_i}}.
\tag{I.44}
$$

Another short timescale is the orbital period, on which all our equations have been averaged

$$
P_{\text{orb}} \equiv \frac{2\pi}{n} = \sqrt{\frac{4\pi^2 a^3}{G(M_1 + M_2)}}.
\tag{I.45}
$$

However, viscous processes produce only a weak secular perturbation of the orbital motion, and their effect occur on much longer timescales. To scale these effects, we can define a viscous time as follows

$$
\tau_{\text{v}} \equiv \frac{1}{4\pi^2} \left(\frac{T_{\text{dyn}}}{k_{2,i} \Delta t_i} \right) T_{\text{dyn}} = \frac{\bar{R}_i^3}{GM_i k_{2,i} \Delta t_i}.
\tag{I.46}
$$

From Eqs. (5.12) and (5.11), we see that two comparable timescales arise for the evolution of the orbital elements. The first one, also called the circularization timescale (due to the body i), is proportional to the ratio of the orbital energy over the typical dissipation rate in the body under consideration

$$
\tau_{\text{circ}} \equiv -\frac{e}{\dot{e}} \Big|_{\omega=\omega_{\text{eq}}, e \to 0} = \frac{1}{7} \frac{GM_1 M_2}{a K_i}.
\tag{I.47}
$$

It measures the time needed to damp the eccentricity of a nearly circular orbit. For exoplanets, this timescale will be of particular interest, as it will set the rate at which gravitational energy is released into

the primary during the circularization of the orbit (see § 5.5.1). Noting $p = M_i/M_j$ the ratio of the mass of the body under consideration over the mass of the secondary, this rewrites

$$\tau_{\text{circ}} = \frac{2}{21} \frac{p^2}{1+p} \left(\frac{a}{\bar{R}_i}\right)^8 \tau_v. \tag{I.48}$$

It is comparable to the typical timescale for the evolution of the semi-major axis, or infall timescale, that can be derived from Eq. (5.11) using

$$\tau_{\text{in}} \equiv -\frac{a}{\dot{a}}\bigg|_{\omega=0,\,e=0} = \frac{1}{6} \frac{p^2}{1+p} \left(\frac{a}{\bar{R}_i}\right)^8 \tau_v. \tag{I.49}$$

From Eqs. (I.25) and (I.30), we see that the evolution of timescales for the (pseudo) synchronization and the coplanarization are also equal and can defined as

$$\tau_{\text{sync}} \equiv \frac{\omega - n}{\dot{\omega}}\bigg|_{e=0} = \frac{1}{3} r_{\text{gyr}}^2 p^2 \left(\frac{a}{\bar{R}_i}\right)^6 \tau_v. \tag{I.50}$$

I.2.2 Validity of the weak friction approximation

We are now able to quantify more precisely the weak friction approximation and to define what is a *small* time lag (Δt). In our calculations, this approximation appeared under two different forms. First, in computing the positions and masses of the tidal bulges (see Eqs. (I.13) and (I.14)), where we truncated our development to linear order in Δt, and second in averaging the effects of the tidal forces over an unperturbed Keplerian orbit. Thus the linear approximation is justified if both, the principal tidal driving period is large compared to the time lag, and the orbital period is small with respect to the timescales linked to the tidal evolution (both τ_{circ} and τ_{sync}).

In reasonable cases, the first constraint is the most stringent and can be rewritten either $2|\omega - n|\Delta t \ll 1$ for non-synchronous objects, or $n\Delta t \ll 1$ in the pseudo-synchronous case. Even for rigid objects like the Earth ($\Delta t \approx 630\text{s}$[2] ; Mignard 1979 ; Neron de Surgy and Laskar 1997), this assumption is well justified.

However, another subtle averaging has been made to obtain a torque which is independent of the relative orientation of the spin with respect to the perihelion of the orbit in Eq. (I.21). While the tidal processes still occur on a much longer timescale than the precession period, possible resonances of this precession with other secular perturbation of the system, by a distant third companion for example, can occur. Therefore, the object can be trapped in a spin-orbit resonance, also called Cassini state (see Levrard et al. 2007 ; while this seems improbable for giant close in planets as shown by Fabrycky et al. 2007), or a Kozai-Lidov resonance (Fabrycky and Tremaine 2007), which cannot be described by the above equations as they are.

I.2.3 Pseudo-Synchronization

While the evolution of a and e arise on quite comparable timescales, synchronization, however, can proceed much faster. Indeed, considering a planet, $p = M_p/M_\star \ll 1$, yielding

$$\frac{\tau_{\text{sync}}}{\tau_{\text{circ}}} \propto \left(\frac{R_p}{a}\right)^2 \ll 1.$$

---

[2]This value is of the time lag is the one needed to recover the increase of the Earth-Moon semi-major axis measured with Lunar Laser Ranging, and which is currently $\approx 4\,\text{cm}$ per year.

Therefore one can make the assumption than tidally evolve exoplanets must be in a state of pseudo synchronization with their orbit. The value of the pseudo synchronized angular velocity can be found by either setting Eq. (I.25) equal to zero or by minimizing the rate of tidal dissipation at fixed semi-major axis, eccentricity and obliquity. This reads

$$\omega_{\text{eq}} = \frac{N(e)}{\Omega(e)} \frac{2x_{\text{i}}}{1+x_{\text{i}}^2} n = \frac{N(e)}{\Omega(e)} n, \tag{I.51}$$

for a zero inclination. When the orbit is circularized, this reduces to the simple synchronization $\omega_{\text{eq}} = n$. As the obliquity equation involves the same typical timescale as the evolution of the angular velocity, the planet obliquity must rapidly be damped by tides and we can make the assumption of alignment between orbital and planetary angular momentum ($\varepsilon_{\text{i}} \approx 0$).
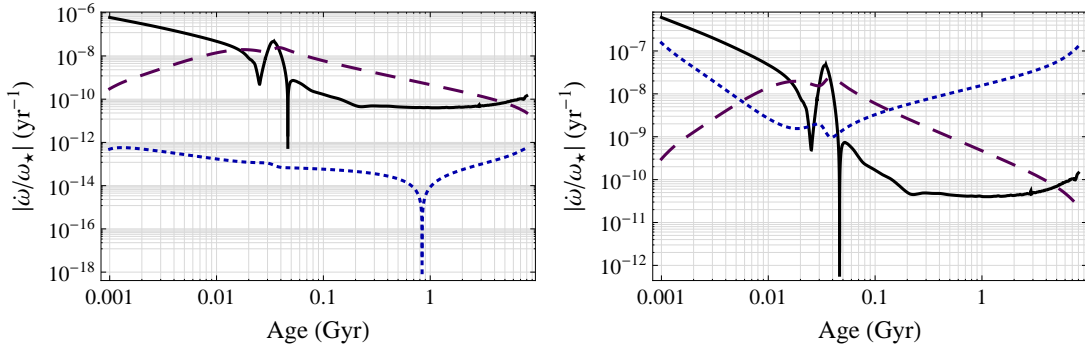
I.2.4 Stellar spin

Figure I.2: Absolute value of $\dot{\omega}_\star/\omega_\star$ due to the winds (dashed), radius variation (solid) and tides (dotted) for a Jupiter-Sun like system on a circular orbit with $a = 0.1$ AU (left) and 0.02 AU (right). Here, $k_2 \Delta t_\star = 2 \times 10^{-2}$. The contraction always dominates on the pre main sequence, spinning up the star, but is counteracted by magnetic winds later on. The tides raised by the planet only play a significant role for very short period orbits, when the planet and star are nearly merging.

On the contrary, for stars, $p = M_\star/M_{\text{p}} \gg 1$, $\tau_{\text{sync}}/\tau_{\text{circ}} \propto p \left(\frac{R_\star}{a}\right)^2$ and a pseudo synchronization and coplanarity hypothesis is no longer justified in most cases. The spin state of the star must then be taken into account. However, this is not as simple as integrating Eq. (I.25) at constant C_1. First, the star contracts during the pre main sequence, or expand on the main sequence, and the angular momentum conservation entails an additional term in the spin rate variation[3]. In addition, as is well known, stars loose angular momentum through the ejection of magnetized winds. Following the parametrization of Bouvier et al. (1997) for the stellar winds, we get

$$\frac{\dot{\omega}_\star}{\omega_\star} = -\frac{K_{\text{i}}}{C_\star \omega_\star n} \left[(1+x_\star^2) \, \Omega(e) \frac{\omega_\star}{n} - 2x_{\text{i}} N(e) \right] - \frac{\dot{C}_\star}{C_\star} - \frac{K_{\text{wind}}}{C_\star} \min[\omega_\star^2, \omega_{\text{sat}}^2] \sqrt{\frac{R_\star}{M_\star}}, \tag{I.52}$$

where K_{wind} and ω_{sat} are constant for a given star. The strength of the various terms is compared in Fig. I.2 for a Jupiter-Sun like system. This shows that angular momentum losses are far from being negligible, but including these effects in our model adds many additional free parameters (e.g. K_{wind} and ω_{sat} which are only weakly constrained, but also the lifetime of the circumstellar disk which determines

---

[3] As I kept C_1 in the time derivative of Eq. (I.25), this term is already implicitly included.

the initial spin rate of the star ; Bouvier et al. 1997). Thus, in order to keep the number of unknown as low as possible, I decided to do not take into account these additional terms in the general study described in the following sections. The initial angular momentum of the star used in our simulations can then directly be deduced from the observed one.

I.2.5 Tidal heating

One can see from Eq. (I.43) in § I that in the special case of a body in pseudo-synchronous rotation, as expected for fluid objects ($\varepsilon_1 = 0$, $\omega_1 = \omega_{eq}$), the tidal energy dissipation rate is given by

$$\dot{E}_{tid} = 2K_1 \left[N_a(e) - \frac{N^2(e)}{\Omega(e)} \right] \; ; \; (\omega_1 = \omega_{eq}). \tag{I.53}$$

The dissipated heat is deposited over the whole planet's interior.

For a rocky planet, however, the external gravitational potential created by its permanent quadrupole moment can cause its locking into synchronous rotation ($\omega_p = n$), and the dissipation rate reads in that case

$$\dot{E}_{tid} = 2K_1 \left[N_a(e) - 2N(e)x_p + \left(\frac{1+x_p^2}{2} \right) \Omega(e) \right] ; \; (\omega = n). \tag{I.54}$$

This equation fully agrees with Eq. (30) of Wisdom (2008) who calculated it for a homogeneous, incompressible with a radial displacement Love number $h_2 = 5k_2/3$. Note that our derivation does not require such an hypothesis and all the uncertainties in the radial distribution of material and its physical properties (e.g., density, compressibility, elasticity) are lumped into the k_2 parameter (Levrard 2008).

Appendix J

CHESS user guide

J.1 Goal

CHESS is a Code computing Hydrostatic Equilibrium Structure by Shooting method. It can basically run in two different modes:

- Find and compute a structure in hydrostatic equilibrium (HSE) for a given set of planetary parameters such as T_{atm}, P_{atm} (or T_{eff}, $\log g$ if a numerical grid is used for the atmospheric boundary condition), Y, M_c, ω_1, etc... In this mode, several quantities characterizing the structure are computed as outputs (P_c, T_c, R_p, $\bar{R}_p$, k_2, C_1, etc...).

- Can find the values of a specified set of parameters (M_c, ice to rock mass ratio, Y, dY/dm, ...) that fit best the observable parameters of the planet (R_{eq}, ω_p, J_2, J_4, J_6, Z_{atm}) by an optimized Newton-Raphson procedure.

J.2 Code Structure

J.2.1 Equations

To find the HSE, CHESS integrates the standard set of stellar structure equations in the Lagrangian form

$$\frac{\partial P}{\partial m} = -\frac{g}{4\pi \bar{r}^2} + \frac{\omega_p^2}{6\pi \bar{r}} + \varphi_\omega, \tag{J.1}$$

$$\frac{\partial \bar{r}}{\partial m} = \frac{1}{4\pi \bar{r}^2 \rho}, \tag{J.2}$$

$$\frac{\partial L}{\partial m} = \dot{\varepsilon} - T \frac{\partial \tilde{S}}{\partial t}, \tag{J.3}$$

$$\frac{\partial T}{\partial m} = \frac{T}{P} \frac{\partial P}{\partial m} \nabla_T, \tag{J.4}$$

where φ_ω is given by Eq. (E.17). In the code, the set of variables is $\{y_i\}_{i=1,4} = \{\log P, (\bar{r}/\bar{R}_p)^{\bar{\beta}}, (l/L_{int})^{\bar{\gamma}}, \log T\}$, and the parameter is the reduced Lagrangian mass $\mu = (m/M_p)^{\bar{\alpha}}$. Note that the term due to the centrifugal force in the pressure equation is valid to 3rd order (see Appendix E).

The equations solved thus read

$$\frac{\partial y_1}{\partial \mu} = \left[-\frac{GM_p^2}{4\pi\,\bar{\alpha}\,\bar{R}_p^4}\frac{\mu^{2/\bar{\alpha}-1}}{y_2^{4/\bar{\beta}}} + \frac{\omega_p^2 M_p}{6\pi\,\bar{\alpha}\,\bar{R}_p}\frac{\mu^{1/\bar{\alpha}-1}}{y_2^{1/\bar{\beta}}} + \frac{M_p\mu^{1/\bar{\alpha}-1}}{\bar{\alpha}}\varphi_\omega \right]\frac{10^{-y_1}}{\ln 10}, \tag{J.5}$$

$$\frac{\partial y_2}{\partial \mu} = \frac{\bar{\beta}\,M_p}{4\pi\,\bar{\alpha}\,\bar{R}_p^3}\frac{y_2^{1-3/\bar{\beta}}}{\rho\,\mu^{1-1/\bar{\alpha}}}, \tag{J.6}$$

$$\frac{\partial y_3}{\partial \mu} = \frac{\bar{\gamma}M_p}{\bar{\alpha}L_p}\frac{y_3^{1-1/\bar{\gamma}}}{\mu^{1-1/\bar{\alpha}}}\left(\dot{\varepsilon} - T\frac{\partial S}{\partial t}\right), \tag{J.7}$$

$$\frac{\partial y_4}{\partial \mu} = \frac{\partial y_1}{\partial \mu}\nabla_T, \tag{J.8}$$

The power law indices $\bar{\alpha}$, $\bar{\beta}$ and $\bar{\gamma}$ can be chosen so that the equations do not show any singularity at the boundaries. This is achieved using $\bar{\alpha} = 2/3$, $\bar{\beta} = 2$ and $\bar{\gamma} = 2/3$.

Because the luminosity cannot be calculated self-consistently without any knowledge on the evolution, some assumptions must be made. Here we will assume that the interior is strictly adiabatic. For planets below the deuterium burning limit, the luminosity can therefore be integrated as follows

$$l(m) = \int_{m=0}^{m}\left(\dot{\varepsilon} - T\frac{\partial \tilde{S}}{\partial t}\right)dm \approx -\frac{\partial \tilde{S}}{\partial t}\int_{m=0}^{m} T\,dm = -\bar{T}(m)\frac{\partial \tilde{S}}{\partial t}M_p, \tag{J.9}$$

defining a mean temperature $\bar{T}(m)$ (with $\bar{T} = \bar{T}(M_p)$). In our models with semi-convection, we will use this equation even if it is not strictly valid. To avoid adding a free parameter to be adjusted in our shooting method, we will go beyond this hypothesis and assume that "for the luminosity", the temperature profile follows a square law

$$T = T_c - x^2(T_c - T_{atm}), \tag{J.10}$$

$$\bar{T} = \frac{2}{3}T_c + \frac{1}{3}T_{atm}. \tag{J.11}$$

This means that, although the temperature profile is computed using Eq. (J.4), the luminosity is computed using

$$l(x) = -\frac{\partial \tilde{S}}{\partial t}\left(xT_c - \frac{x^3}{3}(T_c - T_{atm})\right),$$

$$\frac{\partial \tilde{S}}{\partial t} = -\frac{L_{int}}{\bar{T}\,M_p}. \tag{J.12}$$

J.2.2 Boundary conditions

With the set of equations described above, one needs only 3 initial conditions at each edge to compute a structure (not necessarily in HSE). In CHESS, these initial conditions are $r = 0$, $P = P_c$ and $T = T_c$ at the center and $\bar{r} = \bar{R}_p$, $P = P_{atm}$ and $T = T_{atm}$ at the outer edge. The Boundary conditions on the luminosity are already enforced by Eq. (J.12).

J.2.3 Parameter adjustment

When CHESS is searching for a structure in HSE, P_c, T_c and $\bar{R}_p$ are varied until the discrepancy at the mid point in the structure reaches zero to numerical precision.

The code can find the values fitting the observable constraints (R_{eq}, J_2, J_4) for any specified set of variables including up to 3 variables from : T_{atm} (or T_{int}), $\bar{Y}$, $\frac{dY}{dm}$, M_c, M_{rock}/M_c. At each step, new values of P_c, T_c and $\bar{R}_p$ are computed to satisfy the HSE.

J.3   Principal variables list

The main variables describing the planet physical structure are:

- `Mass_p`: Planet mass (M_p)

- `R_mean_g`: Mean radius of the $P = P_{atm}$ isobar ($\bar{R}_p$). If the rotation is set to zero, $\bar{R}_p = R_{eq} = R_p$.

- `R_equatorial`: Equatorial radius (R_{eq}).

- `lPc_g`: Log of central pressure ($\log P_c$).

- `lTc_g`: Log of central temperature ($\log T_c$).

- `lT_atm`: Log of temperature at the atmospheric boundary condition ($\log T_{atm}$).

- `lP_atm`: Log of pressure at the atmospheric boundary condition ($\log P_{atm}$).

- `Teff_p`: Planet effective temperature (T_{int})

- `Ltot_p`: Total luminosity (L_{int}). This is recomputed each time that either `R_mean_g` or `Teff_p` changes.

- `w_rot`: Angular velocity (ω_p)

- `m_rot_g`: dimensionless rotation parameter ($\frac{\omega_p^2 \bar{R}_p^3}{GM_p}$)

- `M_core_g`: Core mass (M_c).

- `x_core_g`: Ratio of core to total mass (M_c/M_p).

- `alpha_core_g`: Ratio of rocky core to total core mass (M_{rock}/M_c).

- `YHe_g`: Mean Helium and heavy elements mass ratio ($\bar{Y}'$, where $Y' = Y + Z$).

- `DYHe_g`: Mean Helium and heavy elements mass ratio gradient ($\frac{dY'}{dm}$).

- `f_YHe_mod`: Function to use to compute the Helium and heavy elements mass ratio at each point knowing `YHe_g` and `DYHe_g` (integer).

- `core_EOS`: EOS to use for the core (integer).

Unless stated otherwise, these variables are double precision real given in SI units (MKS system) and log is the decimal logarithm. These variables are contained in the module `Param_Global`. They are global variables used by all the subroutines to compute the structure without having to specify them as input variables. They are initialized by the loading subroutines in `load.f90`.

To run CHESS in different modes, the main program can access the module `Options` and switch the following parameters to the required value. They are listed here with their default value.

- `Param_io_channel=0`: =1 if the physical parameters are provided by the main program, =0 if CHESS must read them in the specified files.

- `EOS_init=0`: If = 1, the EOS for Hydrogen and Helium (SCvH) has already been loaded. = 0 for normal initialization.

- `ANEOS_init=0`: If = 1, ANEOS has already been loaded. =0 for normal initialization.

- `OpaCOND_init=0`: If = 1, COND opacities have already been loaded. =0 for normal initialization.

- `CONDALL_init=0`: If = 1, Conductive opacities have already been loaded. =0 for normal initialization.

- `atm_init=0`: If = 1, atmospheric boundary conditions have already been loaded. =0 for normal initialization.

- `what_should_I_do=-1`: If < 0 CHESS only carries out initialization (test mode), =0 compute HSE for the given parameters, =i>1 fit i parameters, with the i constraints.

- `FitParameter=['YHe','x_core','DYHe']`: parameters to constrain.

- `Constraint=['R_equa','J2','J4']`: Constraints to use.

- `use_atm_BC=1`: If =0 the program uses `lP_atm` and `lT_atm` given in the init file as external boundary conditions. If =1, CHESS will use the `atm_files` along with the specified `Teff_p` and `logg_p` (computed from `Mass_p` and `R_mean_g`) to infer the atmospheric Boundary Conditions.

- `write_res=1`: If = 0 does nothing, =1 writes the fitted parameters in the file specified in `chess.f90`.

- `write_struc=0`: If = 0 does nothing, =1 writes the structure in the file specified in `chess.f90` with the number of point given by `NbrPointOutput`, =2 writes the structure in an unformatted file compatible with the evolution code (thus `PrintOutFormat` must be 17)

- `write_mode=0`: If = 0 normal mode: The code writes only most useful quantities. =1, writes additional physical quantities (opacities, temperature gradients...)

- `write_figures=0`: If = 0 does nothing, =1 writes the figure functions in the file specified in `chess.f90` with the number of point given by `NbrPointOutput` (works only if `write_struc>=1`)

- `NbrPointOutput=300`: Number of grid points for the structure output.

- `PrintOutFormat=9`: Number of digits (after the coma) to print out in the `ResultStructure.dat` file. 17 is the max in double precision

Bibliography

Adams, E. R., Seager, S., & Elkins-Tanton, L. Ocean Planet or Thick Atmosphere: On the Mass-Radius Relationship for Solid Exoplanets with Massive Atmospheres. *ApJ*, 673:1160–1164, February 2008.

Alexander, M. E. The Weak Friction Approximation and Tidal Evolution in Close Binary Systems. *Ap&SS*, 23:459–510, August 1973.

Alibert, Y., Mordasini, C., & Benz, W. Extrasolar planet population synthesis. III. Formation of planets around stars of different masses. *A&A*, 526:A63+, February 2011.

Alibert, Y., Mordasini, C., Benz, W., & Winisdoerffer, C. Models of giant planet formation with migration and disc evolution. *A&A*, 434:343–353, April 2005.

Allard, F., & Hauschildt, P. H. Model atmospheres for M (sub)dwarf stars. 1: The base model grid. *ApJ*, 445:433–450, May 1995.

Allard, F., Hauschildt, P. H., Alexander, D. R., & Starrfield, S. Model Atmospheres of Very Low Mass Stars and Brown Dwarfs. *ARA&A*, 35:137–177, 1997.

Baines, P. G., & Gill, A. E. On thermohaline convection with linear gradients. *Journal of Fluid Mechanics*, 37:289–306, 1969.

Bakos, G. Á., et al. HAT-P-20b–HAT-P-23b: Four Massive Transiting Extrasolar Planets. *ArXiv e-prints*, August 2010.

Baraffe, I., Alibert, Y., Chabrier, G., & Benz, W. Birth and fate of hot-Neptune planets. *A&A*, 450:1221–1229, May 2006.

Baraffe, I., Chabrier, G., Allard, F., & Hauschildt, P. H. Evolutionary models for solar metallicity low-mass stars: mass-magnitude relationships and color-magnitude diagrams. *A&A*, 337:403–412, September 1998.

Baraffe, I., Chabrier, G., & Barman, T. Structure and evolution of super-Earth to super-Jupiter exoplanets. I. Heavy element enrichment in the interior. *A&A*, 482:315–332, April 2008.

Baraffe, I., Chabrier, G., & Barman, T. The physical properties of extra-solar planets. *Reports on Progress in Physics*, 73(1):016901–+, January 2010.

Baraffe, I., Chabrier, G., Barman, T. S., Allard, F., & Hauschildt, P. H. Evolutionary models for cool brown dwarfs and extrasolar giant planets. The case of HD 209458. *A&A*, 402:701–712, May 2003.

Barker, A. J., & Ogilvie, G. I. On the tidal evolution of Hot Jupiters on inclined orbits. *MNRAS*, 395:2268–2287, June 2009.

Barker, A. J., & Ogilvie, G. I. On internal wave breaking and tidal dissipation near the centre of a solar-type star. *MNRAS*, 404:1849–1868, June 2010.

Barman, T. S., Hauschildt, P. H., & Allard, F. Irradiated Planets. *ApJ*, 556:885–895, August 2001.

Batygin, K., & Stevenson, D. J. Inflating Hot Jupiters with Ohmic Dissipation. *ApJ*, 714:L238–L243, May 2010.

Bodenheimer, P., Lin, D. N. C., & Mardling, R. A. On the Tidal Inflation of Short-Period Extrasolar Planets. *ApJ*, 548:466–472, February 2001.

Borucki, W. J., et al. Characteristics of planetary candidates observed by Kepler, II: Analysis of the first four months of data. *ArXiv e-prints*, February 2011.

Bouvier, J., Forestini, M., & Allain, S. The angular momentum evolution of low-mass stars. *A&A*, 326: 1023–1043, October 1997.

Brouwer, D., & Clemence, G. M. *Methods of celestial mechanics*. 1961.

Burrows, A., Hubeny, I., Budaj, J., & Hubbard, W. B. Possible Solutions to the Radius Anomalies of Transiting Giant Planets. *ApJ*, 661:502–514, May 2007.

Burrows, A., et al. On the Radii of Close-in Giant Planets. *ApJ*, 534:L97–L100, May 2000.

Burrows, A., et al. A Nongray Theory of Extrasolar Giant Planets and Brown Dwarfs. *ApJ*, 491:856–+, December 1997.

Busse, F. H. A simple model of convection in the Jovian atmosphere. *Icarus*, 29:255–260, October 1976.

Caballero, J. A., et al. The substellar mass function in σ Orionis. II. Optical, near-infrared and IRAC/Spitzer photometry of young cluster brown dwarfs and planetary-mass objects. *A&A*, 470: 903–918, August 2007.

Cabrera, J., et al. Transiting exoplanets from the CoRoT space mission . XIII. CoRoT-13b: a dense hot Jupiter in transit around a star with solar metallicity and super-solar lithium content. *A&A*, 522: A110+, November 2010.

Caillabet, L., Mazevet, S., & Loubeyre, P. Multiphase equation of state of hydrogen from ab initio calculations in the range 0.2 to 5 g/cc up to 10 eV. *Phys. Rev. B*, 83(9):094101–+, March 2011.

Callen, H. *Thermodynamics: an introduction to the physical theories of equilibrium thermostatics and irreversible thermodynamics*. Wiley international edition. Wiley, 1960. URL http://books.google.fr/books\relax\unskip\kern.2em?id=v1OwAAAAIAAJ.

Campbell, J. K., & Anderson, J. D. Gravity field of the Saturnian system from Pioneer and Voyager tracking data. *AJ*, 97:1485–1495, May 1989.

Campbell, J. K., & Synnott, S. P. Gravity field of the Jovian system from Pioneer and Voyager tracking data. *AJ*, 90:364–372, February 1985.

Carter, J. A., & Winn, J. N. Empirical Constraints on the Oblateness of an Exoplanet. *ApJ*, 709:1219–1229, February 2010a.

Carter, J. A., & Winn, J. N. The Detectability of Transit Depth Variations Due to Exoplanetary Oblateness and Spin Precession. *ApJ*, 716:850–856, June 2010b.

Cassisi, S., Potekhin, A. Y., Pietrinferni, A., Catelan, M., & Salaris, M. Updated Electron-Conduction Opacities: The Impact on Low-Mass Stellar Models. *ApJ*, 661:1094–1104, June 2007.

Cébron, D., Moutou, C., Le Bars, M., Le Gal, P., & Farès, R. Tidal instability in exoplanetary systems evolution. *Detection and Dynamics of Transiting Exoplanets, St. Michel l'Observatoire, France, Edited by F. Bouchy ; R. Díaz ; C. Moutou ; EPJ Web of Conferences, Volume 11, id.03003*, 11:3003–+, February 2011.

Chabrier, G. *L'équation d'état en astrophysique*. 1990.

Chabrier, G., & Baraffe, I. Theory of Low-Mass Stars and Substellar Objects. *ARA&A*, 38:337–377, 2000.

Chabrier, G., & Baraffe, I. Heat Transport in Giant (Exo)planets: A New Perspective. *ApJ*, 661:L81–L84, May 2007.

Chabrier, G., & Baraffe, I. Structure and evolution of low-mass stars. *A&A*, 327:1039–1053, November 1997.

Chabrier, G., Baraffe, I., Leconte, J., Gallardo, J., & Barman, T. The mass-radius relationship from solar-type stars to terrestrial planets: a review. In E. Stempels, editor, *American Institute of Physics Conference Series*, volume 1094 of *American Institute of Physics Conference Series*, pages 102–111, February 2009. doi: 10.1063/1.3099078.

Chabrier, G., Barman, T., Baraffe, I., Allard, F., & Hauschildt, P. H. The Evolution of Irradiated Planets: Application to Transits. *ApJ*, 603:L53–L56, March 2004.

Chabrier, G., Gallardo, J., & Baraffe, I. Evolution of low-mass star and brown dwarf eclipsing binaries. *A&A*, 472:L17–L20, September 2007a.

Chabrier, G., Saumon, D., Hubbard, W. B., & Lunine, J. I. The molecular-metallic transition of hydrogen and the structure of Jupiter and Saturn. *ApJ*, 391:817–826, June 1992.

Chabrier, G., et al. Gaseous Planets, Protostars, and Young Brown Dwarfs: Birth and Fate. In Reipurth, B., Jewitt, D., & Keil, K., editors, *Protostars and Planets V*, pages 623–638, 2007b.

Chandrasekhar, S. *An introduction to the study of stellar structure*. Chicago, Ill., The University of Chicago press [1939], 1939.

Charbonneau, D., et al. A super-Earth transiting a nearby low-mass star. *Nature*, 462:891–894, December 2009.

Chauvin, G., et al. Deep imaging survey of young, nearby austral stars . VLT/NACO near-infrared Lyot-coronographic observations. *A&A*, 509:A52+, January 2010.

Chauvin, G., et al. A giant planet candidate near a young brown dwarf. Direct VLT/NACO observations using IR wavefront sensing. *A&A*, 425:L29–L32, October 2004.

Clairaut, A. C. *Théorie de la Figure de la Terre, Tirée des Principes de l'Hydrostatique*. Chez David Fils, Libraire, rue Saint-Jacques, à la plume d'or., 1743.

Correia, A. C. M., & Laskar, J. The four final rotation states of Venus. *Nature*, 411:767–770, June 2001.

Cox, J. P., & Giuli, R. T. *Principles of stellar structure*. 1968.

Daemgen, S., et al. Binarity of transit host stars. Implications for planetary parameters. *A&A*, 498: 567–574, May 2009.

Darwin, G. H. *Scientific Papers*. New York: Cambridge University Press, 1908.

Darwin, G. H. On the Secular Changes in the Elements of the Orbit of a Satellite Revolving about a Tidally Distorted Planet. *Royal Society of London Philosophical Transactions Series I*, 171:713–891, 1880.

Darwin, G. H. Earth, theory of the figure of the. *MNRAS*, 60:82–+, December 1899.

de Sitter, W. The Motions of the Lunar Perigee and Node and the Figure of the Moon. *Koninklijke Nederlandse Akademie van Weteschappen Proceedings Series B Physical Sciences*, 17:1309–1321, 1914.

Dobbs-Dixon, I., Lin, D. N. C., & Mardling, R. A. Spin-Orbit Evolution of Short-Period Planets. *ApJ*, 610:464–476, July 2004.

Eddington, A. S. *The Internal Constitution of the Stars*. 1926.

Efroimsky, M., & Williams, J. G. Tidal torques: a critical review of some techniques. *Celestial Mechanics and Dynamical Astronomy*, 104:257–289, July 2009.

Eggleton, P. P., Kiseleva, L. G., & Hut, P. The Equilibrium Tide Model for Tidal Friction. *ApJ*, 499: 853–+, May 1998.

Fabrycky, D., & Tremaine, S. Shrinking Binary and Planetary Orbits by Kozai Cycles with Tidal Friction. *ApJ*, 669:1298–1315, November 2007.

Fabrycky, D. C., Johnson, E. T., & Goodman, J. Cassini States with Dissipation: Why Obliquity Tides Cannot Inflate Hot Jupiters. *ApJ*, 665:754–766, August 2007.

Ferguson, J. W., et al. Low-Temperature Opacities. *ApJ*, 623:585–596, April 2005.

Ferraz-Mello, S., Rodríguez, A., & Hussmann, H. Tidal friction in close-in satellites and exoplanets: The Darwin theory re-visited. *Celestial Mechanics and Dynamical Astronomy*, 101:171–201, May 2008.

Fortney, J. J., Ikoma, M., Nettelmann, N., Guillot, T., & Marley, M. S. Self-consistent Model Atmospheres and the Cooling of the Solar System's Giant Planets. *ApJ*, 729:32–+, March 2011.

Fortney, J. J., Lodders, K., Marley, M. S., & Freedman, R. S. A Unified Theory for the Atmospheres of the Hot and Very Hot Jupiters: Two Classes of Irradiated Atmospheres. *ApJ*, 678:1419–1435, May 2008.

Fortney, J. J., Marley, M. S., & Barnes, J. W. Planetary Radii across Five Orders of Magnitude in Mass and Stellar Insolation: Application to Transits. *ApJ*, 659:1661–1672, April 2007.

Fortney, J. J., & Nettelmann, N. The Interior Structure, Composition, and Evolution of Giant Planets. *Space Sci. Rev.*, 152:423–447, May 2010.

Garaud, P., Ogilvie, G. I., Miller, N., & Stellmach, S. A model of the entropy flux and Reynolds stress in turbulent convection. *MNRAS*, 407:2451–2467, October 2010.

Gautier, D., Hersant, F., Mousis, O., & Lunine, J. I. Enrichments in Volatiles in Jupiter: A New Interpretation of the Galileo Measurements. *ApJ*, 550:L227–L230, April 2001.

Goldreich, P. On the eccentricity of satellite orbits in the solar system. *MNRAS*, 126:257–+, 1963.

Goldreich, P. Final spin states of planets and satellites. *AJ*, 71:1–+, February 1966.

Goldreich, P., & Soter, S. Q in the Solar System. *Icarus*, 5:375–389, 1966.

Goodman, J., & Lackner, C. Dynamical Tides in Rotating Planets and Stars. *ApJ*, 696:2054–2067, May 2009.

Greenberg, R. Frequency Dependence of Tidal q. *ApJ*, 698:L42–L45, June 2009.

Guillot, T. THE INTERIORS OF GIANT PLANETS: Models and Outstanding Questions. *Annual Review of Earth and Planetary Sciences*, 33:493–530, January 2005.

Guillot, T. The composition of transiting giant extrasolar planets. *Physica Scripta Volume T*, 130(1): 014023–+, August 2008.

Guillot, T. On the radiative equilibrium of irradiated planetary atmospheres. *A&A*, 520:A27+, September 2010.

Guillot, T., Burrows, A., Hubbard, W. B., Lunine, J. I., & Saumon, D. Giant Planets at Small Orbital Distances. *ApJ*, 459:L35+, March 1996.

Guillot, T., Gautier, D., Chabrier, G., & Mosser, B. Are the giant planets fully convective ? *Icarus*, 112: 337–353, December 1994.

Guillot, T., Stevenson, D. J., Hubbard, W. B., & Saumon, D. *The interior of Jupiter*, pages 35–57. 2004.

Guillot, T., et al. A correlation between the heavy element content of transiting extrasolar planets and the metallicity of their parent stars. *A&A*, 453:L21–L24, July 2006.

Hansen, B. M. S. On the Absorption and Redistribution of Energy in Irradiated Planets. *ApJS*, 179: 484–508, December 2008.

Hansen, C. J., & Kawaler, S. D. *Stellar Interiors. Physical Principles, Structure, and Evolution.* 1994.

Hebb, L., et al. WASP-12b: The Hottest Transiting Extrasolar Planet Yet Discovered. *ApJ*, 693:1920–1928, March 2009.

Heller, R., Leconte, J., & Barnes, R. Tidal obliquity evolution of potentially habitable planets. *A&A*, 528:A27, April 2011.

Hennebelle, P., & Chabrier, G. Analytical Theory for the Initial Mass Function: CO Clumps and Prestellar Cores. *ApJ*, 684:395–410, September 2008.

Henry, G. W., Marcy, G. W., Butler, R. P., & Vogt, S. S. A Transiting "51 Peg-like" Planet. *ApJ*, 529: L41–L44, January 2000.

Hood, B., Wood, K., Seager, S., & Collier Cameron, A. Reflected light from 3D exoplanetary atmospheres and simulation of HD 209458b. *MNRAS*, 389:257–269, September 2008.

Hori, Y., & Ikoma, M. Gas Giant Formation with Small Cores Triggered by Envelope Pollution by Icy Planetesimals. *ArXiv e-prints*, June 2011.

Hubbard, W. B. Thermal structure of Jupiter. *ApJ*, 152:745–754, June 1968.

Hubbard, W. B. Tides in the giant planets. *Icarus*, 23:42–50, September 1974.

Hubbard, W. B., & Marley, M. S. Optimized Jupiter, Saturn, and Uranus interior models. *Icarus*, 78: 102–118, March 1989.

Hubeny, I., Burrows, A., & Sudarsky, D. A Possible Bifurcation in Atmospheres of Strongly Irradiated Stars and Planets. *ApJ*, 594:1011–1018, September 2003.

Hut, P. Stability of tidal equilibrium. *A&A*, 92:167–170, December 1980.

Hut, P. Tidal evolution in close binary systems. *A&A*, 99:126–140, June 1981.

Huyghens, C. *Discours sur la cause de la pesanteur*. 1690.

Iaroslavitz, E., & Podolak, M. Atmospheric mass deposition by captured planetesimals. *Icarus*, 187: 600–610, April 2007.

Ibgui, L., & Burrows, A. Coupled Evolution with Tides of the Radius and Orbit of Transiting Giant Planets: General Results. *ArXiv e-prints*, February 2009.

Ibgui, L., Spiegel, D. S., & Burrows, A. Explorations into the Viability of Coupled Radius-Orbit Evolutionary Models for Inflated Planets. *ArXiv e-prints*, October 2009.

Jackson, B., Greenberg, R., & Barnes, R. Tidal Heating of Extrasolar Planets. *ApJ*, 681:1631–1638, July 2008.

Jeffreys, H. *The earth. Its origin, history and physical construction*. 1970.

Kaula, W. M. Tidal Dissipation in the Moon. *J. Geophys. Res.*, 68:4959–+, September 1963.

Kaula, W. M. Tidal Dissipation by Solid Friction and the Resulting Orbital Evolution. *Reviews of Geophysics and Space Physics*, 2:661–685, 1964.

Kepler, J. *Astronomia nova*. Kepler, J., 1609.

Kippenhahn, R., & Weigert, A. *Stellar Structure and Evolution*. Stellar Structure and Evolution, XVI, 468 pp. 192 figs.. Springer-Verlag Berlin Heidelberg New York. Also Astronomy and Astrophysics Library, 1990.

Knutson, H. A., Charbonneau, D., Noyes, R. W., Brown, T. M., & Gilliland, R. L. Using Stellar Limb-Darkening to Refine the Properties of HD 209458b. *ApJ*, 655:564–575, January 2007.

Krishnamurti, R. Low frequency oscillations in turbulent Rayleigh-Benard convection: laboratory experiments. *Fluid Dynamics Research*, 16:87–108, August 1995.

Lafrenière, D., et al. The Gemini Deep Planet Survey. *ApJ*, 670:1367–1390, December 2007.

Lai, D., Rasio, F. A., & Shapiro, S. L. Ellipsoidal figures of equilibrium - Compressible models. *ApJS*, 88:205–252, September 1993.

Lai, D., Rasio, F. A., & Shapiro, S. L. Equilibrium, stability, and orbital evolution of close binary systems. *ApJ*, 423:344–370, March 1994.

Laughlin, G., Crismani, M., & Adams, F. C. On the Anomalous Radii of the Transiting Extrasolar Planets. *ApJ*, 729:L7+, March 2011.

Leconte, J., Baraffe, I., Chabrier, G., Barman, T., & Levrard, B. Structure and evolution of the first CoRoT exoplanets: probing the brown dwarf/planet overlapping mass regime. *A&A*, 506:385–389, October 2009.

Leconte, J., & Chabrier, G. A new vision on giant planet interiors: the impact of double diffusive convection. *ArXiv e-prints*, January 2012.

Leconte, J., Chabrier, G., & Baraffe, I. Uncertainties in tidal theory: Implications for bloated hot Jupiters. In A. Sozzetti, M. G. Lattanzi, & A. P. Boss, editor, *IAU Symposium*, volume 276 of *IAU Symposium*, pages 248–251, November 2011a. doi: 10.1017/S1743921311020266.

Leconte, J., Chabrier, G., Baraffe, I., & Levrard, B. Is tidal heating sufficient to explain bloated exoplanets ? Consistent calculations accounting for finite initial eccentricity. *A&A*, 516:A64+, June 2010a.

Leconte, J., Chabrier, G., Baraffe, I., & Levrard, B. The radius anomaly in the planet/brown dwarf overlapping mass regime. *EPJ Web of Conferences*, 11:03004, 2011b.

Leconte, J., Lai, D., & Chabrier, G. Distorted, non-spherical transiting planets: impact on the transit depth and on the radius determination. *A&A*, 528:A41, April 2011c.

Leconte, J., et al. The Lyot Project Direct Imaging Survey of Substellar Companions: Statistical Analysis and Information from Nondetections. *ApJ*, 716:1551–1565, June 2010b.

Ledoux, P. Stellar Models with Convection and with Discontinuity of the Mean Molecular Weight. *ApJ*, 105:305–+, March 1947.

Levrard, B. A proof that tidal heating in a synchronous rotation is always larger than in an asymptotic nonsynchronous rotation state. *Icarus*, 193:641–643, February 2008.

Levrard, B., Winisdoerffer, C., & Chabrier, G. Falling Transiting Extrasolar Giant Planets. *ApJ*, 692: L9–L13, February 2009.

Levrard, B., et al. Tidal dissipation within hot Jupiters: a new appraisal. *A&A*, 462:L5–L8, January 2007.

Lyapunov, A. M. *Recherches dans la théorie de la figure des corps célestes*. 1903.

Lyon, S. P., & Johnson, J. D. SESAME: The Los Alamos National Laboratory Equation of State Database. *Los Alamos National Laboratory Technical Report*, LA-UR-92-3407, 1992.

MacDonald, G. J. F. Tidal Friction. *Reviews of Geophysics and Space Physics*, 2:467–541, 1964.

Mardling, R. A. Long-term tidal evolution of short-period planets with companions. *MNRAS*, 382: 1768–1790, December 2007.

Mardling, R. A., & Lin, D. N. C. Calculating the Tidal, Spin, and Dynamical Evolution of Extrasolar Planetary Systems. *ApJ*, 573:829–844, July 2002.

Marley, M. S., Fortney, J. J., Hubickyj, O., Bodenheimer, P., & Lissauer, J. J. On the Luminosity of Young Jupiters. *ApJ*, 655:541–549, January 2007.

Marois, C., Zuckerman, B., Konopacky, Q. M., Macintosh, B., & Barman, T. Images of a fourth planet orbiting HR 8799. *Nature*, 468:1080–1083, December 2010.

Mayor, M., & Queloz, D. A Jupiter-mass companion to a solar-type star. *Nature*, 378:355–359, November 1995.

McCullough, P. R., et al. XO-4b: An Extrasolar Planet Transiting an F5V Star. *ArXiv e-prints*, May 2008.

Meibom, S., & Mathieu, R. D. A Robust Measure of Tidal Circularization in Coeval Binary Populations: The Solar-Type Spectroscopic Binary Population in the Open Cluster M35. *ApJ*, 620:970–983, February 2005.

Mignard, F. Multiple expansion of the tidal potential. *Celestial Mechanics*, 18:287–294, October 1978.

Mignard, F. The evolution of the lunar orbit revisited. I. *Moon and Planets*, 20:301–315, May 1979.

Mignard, F. The evolution of the lunar orbit revisited. II. *Moon and Planets*, 23:185–201, October 1980.

Mihalas, D. *Stellar atmospheres /2nd edition/*. 1978.

Militzer, B., Hubbard, W. B., Vorberger, J., Tamblyn, I., & Bonev, S. A. A Massive Core in Jupiter Predicted from First-Principles Simulations. *ApJ*, 688:L45–L48, November 2008.

Miller, N., Fortney, J. J., & Jackson, B. Inflating and Deflating Hot Jupiters: Coupled Tidal and Thermal Evolution of Known Transiting Planets. *ApJ*, 702:1413–1427, September 2009.

Mirouh, G. M., Garaud, P., Stellmach, S., Traxler, A. L., & Wood, T. S. A new model for mixing by double-diffusive convection (semi-convection): I. The conditions for layer formation. *ArXiv e-prints*, December 2011.

Mordasini, C., Alibert, Y., & Benz, W. Extrasolar planet population synthesis I: Method, formation tracks and mass-distance distribution. *ArXiv e-prints*, April 2009.

Mordasini, C., Alibert, Y., Benz, W., & Naef, D. Giant Planet Formation by Core Accretion. In Fischer, D., Rasio, F. A., Thorsett, S. E., & Wolszczan, A., editors, *Astronomical Society of the Pacific Conference Series*, volume 398 of *Astronomical Society of the Pacific Conference Series*, pages 235–+, 2008.

Murray, C. D., & Dermott, S. F. *Solar system dynamics*. 1999.

Naef, D., et al. HD 80606 b, a planet on an extremely elongated orbit. *A&A*, 375:L27–L30, August 2001.

Neron de Surgy, O., & Laskar, J. On the long term evolution of the spin of the Earth. *A&A*, 318:975–989, February 1997.

Nettelmann, N., et al. Ab Initio Equation of State Data for Hydrogen, Helium, and Water and the Internal Structure of Jupiter. *ApJ*, 683:1217–1228, August 2008.

Newton, I. *Philosophiae naturalis principia mathematica, vol. 1 - 4*. Halley, E., 1687.

Ogilvie, G. I., & Lin, D. N. C. Tidal Dissipation in Rotating Solar-Type Stars. *ApJ*, 661:1180–1191, June 2007.

Oppenheimer, B. R., Kulkarni, S. R., Matthews, K., & Nakajima, T. Infrared Spectrum of the Cool Brown Dwarf Gl 229B. *Science*, 270:1478–1479, December 1995.

Padoan, P., & Nordlund, Å. The "Mysterious" Origin of Brown Dwarfs. *ApJ*, 617:559–564, December 2004.

Pál, A., et al. HAT-P-7b: An Extremely Hot Massive Planet Transiting a Bright Star in the Kepler Field. *ApJ*, 680:1450–1456, June 2008.

Pál, A., et al. Refined stellar, orbital and planetary parameters of the eccentric HAT-P-2 planetary system. *MNRAS*, 401:2665–2674, February 2010.

Peale, S. J., & Cassen, P. Contribution of tidal dissipation to lunar thermal history. *Icarus*, 36:245–269, November 1978.

Philosophical Transactions. A more particular account of those observations about jupiter, that were mentioned in numb. 8. *Philosophical Transactions*, 1(1-22):171–173, 1665.

Pollack, J. B., et al. Formation of the Giant Planets by Concurrent Accretion of Solids and Gas. *Icarus*, 124:62–85, November 1996.

Potekhin, A. Y. Electron conduction in magnetized neutron star envelopes. *A&A*, 351:787–797, November 1999.

Potekhin, A. Y., Baiko, D. A., Haensel, P., & Yakovlev, D. G. Transport properties of degenerate electrons in neutron star envelopes and white dwarf cores. *A&A*, 346:345–353, June 1999.

Radko, T. A mechanism for layer formation in a double-diffusive fluid. *Journal of Fluid Mechanics*, 497:365–380, December 2003.

Radko, T. What determines the thickness of layers in a thermohaline staircase? *Journal of Fluid Mechanics*, 523:79–98, January 2005.

Ragozzine, D., & Wolf, A. S. Probing the Interiors of very Hot Jupiters Using Transit Light Curves. *ApJ*, 698:1778–1794, June 2009.

Reif, F. *Fundamentals of Statistical and Thermal Physics*. McGraw-Hill International editions, 1985. ISBN 9781577666127. URL http://books.google.fr/books\relax\unskip\kern.2em?id=gYpBPgAACAAJ.

Rieutord, M. Evolution of Rotation in Binaries: Physical Processes (Invited Review). In A. Maeder & P. Eenens, editor, *Stellar Rotation*, volume 215 of *IAU Symposium*, pages 394–+, June 2004.

Rieutord, M. *Une introduction à la dynamique des fluides: cours avec exercices corrigés*. Enseignement de la physique. Masson, 1997. ISBN 9782225830587. URL http://books.google.fr/books\relax\unskip\kern.2em?id=MEV1PgAACAAJ.

Rieutord, M., & Zahn, J.-P. Ekman Pumping and Tidal Dissipation in Close Binaries: A Refutation of Tassoul's Mechanism. *ApJ*, 474:760–+, January 1997.

Rosenblum, E., Garaud, P., Traxler, A., & Stellmach, S. Turbulent Mixing and Layer Formation in Double-diffusive Convection: Three-dimensional Numerical Simulations and Theory. *ApJ*, 731:66–+, April 2011.

Sakashita, S., & Hayashi, C. Internal Structure and Evolution of Very Massive Stars. *Progress of Theoretical Physics*, 22:830–834, December 1959.

Saumon, D., Chabrier, G., & van Horn, H. M. An Equation of State for Low-Mass Stars and Giant Planets. *ApJS*, 99:713–+, August 1995.

Saumon, D., & Guillot, T. Shock Compression of Deuterium and the Interiors of Jupiter and Saturn. *ApJ*, 609:1170–1180, July 2004.

Saumon, D., Hubbard, W. B., Chabrier, G., & van Horn, H. M. The role of the molecular-metallic transition of hydrogen in the evolution of Jupiter, Saturn, and brown dwarfs. *ApJ*, 391:827–831, June 1992.

Schwarzschild, M., & Härm, R. Evolution of Very Massive Stars. *ApJ*, 128:348–+, September 1958.

Showman, A. P., & Guillot, T. Atmospheric circulation and tides of "51 Pegasus b-like" planets. *A&A*, 385:166–180, April 2002.

Spiegel, D. S., Burrows, A., & Milsom, J. A. The Deuterium-burning Mass Limit for Brown Dwarfs and Giant Planets. *ApJ*, 727:57–+, January 2011.

Stahler, S. W., Shu, F. H., & Taam, R. E. The evolution of protostars. I - Global formulation and results. *ApJ*, 241:637–654, October 1980.

Stern, M. E. The salt-fountain and thermohaline convection. *Tellus*, 12:172–+, May 1960.

Sterne, T. E. Apsidal motion in binary stars. *MNRAS*, 99:451–462, March 1939.

Stevenson, D. J. Semiconvection as the occasional breaking of weakly amplified internal waves. *MNRAS*, 187:129–144, April 1979a.

Stevenson, D. J. Turbulent thermal convection in the presence of rotation and a magnetic field - A heuristic theory. *Geophysical and Astrophysical Fluid Dynamics*, 12:139–169, 1979b.

Stevenson, D. J. Formation of the giant planets. *Planet. Space Sci.*, 30:755–764, August 1982.

Stevenson, D. J. Cosmochemistry and structure of the giant planets and their satellites. *Icarus*, 62:4–15, April 1985.

Stevenson, D. J., & Salpeter, E. E. The phase diagram and transport properties for hydrogen-helium fluid planets. *ApJS*, 35:221–237, October 1977a.

Stevenson, D. J., & Salpeter, E. E. The dynamics and helium distribution in hydrogen-helium fluid planets. *ApJS*, 35:239–261, October 1977b.

Sudarsky, D., Burrows, A., & Hubeny, I. Theoretical Spectra and Atmospheres of Extrasolar Giant Planets. *ApJ*, 588:1121–1148, May 2003.

Thompson, S., & Lauson, H. Improvements in the chart d radiation-hydrodynamics code iii: revised analytic equation of state. *Technical Report Technical Report SC-RR-61 0714, Sandia National Laboratories*, 1972.

Touma, J., & Wisdom, J. The chaotic obliquity of Mars. *Science*, 259:1294–1297, February 1993.

Touma, J., & Wisdom, J. Evolution of the Earth-Moon system. *AJ*, 108:1943–1961, November 1994.

Turner, J. Salt fingers across a density interface. *Deep Sea Research and Oceanographic Abstracts*, 14 (5):599 – 608, IN21, 609–611, 1967.

Udry, S., & Santos, N. C. Statistical Properties of Exoplanets. *ARA&A*, 45:397–439, September 2007.

Walin, G. Note on the stability of water stratified by both salt and heat. *Tellus*, 16:389–393, 1964.

Welsh, W. F., et al. The Discovery of Ellipsoidal Variations in the Kepler Light Curve of HAT-P-7. *ApJ*, 713:L145–L149, April 2010.

Winn, J. N., Holman, M. J., & Roussanova, A. The Transit Light Curve Project. III. Tres Transits of TrES-1. *ApJ*, 657:1098–1106, March 2007a.

Winn, J. N., et al. The Transit Light Curve Project. XI. Submillimagnitude Photometry of Two Transits of the Bloated Planet WASP-4b. *AJ*, 137:3826–3833, April 2009.

Winn, J. N., et al. Spin-Orbit Alignment for the Eccentric Exoplanet HD 147506b. *ApJ*, 665:L167–L170, August 2007b.

Wisdom, J. Tidal dissipation at arbitrary eccentricity and obliquity. *Icarus*, 193:637–640, February 2008.

Zahn, J. Tidal evolution of close binary stars. I - Revisiting the theory of the equilibrium tide. *A&A*, 220: 112–116, August 1989.

Zahn, J., & Bouchet, L. Tidal evolution of close binary stars. II - Orbital circularization of late-type binaries. *A&A*, 223:112–118, October 1989.

Zahn, J.-P., Ranc, C., & Morel, P. On the shape of rapidly rotating stars. *A&A*, 517:A7+, July 2010.

Zharkov, V. N., Makalkin, A. B., & Trubitsyn, V. P. Integration of Equations of the Theory of Planetary Figures. *Soviet Astronomy*, 17:97–+, August 1973.

Zharkov, V. N., & Trubitsyn, V. P. Theory of the Figure of Rotating Planets in Hydrostatic Equilibrium-A Third Approximation. *Soviet Ast.*, 13:981–+, June 1970.

Zharkov, V. N., & Trubitsyn, V. P. *Physics of planetary interiors*. 1978.

Zharkov, V. N., & Trubitsyn, V. P. *The physics of planetary interiors*. 1980.